Design, Fabrication and Characterization of Electrokinetically Pumped Microfluidic Chips for Cell Culture Applications

by

Tomasz Glawdel

A thesis
Presented to the University of Waterloo
in fulfillment of the
thesis requirement for the degree of
Master of Applied Science
in
Mechanical Engineering

Waterloo, Ontario, Canada, 2007

Author's Declaration

I hereby declare that I am the sole author of this thesis. This is a true copy of the thesis, including any required final revisions, as accepted by my examiners.

I understand that my thesis may be made electronically available to the public.

Abstract

Continuous perfusion cell culture chips offer the biomedical researcher unprecedented control over the microenvironment surrounding the cell which is not feasible with conventional static cell culture procedures. Applying microfluidics technology to these devices provides several benefits including increased fluid and media control, reduced consumption of reagents, continuous monitoring of cells and the potential for massively parallel experiments. In recent years, a number of microfluidic cell culture systems have been developed but most lack the flexibility and dynamic on-chip control required for injection of small sample of drugs. This is because off-chip syringe pumps are used as sources of fluid flow combined with an external flow network of valves and junctions which have a low temporal response and large dead volume. Electroosmotic flow is compact method of pumping fluids on-chip that takes advantage of an interfacial phenomenon that occurs on the microscale when a liquid comes in contact with a microchannel wall. With EOF flow rate and direction can be accurately controlled by simply manipulating applied voltages at the reservoirs of the microchannels.

In this work a new continuous perfusion cell culture chip is studied that utilizes electroosmotic pumping to control fluid flow. Electroosmotic flow is not typically used for living cells due to the inherently high electric fields that may harm cells. Problems associated with EOF and cells are solved by incorporating electroosmotic pumps (EO pumps) which generate an induced pressure driven flow in regions with cells. Several advantages of EO pumps include pulse free flow, quick flow control and precise movement of minute volumes of fluid. However, the high salt concentration in cell culture medium creates significant problems for EO pumps such as decreased flow rate due to low zeta potential, increased electrolysis due to large current draw, significant joule heating, bubble formation and polarization. Attempts to solve these problems with the proposed microfluidic chip are discussed.

The microfluidic chip is fabricated using soft lithography techniques developed as part of this work. To effectively incorporate EOF flow into a microfluidic application, the electroosmotic mobility for the microchannel/liquid must be well known. A new Y-channel design was developed to measure the mobility using the current monitoring technique. Two types of EO pumps were developed based on the integration of commercial ion exchange membranes and the fabrication of *in situ* gel salt bridges. The designs were modelled using a combination of numerical simulations with a commercial software program and compact circuit modelling. The

final pump design was tested with the cell culture medium and the performance curve was determined using fluorescent flow field visualization techniques. To improve stability, the EO pumps were operated in a constant current configuration and large electrode reservoirs with well buffered solutions were used. Improvements to the performance of the pumps were also attempted through various surface modifications of the PDMS to increase the electoosmotic mobility.

The pumps were integrated on-chip into a cell culture perfusion chip using 1D circuit modelling to describe the design and operation of the network. The chip is adaptable due to the flexibility of the EO pumps to work as both pressure sources and virtual valves for regulating the fluid flow. Fluorescent flow field visualization is used to demonstrate the operation of the pump in various modes. Experiments with rainbow trout gill cells (RT-gill W1) were performed in order to validate the use of EO pumps for cell culture. Several additional factors were considered including sterilization of the chip, cell attachment, and maintaining sterility while imaging the cells. The cells were continuously perfused with culture medium supplied by the EO pump. Results show that the cells are not affected by the presence of the EO pumps as the electric field is isolated from the cells. However, the pumps were only able to operate continuously for eight hours before electrolysis effects stopped fluid flow. As a proof of concept, this shows that it is feasible to use EO pumps within a cell culture network. Recommendations for a next generation design are also provided.

Acknowledgements

First and foremost, I would like to thank my advisor, Dr. Carolyn Ren, for giving me the opportunity to work under her guidance. Her passion, support and encouragement are truly appreciated.

My experience would not have been as meaningful without the other members at the Microfluidics and Biochip Lab. My gratitude goes to my fellow colleagues, Jay Taylor and Razim Samy, who worked closely with me to setup the Lab during the first year of my study. At the time, none of us had any experience in microfluidics or microfabriation but we persevered and solved many problems along the way. It was truly a great learning experience. I would also like thank others in the group who I worked closely with on several projects: Zeyad Almutairi who worked with me on the Y-channel electroosmotic mobility testing system and other members who provided valuable thoughts and insights during my thesis, Dr. Lin Gui, Doit Shao, Sean Wang, and Junjie Ou.

The interdisciplinary nature of my work has allowed me to have many great collaborators. I would like to thank Dr. Lucy Lee at Sir Wilfred Laurier University and her students Jackie Beitz, Mary Rose Bufalino and Bounmy Inthavong for their help in the biological aspect of this thesis. It has been a great pleasure to work with other researchers from a different discipline.

I would like to thank Ontario Graduate Scholarship program for their financial support during my first year of study and the National Sciences and Engineering Research Council for their financial support during my second year. As well, the support from Dr. Carolyn Ren is gratefully acknowledged.

I am deeply grateful to my friends and family whose support is truly appreciated. Especially, I want to thank Leanne Whiteford whose love, support, and company has been one of the greatest sources of strength for me. I would also like to extend thanks to several others: Doug Hillier, Mike Riemann, Cam Dunning, Brett Campbell.

Table of Contents

Author's Declaration ii

Abstract iii

Acknowledgements v

List of Figures xi

List of Tables xviii

Nomenclature xix

Chapter 1 Introduction 1

1.1 Background 1

1.1 Justification of Research and Objective of this Thesis 3

Chapter 2 Literature Review 7

2.1 Microfluidics for Chemical and Biological Applications 8

2.2 Microfluidic Transport Phenomenon 9

2.2.1 Electric Double Layer 10

2.2.2 Fluid Flow 13

2.2.2.1 Pressure Driven Flow 13

2.2.2.2 Electroosmotic Flow 15

2.2.2.3 Undesired Pressure Effects in Microfluidic Systems 20

2.2.3 Electrophoresis 22

2.2.4 Mass Transport 23

2.2.5 Heat Transfer 25

2.3 Design Techniques 27

2.3.1 Numerical Simulations 27

2.3.2 System Design Models 28

2.4 Fabrication of Microfluidic Devices 29

2.4.1 Glass and Silicon Devices 30

2.4.2 Polymer Devices 31

2.4.2 Soft-Lithography 31

2.5 Design Evaluation Methods 32

2.5.1 Temperature Measurements 32

2.5.2 Flow Field Measurements 33

2.5.3 Electroosmotic Mobility Measurements 34

2.5.3.1 Streaming Potential 34

2.5.3.2 Electroosmotic Flow 35
2.6 Micropumps 38
2.6.1 Mechanical Pumps 38
2.6.2 Non-Mechanical Pumps 41
2.6.3 Electroosmotic Pumps 42
2.7 Microfluidic Cell Culture 48
2.8 Summary 52
Chapter 3 Experimental Techniques for Design Characterization 53
3.1 Fluorescent Flow Field Visualization Methodology 53
3.2 Working Solutions 54
3.2.1 Solution Properties 54
3.2.2 Fluorescein Dye 55
3.2.3 Fluorescent Particles 55
3.3 Microscopy 56
3.4 Flow control 58
3.4.1 Syringe Pump 58
3.4.2 HV Power supply 58
3.5 Chip Holder 59
3.6 Flow Field Visualization 60
3.7 Channel Dimension Measurement 61
3.8 Safety 63
3.8.1 High Voltage Safety 63
3.8.2 Chemical Safety 63
Chapter 4 Designing Microfluidic Chips using Numerical Methods 64
4.1 1D Equivalent Circuit Modeling 64
4.2 COMSOL MULTIPHYSICS Numerical Models 70
4.2.1 Potential Field 72
4.2.2 Velocity Field 73
4.2.3 Concentration Field 73
4.2.4 Temperature Field 74
4.2.5 Coupling of Equations 74
4.4 Application of Numerical Models 75
4.4.1 Undesired Pressure Effects in Microfluidic Systems 75
4.3.2 Expansion Channel with Multiple Wall Materials under EOF 77

4.4 Summary 80
Chapter 5 Techniques Developed for Fabricating Microfluidic Chips: Soft Lithography, Multi Level Fabrication and Fluid Connectors. 81
5.1 Soft Lithography Overview 81
5.2 Master Fabrication 84
5.2.1 Mask Design 85
5.2.2 Substrate Selection 86
5.2.3 Spin Coating 87
5.2.4 UV exposure and Thermal Cross-linking 93
5.2.5 Development of Features 98
5.3 Multi-Level Fabrication Technique 98
5.4 Replica Molding with PDMS 100
5.4.1 Plasma Treatment and Bonding 101
5.5 Attaching Fluid Connectors and Reservoirs 103
5.6 Summary 106
Chapter 6 Design and Development of a Novel Y-channel Chip for Electroosmotic Mobility Measurements 107
6.1 Details of the Current Monitoring Method 107
6.2 The Y-Channel Design 110
6.2.1 Network Geometry and Dimensions 113
6.2.2 Improvements to the Slope Method 115
6.3 Numerical Modelling of Y-Channel Replacement 116
6.3.1 1D Displacement Model 116
6.3.2 2D COMSOL MULTIPHYSICS MODEL 120
6.4 Experimental Setup and Methods 123
6.4.1 Fabrication of Test Chips 123
6.4.2 Experimental Set up 125
6.4.3 Experimental Procedure 126
6.4.4 Data Analysis and System Errors 127
6.5 Experimental Results 128
6.5.1 Visualization of Switching Process 128
6.5.2 Validation of the Y-channel Design 129
6.5.3 Results for Various Solutions and Surface Treatments 130
6.6 Recommendations 132

Chapter 7 Design, Fabrication and Operation of Electroosmotic Pump..... 133
7.1 Background 133
7.2 Planar EO Pump Fundamentals 134
7.3 Fabrication of EO Pumps 137
7.3.1 General Fabrication Notes 137
7.3.2 Ion Exchange Membrane 137
7.3.3 Gel Salt Bridge 140
7.4 Flow Rate Measurements 143
7.5 Design Iterations 144
7.5.1 Preliminary Designs 1-EC and 2-EC 144
7.5.2 1st Generation EO Pump 145
7.5.3 2nd Generation EO Pump 147
7.5.4 3rd Generation EO Pump 148
7.5.5 4th Generation EO Pump 151
7.6 Further Design Evaluation 152
7.6.1 Network Dimensions of Master 153
7.6.2 Flow Rate Measurements 153
7.6.3 Electrolysis Effects 154
7.6.4 Joule Heating 155
7.6.5 Transport Phenomenon in with Gel 156
7.7 Improvements to Pump Performance 157
7.8 Summary and Recommendations 162
Chapter 8 Microfluidic Network for Cell Culture with Integrated EO Pumps..... 163
8.1 Cell Culture Microfluidic Network 163
8.2 Operation Modes of Network 165
8.3 1D Circuit Equivalency Network Analysis 167
8.4 Visualization of Network Operation Modes 170
8.5 Summary 173
Chapter 9 Testing of the EO pump Cell Culture Chip 174
9.1 Cell Culture Experimental Setup 174
9.1.1 Cell Line: RT-gill W1 174
9.1.3 Imaging System 175
9.2 General Experimental Procedure 175
9.2.1 Sterilization of Chip 177

9.2.2 Cell Seeding 179
9.2.3 System for Maintaining a Sterile Environment 180
9.2.4 Perfusion Setup 181
9.3 Experimental Results 182
9.3.1 Low Concentration Culture with Cells 182
9.3.2 On-chip Perfusion with EO pumps 183
9.4 Conclusions and Recommendations 187
Chapter 10 Conclusions and Recommendations 188
10.1 Contributions of this Thesis 188
10.1 Recommendations for Extension of Work 191
References 193
Appendix A: Circuit Equivalency Analysis 1-EC EO Pump 209
Appendix B: Circuit Equivalency Analysis 2-EC EO Pump 211
Appendix C: Chip Fabrication Procedure 213
Appendix D: Diverting flow to the cell chamber with the EO pump 219
Appendix E: EO Pump operation has no affect on other pump 220
Appendix F: EO Pump injection into main stream 221
Appendix G: Cell inflow during seeding 222

List of Figures

Figure 2.1 Schematic representation of the electric double layer (ED) near a charged solid surface (a) the non-uniform ion distribution and characteristics of the EDL and (b) the corresponding potential distribution with the Debye length and zeta potential (c) the corresponding ionic densities in the Debye layer.....11

Figure 2.2 Schematic representation of the ideal electroosmotic flow (EOF) in a microchannel with negatively charged walls. The velocity profile is "plug" like with the centerline value equation to the Helmholtz-Smoluchowski slip condition. The charge density profile is shown in dark grey and the thickness of the EDL by the dashed line. The body force is only exerted on the ions in the EDL. No pressure drop occurs across the channel in this ideal case. The external electric field is setup by a DC power source.....15

Figure 2.3 Diagram of the mechanisms contributing to undesired pressure driven flow generated by differences in Laplace and hydrostatic forces. 21

Figure 2.4 T-channel micromixer: two streams are brought together in a single mixing channel under laminar flow conditions. Mixing occurs cross-stream only through diffusion. 24

Figure 2.5 Temperature dependence of several fluid properties (water): dielectric constant, thermal conductivity, electrical conductivity, electroosmotic mobility (due to dielectric constant and viscosity changes) and viscosity non-dimensionalized with the value at 25°C. 27

Figure 2.6 A schematic of the current monitoring method for measuring the electroosmotic mobility of a test solution. The motion of the interface is traced as the current changes due to the difference in electrical conductivity between the two solutions. If the two solutions are close together in concentration then the current drop is linear and the velocity can be determined from the displacement time. 37

Figure 2.7 Reciprocating micropump design with check valves. A diaphragm is deflected by an actuator which either increases or decreases the volume of fluid in the pump chamber. Check valves are used to allow for flow in only one direction during the discharge and suction strokes.....39

Figure 2.8 (a) Schematic of the working principal of an EO pump. Electrodes apply an electric field in a limited region of the microchannel generating EOF. A pressure gradient forms to continue pumping the fluid through the rest of the microchannel. Due to the gradient a back-pressure flow also occurs in the EOF region. (b) Q-P characteristics of an EO pump for various applied electric fields Q_{max} is when there is not load on the channel and P_{max} when there is no net flow (c) Relationship between flow rate and the applied current.....43

Figure 2.9. Typical setup of a microfluidic perfusion system consisting of a microfluidic chip connected to a pump and outlet reservoir. 51

Figure 3.1 Example of the use of fluorescein dye to study hydrodynamic focusing in a cross microchannel design. Images are inverted (black represents fluorescence): (a) Fluorescein dye is added to all streams to show the geometry of the intersection and (b) dye is added only to the sample stream

in order to demonstrate the degree of focusing. Images obtained with assistance from Barsam Tabrizi. 55

Figure 3.2 Fluorescence microscopy system used for flow visualization and dimension measurements. The system consists of an Olympus GX-71 inverted microscope, CCCD camera, halogen and mercury lamps and computer. Also included are the HV power sequencer and syringe pump. 57

Figure 3.3 Custom chip mount fabricated for the PDMS microfluidic chips and distributing the applied electric potentials from the HV power sequencer. 59

Figure 3.4 Streamline patterns obtained from particle streak velocimetry technique for pressure driven flow in (a) T-junction and (b) corner. 61

Figure 3.5 Particle tracking combined with particle streak velocimetry to measure flow velocity in a 500μ(w)X100μm(h) channel under pressure driven flow. Exposure time is 200ms and time between images is 515ms. The long exposure time makes it easier to determine which particles are moving. The streak length for the highlighted particle is 32.5μm and the distance traveled for the tracking particle is 84.32μm which corresponds to velocities of 162.5μm/s and 163.5μm/s. 61

Figure 3.6 Example microchannel profile obtained from the profilometer (SJ-400, Mitutoyo). The angular profile is due to tilting of the silicon wafer caused by bowing. 62

Figure 4.1 Schematic of (a) example double cross microfluidic network under combined EOF/pressure driven flow and (b) the equivalent electric and flow field resistance networks. 65

Figure 4.2 (a) Schematic of the hydraulic resistance element incorporated into a straight channel (b) Plot of the ratio of undesired pressure driven flow to EOF flow (solid line) and the corresponding change in hydraulic resistance width (dashed line) for variations in height of the hydraulic resistance. Calculations performed for ΔP=48.8Pa, ΔV=500V, L=5cm, w=100μm, L_{hyd}=1cm. 76

Figure 4.3 Schematic of the expansion channel composed of two different materials. Material 1 composes the top and sides of the channel and Material 2 the bottom. The first material supports a strong EOF, $\mu_e=7x10^{-8}$ $m^2/(Vs)$, while the second supports no EOF, $\mu_e=0$ $m^2/(Vs)$). The equivalent 1D circuit model of the microchannel is included as well. 77

Figure 4.4 A slice plot of the velocity field (m/s) in the expansion channel calculated using COMSOL Multiphysics. An arrow plot is overlaid to show the flow direction. 79

Figure 5.1 Illustration of the procedure for fabricating a microfluidic chip using soft lithography. 83

Figure 5.2 Photomask used for calibrating the SU-8 photolithography process. 84

Figure 5.3 Example of calibrations results for 100μm channels with SU-8 2005 (7.5μm). Exposure doses of (a) 200 mJ/cm^2 (b) 300 mJ/cm^2 (c) 400 mJ/cm^2 (d) 500 mJ/cm^2 (e) 600 mJ/cm^2 . (a)-(c) show considerable lift off (white features) and poor edge definition, (d) and (e) are nearly optimal but (e) has slightly better characteristics and was considered the optimum exposure dose. 85

Figure 5.4 Images of the transparency photo masks: (a) bubbles and scratches in the Mylar film (b) photomask printed in house (c) 20000dpi print obtain from CAD/Art Services.....85

Figure 5.5 Substrates used for master fabrication: 4x3" glass slide, microscope slide, 4" silicon wafer. 87

Figure 5.6 Thickness versus spin speed curve for SU-8 obtained during calibration.....89

Figure 5.7 Illustration of the spin coating procedure (a) static dispensing (b) dynamic dispensing. 90

Figure 5.8 Images of (a) the spin coating system and (b) a close up of the dispensing system and technique.....91

Figure 5.9 Exposure dose for a film thickness that must be entered into the UV exposure system. 94

Figure 5.10 Demonstration of loses through the UV assemble measured using a UV radiometer.....94

Figure 5.11 Emission spectrum of (a) UV light source 6295 1000W Hg(Xe) Ozone Free Lamp [Oriel Product Training Manual] (b) transmission spectrum of Float Glass 49220 filter [Omega Optical].....95

Figure 5.12 Illustration of (a) Fresnel diffraction effect on exposure with gap and (b) resulting structure with negative sloping side walls. 96

Figure 5.13 Cracking of SU-8 features and lift-off caused by CTE mismatch during cooling. 97

Figure 5.14. Schematic showing the oxidation of PDMS and subsequent bonding and liquid contact phenomenon.....102

Figure 5.15 Nano-port components (Upchurch Scientific) used for interfacing with external flow network.....104

Figure 5.16 Luer type polypropylene components used to interface with PDMS chips. 105

Figure 6.1 A schematic of the current monitoring method for measuring the electroosmotic mobility of a test solution.....108

Figure 6.2. A schematic of the principals governing the Y-channel design for performing current monitoring experiments.....111

Figure 6.3 Current plot obtained from an experiment with 1mM KCl and the Y-channel design. The current draw falls when the low concentration solution replaces the high (L/H) and vice versa (H/L). Complete replacement of the solution is marked by a plateau in the current.....112

Figure 6.4 Dimensions of the Y-channels used for the current monitoring experiments. 114

Figure 6.5 Equivalency model used for the 1D analysis of the displacement process in the Y-channel.....117

Figure 6.6 1D equivalence model results for the Y-channel model with ζ=-80mV (a) Current draw for concentration ratios (c_2/c_1) 0.95, 0.9, 0.8, 0.7, 0.6, 0.5 with equal electroosmotic mobility between the two solutions. (b) Pressure generated at the interface as it travels through the channel for different concentration ratios. (c) Current raw for a conductivity ratio of (c_2/c_1=0.95)

and electroosmotic mobility ratios (μ_{e2}/μ_{e1}) 1, 0.95, 0.9, 0.8, 0.7, 0.6, 0.5. (d) Flow rate through the microchannel during the displacement for different electroosmotic mobility ratios. 119

Figure 6.7 Error for calculating the electroosmotic mobility from the current draw for electroosmotic mobility ratios (a) slope method (b) total length method compared to the "test" solution and (c) slope method (b) total length method compared to the average electroosmotic mobility of the two solutions. 119

Figure 6.8 Time-lapse contour plot of the concentration at the intersection for the numerical simulation during the displacement process at times (t=0, 0.5, 1, 1.5, 2, 5, 60s). The low concentration solution (dark) replaces the high concentration solution (light).....121

Figure 6.9 Contour plot of the electric field and arrow plot of the velocity field at the intersection for the numerical simulation during at t=5s. A strong electric field appears near the inside corner of intersection. 122

Figure 6.10 Current draw plots for 10mM KCl ($D=2x10^{-9}m^2/s$, ζ=-47mV) from the 1D model, numerical simulation and experimental results. Experimental results obtained for 10mM KCl in PDMS/PDMS chip with HEMA treatment, measured zeta potential from analysis ζ=-47mV.....122

Figure 6.11 Photography of a complete PDMS/glass Y-channel chip used for current monitoring experiments.....125

Figure 6.12 Schematic of the experimental setup for the Y-channel current monitoring experiments, courtesy Zeyad Almutairi.....125

Figure 6.13 Matlab GUI used to analyze the current monitoring data. The user selects the pre, post and displacement times for analysis. 127

Figure 6.14 Time-lapse images of the displacement process with 100μM fluorescein dye added to 10mM KCl solution for an applied potential of 1000V. Images are taken at approximately t=0, 400m, 600ms, 1s, 2s, 10s after the switch. 129

Figure 6.15 Zeta potential measured using the Y-channel design for various fluids in PDMS/PDMS (P/P) and PDMS/glass (P/G) chips. Dark columns are for calculations using the slope method and light the total length method. Error bars represent a 90% confidence level.....131

Figure 7.1 Schematic of the 1-EC pump design describing the electrical and flow fields. 134

Figure 7.2 Schematic of a 2-EC EO pump design describing the electric and flow fields.....135

Figure 7.3 Diagram of Nafion membrane fabrication. Membrane is placed over top of the reservoir connecting to the microchannel. During this process a bubble would often get trapped under the membrane eliminating any electrical connection with the fluid below. 138

Figure 7.4. Schematic of the transient operation of Nafion/PDMS EO Pump device.....139

Figure 7.5 Diagram of the procedure for fabricating gel salt bridges within the microchannel network. 141

Figure 7.6 Phase contrast image of gel salt bridge integrated into the chip using a photopolymerization technique. PDMS posts in the mold help anchor the gel when exposed to high pressure differentials.....141

Figure 7.7. Fabrication issues with the gel salt bridge fabrication (a) poor gel to PDMS bonding without Bind-Silane treatment (b) gel solution residue left behind due to insufficient flushing (c) plasticizer residue from Tygon tubing covalently bonded to the PDMS surface (d) PDMS lift-off from glass substrate after flushing with 10%NaOH (v/w). 142

Figure 7.8 3D models of the 1-EC and 2-EC pump designs initially fabricated and tested. 145

Figure 7.9 Comparison of the flow rate vs. current draw for the 1-EC and 2-EC pump designs (1X TBE working fluid with gel salt bridge) compared with approximations from the 1D models presented in Appendix A and B. Dimensions measured with profilometer: EOF channel 500µm W and 5.8µm H and fluid properties λ_b=0.13 S/m and ζ=47mV.....145

Figure 7.10 Diagram of the 1st generation EO pump designed. Also included are images of the PDMS microchannel mold in various regions of the pump. 146

Figure 7.11 Numerical simulation result of the normalized electric field as a surface plot along with streamlines for the 1st generation EO pump. Gel posts were left out of the model in order to simplify the meshing.....147

Figure 7.12 Diagram of the 2nd generation EO pump design with inset showing the fabricated network in PDMS. 147

Figure 7.13 Numerical simulation result of the normalized electric filed and streamlines for the 2nd generation EO pump design. 148

Figure 7.14 Diagram of the 3rd generation EO pump design with insets showing the fabricated network in PDMS. 149

Figure 7.15 Numerical simulation result of the normalized electric filed and streamlines for the 3rd generation EO pump design. 149

Figure 7.16 Numerical simulation results of the 3rd generation EO pump design (a) flow field with arrow plot indicating the flow direction (b) pressure field within the EO pump. 150

Figure 7.17 Diagram of the 4th generation EO pump design with insets showing the fabricated network in PDMS. 151

Figure 7.18 Numerical simulation results of the 3rd generation EO pump design (a) flow field with arrow plot indicating the flow direction (b) pressure field within the EO pump. 152

Figure 7.19 Flow rate measurements of the 4th generation EO pump with L15ex and buffers in the electrode reservoir 1XTBE and Bufferall refer to Chapter 3 for details on these solutions. 153

Figure 7.20 Numerical simulation (2D) of PDMS/glass chip with EOF channels under joule heating. The dimensions of the channel are 3.5mm and 2.7µm. The joule heating is entered as a volumetric heating for 500µA for L15ex λ_b=1.1 S/m, where the temperature coefficient is 2%/°C. Three cases were studied: (top) top surface h=10 W/m^{2}K, bottom T=22°C, (middle) top surface h=10 W/m^{2}K, bottom h=200 W/m^{2}K and (bottom) top surface h=10 W/m^{2}K, bottom h=10 W/m^{2}K 156

Figure 8.1 Schematic of the microfluidic network design with integrated EO pumps used for cell culture experiments. Insets show the fabricated design at specific location in the network. 164

Figure 8.2 Fabricated chip PDMS with dye solution added to the channels to illuminate the microfluidic network. 164

Figure 8.3 The possible operational modes for the microfluidic network (a) EO pump operates independently (b) EO pumps regulate flow from another principal source to the cell culture chambers (c) EO pumps inject fluid continuously or discretely into the main fluid flow. 166

Figure 8.4 1D circuit equivalent network of the microfluidic cell culture chip with two EO pumps. 167

Figure 8.5 Location in the network where the videos were taken during experiments. 171

Figure 8.6 Field of view of video #1. On the right a close up of the network geometry in the video indicating the flow direction and locations of the EO pump and cell chamber channels.....171

Figure 8.7 Field of view of video #2. On the right a close up of the network geometry in the video indicating the flow direction and locations of the EO pump and cell chamber channels.....172

Figure 8.8 Field of view of video #3. On the right a close up of the network geometry in the video indicating the flow direction and locations of the EO pump and cell chamber channels.....172

Figure 9.1 Schematic of the procedure for setting up the microfluidic chip for cell culture. 176

Figure 9.2 Gel shrinking and separation (highlighted red) from the PDMS wall caused by flushing the chip with 70% ethanol solution for sterilization. 178

Figure 9.3 System for maintain sterile microfluidic network outside the bio hood using specialized bottles and caps for the reservoirs.....180

Figure 9.4 Experimental setup of the chip on the phase contrast microscope for EO pumping with the microfluidic chip showing (a) the laptop, HV supply and microscope (b) a close up of the microscope, microfluidic chip, holder and sterile bottle system. 181

Figure 9.5 Phase contrast images during the osmolarity test with RT-gill W1 cells. Cells were subject to various concentrations of L15ex (100%, 50%, 25%) over a 7 day period. Courtesy Jackie Bietz. 182

Figure 9.6 Phase contrast images of cells in the chamber (a) immediately after infusing cells into the chamber and (b) 2.5 hrs later cells have mostly attached to the fibronectin coated glass substrate and (c) cells seeded in a conventional static cell culture flask for comparison. The small black areas in the cell are the nucleus. 184

Figure 9.7 Phase contrast images of cells while EO pump perfusion was applied with L15ex medium. The same group of cells was photographed at several time intervals after starting perfusion (a) 0hrs (b) 2 hrs (c) 5hrs and (d) 18hrs.....185

Figure 9.8 Voltage plot of EO pump during cell culture test. Highlighted area shows the drastic increase in applied voltage caused by electrolysis effects. 186

Figure A.1 Schematic of the 1-EC pump design describing the electrical and flow fields. 209

Figure B.1 Schematic of the 2-EC pump design describing the electrical and flow fields. 211

Figure D.1 Field of view of video #1. On the right a close up of the network geometry in the video indicating the flow direction and locations of the EO pump and cell chamber channels.....219

Figure E.1 Field of view of video #2. On the right a close up of the network geometry in the video indicating the flow direction and locations of the EO pump and cell chamber channels.....220

Figure F.1 Field of view of video #3. On the right a close up of the network geometry in the video indicating the flow direction and locations of the EO pump and cell chamber channels.....221

List of Tables

Table 4.1 Variation of the EDL displacement thickness for a symmetric electrolyte as a function of ionic energy parameter. The equivalent zeta potential is included as a reference. 68

Table 5.1 Suggested components and set up for the pneumatic dispenser (EFD). 91

Table 6.1 Channel dimensions of all silicon masters used in fabricating Y-channel chips for electroosmotic mobility measurements. Right to left refers to the three designs fabricated on one master when the main channel of the Y-channel design is pointing away from the observer. 124

Table 6.2 Comparison of electroosmotic mobility measurements obtained with the Y-channel design and those published by Venditti *et al.* (2006). For 50mM $NaHCO_3/Na_2CO_3$ the reference value refers to a straight channel measurement obtained internally. 130

Table 7.1 Comparison of experimental (Exp), 3D numerical results (Num. Model) and 1D circuit analysis results for 1XTBE with the 3rd generation pump design. 151

Table 7.2 Results of current monitoring experiments for: (a) L-15ex at 21 °C, PDMS/PDMS channel, (b) 50 % L-15ex at 24.4°C, PDMS/PDMS channel, (c) L15ex with 10%FBS at 24.3 °C, PDMS/glass, (d) L15ex 10%FBS at 45 °C , PDMS/glass. Results courtesy Zeyad Almutari. 158

Nomenclature

Acronyms:

1D	One Dimensional
2D	Two Dimensional
3D	Three Dimensional
AC	Alternating Current
CAD	Computer Aided Design
CCD	Charged Coupled Device
CFD	Computational Fluid Dynamics
DAQ	Data Acquisition
DC	Direct Current
DI	De-ionized
DPI	Dots per inch
EC	Electrode Channel
EDL	Electric Double Layer
EOF	Electroosmotic Flow
EO	Electroosmotic (pump)
EPPS	3-[4-(2-Hydroxyethyl)-1-piperazinyl]propanesulfonic acid
FBS	Fetal Bovine Serum
HEPES	4-(2-hydroxyethyl)-1-piperazineethanesulfonic acid
HEMA	poly(2-hydroxyethyl methacrylate
HV	High Voltage
IPA	Isopropyl Alcohol
LMQ	Low Molecular Weight
LOC	Lab-on-a-Chip
MEMS	Micro Electro-Mechanical Systems
MOPS	3-(N-morpholino)propanesulfonic acid
NA	Numerical Aperture
PAA	Poly(acrylamide)
PC	Poly(carbonate)
PCR	Polymerase Chain Reaction
PDMS	Poly(dimethylsiloxane)

PEB	Post Exposure Bake
PGMEA	Propylene Glycol Methyl Ether Acetate
PMMA	Poly(methyl methacrylate)
PSV	Particle Streak Velocimetry
PTV	Particle Tracking Velocimetry
SB	Soft Bake
TAE	Tris/acetate/EDTA
TBE	Tris/Borate/EDTA.
TCMS	trimethylchlorosilane
µPIV	Micro Particle Image Velocimetry
µTAS	Micro Total Analysis Systems
UP	Ultra Pure
UV	Ultraviolet

Mathematical Symbols:

a	Radius (capillary, sphere) (m)
A_c	Cross-sectional Area (m^2)
c_i	Concentration of ith species (mol/m^3)
c_p	Specific heat capacity (J/KgK)
D	Diffusion Coefficient
e	Electron charge ($e=1.602 \times 10^{-19}$ C)
$\vec{E}$	Electric field vector (V/m)
E_x, E_y, E_z	Electric field strength in x, y, z direction (V/m)
F	Faradays Constant (96485 C/mol)
$\vec{F}$	Body force vector (N/m^3)
g	Gravity acceleration ($9.81\ m/s^2$)
G	Geometric factor
f_i	Form factor
h	Height (m)
I	Current Draw (A)
I_c	Conduction current (A)
I_s	Streaming current (A)
k	Thermal Conductivity (W/mK)

k_b	Boltzmann's Constant ($1.3806503 \times 10^{-23}$ m^2 kgK/s^2)
L	Length (m)
N	Number (images, capillaries)
n_o, n_∞	Bulk concentration (mol/m^3)
n_{oEQV}	Equivalent concentration to KCL (mol/m^3)
p,P	Pressure (Pa)
Pe	Peclet number
P_w	Wetted perimeter (m)
Q	Flow rate (m^3/s)
$\dot{Q}$	Joule heating (W/m^3)
v_{res}	Reservoir volume (m^3)
Q_{eof}	Electroosmotic flow rate (m^3/s)
Q_p	Pressure flow rate (m^3/s)
r_m	Radius of meniscus (m)
Re	Reynolds number
R_e	Electrical resistance (ohms)
R_{ehyd}	Electrohydrodynamic resistance (s/m^3V)
R_{hyd}	Hydrodynamic resistance (s/m^3Pa)
R_i	Volumetric reaction rate (mol/m^3)
T	Temperature (K)
w	Width (m)
$\dot{W}_{P,\max}$	Maximum pressure work (W)
$\vec{u}$	Velocity Vector (m/s)
$\vec{u}_{eof}$	Electroosmotic velocity vector (m/s)
$\vec{u}_{ep}$	Electrophoretic velocity vector (m/s)
u_x, u_y, u_z	Velocity in x, y, z directions (m/s)
V	Electric potential (V)
z	Valence of ion
α	Thermal coefficient
δ^*	Displacement thickness (m)
ε_o	Permittivity of free space ($8.8541878176 \times 10^{-12}$ $C^2N^{-1}m^{-2}$)
ε_r	Relative permittivity

ε_{BM}	Error due to Brownian Motion
ε_T	Total error
κ	Debye Hückel parameter
λ_b, λ_{fluid}	Bulk conductivity (S/m)
λ_d	Debye layer thickness (m)
λ_s	Surface conductivity (S)
σ	Bulk conductivity (S/m)
ρ	Density (kg/m^3)
ρ_e	Net charge density (C)
ϕ	Electric potential (V)
η	Efficiency
τ_{dep}	Time until depletion (s)
μ	Viscosity (Ns/m^2)
μ_{eof}	Electroosmotic mobility (m^2/Vs)
μ_{ep}	Electrophoretic mobility (m^2/Vs)
Ψ	Electric potential in electric double layer (V)
γ	Surface tension (N/m)
ζ	Zeta potential (V)
Δt	Time difference
ΔV	Voltage difference

Chapter 1

Introduction

1.1 Background

Over the past decade the development of Lab-on-a-chip (LOC) devices or micro-Total Analysis Systems (μTAS) has been the focus of intense research by the academic community. These devices are capable of scaling multi-step chemical and biological processes down to a chip only a few centimetres in size. The benefits of miniaturization and integration include lower fluid consumption, greater analysis control, shorter reaction times, increased sensitivity, and higher throughput and reduced cost. Several applications exist for LOC and μTAS systems including drug discovery, drug delivery, clinical diagnostics, genetics research, chemical synthesis, cellular analysis, and bioweapons detection [Dittrich *et al.* (2006)]. However, the greatest potential of LOC devices lies in the development of new techniques that utilize microscale phenomenon to perform experiments that are impossible on the macroscale.

A typical LOC device consists of a network of microchannels and microfluidic components such as valves, mixers, and pumps connected together to perform a specific function. Combined with micro-electronic sensors and other analysis tools these device are fully automated systems. Original microfluidic devices were fabricated in silicon and glass using pre-existing technology available from the microelectronics and MEMS industry. The expansion of microfluidics coincided with the development of a new technique for fabricating polymer devices that was accessible to anyone in biology, chemistry and engineering. Soft lithography refers to the fabrication of chips from polydimethylsiloxane (PDMS) using a specialized casting technique [Xia and Whitesides (1998)]. Masters fabricated using photolithography can have multi-dimensional features allowing for complex microfluidic components to be transferred to the PDMS mold. Due to the relatively low cost and speed of soft lithography it is ideal method for rapidly prototyping new devices.

The ability to scale down macroscale fluid handling components such as pumps, valves and mixers to the microscale is vital to the future success of LOC devices. Scaling down macro scale components is easier said then done since new phenomenon on the microscale begins to dominate the physics of a device; however, this also opens up the possibility of exploiting microscale

phenomenon to manipulate fluids and particles using pressure forces, electric fields, magnetic fields , capillary forces, optical forces, and chemical forces. Micropumps are one of these types of components that have been developed using non-mechanical transport effects such as electrohydrodynamics, electrokinetics, acoustic streaming and magnetohydrodynamics [Laser and Santiago (2004)]. Electroosmotic (EO) pumps are a subset of non-mechanical pumps that leverage the surface charge and the electric double layer (EDL) that forms at a solid/liquid interface. The liquid phase can be set in motion by applying an electric field tangential to the microchannel wall. EO pumps posses several features that are tailored for microfluidics including pulsed free flow, almost instant flow control, reversible operation and precise movement of minute volumes of fluid (μL-pL) by simply manipulating applied voltages. The development of EO pumps has primarily focused on devices for drug delivery and microfluidic flow control.

One application for LOC devices is the development of microfluidic cell culture systems. Traditional static culture systems, where cells are incubated in a flask, are unable to successfully simulate the *in vivo* microenvironment that cell communities form in tissues. Microfluidic cell culture systems have garnered great interest from the biomedical community looking to gain added functionality and control that is only possible with a miniaturized system. Culturing cells at the microscale provides unparalleled control over the cellular microenvironment including the perfusion of soluble factors such as nutrients and oxygen, creation of mechanical strain through shear stress, cell-cell interaction and design of the extra cellular matrix [El-Ali *et al.* (2006)]. Continuous perfusion microfluidic devices also posses the additional advantage of reduced consumption of reagents, continuous monitoring of cells and the potential for massively parallel experiments. The development of microfluidic cell culture systems will be critical in the exploration of new biological diagnostic tools for biomedical and pharmaceutical research.

Microfluidics and LOC systems are still in their infancy and a great deal of work still needs to be done before this technology becomes a standard among the biomedical field. Significant challenges still exist, especially for applications with cells on chip. Therefore, it is important to continue exploring new and interesting methods for solving these problems in order to advance the progress of LOC devices.

1.1 Justification of Research and Objective of this Thesis

Several PDMS microfluidic cell culture chips have been developed in recent years with the ability to provide medium perfusion with gas exchange and temperature regulation [Kim *et al.* (2006); Hung *et al.* (2005); Wu *et al.* (2006); Futai *et al.* (2006)]. However, most of these designs have a rigid microchannel system where flow is fixed to each chamber. External syringe pumps and valves connected to the chip are used to control the fluid. This setup does not permit quick and efficient flow control that may be required for dynamic studies involving the careful injection of small amounts of fluid such as drugs into the cell chamber. If several drugs are to be supplied simultaneously, the standard system would require multiple syringe pumps to operate independently greatly increasing the size and complexity of the experimental setup. Furthermore, pressure driven flow from a syringe pump tends suffers from longer delay times when valving due to the elasticity of the tubing and polymer channels.

Besides pressure driven flow, the most common pumping method for microfluidic chips is electroosmotic flow (EOF). EOF pumping is a compact method of pumping fluids in microfluidic chips where flow rate and direction can be accurately controlled by simply manipulating applied voltages at the reservoirs. However, EOF pumping has not been directly applied to cell culture for a variety of reasons; mostly notably the high electric field associated with EOF is hazardous to cells. Although the advantages of EOF can still be realized by utilizing electroosmotic pumps (EO) which generate pressure driven flow from EOF. The electric field is then confined to the EOF region of the pump and will not affect the cells. EO pumps posses several features that are valuable for dynamic applications including quick response time, reversible operation and precise volume control.

One of the negative aspects of EO pumps is that their performance depends greatly on the fluid being pumped. The optimum fluid is one that has a low conductivity and high electroosmotic mobility. However, cell culture medium is saline based and contains high concentrations of ions (e.g. 100mM NaCl) which magnifies the problems associated with EO pumps: (a) significant joule heating due to large current draw, (b) reduced pump performance due to lower zeta potentials and (c) large amounts of electrolysis and bubble formation which reduces stability and operation time. However, considering the advantages that integrated EO pumps may offer it is worthwhile to try and minimize many of the problems and apply EO pumps to cell culture. Therefore, the objective of this work is to investigate the possibility of combining on-chip electroosmotic pumps in a microfluidic cell culture network.

The goals of this thesis are as follows:

1. Develop a procedure for fabricating microfluidic chips in PDMS using soft lithography techniques.
2. Design a system for measuring the electrokinetic properties of various fluids of interest including those used for cell culture.
3. Design and fabricated integrated EO pumps on-chip that can pump cell culture solutions for prolonged periods of time.
4. Implement the EO pumps into a cell culture network and demonstrate the benefit of using these pumps for controlling fluid flow.
5. Test the effect of using EO pumps on cells through experimentation.
6. Evaluate the performance of the EO pumps for cell culture and suggest recommendations for future design iterations.

In Chapter 2, an overview of microfluidics is provided discussing the benefits of miniaturizing current chemical and biological systems. This is followed by a discussion of the major transport phenomenon influencing microfluidic chip design: fluid flow, mass transport and heat transfer. Details on the various fabrication techniques are provided for silicon/glass based devices and polymer devices including soft-lithography. Numerical methods for design microfluidic chips using finite element modelling and system level modelling with 1D circuit equivalency models is presented. Techniques for evaluating microfluidic chips in terms of measuring fluid flow, temperature and electrokinetic properties of microchannels are presented. A review of micropumps is provided with specific focus on electroosmotic pumps. This is followed by a summary of cell culture in microfluidic chips discussing the major component and requirements.

In Chapter 3, the experimental setup and procedures used throughout this thesis are summarized. This includes techniques and equipment for performing flow field visualization using fluorescent microscopy, measuring solution properties, measuring microchannel dimensions and generating pressure driven and electroosmotic flow.

In Chapter 4, numerical tools used to design and develop microfluidic chips are presented. Details are provided for full 2D/3D modeling of microfluidic phenomenon such as fluid flow (pressure and electroosmotic), species transport and heat transfer using the commercial software program COMSOL Multiphysics. As well, simplified global system models are developed for fluid flow in

complex microfluidic networks using 1D circuit equivalency analysis. Both of these numerical tools are used extensively to design the electroosmotic pump and cell culture network.

In Chapter 5, the procedures developed for fabricating poly (dimethylisiloxane) (PDMS) microfluidic chips using soft lithography techniques are presented. This chapter provides specific protocols for fabricating PDMS chips including master fabrication, replica molding, chip bonding and attaching chip to world interfaces such as reservoirs and fluid connectors. Procedures for fabricating multi-level level channels are presented as well. These microfabrication techniques are used extensively to fabricate the EO pump and cell culture chips. Problems that were encountered and their solutions are offered as guidance to future researchers.

In Chapter 6, a novel Y-channel chip design is developed for measuring the electroosmotic mobility of microchannels using the current monitoring technique. The new Y-channel design demonstrates superior performance over the traditional straight channel design in terms of sharper start and end points and higher throughput. Additional measures were taken to improve the performance by the suppressing the negative effects of undesired pressure driven flow, electrolysis and joule heating. The Y-channel was designed and evaluated using numerical simulations and 1D circuit modeling. The performance of the Y-channel was validated by comparing with straight channel measurements presented in literature. Afterwards the Y-channel design was applied to measure the electrokinetic properties of several fluids relevant to biomedical applications.

In Chapter 7, the development process of the EO pump is discussed. This includes fabrication techniques for integrating ion exchange membranes into PDMS chips. Two types of EO pumps were developed: one based on the use of commercial ion exchange membranes and the other on integrated membranes fabricated inside the chip. Using a combination of full 3D modeling and 1D equivalent circuit modelling several EO pumps were designed with successive improvements to the fabrication and overall performance. The performance of the EO pumps was tested flow with the cell culture medium used in this study. The high salt concentration in cell culture medium creates significant problems for EO pumps such as decreased flow rate due to low zeta potential, increased electrolysis due to high current draw, significant joule heating, bubble formation and polarization. Attempts to solve these problems are presented.

In Chapter 8, the design of a microfluidic cell culture network with integrated EO pumps is described. The network demonstrates the flexibility of using integrated EO pumps to regulate fluid flow on-chip. A 1D circuit model is developed to describe the three potential modes of operation of the microfluidic chip. Experimental results in the form of fluorescent flow field visualization movies are presented to show the operation of the microfluidic chip in these three modes.

In Chapter 9, the microfluidic cell culture chip is applied to test the feasibility of using EO pumps by culture rainbow trout gill cells. As part of this work procedures for attaching the cells and sterilizing the chip are presented. A system for maintaining sterility outside the bio hood while visualizing the cells was developed and is discussed. Experimental results with the cells are presented and the performance of the EO pump is evaluated.

In Chapter 10, a summary of this work is presented and recommendations for improving the current design are provided. These recommendations focus on improvements to the EO pump in order to increase flow rate combined with suggestions for designing the microfluidic cell culture network.

Chapter 2

Literature Review

Developing a Lab-on-a-Chip device is truly a multi-disciplinary task pulling knowledge from biology, chemistry, mechanical engineering, physics, and electrical engineering. What role does the mechanical engineer play? Well the mechanical engineer can assist in the design of various components that constitute a microfluidic network including pumps, valves, connectors, channels and sensors. A mechanical engineer can apply computational fluid dynamics techniques to study and optimize various physical phenomenon and transport processes such as fluid flow, mass transport and heat transfer; as well as developing techniques for metering these transport processes. The mechanical engineer can also provide valuable knowledge in fabricating, packaging and manufacturing microfluidic devices. Therefore, the mechanical engineer has a lot to offer, and plays a vital role in the development of Lab-on-a-Chip and μTAS systems.

This chapter provides the background information required for understanding the process for developing a microfluidic chip for cell culture with integrated electroosmotic pumps. The advantages of using microfluidics to improve current chemical and biological assays are introduced. This is followed by a discussion regarding the relevant phenomenon affecting chip design on the microscale including fluid flow, both pressure and electrokinetic, mass transport and heat transfer. Techniques for designing microfluidic devices using numerical simulations and system level modelling are presented. This is followed by a review of fabrication techniques for microfluidic devices, particularly, polymer devices fabricated from PDMS using soft lithography. Methods for evaluating the performance of microfluidic devices in terms of measuring fluid flow, heat transfer and electrokinetic properties of surfaces for electroosmotic flow are presented. A summary of micropumps, both mechanical and non-mechanical, is provided, followed by a more focused review of the general principals behind electroosmotic pumps. Finally, a review is provided for the development of microfluidic cell culture systems.

2.1 Microfluidics for Chemical and Biological Applications

Applying microfluidics to conduct biochemical research has a number of significant advantages. The reduction in scale brings the size of the device down to the level of the materials to be analyzed. This allows for greater sensitivity, automation, reductions in processing times for diffusion and chemical reactions, and higher throughput through parallelization. The volume of fluids required is very small, typically on the order of pico-litres to nano-litres, thus reagent and analytes consumption is reduced. In addition, the higher surface-to-volume ratios of the microfluidic components provide unprecedented control over heat transfer. The domain of Lab-on-a-Chip (LOC) or micro Total Analysis Systems (μTAS) involves integrating several microfluidic components such as cytometers, separators, mixers, bioreactors and detectors together on a single device. By directly connecting these components there is no loss or degradation of the sample as it passes through each transition. Miniaturization also provides a means for making many diagnostic systems portable. [Dittrich *et al.* (2006); Tabeling (2003); Whitesides (2006); Stone *et al.* (2004)]

Over the last 10 years, interest in microsystems from the chemistry and biomedical field has propelled the development of microfluidic and LOC devices. A number of review articles outline the development and progress of LOC: Vilkner *et al.* (2004), Abgrall and Gué (2007); Dittrich *et al.* (2006); Sia and Whitesides (2003); Chin *et al.* (2006); Haeberle and Zengerle (2007); Erickson and Li (2004). Several LOC devices already exist for performing biological analysis such as DNA replication [Zang *et al*. (2006)], cell sorting and detection [Applegate e*t al.* (2006)], blood typing [Kim *et al*. (2006)] and micro-environmental control for cellular studies [Hung *et al.* (2005)]. To integrate separate processes together into a fully functional LOC requires a number of fundamental microfluidic components which have also been reviewed: micropumps [Laser and Santiago (2004)], microvalves [Oh and Ahn (2006)], micromixers [Nguyen and Wu (2005)] and interconnects or what are known as chip-to-world interfaces [Fredrickson and Fan (2004)]. At the present, LOC and microfluidic is beginning a transition period from concept to reality. A variety of commercial devices are currently on the market from such companies as Agilent Technologies (2100 Bioanalyzer), Caliper Life Sciences (Lab Chip 90) and BioRad Laboratories (Experion) just to name a few.

However, several issues still exist for LOC devices: (a) practical issues such as contamination, blockages, interfacing (b) lack of optimization of current components such as pumps, valves, mixers ect. (c) problems with extracting samples which are often dilute (d) fabrication and material issues and (e) complete system integration issues and (f) a lack of standardization [Whitesides (2006); Abgrall and Gué (2007)]. These problems are similar to those faced by the microelectronics industry during its infancy. A great deal of work still needs to be done, and in a few years we should see the incorporation of LOC technology in many fields.

2.2 Microfluidic Transport Phenomenon

A wide variety of phenomena occur in microfluidic devices, many of which are irrelevant on the macroscale but play an important role in microscale systems. For example, gravitational forces become negligible in the microscale, and instead surface forces and electrostatic forces increase in dominance. In addition, exploiting the available microscale phenomenon opens up new functionality and design possibilities that were not possible with previous macroscale devices.

Although microfluidics involves fluid flow in microchannels that are small (10-100μm), the intermolecular distance of liquids is approximately 0.3μm and the continuum hypothesis is still valid. Therefore, physical quantities such as mass, momentum and energy are associated with mesoscopic volumes. However, this theory breaks down for nano-channel configurations where the system size approaches the molecular scale. The Reynold's numbers ($\mathrm{Re} = \rho UL/\mu$) typically encountered in microfluidics are small (Re<1) and the flow in most situations is laminar. Consequently, inertia forces can be neglected which linearilizes the Navier-Stokes equations and allows for superposition of various closed-formed solutions. Eliminating the non-linearity creates the sense that solving the Navier-Stokes equations is mundane; however, the multiple physical phenomena that must be considered in a microfluidic analysis increases the complexity of many problems. In addition, the length scales encountered can range from several nanometres (such as the electric double layer) to several centimetres over the length of a microchannel. The reduction in length scales also introduces interfacial phenomenon that can be used for pumping fluids such as electroosmotic flow and electrophoresis. One of the consequences of low Reynold's number flow is that mixing can be quite difficult on the microscale. Without the chaotic mixing regime created by turbulent flow, mixing in microfluidics is dominated by diffusion which can result in long mixing times and lengths. However, there is not a characteristic order of magnitude for the Peclet number ($Pe = UL/D$) as a wide range of Peclet numbers are encountered for different mixing particles.

In the following discussion a brief review is provided for the relevant phenomena important to this work including fluid flow (pressure and electroosmotic), mass transport and heat transfer. For a more detailed discussion on fluid flow refer to the texts by White (1999, 1974) and for heat transfer Incropera and DeWitt (2002). Texts available for electrokinetic flow include Hunter (1981), Masliyah (1994), Probstein (1994), Tabeling (2005) and Li (2004). These texts are complemented with several review articles discussing the abundance of phenomenon utilized in microfluidics: Squires and Quake (2005), Beebe *et al.* (2002), Stone *et al.* (2004), Ghosal (2004), de Mello (2006), Ho and Tai (1998) and Wong *et al.* (2004).

2.2.1 Electric Double Layer

One of the most important physical phenomena in microfluidics is the formation of the electric double layer. When a solid surface comes in contact with an aqueous solution an electric charge develops at the interface. The surface charge influences the nearby ions in the solution attracting counter-ions and repelling co-ions creating a non-uniform ionic distribution near the interface known as the electric double layer (EDL). Several chemical mechanisms generate the surface charge including ionization, ion adsorption and ion dissolution [Masliyah (1994); Hunter (1981); Probstein (1994)].

Helmholtz (1879) performed the earliest study on the nature of the EDL and proposed that the charged interface is surrounded by two condensed planes of oppositely charged ions. In reality, thermal forces spread out the ions and create a diffuse region outside the internal layer of ions. Gouy (1910) and Chapman (1913) applied the kinetic molecular theory to the diffuse region of ions and determined the electric potential and charge distributions using the Poisson-Boltzmann equation of statistical physics. The Gouy-Chapman model treats the ions as point charges, however, this is not entirely true because ions have a finite size that limits the distance they can approach a surface. To resolve this issue Stern (1924) divided the EDL into two regions, an inner compact layer where the size of the ions is considered and an outer diffuse layer where the Gouy-Chapman model is still applied.

The Stern model of the EDL is shown in Figure 2.1. In the Stern layer (compact), counter-ions experience a strong electrostatic force that essentially immobilizes the ions. Ions outside the Stern plane experience a weaker electrostatic attraction and represent the mobile phase of the EDL. The boundary separating the mobile and immobile portions of the EDL is known as the Stern plane.

The electric potential generated at this plane is called the zeta potential (ζ). Because the zeta potential is located at the division between the mobile/immobile phases it is an important parameter for analyzing a variety of electrokinetic phenomenon. The thickness of the diffuse region of the EDL is characterized by the Debye length:

$$\lambda_d = \left(\frac{\varepsilon_r \varepsilon_o k_b T}{e^2 \sum z_i^{\,2} n_{i\infty}} \right)^{1/2} \qquad \textbf{(2.1)}$$

where ε_r is the relative permittivity, ε_o =8.854x10^{-12} C/Vm is the permittivity of a vacuum, k_b=1.381x10^{-23} m^{2}kg/s^{2}K is Boltzmann's constant, e=1.602x10^{-19} C is the charge of an electron, T is the temperature (K), z is the ion valence and $n_{i\infty}$ is the bulk ion density. Note that the thickness of the EDL depends only on the solution properties and ranges from 1nm for high concentration solutions (100mM) to 300nm for pure water. Within the EDL the presence of surplus ions results in a higher conductivity than the bulk fluid; this effect is termed the surface conductance and is represented by a thin conducting sheet along the wall.

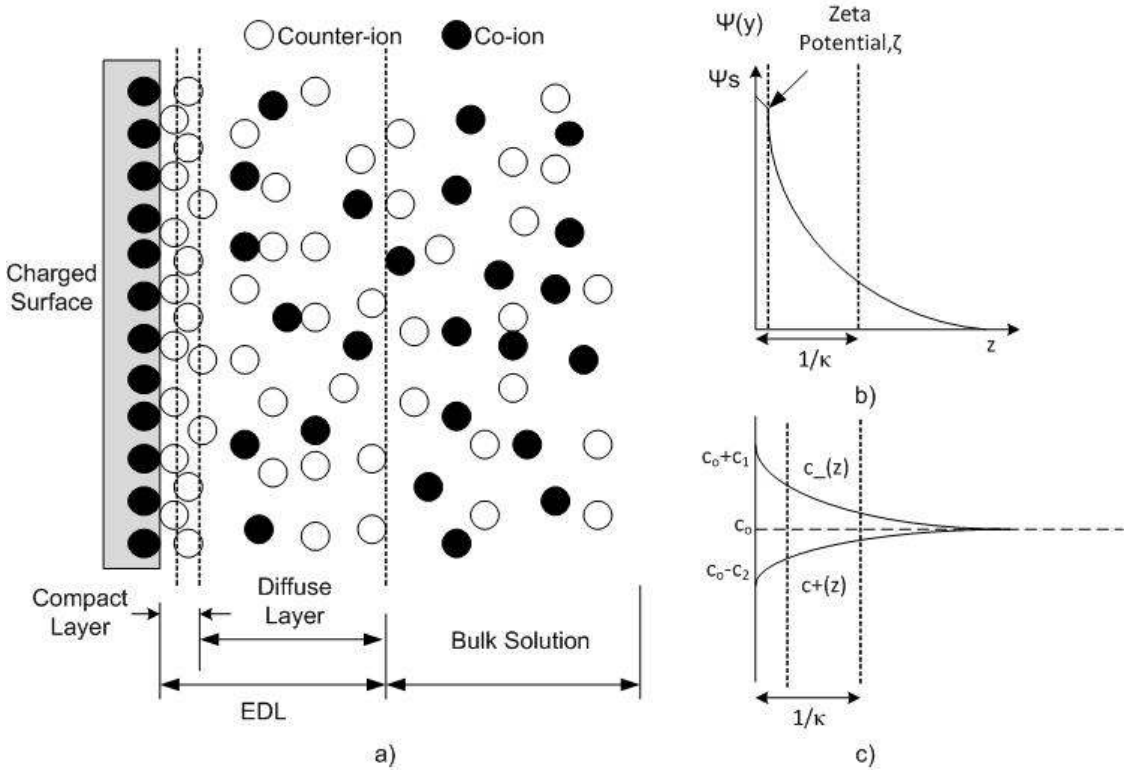

Figure 2.1 Schematic representation of the electric double layer (ED) near a charged solid surface (a) the non-uniform ion distribution and characteristics of the EDL and (b) the corresponding potential distribution with the Debye length and zeta potential (c) the corresponding ionic densities in the Debye layer.

As mentioned before, the electric potential and net charge density in the EDL are described by the Poisson-Boltzmann equation which gives the electric field within a dielectric medium:

$$\nabla \cdot (\nabla \psi) = \frac{-\rho_e}{\varepsilon_r \varepsilon_o} \qquad \textbf{(2.2)}$$

The net charge density, ρ_e, is the sum of negative and positive ions in the solution:

$$\rho_e = \sum_i z_i e n_i \qquad \textbf{(2.3)}$$

Assuming that the Boltzmann distribution is valid, the ionic concentration in the EDL is given by:

$$n_i = n_{i\infty} \exp\left(\frac{-z_i e \psi}{k_b T}\right) \qquad \textbf{(2.4)}$$

where n_i is the specific number of the *i-th* ion. Combining the last two equations leads to the Poisson-Boltzmann equation:

$$\nabla \cdot (\nabla \psi) = \frac{-\sum_i^N z_i e n_o \exp\left(\frac{-z_i e \psi}{k_b T}\right)}{\varepsilon_r \varepsilon_o} \qquad \textbf{(2.5)}$$

For most microfluidic applications involving microchannels the appropriate boundary conditions for solving Eqn. 2.5 are $\psi = \zeta$ at the shear plane and the assumption that $\psi \to 0$ as $x \to \infty$. However, this is not the case for nano channels where over-lapping boundary layers invalidate the assumption of uniform bulk properties far from the wall [Pennathur and Santiago (2005)]. Numerical techniques are usually employed to solve the Poisson-Boltzmann explicitly for complex solutions in order to determine the net charge density and electric potential distribution. Analytical solutions are possible for a few cases where simplified assumptions are justified such as symmetric electrolytes and a low surface charge (Debye-Hückel approximation). Electrokinetic phenomena arise when an externally applied electric field exerts a force on the mobile ions in the EDL generating relative motion between the solid and liquid phases. The electrokinetic phenomena relevant to microfluidics include electroosmotic flow, streaming potential and electrophoresis.

2.2.2 Fluid Flow

Modelling of fluid flow in microchannels is extremely important for designing new microfluidic devices. In this thesis, the liquids of interest are assumed to be Newtonian, incompressible and constant viscosity. The fluid flow is governed by the Navier-Stokes equations consisting of the continuity equation [White (1999)]:

$$\nabla \cdot \vec{u} = 0 \qquad \textbf{(2.6)}$$

and the momentum equation:

$$\rho\left[\frac{\partial \vec{u}}{\partial t} + \left(\vec{u} \cdot \vec{\nabla}\right)\vec{u}\right] = -\vec{\nabla}p + \mu\vec{\nabla}^2\vec{u} + \vec{F} \qquad \textbf{(2.7)}$$

where $\vec{u}$ is the velocity vector, ρ is the density, p is the pressure, μ is the viscosity and $\vec{F}$ is the body force vector. When inertial forces are small compared to viscous forces, as is the case for microfluidics, the inertial term on the left hand side is negligible, leaving the Stoke's approximation:

$$\rho\frac{\partial \vec{u}}{\partial t} = -\vec{\nabla}p + \mu\vec{\nabla}^2\vec{u} + \vec{F} \qquad \textbf{(2.8)}$$

If the time scale of the flow is small then the acceleration term on the left hand side may also be neglected. This linearizes the governing fluid equations and permits the superposition of elementary solutions for a given flow. The body forces can include a variety of effects, many of which have been utilized to pump fluids in microchannels, including gravity, electrostatics (electroosmotic flow, electrohydrodynamic flow, electrowetting), magnetism (magnetohydrodynamic, magnetocaloric), surface tension (capillary force), rotation (centrifugal) and acoustics [Squires and Quake (2005); Tsai and Sue (2007); Laser and Santiago (2003); Stone *et al.* (2004)]. The following subsections outline the two main flows relevant to this thesis: pressure driven flow and electroosmotic flow.

2.2.2.1 Pressure Driven Flow

Due to the low Reynold's numbers encountered in microfluidics, in most cases it is safe to assume that the flow is strictly laminar and reversible. Under these conditions, flow in a microchannel of arbitrary shape can be expressed by the Hagen-Poiseuille law:

$$Q = \frac{\Delta p}{R_{hyd}} \qquad \textbf{(2.9)}$$

where Q is the flow rate, p the pressure and R_{hyd} the hydrodynamic resistance. The hydrodynamic resistance depends on the dimensions of the microchannel and the viscosity. As an example, consider flow between parallel plates which is a valid approximation for rectangular microchannels with high aspect ratios. Applying the steady state Navier-Stokes equations the velocity profile is simple parabolic flow:

$$u_x = \frac{\Delta p}{2\mu L}(h - y)y \qquad \textbf{(2.10)}$$

And the flow rate Q through a section of width w is found as:

$$Q = \int_o^h dy \int_o^w dz \frac{\Delta p}{2\mu L}(h - y)y = \frac{wh^3}{12\mu L}\Delta p \qquad \textbf{(2.11)}$$

Thus the hydrodynamic resistance of the channel is given by the terms in front of the pressure drop:

$$R_{hyd} = \frac{wh^3}{12\mu L} \qquad \textbf{(2.12)}$$

Equivalent analytical solutions are also available for a variety of channel cross-sectional shapes (ellipse, circular, triangle) [White (1974); Bahrami *et al.* (2006)]. For extremely complex channels numerical simulations can be performed to determine the hydrodynamic resistance for any particular shape. The most common shape for microchannels is a rectangular cross-section where the hydrodynamic resistance is given as:

$$R_{hyd} = \frac{12\mu L}{wh^3}\left[1 - \frac{h}{w}\left(\frac{192}{\pi^5}\sum_{n=1,3,5}^{\infty}\frac{1}{n^5}\tanh\left(\frac{n\pi w}{2h}\right)\right)\right]^{-1} \qquad \textbf{(2.13)}$$

If w>>h (i.e. high aspect ratio) then the solution reduces to Eqn. 2.12, as would be expected. Under certain conditions, the above derivations are not suitable, even for laminar flow. Pressure driven flow in small microchannels may also generate an electrokinetic effect known as the streaming potential. Due to the presence of the EDL, the fluid flow generates an electric current known as the streaming current which creates a potential difference (streaming potential) across the length of the channel. This potential difference generates a counter current called the conduction current. The potential difference that is generated creates a backwards electroosmotic flow (discussed in subsequent section) that retards the pressure driven flow making it appear as though the fluid has a higher viscosity. This is known as the electro-viscous effect and causes

deviations from the expected solutions for pressure driven flow. However, this effect is limited to small microchannels with very dilute solutions where the EDL thickness and channel dimensions are comparable [Ren *et al.* (2001)]. The streaming potential technique is also used to probe the characteristics of the EDL such as the surface conductance and zeta potential [Gu and Li (2000); Werner *et al.* (2001); Erickson *et al.* (2000)].

2.2.2.2 Electroosmotic Flow

Electroosmotic flow is the relative motion of the fluid to a stationary charged surface by an applied electric field. The principal of electroosmotic flow (EOF) is shown in Figure 2.2. An EDL is formed at the surfaces of the microchannel resulting in a non-uniform distribution of charges near the walls. In this example, the walls are assumed to have a negative surface charge. Electrodes are situated at either end of the microchannel and an electric field is applied within the microchannel.

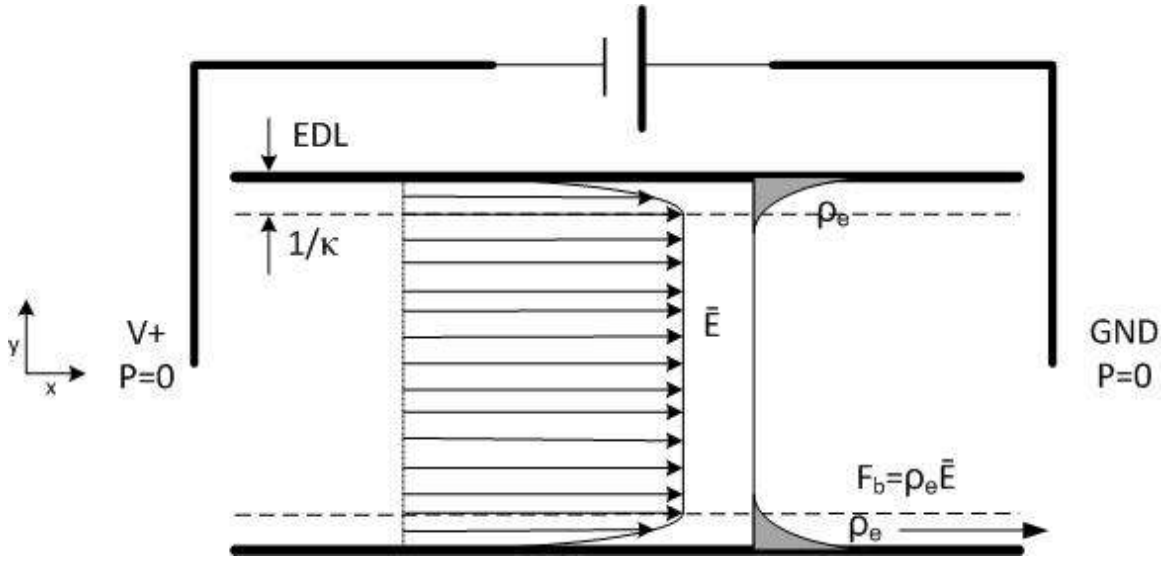

Figure 2.2 Schematic representation of the ideal electroosmotic flow (EOF) in a microchannel with negatively charged walls. The velocity profile is "plug" like with the centerline value equation to the Helmholtz-Smoluchowski slip condition. The charge density profile is shown in dark grey and the thickness of the EDL by the dashed line. The body force is only exerted on the ions in the EDL. No pressure drop occurs across the channel in this ideal case. The external electric field is setup by a DC power source.

The potential field is composed of two components: the applied potential and the potential in the EDL due to the surface charge. If the flow velocity is sufficiently low (ie. inertia is not a concern) then the two fields can be decoupled [Masliyah (1994)].

The equation for the applied potential field is defined as:

$$\nabla(\sigma \cdot \nabla \phi) = 0 \qquad \textbf{(2.14)}$$

$$\vec{E} = -\nabla \phi \qquad \textbf{(2.15)}$$

where σ is the electrical conductivity of the solution and Φ the applied electric potential. The external electric field exerts a body force ($\vec{F} = \rho_e \vec{E}$) only in the Debye layer where there is a non-uniform charge density. Fluid flow in the surrounding fluid is generated through viscous drag as the ions migrate towards the appropriate electrode. In the following discussion an expression for the electroosmotic velocity in the flow field is calculated for a parallel surface configuration.

Given the charge density from the Poisson-Boltzmann solution (ρ_e), the steady state Stoke's equation can be used to determine the velocity profile:

$$0 = -\vec{\nabla} p + \mu \vec{\nabla}^2 \vec{u} + \rho_e \vec{E} \qquad \textbf{(2.16)}$$

Considering only flow in the x-direction and substituting for the charge density from the Poisson-Boltzmann equation, the result is:

$$0 = -\frac{\partial p}{\partial x} + \mu \frac{\partial^2 u}{\partial y^2} - \varepsilon_o \varepsilon_r E_x \frac{\partial^2 \psi}{\partial y^2} \qquad \textbf{(2.17)}$$

Assuming there is not pressure gradient the equation presents itself as:

$$0 = \frac{\partial}{\partial y}\left(u(y) - \frac{\varepsilon_o \varepsilon_r E_x}{\mu} \psi(y) \right) \qquad \textbf{(2.18)}$$

Applying the no-slip condition along the walls ($u(\pm h/2)=0$) and the electric potential equals the zeta potential ($\Psi(\pm h/2)=\zeta$), a solution is obtained:

$$u(y) = \frac{\varepsilon_o \varepsilon_r E_x}{\mu}(\psi - \zeta) \qquad \textbf{(2.19)}$$

Outside the EDL the potential is zero and the equation reduces to the Helmholtz-Smoluchowski velocity:

$$u_{eof} = -\frac{\varepsilon_o \varepsilon_r E_x}{\mu} \zeta = \mu_{eof} E_x \qquad \textbf{(2.20)}$$

where μ_{eof} is termed the electroosmotic mobility. In most cases the thickness of the EDL is several orders of magnitude smaller than channel, therefore, the variation in velocity is negligible and the flow is essentially "plug" like. To an observer it appears as if the fluid "slips" by the surface. The Helmholtz-Smoluchowski velocity at the edge of the EDL can therefore be used as a slip condition along the wall. Since the velocity only varies in the EDL, and it is assumed to be negligible, the total flow rate through the channel is given by:

$$Q = \int_o^w dy \int_o^h dz \mu_{eof} E_x = \mu_{eof} E_x A_c = \mu_{eof} A_c \frac{|\Delta V|}{L} \qquad \textbf{(2.21)}$$

Analogous to the hydrodynamic resistance an electroosmotic hydrodynamic resistance can also be defined:

$$R_{ehyd} = \frac{L}{\mu_{eof} A_c} \qquad \textbf{(2.22)}$$

Similarly, using Ohm's law the electric current generated by the applied potentials can be determined from:

$$I = \frac{\Delta V}{R_e} \qquad R_e = \frac{L}{\sigma A_c} \qquad \textbf{(2.23)}$$

By comparing the last two results one notices that there is a very close relationship between flow rate and the electric current. Several researchers have used this fact to apply electric circuit theory to solve flow rates in complex microfluidic networks. A more detailed discussion on this topic is left for Section 3.3.3 and Chapter 4.

There are several advantages of EOF which make it an attractive method of pumping fluids in microchannels compared to pressure driven flow. The uniform velocity profile of EOF reduces the amount of dispersion when transporting samples [Paul *et al.* (1998); Ghosal (2004); Squires and Quake (2005)]. On the other hand, the parabolic profile of pressure driven flow suffers from Taylor dispersion which quickly smears the sample plug [Tabeling (2005)]. With EOF through simple manipulation of the applied voltages the flow rate can be precisely controlled without any moving mechanical parts such as pumps or valves. For control over multiple fluid streams, pressure driven flow requires several pumps/valves operating in unison. These valves/pumps can be integrated on chip, though with great difficulty, or off-chip which increases the supporting infrastructure for the chip [Harmon *et al.* (2003); Unger *et al. (*2000)]. Oh and Ahn (2006) provide an excellent review on the recent development of microvalves for microfluidics applications. On the other hand, EOF only requires electrodes to be placed in the reservoirs and a

high voltage sequencer to co-ordinate the flow. Electrodes can also be patterned on the substrate and integrated directly on-chip [Dunphy *et al.* (2005); Kovarik *et al.* (2004)]. In addition, EOF has a characteristically fast response time (~30ms) [Yan *et al.* (2006); Taylor (2007)], and the electrodes can be operated at high frequencies for dielectrophoresis applications [Castellanos *et al.* (2003); Wong *et al.* (2004)] and AC electroosmotic flow [Studer *et al.* (2004]. Conversely, pressure driven flow has a surprisingly long transient response (up to several minutes) due to the compressibility of water and the elasticity of the polymer microchannels and tubing [Stone *et al.* (2004)].

Since EOF largely depends on the zeta potential, effective surface patterning can create heterogeneous EOF conditions [Hu *et al.* (2004)] that can be used for a variety of applications such as mixing [Erickson and Li (2002)] or microfluidic flow field effect transistors (FET) for active control of the zeta potential [Moorthy *et al.* (2001)]. The surface dependency of EOF can also have several negative effects. Unintentional surface variations create undesired induced pressure fields in a microchannel that lead to additional dispersion and band broadening of samples [Zang *et al.* (2004)]. Over time, surface properties can change [Wang *et al.* (2003)] and adsorption of samples and particles can create a heterogeneous zeta potential [Ghosal (2002)]. In fact, zeta potential depends on a number of factors including surface chemistry and several solution properties such as pH, composition and temperature [Kirby and Hasselbrink (2004a); Kirby and Hasselbrink (2004b)]. Consequently, the zeta potential for a solid/liquid interface is largely unique. Thus several solutions operating under the same electric fields will have different flow rates making it difficult to universalize a new design. On the other hand, in pressure driven flow the viscosity is the only dependent fluid property. Since most solutions are water based, almost any solution can be pumped under the same conditions without having to modify the microfluidic design.

There are several additional disadvantages to using EOF. To achieve adequate flow rates with EOF high voltages on the order of several hundreds to thousands of volts must be applied across the microchannels. Generating the applied potentials requires a high voltage source which is typically the same size as many macro-scale pumps that can achieve similar flow rates. However, compact portable battery based power supplies have been developed for certain microfluidic applications [Jackson *et al.* (2003); Garcia *et al.* (2003)]. Integrating sensors on chip can also be an issue since any highly conductive material can divert the electric field and disturb the EOF.

The strong electric fields can also affect many biological samples. For instance, under high electric field cells undergo electroporation which is the formation of small pores in the cell membrane [Chang *et al.* (1992); Neumann *et al.* (1989)]. This technique is often used to transport foreign mater inside the cells such as DNA or RNA. A temporary pulsed electric field (10-50ms) is required so that the cells can recover and re-close the pores. Continuous exposure to the applied electric field will eventually lead to cell lysis.

With highly conductive solutions large current draws may lead to excessive Joule heating [Xuan *et al.* (2004)]. Internal heat generation due to Joule heating can be expressed by the following equation:

$$\dot{Q} = \frac{I^2}{\sigma(T)A(x)^2} \qquad \textbf{(2.24)}$$

Significant joule heating will generate a temperature field in the microfluidic device. Since many fluid properties are temperature dependent, joule heating can cause local variation in EOF as discussed in Section 2.2.5. Proper consideration of Joule heating is important in designing microfluidic chips that utilize EOF. This is especially true of PDMS devices, since PDMS has a low thermal conductivity (0.15 W/mK) as compared to glass (1.4 W/mK) and acts as an insulator.

The application of a high electric field in water will also cause electrolysis at the electrodes. The electrolysis reaction decomposes water molecules according to the following reaction [Bello (1996)].

Anode (oxidation):	$2H_2O(l) \rightarrow O_2(g) + 4H+(aq) + 4e^-$	E^o_{ox}=-1.23V
Cathode(reduction):	$2H_2O(l) + 2e^- \rightarrow H_2(g) + 20H^-(aq)$	E^o_{red}=-0.83V
Overall:	$2H_2O \rightarrow 2H_2(g) + 0_2\ (g)$	

Inert electrodes are used such as platinum so that the products do not react with the electrode. The process is dependent on the current draw and speeds up substantially with highly conductive solutions. Electrolysis causes several problems related to EOF. The reactions generate excessive H^+ and OH^- ion which change the pH value at the electrodes. At the anode the pH decreases and the solution becomes more acidic, at the cathode the pH increases and the solution becomes basic [Macka *et al.* (1998)]. Zeta potential is pH dependent so significant electrolysis can cause perturbations in EOF reducing overall stability. The ion generation also increases the amount of current carrying ions (H^+, OH^-), thus increasing the conductivity of the solution [Rodriguez and

Chandrasekhar (2005)]. In addition, the generation of hydrogen and oxygen gas creates bubbles on the electrodes which can destabilize the electrical connection to the fluid. In fact, bubble generation from electrolysis has been used to generate electro-chemical pumps that deflect a membrane and force the fluid flow [Tsai and Sue (2007); Böhm *et al.* (2000]. Moreover, the electrolysis reaction consumes water in the reservoirs and after a long period of time the electrode will lose contact with the fluid stopping EOF.

The magnitude of these effects depends on a number of factors including the applied current, volume of the reservoirs, solution properties and solution buffering capacity [de Jesus *et al.* (2005)]. For simple electrolytes such as KCl, electrolysis will create severe pH changes (±4 pH) in a few minute of operation for small volumes reservoirs (100μL). While in well buffered solutions with a high buffering capacity there may be a negligible change for a certain period of time. However, after long term pumping the buffer will be eventually depleted and the pH will change dramatically. For high currents the affects of electrolysis must be considered in the design of a microfluidic device utilizing EOF, in order to determine the overall operating time. In conclusion, EOF is a flexible method of controlling fluids on-chip; however, great consideration must be taken in the design of a microfluidic device to either eliminate or suppress the negative aspects of EOF.

2.2.2.3 Undesired Pressure Effects in Microfluidic Systems

Microfluidic chips operating under electroosmotic flow (EOF) are also inadvertently subject to undesired pressure driven flow [Crabtree *et al.* (2001); Duong *et al.* (2006)]. These pressure disturbances arise from minute differences in meniscus shape (Laplace pressure) and liquid levels (hydrostatic pressure) at the reservoirs as shown in Figure 2.3. As a matter of fact, both of these mechanisms have been employed to pump fluids in microfluidic chips using gravity [Tourovskaia *et al.* (2005)] and surface tension forces [Tseng (2006); Walker *et al.* (2002)]. The presence of these pressure gradients can generate an undesired pressure driven flow that is of the same magnitude of the desired EOF flow, essentially negating any control over the device.

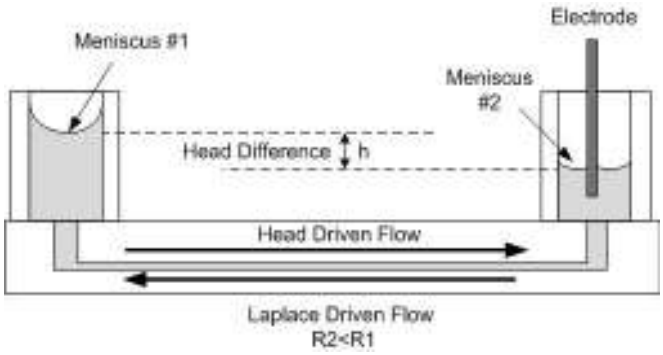

Figure 2.3 Diagram of the mechanisms contributing to undesired pressure driven flow generated by differences in Laplace and hydrostatic forces.

The Laplace pressure balances the surface tension force at a meniscus interface. For a spherical meniscus the Laplace pressure is defined by the following equation:

$$\Delta P_L = \frac{2\gamma}{r_m} \tag{2.25}$$

where γ is the surface tension for the liquid-air interface and r_m is the radius of the meniscus. The radius of curvature can be estimated from the radius of the reservoir, r_{res}, and the contact angle of the liquid-surface, Θ_{ca}:

$$r_m = \frac{r_{res}}{\cos\theta_{ca}} \tag{2.26}$$

The actual shape of the meniscus is not a sphere since the electrode distorts the surface. A difference in placement of the electrodes between two reservoirs will generate a Laplace pressure difference. Similarly, a difference in liquid level height will generate a hydrostatic head:

$$\Delta P_H = \rho g h \tag{2.27}$$

where ρ is the density, g is gravity and h is the height difference. A difference in liquid levels may initially exist if the two reservoirs are not filled with the same volume of fluid. More importantly, during operation the hydrostatic head can change as the fluid is transported from one reservoir to another. During this process the shape of the meniscus may also change as the liquid level rises or drops. The result is a dynamic system that continuously alters the flow field unpredictably while the chip is operating. The solution to this problem is to design the microfluidic network accordingly to suppress undesired pressure driven flow. This is accomplished by incorporating channels with a high hydrodynamic resistance to pressure driven flow in the design. A more in depth discussion on this topic is provided in Chapter 4.

2.2.3 Electrophoresis

Electrophoresis refers to the movement of a charged surface relative to a stationary liquid. A charged particle placed in an electrolyte will generate an electric double layer with a thickness equivalent to the Debye length ($\lambda_d = 1/\kappa$). The motion of a particle solely due to the applied electric field is given by the electrophoretic velocity:

$$\vec{u}_{ep} = \mu_{ep}\vec{E} \qquad \textbf{(2.28)}$$

where μ_{ep} is called the electrophoretic mobility of the particle. The thickness of the EDL relative to the size of the particle determines the method of analysis for calculating the mobility of the particles [Masliyah (1994)]. The general formulation of the electrophoretic mobility related to the zeta potential is:

$$\mu_{ep} = \frac{2\varepsilon_o \varepsilon_r \zeta}{3\mu} f(\kappa a) \qquad \textbf{(2.29)}$$

where a is the radius of the particle, μ is the viscosity of the liquid, κ is the Debye-Hückel parameter and $f(\kappa a)$ is Henry's function which depends on the ratio between the EDL thickness and particle size. For small particles, where the Debye length is large in comparison ($\kappa a << 1$), the particle is treated as a point charge and Henry's function, $f(\kappa a) \to 1$. The electrophoretic mobility reduces to Hückel's expression:

$$\mu_{ep} = \frac{2\varepsilon_o \varepsilon_r \zeta}{3\mu} \qquad \textbf{(2.30)}$$

In contrast, for a small EDL compared to the size of the particle ($\kappa a >> 1$) Henry's function, $f(\kappa a) \to 3/2$, and the electrophoretic mobility reduces to:

$$\mu_{ep} = \frac{\varepsilon_o \varepsilon_r \zeta}{\mu} \qquad \textbf{(2.31)}$$

This is similar to the electroosmotic mobility, which should be expected, since electrophoresis is a complement to electroosmosis. For intermediate values of κa, Henry's function lies between the two asymptotes 1 and 1.5. This discussion assumes a spherical non-conducting particle, however, corrections factors for others shapes, both non-conducting and conducting, are also available in literature [Hunter (1981)]. Under electroosmotic flow the observed particle velocity is a combination of the bulk flow and electrophoretic velocity ($\vec{u}_{obs} = \vec{u} + \vec{u}_{ep_i}$). Electrophoretic

mobility differences are used extensively in to separate and analyze a variety of particles such as proteins, DNA and nucleic acids on-chip [Harrison *et al.* (1992); Kohlheyer *et al.* (2006)]. Electrophoresis also affects other particles such as dyes and beads used for flow field visualization.

2.2.4 Mass Transport

In many lab-on-a-chip applications several species must be transported or mixed together for a chemical reaction to take place [deMello (2006)]. For instance, the uniform transport of soluble factors to cells is important in the design of microfluidic cell culture chambers [Kim *et al.* (2007)]. Alternatively, in applications requiring separation such as on-chip electrokinetic separation, controlling the amount of dispersion is critical [Sinton *et al.* (2002)]. Fluorescent particles (dyes and beads) used in flow visualization techniques are subject not just to advection, but also to diffusion and electrophoresis, which causes the motion of the tracer particle to differ from the bulk fluid. The concentration field for a given species, considering advection, diffusion, electrophoresis and reactive generation is given as [Masliyah (1994)]:

$$\frac{\partial c_i}{\partial t} + \vec{u} \cdot \left(\vec{\nabla} c_i\right) = D_i \nabla^2 c_i - \mu_{ep_i} \vec{\nabla}\left(c_i \vec{E}\right) + R_i \qquad \textbf{(2.32)}$$

where c_i is the molar concentration of species *i*, $\vec{u}$ is the velocity vector, D_i is the diffusion coefficient of the i^{th} species, μ_{ep_i} is the electrophoretic mobility of the i^{th} species, $\vec{E}$ is the applied electric field and R_i is the volumetric rate of generation of the i^{th} species by chemical reaction. The second term on the right side of the equation containing the electric field is the contribution of electrophoresis. The equation can be rearranged in a more familiar form, where the electrophoretic velocity, $\vec{u}_{ep_i}$, is included:

$$\frac{\partial c_i}{\partial t} + (\vec{u} + \vec{u}_{ep_i}) \cdot \left(\vec{\nabla} c_i\right) = D_i \nabla^2 c_i + R_i \qquad \textbf{(2.33)}$$

The reason that the electrophoretic term can be moved to the left side is because under Sotke's flow electrophoretic migration force is balanced by the drag force which is proportional to the velocity. Therefore, the electrophoretic motion can be expressed as a velocity component. Note that $\vec{u}$ is the bulk fluid velocity vector and $\vec{u}_{ep_i}$ is the specific electrophoretic velocity for the species of interest.

For a charged particle the electrophoretic velocity is given by Eqn. 2.28. On the other hand, dye particles can be approximated as a point charge where the electrophoretic velocity is given as:

$$\vec{u}_{ep} = \mu_{ep_i}\vec{E} = \frac{D_i z_i e}{k_b T}\vec{E} \qquad \textbf{(2.34)}$$

For instance, consider fluorescein dye and fluorescent beads (3.8μm diameter) used for flow visualization (see Chapter 3). The properties of fluorescein dye are: D=4.37x10^{-10} m^2/s and μ_{ep}=-3.58x10^{-8} m^2/Vs [Taylor (2007)]. The Diffusion coefficient of the beads can be approximated from the Stoke-Einstein equation [Probstein (1994)]:

$$D = \frac{k_b T}{6\pi\mu a} \qquad \textbf{(2.35)}$$

Thus for the given particle diameter (3.8μm) the diffusion coefficient is: D=5.6835x10^{-14} m^2/s and the measured electrophoretic mobility is μ_{ep}=-3.95x10^{-8} m^2/Vs in 50mM sodium (bi)carbonate buffer [Taylor (2007)]. Consider electroosmotic flow in a straight microchannel with an electric field strength of 10kV/m and electroosmotic mobility of 5.7e-8 m^2/Vs. The bulk fluid velocity is 570 μm/s and the electrophoretic velocity of the dye is -358 μm/s and beads is -395 μm/s. Thus the observed particle velocities are 212μm/s and 175μm/s. Consequently, in regions of strong electric fields the bulk fluid motion cannot be inferred from the motion of the tracer particles without considering electrophoretic effects.

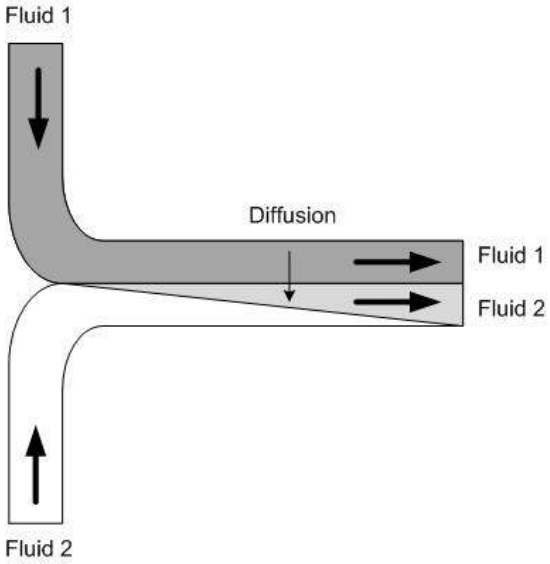

Figure 2.4 T-channel micromixer: two streams are brought together in a single mixing channel under laminar flow conditions. Mixing occurs cross-stream only through diffusion.

Unlike the Reynolds number, the Peclet number does not have a characteristic order of magnitude in microfluidics. To demonstrate, consider the Peclet values under the above flow conditions in a T-channel mixer as shown in Figure 2.4. A T–channel mixer consists of two streams, one with the sample and the other without, which are brought together in the main channel where mixing occurs through cross-stream diffusion. For a 100μm mixing channel the Peclet values for the dye and beads are Pe=48.5 and Pe=3.08x10^5. These values are analogous to mixing small proteins (5nm) and mammalian cells (10μm) in a bioreactor [Squires and Quake (2005)]. For a completely homogeneous solution at the outlet of the main channel, the approximate mixing channel length for the dye would be need to be 0.485mm with a mixing time of 48.5s, and for the beads 30.8m and 85.5hrs! This indicates that for small particles mixing by diffusion is possible in microfluidic systems; however, for large particles diffusive mixing is impractical due to the long mixing length and time. To increase the rate of mixing some active component is required that introduces instabilities into the flow field which creates a chaotic regime favourable for mixing. A great deal of effort has been put forth by the microfluidic community to develop novel mixers to overcome the problems of laminar flow. Nguyen and Wu (2005) provide an excellent review of the various types of micromixers, both passive and active, that have been developed to date for a wide range of Peclet and Reynolds numbers.

2.2.5 Heat Transfer

Many microfluidic applications require precise temperature control on-chip. For example, polymerase chain reaction (PCR) chips for DNA amplification the sample must undergo a series of chemical reactions at three well controlled temperatures: 95^{o}C for denaturing DNA samples, 72^{o}C for annealing and 60^{o}C for extension [Kopp *et al.* (1998)]. The general equation for the temperature field is described by the conservation of energy equation [Incropera and DeWitt (2002)]

$$\rho c_p\left[\frac{\partial T}{\partial t}+\vec{u}\cdot\vec{\nabla}T\right]=\vec{\nabla}\cdot\left(k(T)\vec{\nabla}T\right)+\sigma(T)\vec{E}\cdot\vec{E} \qquad \textbf{(2.36)}$$

where ρ is the density, c_p the specific heat, $k(T)$ the temperature dependent thermal conductivity and $\vec{u}$ is the velocity vector. The term on the far right of the equation is the internal heat generation due to Joule heating as discussed in Section 2.2.2.2. Most solid material properties remain relatively constant over the temperature range considered in microfluidics (25-80ºC).

On the other hand several fluid properties such as electrical conductivity, thermal conductivity, viscosity, dielectric constant are temperature dependent. The electrical conductivity of a solution versus temperature can be expressed as [Lide (1998)]:

$$\sigma(T) = [1 + \alpha(T - T_o)]\sigma_o \quad \textbf{(2.37)}$$

where α is the thermal coefficient (typically 2%/°C) and σ_o is the conductivity at the reference temperature T_o.

The viscosity, dielectric constant and thermal conductivity are given as [Incropera and DeWitt (1990), Xuan *et al.* (2004)]:

$$\mu(T) = 2.761x10^{-6} e^{1,713/T} \quad \textbf{(2.38)}$$

$$\varepsilon_r(T) = 305.7e^{-T/219} \quad \textbf{(2.39)}$$

$$k(T) = 0.61 + 0.0012(T - 293) \quad \textbf{(2.40)}$$

The temperature variance of the liquid properties also affects the electroosmotic and electrophoretic mobilities. The temperature dependence of the fluid properties mentioned above is plotted in Figure 2.5. As the figure shows, the electroosmotic mobility can increase by over 50% strictly due to changes in viscosity and dielectric constant. As well, there is evidence that for some liquid/surface combinations the zeta potential is also temperature dependent which would further increase the electroosmotic mobility [Venditti *et al.* (2006)]. Thus for solutions that are hard to pump under EOF due to low mobilities, a possible solution is to increase the temperature. The large surface-to-volume ratio of microchannels increases the rate of heat transfer in and out of the fluid. Miniaturization reduces the time for a sample to reach thermal equilibrium allowing for fine thermal control that is not available on the macro scale.

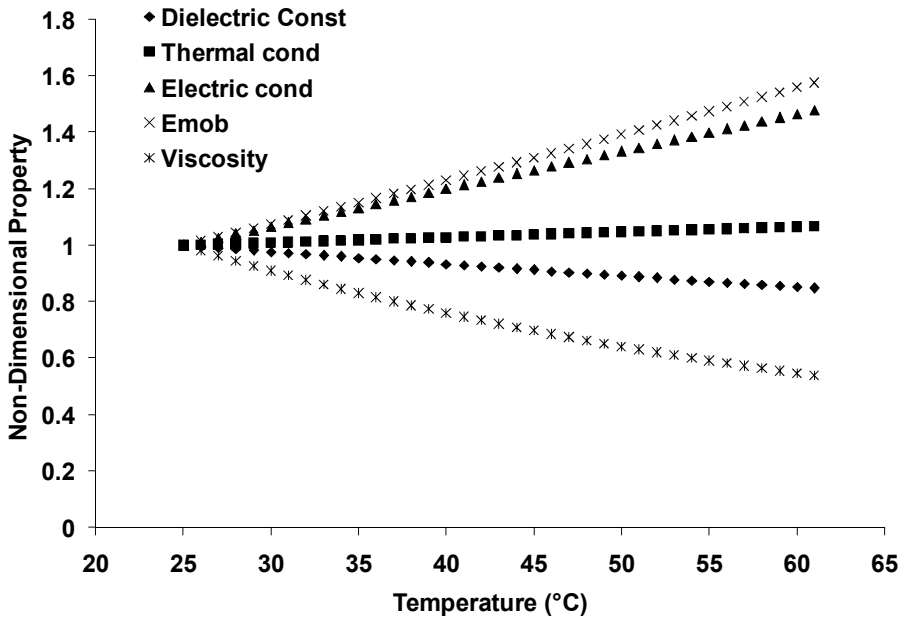

Figure 2.5 Temperature dependence of several fluid properties (water): dielectric constant, thermal conductivity, electrical conductivity, electroosmotic mobility (due to dielectric constant and viscosity changes) and viscosity non-dimensionalized with the value at 25°C.

2.3 Design Techniques

Computation and analytical simulations can significantly reduce the number of design iterations required for a microfluidic chip. By first numerically prototyping the device, several design parameters can be investigated at the concept stage to optimize the design prior to fabrication and testing. For many simple physical problems involving ideal conditions analytical solutions can be found; however, as more phenomena are introduced and the complexity of the device increases numerical simulations are required to obtain the desired design information. Erickson (2005) provides a thorough review of the various numerical techniques applied to solve a multitude of microfluidics problems ranging from fluid flow, mixing, AC electroosmotic flow, magnetic phenomenon, acoustics, cellular transport, chemical reactivity and thermal analysis. The text by Chakrabarty *et al.* (2006) also provides an account of the numerical design and automation tools available to the microfluidic engineer.

2.3.1 Numerical Simulations

Full numerical simulations, whether 2D or 3D, provide valuable information on the physical phenomenon of interest. These simulations can be written in-house using general purpose programming software such as Fortran, C++ and Matlab [Erickson (2005)] or by employing commercialized finite element software such as ANSYS, Conventer, CFDACE and COMSOL Multiphysics. The choice between writing a custom code and using a commercial package

depends on a number of factors. A custom code allows complete control over the dynamics of the simulation; however, developing such codes is a demanding task. Many of these codes are designed to solve a specific problem and may be difficult to re-apply to new problems. Commercial programs are flexible and easy to use; many contain the latest algorithms in solving large numerical problems that are out of reach for the novice programmer. However, commercial codes are much like a black box, where the output is only as good as the input, so the user still needs some knowledge of the physics and computation methods.

The main difficulty with performing numerical simulations on the microscale is the relevant length scales of the different phenomenon. For instance, solving electroosmotic flow requires a fine mesh near the wall to capture the EDL, and a larger mesh outside of the EDL to capture the flow in the microchannel [Dutta *et al.* 2002]. However, by far the most challenging aspect of performing numerical simulations is the large number of physical phenomenon that must be considered together such as fluid flow, mass transport, heat transfer, microelectronics and structural interactions. As a consequence, numerical simulations are often focused on a small section of the entire chip in order to concentrate computational resources. Thus intensive numerical simulations provide valuable data on the specific area of interest but are unable to provide a global analysis of the entire microfluidic chip unless computational resources are spread out. In this work, numerical simulations with the commercial program COMSOL Multiphysics is used throughout to study the performance of the Y-Channel Zeta potential measurement chip (Chapter 6) and electroosmotic pump (Chapter 7). Details on these numerical simulations are provided in Chapter 4.

2.3.2 System Design Models

To address the issues of long computational times for global simulations, compact system (circuit) level simulations have recently been developed [Chatterjee and Aluru (2005); Xuan and Li (2004); Wang *et al.* (2006); Wang *et al.* (2007)]. These models are able to capture the fundamental physical phenomenon with good accuracy at much lower computational expense. This type of modelling allows a top-down approach where the entire system can be simulated first to gain overall insight into the performance and then more detailed numerical simulations can follow for specific regions of the device. The methodology begins with a schematic of the entire microfluidic systems represented by a series of elementary components such as T-mixers, separation channels, cross intersections ect. The behaviour of each component is described by an analytical model which accounts for the physics of the component. Each component has specified

input and output parameters that can be linked between subsequent models. Essentially each microfluidic component can be envisioned as a box with pins representing the inputs and outputs that are linked by wires to other components creating a global network. This methodology is similar to the programs for electrical circuit design such as SPICE or PLECS. For example, electroosmotic flow can be decomposed into the flow field and electric field. Two sets of networks can be developed where each channel is modeled by an electrohydrodynamic resistance (Eqn. 2.12) and electrical resistance (Eqn. 2.22). The two networks can then be solved using electrical circuit nodal analysis techniques.

Several researchers have developed such simplified compact circuit models. Fletcher *et al.* (2001) developed a circuit based model to solve electroosmotic flow in a microfluidic network using the resistance based elements. Qiao *et al.* (2002) and Chien *et al.* (2002) used a similar approach for combined electroosmotic and pressure driven flow. Xuan and Li (2004) extended this model to include variations due to finite electric double layers and streaming potential from pressure driven flow. Chatterjee and Aluru (2005) expanded the models outside of fluid flow and included sample transport, mixing, chemical reaction and electrophoretic separations. Wang et al. (2006) developed behavioural modeling and schematic based simulations with component level multi-physics models tied together in a larger system hierarchy. These models were used to study micromixing and electrophoretic separations on chip, results were compared to full numerical simulations with <5% error and100X decrease in computational time. Bedekar *et al.* (2006) also included the affect of analyte dispersion around a curve in their model. Wang *et al.* (2007) used a "mixed" methodology for system level modeling where both numerical schemes and analytical solutions are integrated together to solve the multi-physics behaviour including surface reaction modeling. In fact, a commercial software version called Pharos using this type of modeling has been recently developed by CFD Research Corp. The continued development of these system level models promises to further increase the microfluidics engineer's capacity to develop new and more complex devices. Equivalent circuit modeling was used in this thesis for modelling the Y-channel design (Chapter 6), EO pump (Chatper 7), and cell culture network (Chapter 8).

2.4 Fabrication of Microfluidic Devices

A number of methods have been developed for fabricating microfluidic devices. Original devices were fabricated in silicon, glass or quartz using well established techniques from the microelectronics and MEMS industries. Starting in the 1990's there was a general shift in the microfluidics community to the use of polymer based devices. The reasons for the shift are two

fold: 1. anticipating the eventual commercialization of microfluidic devices, reducing cost was of the up most concern as many biological devices would need to be disposable 2. the need for rapid prototyping of new designs became more important, so that the long production cycle and clean room condition required for silicon fabrication was impractical for the academic community. Polymer based fabrication methods such as soft lithography allow for development of new microfluidic device within a few hours in ordinary laboratory conditions compared to weeks or months for glass based devices. In the following discussion a brief review is provided for fabricating microfluidic devices using glass and polymers. This is followed by a review of soft lithography fabrication in poly(dimethylsiloxane) (PDMS) which is extended in Chapter 5. This review does not intend to be exhaustive, for a detailed information on the various fabrication techniques available for microfluidics please refer to the available literature by Madou (2000), Oosterbroek (2003), Nguyen and Werely (2002), Geshke et al. (2004).

2.4.1 Glass and Silicon Devices

The majority of glass devices are fabricated using photolithography and bulk etching techniques. In this method, a high resolution photolithography mask is made with the desired microfluidic design. A photoresist is spin coated onto the substrate (glass or silicon) and mask pattern is transferred using optical lithography. Depending on the type of resist the exposed regions will become either soluble (positive resist) or insoluble (negative resist) to the developing solvent. The insoluble regions are dissolved in a solvent which leaves behind the exposed silicon or glass substrate. Using a variety of etching techniques (wet, dry, anisotropic ect.) the exposed silicon is chemically attacked to form the microchannel cavities. Depending on the etching conditions (time, type of etch, ect.) the depth of the microchannels can be controlled. After etching, the photoresist layer is stripped and the substrate contains the microcanals of the microfluidic network. To complete the device the channels must be enclosed by bonding to another substrate. This is typically accomplished through direct bonding (high temperatures) or anodic bonding (high electric fields). To obtain fluidic access to the microchannels small holes are drilled with a diamond bit or etched before hand, thus completing the microfluidic device. An additional advantage of using silicon devices is that electrodes and sensors can be directly fabricated at the same time as the microfluidic network. However, the characteristically long processing times for glass devices make it difficult for prototyping new devices as one design iteration can take several months. Coupled with the high material and fabrication costs, silicon and glass based devices are not ideal for mass producing disposable devices for the medical community.

2.4.2 Polymer Devices

Polymer devices have been fabricated from a variety of plastics including poly (methyl methacrylate) (PMMA), polycarbonate (PC), parylene and poly (dimethylsiloxane) (PDMS). The two major forms of fabricating polymer devices are direct machining or replication from a master. Examples of micro aching techniques include laser ablation, micro milling, X-ray and ultraviolet lithography. The most popular fabrication techniques rely on replication such as hot embossing, micro-injection molding and casting. Critical to the replication process is a high quality master which is typically fabricated using silicon technologies. Durability of the master is especially important for high temperature molding techniques. Consequently, fabricating a master can be expensive making some polymer techniques such as micro-injection molding only feasible for mass production. However, it was the development of a new fabrication technique known as soft lithography which allowed for quick and inexpensive fabrication of microfluidic devices.

2.4.2 Soft-Lithography

Soft lithography refers to a specialized subset of casting techniques which uses PDMS and a rapid prototyping framework to fabricate microfluidic devices. Original developed by Whitesides group at Harvard [Xia and Whitesides (1998); McDonald *et al.* (2000); Duffy *et al.* (1998)], soft lithography is the predominant fabrication technique used among the microfluidics community. Soft lithography is composed of two separate techniques: rapid fabrication of a master and replica molding. Masters are fabricated with positive relief microchannel structures using contact photolithography and inexpensive high resolution transparency masks. This process still requires semi-clean room conditions but eliminates the expensive chrome masks used in silicon fabrication and dangerous etching chemicals. In replica molding, liquid pre-polymer PDMS is poured over the mold and cured at moderately elevated temperatures (~80°C) producing a replica containing the imprinted channels. The resolution of the mold is surprisingly high, usually with sub-micron precision. Of course the accuracy of the mold can not exceed the accuracy of the master. Due to the flexible properties of PDMS, the mold can be easily peeled from the master and then bonded to another substrate to enclose the channels. Bonding can be temporary by simply placing the PDMS on another planar substrate, or permanent using plasma treatment to generate covalent bonding [McDonald *et al.* (2000)]. The time from design of a new device to fabrication is often several day and costs approximately $10-50/chip making it ideal for rapid prototyping of new designs.

PDMS is an excellent material for microfluidics applications as it is optically transparent down to 280nm, chemically inert, deforms reversibly, large temperature range (-100-100°C) and can be modified easily by several well established surface treatments [Makamba *et al.* (2003); Xia and Whitesides (2003)]. The elasticity of PDMS facilitates the fabrication of flexible membranes for valves [Unger *et al.* (2000)] and pumps directly on-chip [Melin and Quake (2007]. Several layers of PDMS can be bonded together to form a three dimensional multi-layer device. In addition, PDMS is biologically compatible and highly permeable to gases an ideal property for cell culture applications [Mata *et al.* (2005); Kim *et al.* (2007)].

There are also several disadvantages of PDMS. Many organic solvents cause PDMS to swell [Lee *et al.* (2003)]. The flexibility of PDMS can also be a hindrance since high aspect ratio channels will result in sagging. PDMS networks are also subject to inadvertent flow caused by deflection of the PDMS from outside forces. Natural PDMS is also hydrophobic and must be treated through either plasma or UV treatment to render the surface hydrophilic. However, this treatment is only temporary, as is the case for many properties of PDMS which are unpredictable and time dependent. Nevertheless, PDMS possess an appealing set of properties that are suitable for constructing microfluidic devices. As part of this thesis, the soft lithography technique was developed for fabricating microfluidic devices. Details are provided in Chapter 5.

2.5 Design Evaluation Methods

After fabrication is complete the new device must be tested and evaluate to verify that the models developed during the prototyping stage correspond with experimental results. To date a wide range of diagnostic techniques have been developed for microfluidics. These techniques are able to provide high spatial and temporal resolution at the micron level. In the following discussion a brief review is provided for techniques used for determining temperature fields, flow fields, and electrokinetic properties of microfluidic devices.

2.5.1 Temperature Measurements

Several techniques exist for measuring temperature inside microfluidic devices. For point measurements thermocouples can be directly embedded into the device; however, to obtain a temperature map several thermocouples are needed which complicates both the fabrication and data acquisition. In addition, directly inserting the thermocouple into the fluid stream is difficult [Khandurina *et al.* (2000)]. Many other non-invasive methods exists such as on-chip micro machined sensor arrays made in glass [Xue *et al.* (2005)], and Nuclear Magnetic Resonance

(NMR) [Lacey *et al.* (2000)]. However, these techniques require complex fabrication process and have high equipment costs and are thus difficult to implement on-chip. Measurements of fluid temperature based on Brownian motion of particles using u-PIV thermometry have also been used but this requires a large infrastructure and memory allocation to record the necessary images [Hohreiter *et al*. (2002)]. For internal fluid measurements one of the most popular techniques is fluorescence based thermometry. In this method, a fluorescent dye (Rhodamine B) is added to the working fluid and the temperature is determined from the intensity change of the dye with high spatial and temporal resolution [Ross *et al.* (2001)]. One negative of this method is that temperature measurements are limited to the fluid since that is where the dye is contained. Though this method has been successfully applied in a number of applications in glass chips, it was found to be incompatible with PDMS devices due to severe absorption of the dye into the surrounding PDMS [Samy *et al.* (2007)]. Samy *et al.* (2007) used the absorption of Rhodamine B into PDMS to develop a novel thin film Rb/PDMS that could be used to measure the entire chip temperature field at the film depth.

2.5.2 Flow Field Measurements

Characterizing the flow field in a microfluidic device is essential for evaluating the performance of most microfluidic devices. To date several non-invasive optical based techniques have been developed using particle-based, scalar-based and point detection methods as reviewed by Sinton (2004). The most predominant micro scale flow visualization is micro-PIV which was originally developed at Stanford University in the late 1990s [Santiago *et al.* (1998) and Meinhart *et al.* (1999)]. In this method, seed particles are added to the flow field and their particle displacement monitored with fluorescent microscopy. The velocity is determined from the displacement of the particles between two successive images. Due to the length scales of microfluidics the particles are extremely small (~0.2um) and several issues arise with regards to retrieving the required fluorescent signals and determining the velocity field. For instance Brownian motion introduces a random error into the position of the particle. Sophisticated image algorithms are required to extract the position of the particles and cross correlate between the two images to obtain a velocity vector. Currently, micro-PIV is a standard tool used throughout the microfluidics community and has been applied to study a variety of phenomenon in microfluidics [Sinton (2004); Nguyen (2002); Breuer (2003)].

2.5.3 Electroosmotic Mobility Measurements

For electroosmotic flow one of the most important parameters that must be determined for proper design is the electroosmotic mobility or zeta potential of the liquid/surface interface. However, it is not possible to measure the zeta potential directly, instead measurements rely on observations from electrokinetic experiments to backward calculate the zeta potential. These experiments are typically based on the three major electrokinetic phenomena: electroosmotic flow, electrophoresis and streaming potential [Masliyah (1994); Probstein (1994); Hunter (1981); Kirby (2004)]. However, only electroosmotic flow and streaming potential are usually used for determining the electroosmotic mobility of microchannel walls as reviewed by Kirby (2004) and Devasenathipathy and Santiago (2003).

2.5.3.1 Streaming Potential

Under pressure driven flow in a microchannel, charges in the EDL will be forced downstream generating an net ion transport which is called the streaming current [Masliyah (1994); Hunter (1981)]:

$$\vec{I}_s = \int_v \vec{u}\rho_e dv \qquad \textbf{(2.41)}$$

where $\vec{I}_s$ is the streaming current, $\vec{u}$ is the velocity and ρ_e is the net charge density. The current generates a potential difference across the channel known as the streaming potential. Due to this potential a current in the opposite direction is generated which is known as the conduction current. The conduction current is the sum of the bulk and surface conduction (recall EDL has a higher conductivity than the bulk):

$$\vec{I}_c = A_c \vec{E}_s \lambda_b + P_w \vec{E}_s \lambda_s \qquad \textbf{(2.42)}$$

where $\vec{I}_c$ is the conduction current, A_c is the cross-sectional area, $\vec{E}_s$ is the streaming potential electric field, P_w is the wetting perimeter, λ_b and λ_s are the bulk and surface conductivities, respectively. At steady state, the two currents sum to zero and a relationship for the zeta potential as function of the streaming potential and other experimental parameters can be derived.

$$\frac{\Delta P \varepsilon_o \varepsilon_r}{\mu \vec{E}_s \lambda_b} = \frac{1}{\zeta} + \left(\frac{2\lambda_s}{\zeta \lambda_b}\right) f \qquad \textbf{(2.45)}$$

where ΔP is the pressure difference, f is a shape factor for the channel and is given as the ratio of the wetted perimeter to the cross-sectional area ($f = P_w / A_c$). To obtain the zeta potential the streaming potential is measured for a range of applied pressures and a plot is made. The result is a linear trend where the intercept can be used to determine the zeta potential and the slope the surface conductivity. Consequently, a number of measurements need to be made at different pressures and form factors to achieve reliable results.

A common method of measuring the streaming potential is to use a pair of reversible Ag/AgCl electrodes at the end of the channels. The experimental apparatus consists of the microchannel connected through a tubing network to a series of transducer to measure the pressure drop, bulk conductivity and flow rate. The flow direction must be reversed occasionally or the electrodes will become polarized resulting in false readings. Many techniques and correction factors have been developed to measure the streaming potential as detailed by Hunter (1981). However, due to the development of other simpler methods of performing the measurements the streaming potential method is not as widely used as it once was. Today most measurements are based on measuring the zeta potential while monitoring electroosmotic flow.

2.5.3.2 Electroosmotic Flow

The principal behind determining the electroosmotic mobility from electroosmotic flow is to measure the average velocity. Recall that the average velocity under electroosmotic flow is given by the Helmholtz-Smoluchowski slip velocity:

$$u_{eof} = -\frac{\varepsilon_o \varepsilon_r E_x}{\mu}\zeta = \mu_{eof} E_x \qquad \textbf{(2.46)}$$

Under pure EOF the flow is uniform across the channel so the total flow rate is approximated by $Q = u_{HS} A_c$, where A_c is the cross-sectional area of the microchannel. Therefore, it is possible to determine the zeta potential by measuring the fluid velocity or volume flow rate under electroosmotic flow.

In the simplest form the flow rate can be measured from the volume pumped during a specified time. This is typically accomplished by weighing the output of fluid during a time interval and then calculating the flow rate [Hunter (1981)]. This method is difficult to use since the EOF flow rates are small so there is very little mass change. The weighing apparatus must be very sensitive to measure this small change which also makes it susceptible undesired changes in weight caused

by evaporation or condensation. Direct visualization of the flow field is now possible with the variety of fluorescent microflow visualization techniques recently developed [Sinton (2004)]. In these methods the electroosmotic flow is determined from the observation of a neutral marker such as a dye or bead. Devasenathipathy and Santiago (2003) provide a review of several visualization techniques applied to measure the electroosmotic mobility. As it applies to zeta potential measurement, these visualization techniques are used to measure the velocity profile and flow rate under electroosmotic flow. Once the velocity is known electroosmotic mobility or zeta potential are determined from the Helmholtz-Smoluchowski equation. The main advantage of using a flow visualization technique is that the electroosmotic velocity is measured directly and in real time. Conversely, the main disadvantage is that the experimental setup is costly.

One of the more popular methods used today is the current monitoring technique originally developed by Huang *et al.* (1998). In this method the average electroosmotic velocity is measured by monitoring the transient of the current draw as one solution is replaced by a similar solution with slightly different concentration in a straight microchannel as shown in Figure 2.6. The average velocity can be determined from knowing the length of the channel and the displacement time. Typically a 5% difference in solution concentration is used since it provides a measurable conductivity change without introducing significant error from zeta potential mismatch [Pittman *et al.* (2003)]. One of the main difficulties with this method is determining the start and end of displacement since the diffuse interface can generate gradual transitions. Ren *et al.* (2003) developed an alternative analysis technique that does not use the start and end points but the slope of the current-time plot which remains linear even with large transitions. Several researchers have used this method to determine the zeta potential in silica and glass capillaries, glass and polymer microchannels [Kirby and Hasselbrink (2004a); Kirby and Hasselbrink (2004b)]. The results have also been verified with measurements obtained from direct flow visualization indicating that the much simpler current-monitoring method produces accurate results [Pittman *et al.* (2003); Sinton et al. (2002)]

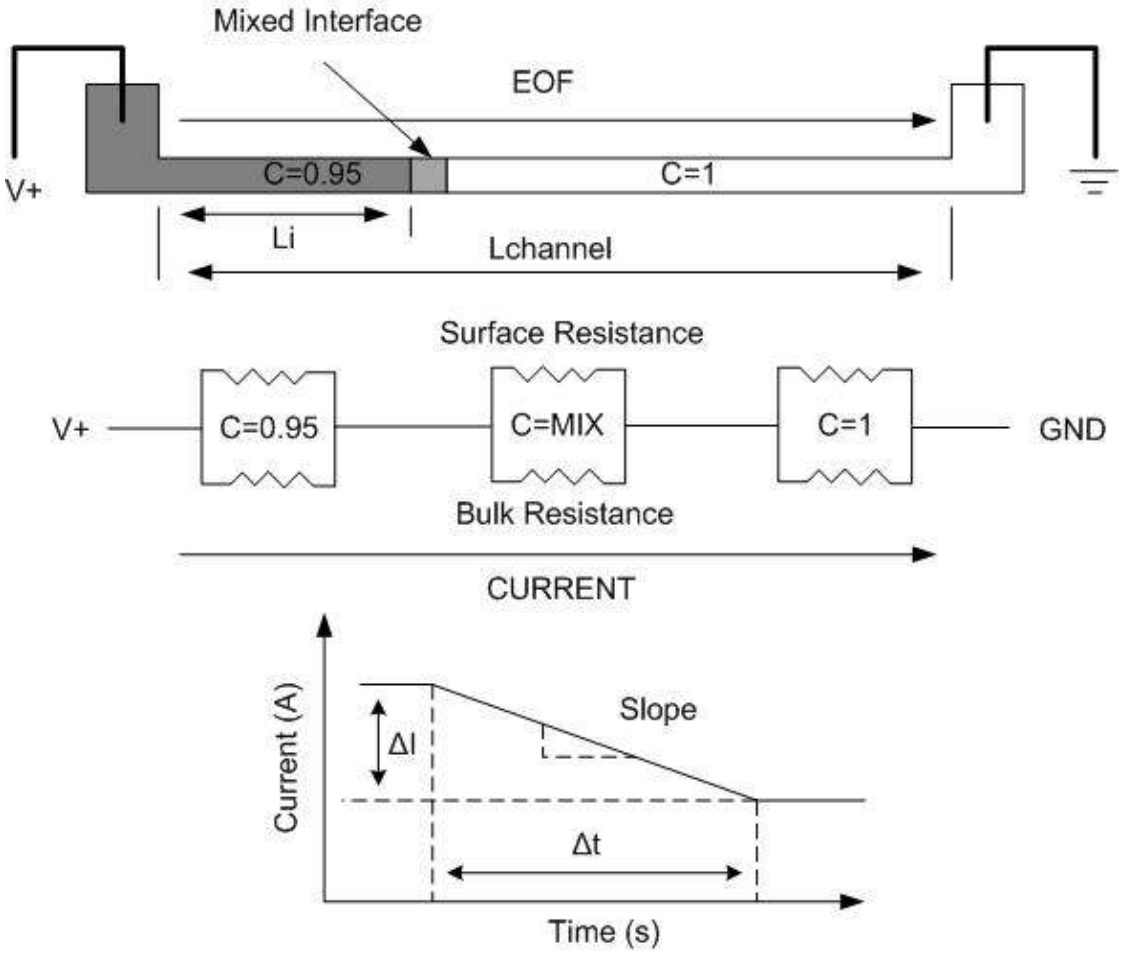

Figure 2.6 A schematic of the current monitoring method for measuring the electroosmotic mobility of a test solution. The motion of the interface is traced as the current changes due to the difference in electrical conductivity between the two solutions. If the two solutions are close together in concentration then the current drop is linear and the velocity can be determined from the displacement time.

There are several disadvantages to using the current monitoring technique. The technique is still based on indirect measurements of the velocity and the flow may not be purely electroosmotic. Differences in concentration will cause small differences in zeta potential which will generate an induced pressure gradient that will alter the flow. In reality, the measured average velocity is an average of the electroosmotic mobility of the two solutions. There are also errors associated with using electroosmotic flow such as joule heating and electrolysis. Electrolysis is especially important since it affects both the zeta potential through the pH change and the electrical conductivity through the generation of extra ions. As well, undesired flow from external pressures (Laplace and hydrostatic) will cause additional flow, thus erroneous measurement of the electroosmotic velocity. There are also issues with performing the experiments. Current methods require extensive interaction with the experimental setup in the filling and refilling of the

reservoirs to achieve the displacing interface. This usually results in very diffuse interfaces causing difficulties in measuring the displacement time. Consequently, several experiments must be performed before a "good" current trend is seen. As part of this thesis an improved method of performing current monitoring measurements which solves many of the above mentioned problems was developed through the effective design of a new Y-channel testing apparatus. The details are provided in Chapter 6.

2.6 Micropumps

Several applications require small volumes of fluid to be pumped with high precision in the nano-litre (nL) to millilitre range (mL). Each application has its own specific design parameters that must be met. For instance, micro-drug delivery requires controlled injection of therapeutic agents into a patient. The pressure requirement is high for these pumps in order to overcome the backpressure present in blood vessels. Micro-electronics cooling requires pumping through long tortuous networks where maximizing flow rate for increased heat transfer is of the utmost importance. While in Lab-on-a-chip devise or μ-TAS miniaturization and low power consumption is required for portability. To date several micropumps have been developed to meet these applications as reviewed by Laser and Santiago (2004), Tsai and Sue (2007), Nguyen *et al.* (2002) and Nguyen and Wereley (2003).

Micropumps can be grouped into either mechanical or non-mechanical pumps based on the method used for generating flow. Mechanical pumps use an actuator or moving boundary to generate pressure forces that induce fluid flow. In non-mechanical pumps, kinetic momentum of the fluid is generated by continuously adding energy to the system. Here a brief review is provided for mechanical pumps as well as non-mechanical pumps followed by a more detailed discussion of EO pumps which are a specific subset of non-mechanical pumps. In this work, EO pumps are integrated in a PDMS chip to control fluid flow in a microfluidic cell culture system.

2.6.1 Mechanical Pumps

The most common mechanical micropump is the reciprocating type where moving boundaries do work on the fluid using a periodic motion similar to piston-based macroscale pumps [Laser and Santiago (2004)]. In microscale pumps the piston is replaced with a deformable membrane that is externally actuated. The structure of a typical reciprocating pump is shown in Figure 2.7. The components are a pumping chamber containing a diaphragm attached to an actuator with passive check valves located at the inlet and outlet of the pump. The pump works when the actuator

deflects the diaphragm either reducing or increasing the volume in the pump chamber. During the suction stroke fluid is drawn into the pump (volume increases) and during the discharge stroke fluid is pumped out (volume decreases). The motion is repeated to provide continuous flow. The performance of the pump depends on the displacement of the membrane (volume of fluid pumped per stroke), frequency of the strokes and sealing of the valves.

A number of different reciprocating micropump configurations have been presented in literature [Laser and Santiago (2004)]. However, the main difference between most designs is the type of actuator used to deflect the diaphragm. These actuators include electrostatic [Richter *et al.* (1998)], piezoelectric [Olsson *et al.* (1997)], and thermo-pneumatic [Jeong and Yang (2000)]. Electrostatic actuators rely on the Coulomb force generated when two charged parallel plates are attracted to each other. Piezoelectric work on the change in shape some materials experience (such as quartz) when a voltage is applied to them. In thermo-pneumatic drivers a secondary fluid behind the diaphragm is heated causing it to expand and exert a pressure. Both electrostatic and piezoelectric result in small deflects (few micron) but are able operate at high frequency (>500Hz) and have reached flow rates in excess of 400μL/min [Laser and Santiago (2004)]. However, these designs suffer from complex fabrication and require high driving voltages. Thermo-pneumatic pumps have achieved similar flow rates an are much simpler to fabricate, operate at lower voltages and posses larger membrane deflection, however, the temporal response is limited by heat transfer so these pumps operate at much lower frequencies (<5Hz).

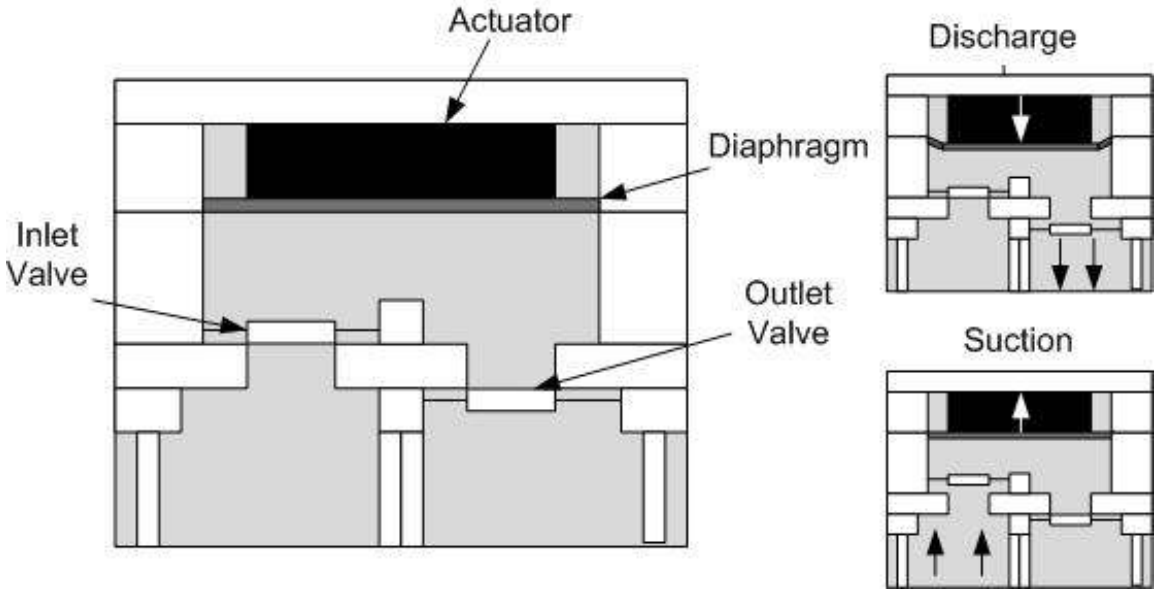

Figure 2.7 Reciprocating micropump design with check valves. A diaphragm is deflected by an actuator which either increases or decreases the volume of fluid in the pump chamber. Check valves are used to allow for flow in only one direction during the discharge and suction strokes.

Peristaltic pumps are another class of micropumps that have also been developed [Nguyen and Wereley (2003)]. The pumping motion is based on moving fluid in a tube by squeezing the tube in a peristaltic motion. Peristaltic micropumps typically contain three chambers with deflectable membranes that are actuated in a peristaltic waveform. Again the deflection of the membranes can be accomplished in several manners similar to the reciprocating pumps but peristaltic pumps do not require check valves which simplifies the operation, though, peristaltic pumps suffer pulsed flow and some leakage due to back pressure in the non-actuated state.

The majority of micropumps developed to date are fabricated in silicon using microfabrication techniques. Of more interest to this project is the integration of micropumps into PDMS based microchips. Only a limited amount of mechanical pumps have been thus far developed in PDMS. Jeong *et al.* (2005) developed a peristaltic pump in a PDMS/glass device using thermo-pneumatic actuation from Cr/Au heaters fabricated on the glass. Their pumped reached a flow rate of 21.6μL/min at 2Hz operation with 20V actuation and has footprint less than a dime. Quake's group has fabricated both peristaltic and rotary pumps using pressurized air to deflect a membrane in a bi-layer PDMS chip [Unger *et al.* (2000); Chou *et al.* (2001)]. These pumps have been combined in multi-plexed networks achieving unprecedented control over fluid flow [Melin *et al.* (2007); Gomez-Sjoberg *et al*. (2007)]. Pan *et al.* (2005) developed a magnetically driven reciprocating pump with ball check valves reaching 774 μL/min flow rates with only 13mW power consumption. In this design a permanent magnet is attached to the diaphragm and another magnet attached to the shaft of a micromotor rotates generating the reciprocating motion. Kim *et al.* (2004) fabricated an all PDMS reciprocating pump using a piezoelectric actuator with diffusers rather than passive valves. The flow rate reached 32.9μL/min with an operating voltage of 150V at 200Hz. The main disadvantageous of integrating mechanical pumps on chip is the more complex fabrication required, pulsed flow and limited lifespan due to eventual mechanical failure. In terms of operation mechanical pumps provide the highest flow rates and most stable performance.

As part of this discussion, it is also important to mention several macroscopic external pumps that are commonly used in microfluidics, particularly for cell culture applications. These include commercial peristaltic pumps and syringe pumps. Macroscale peristaltic pumps operate in a similar manner to microscale except that the actuation is usually mechanical from a rotating cam. Syringe pumps provide high precision flow down to several pL/s and work by simply depressing

the syringe plunger at a steady state. The main disadvantage of the macroscale pumps, other than their obvious size, is that they require large external networks to connect with the chip. Due to these external components there is an inherent lag in temporal response of the network so fine control over the flow field cannot be achieved using either syringe or peristaltic pumps. Furthermore, for multi-fluid applications several of these pumps would need to operate in unison which greatly complicates matters in large μ-TAS and LOC systems.

2.6.2 Non-Mechanical Pumps

Non-mechanical pumps do not require moving parts so are easier to design and are relatively simple to fabricate. However, non-mechanical pumps do not perform as well as their mechanical counterparts in terms of flow rate, response time, and back pressure. A wide range of non-mechanical pumps are found in literature including electrohydrodynamic, electrokinetic, magnetohydrodynamic, electrochemical displacement and electroosmotic as well as many others. The key features of some of these pumps are discussed below.

Electrohydrodynamic (EHD) micropumps are based on electrostatic forces, most notably the Coulomb force acting on ions in a dielectric fluid. EHD pumps can be further categorized into induction and injection pumps. In induction pumps, a travelling wave electric field drags the induced charges in the wave direction. This effect works with dipolar molecules as well as any volume of fluid that differs in either conductivity or permittivity such as fluid-solid interfaces (walls, particles), fluid-fluid interfaces (layered fluids) and heterogeneous conductivity and permittivity caused by temperature changes [Nguyen and Wereley (2003)]. In injection pumps the Coulomb force moves ions that are supplied by the electrodes through an electrochemical reaction. These pumps only work with dielectric fluids which are fluids that do not contain an appreciable amount of ions. Thus EHD pumps are limited to working fluids such as deionized water, ethanol and acetonitrile. As reviewed by Laser and Santiago (2004) a number of EHD pumps have been developed with varying capabilities.

Electrochemical pumps use the expansion of gas bubbles generated by the electrolysis of water to generate flow. Böhm *et al.* (2000) reported an electrochemical displacement pump that is able to achieve a dose volume accuracy of 5nL. Other chemical pumps have been developed based on osmotic pressure. Osmotic flow is generated across a semi permeable membrane when a concentration difference in solute exists. Park *et al.* (2007) developed a PDMS osmotic pump and coupled it to a concentration gradient generated in a cell culture chip. The pump reached flow

rates of 1μL/min and the performance could be tailored by changing the solute concentration. The benefit of using osmotic pumps is that they require no electrical power to operate. The disadvantages are low flow rates and a lack of dynamic control.

Magnetohydrodynamic pumps operate on the principal of the Lorentz force created when an electric current and magnetic field are crossed. Several magnetohydrodynamic pumps have been developed using either DC currents [Huang *et al.* (2000)] or AC currents (to reduce electrolysis) [Lemoff and Lee (2005)]. These pumps can operate in either direction but work best with highly conductive solution and require strong permanent magnets. Another magnetic based pump uses the motion of a ferrofluid plug to push fluid through a microchannel [Hartshorne *et al. (*2004)]. Other types of pumps include those based on ultrasonic waves which include transferring momentum directly to the fluid or to a flexural plate [Nguyen and White (1999)]. Pressure "bombs" increase the atmospheric pressure in a sealed fluid reservoir thereby driving fluid through a microchannel network. Good flow control is achievable with a chip containing several reservoirs by combining pressure bombs together. Braschler *et al.* (2007) showed precise control over a hydrodynamic focuser using four pressure bombs connected to a microfluidic chip. Passive pumps which do not require any external activation include those based on surface tension [Walker and Beebe (2002)] and gravity [Cho *et al*. (2003)], though such pumps lack the dynamic control that may be desired for various applications in microfluidics.

2.6.3 Electroosmotic Pumps

Electroosmotic (EO) pumps are a subset of non-mechanical pumps which convert electroosmotic flow into pressure driven flow. Figure 2.8 shows the working principal. An electric field is applied in only a portion of the microchannel generating electroosmotic flow. Due to continuity, a pressure gradient is created to propel the fluid through the rest of the channel. At the outlet of the EOF region a positive pressure pushes the fluid downstream, while at the inlet of the EOF region a negative pressure draws fluid into the microchannel. The pressure gradient also generates a back pressure flow in the EOF region creating the distorted EOF/parabolic profile.

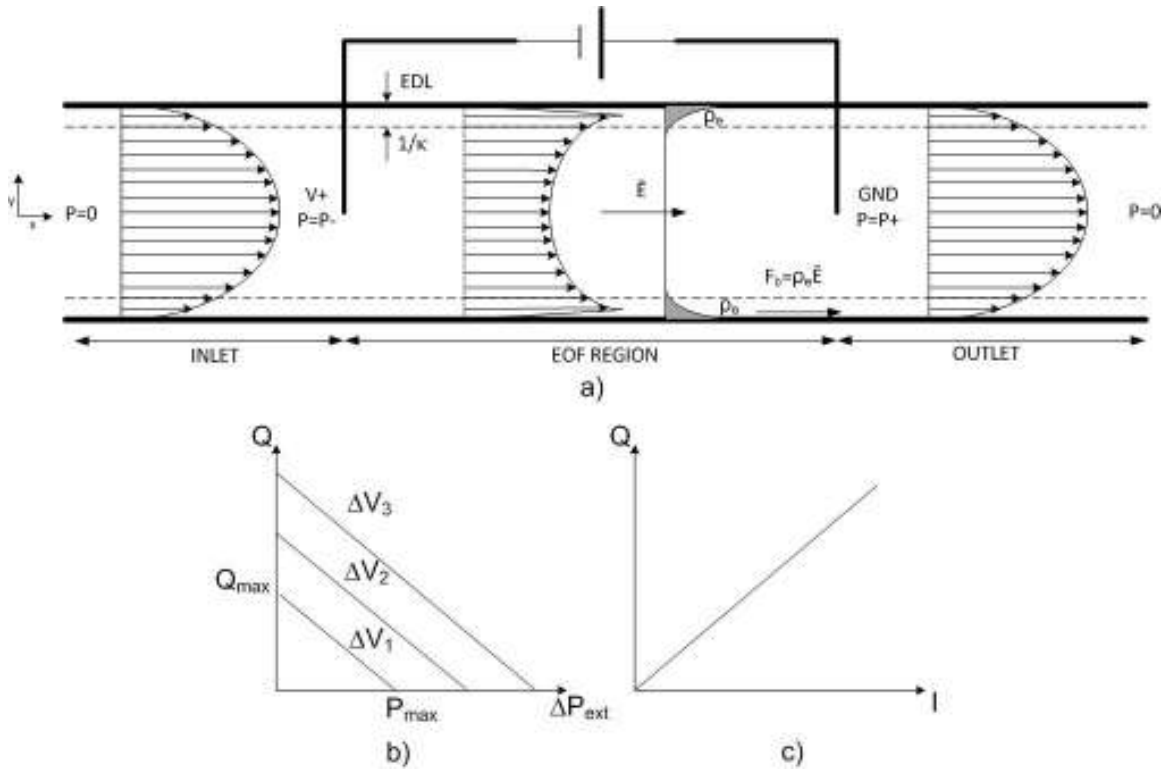

Figure 2.8 (a) Schematic of the working principal of an EO pump. Electrodes apply an electric field in a limited region of the microchannel generating EOF. A pressure gradient forms to continue pumping the fluid through the rest of the microchannel. Due to the gradient a back-pressure flow also occurs in the EOF region. (b) Q-P characteristics of an EO pump for various applied electric fields Q_{max} is when there is not load on the channel and P_{max} when there is no net flow (c) Relationship between flow rate and the applied current..

The operation and design of EO pumps have been reviewed by Yao and Santiago (2003), Yao *et al.* (2003) and Chen and Santiago (2002). Here a brief review of EO principals is provided. Assuming that a capillary is used for the microchannel, the flow rate in the EOF region is a combination of EOF and back pressure flow:

$$Q = \frac{\pi a^4}{8\mu L}\Delta P - \frac{\pi a^2 \varepsilon_o \varepsilon_r \zeta}{L\mu}\Delta V \cdot f(a/\lambda_d) \qquad \textbf{(2.48)}$$

where ΔP is the pressure difference, ΔV the applied electric potential difference, a is the capillary radius and $f(a/\lambda_d)$ is a factor that depends on the relative size between the capillary and the EDL. For the simple case of a symmetric electrolyte with a low surface potential (Debye-Hückel approximation) the factor is given as:

$$f(a/\lambda_d) = 1 - \frac{2}{a/\lambda_d}\frac{I_1(a/\lambda_d)}{I_o(a/\lambda_d)} \qquad \textbf{(2.49)}$$

where I_o and I_1 are zero-order and first-order Bessel functions of the first kind. In the limit of a thin EDL ($a>>\lambda d$) then the factor equals unity and the flow rate equation reduces to:

$$Q = \frac{\pi a^4}{8\mu L}\Delta P - \frac{\pi a^2 \varepsilon_o \varepsilon_r \zeta}{L\mu}\Delta V \qquad \textbf{(2.50)}$$

The flow rate- pressure relationship (Q-P) is linear for a given applied voltage as shown in Figure 2.3b. There exist two important points on the Q-P graph which define the operation of the pump. The first is the maximum flow rate, Q_{max}, which occurs when there is no back pressure and the second is the maximum back pressure, ΔP_{max}, which occurs when there is no net flow:

$$Q_{\max} = -\frac{\pi a^2 \varepsilon_o \varepsilon_r \zeta}{L\mu}\Delta V \qquad \textbf{(2.51)}$$

$$\Delta P_{\max} = \frac{8\varepsilon_o \varepsilon_r \zeta}{a^2}\Delta V \qquad \textbf{(2.52)}$$

Analyzing these equations one can see that to maximize the flow rate and pressure a high zeta potential, and electric field is required. Increasing the radius of the capillary improves the overall flow rate but decreases the maximum pressure that can be generated. To obtain an EO pump with a high flow rate and pressure capabilities several capillaries must be assembled in parallel. In this case, the flow rate scales directly with the number of capillaries, N, but the pressure stays the same as all of the capillaries experience the same back pressure:

$$Q_{\max N} = -N\frac{\pi a^2 \varepsilon_o \varepsilon_r \zeta}{L\mu}\Delta V \qquad \textbf{(2.53)}$$

$$\Delta P_{\max N} = \frac{8\varepsilon_o \varepsilon_r \zeta}{a^2}\Delta V \qquad \textbf{(2.54)}$$

In reality it is difficult to fabricate multiple parallel capillaries and instead porous structures such as glass frits or monoliths are used. For modelling purposes the pores are treated as tortuous capillaries where the flow rate is defined as [Zeng *et al.* (2001); Yao and Santiago (2003)]:

$$Q = \psi A\frac{\pi a^4}{8\mu L}\Delta P - \frac{\psi A}{\tau}\frac{\pi a^2 \varepsilon_o \varepsilon_r \zeta}{L\mu}\Delta V \cdot f(a/\lambda_d) \qquad \textbf{(2.55)}$$

Several parameters define the porous structure: Ψ is the porosity ($\Psi=V_e/V_t$) which is the ratio between the void volume and the total volume, τ is the tortuosity ($\tau=(L_e/L)2$), L_e is the effective

length of the pore, L is the length and A is the total area of the porous structure. The efficiency of an EO pump is defined by the useful work over the total power consumption:

$$\eta = \frac{\Delta P Q}{VI} \tag{2.56}$$

The maximum efficient occurs when the pump is operating half way on the Q-P curve:

$$\eta_{\max} = \frac{\Delta P_{\max} Q_{\max}}{4VI} \tag{2.57}$$

The key parameters that define the performance of an EO pump are (a) the applied electric field (b) the dimensions of the EOF region (i.e. pores, size) (c) the EDL shape with respect to the size of the capillaries (d) the liquid properties most notably ion concentration (electric conductivity, EDL shape) and pH (zeta potential). The ideal solution is one with a low conductivity and high zeta potential such as deionized water. The fact that performance depends largely on the properties of the solution is a serious drawback to using EO pumps. EO pumps must be re-calibrated for each solution that will be pumped, and are subject to instability with time due to changes in solution properties. There are still several advantages of EO pumps that make them suitable for microfluidic applications: (a) they require no moving parts, (b) are relatively easy to fabricate, (c) produce pulse free flow and (d) can generate high pressures and flow rates in a compact area.

A number of EO pumps have been developed in recent years. Traditional EO pumps based on simple capillary structures are driven by extremely high voltages to achieve either adequate flow rates or pressures (several kV) which are impractical for many applications. To increase the flow rate multi-channel EO pumps have been developed [Morf *et al.* (2001a); Morf *et al.* (2001b)]. Morf *et al.* (2001b) integrated these multi-channel EO pumps into a larger u-TAS system for volumetric nano-titration. To achieve high pressures a cascade design can be used which consists of several EO pumps connected in series with the same voltage drop across each pump. Takamura *et al.* (2003) demonstrated a 10 stage cascade EO pump design with 130nm EOF channel region that could reach pressures of 25kPa at 10V. Chen *et al*. (2005) developed a 3 stage pump with porous silica bead packed columns that achieved pressures 10MPa but at a much higher applied voltage (5kV). A zwitteronic solute added to the working fluid can further increase the pressure and efficiency by changing the viscosity and dielectric constant of the fluid [Reichmuth *et al.* (2003)]

Porous based pumps have been fabricated from packed silica beads [Chen *et al.* (2004)] sintered glass frits [Yao *et al.* (2003)], and monoliths [Tripp *et al.* (2004)]. Yao *et al.* (2006) demonstrated an EO pump using silicon membranes, whose pore size can be accurately controlled with microfabrication techniques; flow rates of 3.5mL/min were achieved. Polymer monoliths are particularly promising since the surface chemistry and pore size can be easily controlled. Tripp *et al.* (2004) developed polymer monolith base EO pumps with surface grafted ionisable monomers that could be tailored to increase the pressure or flow rate. Pumps incorporating the monoliths were able to achieve pressures up to 0.38Mpa and flow rates of 0.41mL/min at only 50V. A disadvantage of polymer monoliths is that they tend to swell in certain solutions which may clog the EOF channels.

One of the main issues with using porous structures is the difficulty of integrating these components (frits, beads, monoliths) into microfluidic chips. To solve this problem planar EO pumps have been developed which can be fabricated simultaneously with the microfluidic network [Chen and Santiago (2002)]. In planar pumps the cylindrical capillaries or pores are replaced by short, wide and shallow rectangular channels. Chen and Santiago (2002) and Takamura et al. (2003) both presented planar EO pumps fabricated in glass microchips. Several analytical studies have also been performed to optimize the performance and thermodynamic efficiency of both frit based [Griffiths and Nilson (2005)] and planar [Hu and Chao (2006); Min *et al.* (2006)] EO pumps.

The largest issue plaguing EO pumps is the lack of long-term stability during continuous operation caused by electrolysis at the electrodes. As discussed in Section 2.2.2.2, electrolysis has a double negative effect of generating bubbles and pH changes around the electrodes. Bubbles may disable the electric connection to the fluid or even block fluid flow into the EOF region. After long-term operation the pH of the surrounding fluid at the anode will decrease. Since the anode is also located at the inlet of the EO pump (for negatively charged surfaces) and the zeta potential is pH dependent (decreases with pH), if the pH change is severe the flow will decrease and may eventually stop.

The problem of bubbles entering the EOF region is usually solved by separating the electrodes from the working fluid with an ion exchange system. Commercial ion exchange membranes such as Nafion have been applied to this task. [Morf *et al.* (2001b); Liu *et al.* (2003)]. Nafion is a cation exchange membrane typically used in fuel cell applications. Morf *et al.* (2001b)

demonstrated the use of Nafion membranes in a planar EO chip design made from PMMA/Pyrex. Liu *et al.* (2003) developed a Nafion connector which can be attached to PDMS to decouple the electrode from the working fluid. However, integrating commercial membranes is difficult due to inherent swelling and sealing issues. Nafion swells by approximately 10% in volume [Dupont Fuel Cells] once in contact with water. This makes it difficult to directly integrate these membranes into PDMS chips since PDMS is too elastic to withstand the expansion of the membrane [Jönsson and Lindberg (2006)]. One option presented by Takamura *et al.* (2003) is to fabricate membranes inside the microfluidic network using photopolymerized gel salt bridges. Several EO pumps were presented that can operate at low voltages using these gels. Some of these designs were analyzed using 1D circuit models by Brask *et al.* (2003). Bubbles also increase the electrical resistance of the network and may cause the electric field in the EOF region to fluctuate with time if the pump is run in a constant voltage mode. To improve stability, the pumps should be operated in a constant current mode, as the bubble resistance acts in series with the EOF channels, so the same electric field will always be applied across the EOF channels [Brask *et al.* (2005)].

Although the use of nafion membranes and gels solves the problems of bubbles entering the EOF region they do not eliminate the issue of pH changes affecting EO pump operation. Nafion is a cation exchange membrane and the gel is simply an ion exchange membrane, therefore, neither prevents the passage of H+ ions (which lower the pH) into the working fluid. To solve this issue Brask *et al.* (2005) used an anion exchange membrane system which eliminates the transport of H+ ions into the EOF channels. The pump could run continuously for extend periods of time, even after the buffer in the electrode reservoirs was completely depleted and the pH at the anode was severely acidic (pH=3). An issue with using anion exchange membranes is that they have to be continuously hydrated or small cracks will form causing leakage. A system that recombines the electrolytic gases using a platinum catalyst has also been developed by Yao *et al.* (2003).

This review demonstrates that many EO pumps have been developed. However, most of the pumps that have been discussed are stand alone devices which are still quite large (~5x5cm). Not many EO pumps have actually been integrated into microfluidic devices, especially with PDMS soft lithography fabrication techniques. As part of this thesis an integrated PDMS EO pump is developed, fabricated and tested as discussed in Chapter 7.

2.7 Microfluidic Cell Culture

Continuous perfusion microfluidic cell culture offers the biomedical researcher detailed control over environmental cues that influence cells including the supply of soluble factors, application of mechanical strain from shear, as well as cell-cell and extra cellular matrix interactions. There are also the obvious benefits that come with minituarization including reduced consumption of expensive reagents and the potential for parallelizing experiments to increase throughput. A theoretically complete LOC system for cell culture would include all of the steps in performing a biological analysis: cell growth, treatment, selection, lysis, separation and analysis [El-Ali *et al.* (2006)]. Combining all of these steps into one device will provide rapid and reliable measurements by eliminating the need for labour-intensive handling of samples between components which introduces errors during the analysis. To date many of these components have been developed seperately; however, interconnecting and packaging the system as a whole proves to be challenging. A number of review articles detail the development of cell culture and tissue engineering devices: El-Ali *et al.* (2006), Kim *et al.* (2007), Andersson and van den Berg (2004), Yi *et al.* (2006), Walker *et al.* (2004), Chin *et al.* (2006), Sia *et al.* (2003).

Listing all of various methods for performing cell culture is exhaustive and beyond the scope of this review (and expertise). There are several references available that cover the basics: Martin (1994), Davis (2002), Vunjak-Novakovic (2006) and Butler (2004). Here only a brief overview is provided. In traditional cell culture, cells are seeded in plastic containers such as Petri dishes, flasks, assay plates and roller bottles, which are treated to produce a charged surface for attachment and wetability [Harrison and Rae (1997)]. For cells to survive they must be covered in a fluid and be able to attach to the surface of substrate. The fluid that maintains the cells for prolonged periods of time is known as the cell culture medium. The cell culture medium constitutes a number of essential components for cell survival and growth. First, the medium must be isosmotic or isotonic which means it must have the same concentration of solute molecules that exist inside the cell. This means that a high concentration of salt, typically around 150mM NaCl is required. Higher concentration results in a hypertonic solution which will cause water to leave the cell and the cell will shrink. A lower concentration has the opposite effect and water will enter the cell causing it to swell and possibly rupture. Cells also require a stable pH between (7-7.4) depending on the cell time which is accomplished by adding a buffer to the solution. The medium must also contain the necessary nutrients (amino acids, vitamins), an energy source (glucose) and growth factors (serum). To mimic the conditions cells experience *in vivo* (in a living tissue) the temperature must also be controlled for certain cells. For mammalian cells this

the temperature must be regulated around 37°C. Most incubators provide combined temperature and CO_2 control (5-10%) which is used to strictly regulate the pH of the culture medium. In addition, sterility and biocompatibility with the substrate is also required. The above mentioned factors are the basics of sustaining cell cultures in general and all of these features must also be prevalent in any microscale cell culture system.

Standard cell culture poorly mimics the environment that cells experience in the body. In their natural environment cells are greatly affected by the presence of neighbouring cells by creating strong mechanical and biochemical connections with them [El-Ali *et al.* (2006)]. Cells not only receive signals from the microenvironment but also alter it by producing or consuming soluble factors. Culturing cells on the microscale allows for a more natural microenvironment to form. Because of the decrease in size, the cells have more control over their microenvironment as secreted factors are not quickly diluted into the surrounding medium. For this reason cells in static microculture tend to grow at a slower pace than cells in traditional cell culture flasks [Walker *et al.* (2002)]. Static conditions also result in an accumulation of waste from the cells which may stunt their growth. However, with continuous flow of new medium the waste can be removed.

Continuous perfusion microfluidic cell culture also opens up the possibility of performing a variety of experiments by manipulating the microenvironment through the supply of soluble factors available to the cells. With conventional cell culture the background concentrations of factors and nutrients changes uncontrollably with time as the cells grow. Many studies have been performed with microfluidic cell culture looking at studying the effect of soluble factors [Park *et al*. (2007)]. The laminar nature of microfluidic flow allows for new experiments to be performed. Due to the well defined structure of laminar flow shear stress can be easily controlled. Lu *et al.* (2004) developed a microfluidic device that could culture cells and determine the strength of cell adhesion through shear by linearly changing the flow rate. Laminar flow combined with diffusive mixing can generate concentration gradients across a number of cell chambers through a gradient generator [Lee *et al.* (2005)] or within a single chamber [Park *et al*. (2007)]. Microfluidic cell culture has a greater ability to represent the highly perfused conditions certain cells, such as liver and kidney, experience in their natural setting [Powers *et al.* (2002)].

Kim *et al.* (2007) outlines many of the design parameters that must be considered in a microfluidic cell culture device. The first decision that needs to be made is to determine what material will be used to fabricate the chip. As reviewed in Section 2.4, microfluidic chips have been fabricated from a variety of materials including glass, silicon and several polymers. The most common material is PDMS mainly due to the ease with which microfluidic devices can be fabricated using soft lithography. PDMS also has several properties that are beneficial for cell culture applications: PDMS is bio compatible, autoclavable, transparent, gas permeable and possesses low auto fluorescence [Kim *et al.* (2007); Mata *et al.* (2005); Sia and Whitesides (2003)]. For example, thin sheets of PDMS can be used as membranes for gas exchange with the cell culture medium [Vollmer *et al.* (2005); Kane *et al.* (2007)]. However, there are some issues with using PDMS for cell culture. In addition to being permeable to many gases, PDMS is also permeable to water vapour which can cause changes in solute concentration. This can affect cell culture in PDMS devices by changing the osmolality of the culture medium [Heo *et al.* (2007)]. Heo *et al.* (2007) used a sheet of Parlyene to block the transport of water vapour from the cell culture chambers with good success. Another negative property of PDMS is that it tends to absorb hydrophobic particles; the process is enhanced by the small surface-to-volume ratio typical of microchannels [Toepke and Beebe (2006)]. The loss of soluble factors and secretions from the cells to absorption can greatly alter the microenvironment. In addition, for glass/PDMS hybrid devices the cell culture surface must be modified for the cells to attach. Fortunately, many current cell attachment treatments used for glass can also be applied to PDMS [Boxshall *et al. (*2006); Kim *et al.* (2007); Toworfe *et al.* (2004)].

The design of the cell culture chamber is one of the critical components of any microfluidic perfusion system. The region in which the cell can control is known as the effective culture volume (ECV) [Walker *et al.* (2004)]. As opposed to macro scale designs the microfluidic perfusion culture chamber is characterized by large surface-to-volume ratio and smaller transport scales. Consequently cells have more control over the microenvironment. A simple cell chamber is a straight microchannel with cells attached to the bottom surface. However, this design may not provide the most ideal configuration due to potential non-uniformity in soluble factors. As these factors are transported through the microchannel, cells are consuming or secreting factors and the cells at the end of the channel may not be experiencing the same environment as those at the beginning. A number of cell culture chambers have been design to generate a more uniform culture environment. Lee *et al*. (2005) designed a C-shaped reactor with small perfusion channel around the periphery and Powers *et al*. (2002) fabricated microwells to shield cells from any

shear forces. The design of these chambers included detailed flow field and mass transport analysis using FEM simulations. Note that 2D patterned seeding of the cells is also possible by locally modifying the substrate through a variety of techniques such as microcontact printing [Khademhosseini *et al.* (2004)] and laminar flow patterning [Takayama *et al.* (1999)]. Both of these techniques could be incorporated in the fabrication of the EO pump microfluidic chip to obtain spatially controlled adhesion. As well, 3D scaffolding fabricated from biodegradable materials [Koh and Pishko (2006)] or hydrogels [Vozzi *et al.* (2003)] can also be incorporated for tissue engineering. To maintain the appropriate pH and temperature the entire chip can be placed inside an incubator during culture, though integrated on chip heaters [Stangegaard *et al.* (2006)] and transparent heater films [Futai *et al.* (2006)] have been used.

Sterilizing the chip is essential for performing long term cell culture. There are a variety of techniques available for sterilizing components such as autoclaving, washing with 70% ethanol, chemical sterilization with ethylene oxide gas and irradiation with UV light [Kim *et al.* (2007)]. Not all of these are applicable to microfluidic chips depending on the structures that they contain. For instance, autoclaving uses high temperatures (>120°C) which exceed the melting point of many plastics. The most common method of sterilization is to flush the chip with 70% ethanol, followed by successive flushes of culture medium to assure that no residual ethanol remains. After the chip is sterilized it may only be handled inside a bio hood unless a closed loop system is attached. For opening in the system 0.2µm filters can be attached to maintain the sterile environment [Kim *et al.* (2007)].

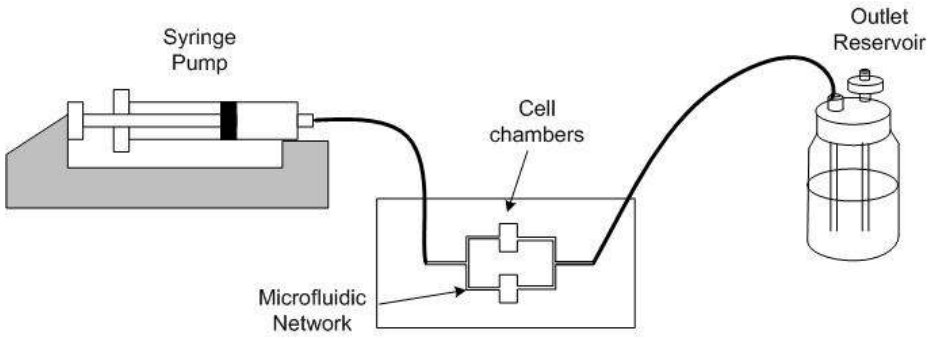

Figure 2.9. Typical setup of a microfluidic perfusion system consisting of a microfluidic chip connected to a pump and outlet reservoir.

A typical flow network used for a cell culture chip consists of an external pump either syringe [Kim *et al.* (2006)], peristaltic [Leclerc *et al.* (2004)] or gravity [Zhu *et al.* (2004)] connected to the chip *via* tubing. The outlet of the chip is connected to a larger reservoir which is kept sterile by attaching a filter to the bottle. The microfluidic network contains a series of microchannels

that distribute the medium to the cell chambers. The overall flow rate to the chip can be controlled but not the flow to each individual cell chamber which is governed by the relative hydrodynamic resistance of each channel [Kim *et al.* (2006)]. Since the pumps are off-chip there is no opportunity for dynamic control such as injecting small amounts of reagent into the flow network.

A few devices have been fabricated with integrated valves and pumps on-chip. Futai *et al.* (2006) developed a recirculating perfusion chip using a Braille display to pump and valve the fluid by deflecting a PDMS membrane. Park *et al*.(2007) combined an off chip osmotic pump in a cell culture chip to generate a well defined concentration gradient of fetal bovine serum in a cell culture chamber. Gomez-Sjoberg *et al.* (2007) used Quake valves to design a fully automated multi-plexed cell culture system with 96 culture chambers. On-chip valves and pumps provide independent control to each of the chambers. The chip was used to perform transient simulations on the proliferation, osteogenic differentiation, and motility of human primary mesenchymal stem cells. This type of device demonstrates the potential of microfluidic cell culture for the systematic screening of factors affecting cell physiology.

Pressure driven flow is the primary pumping method used in cell culture chips. Electroosmotic flow has only been used in very limited cases. Shackman *et al.* (2005) used EOF flow to sample the perfusate and perform an immunoassay for real time monitoring of insulin secretion while culturing Langerhans. Although other applications of EOF with cells have can be found, most are for cell lysis using the strong electric fields inherent to EOF [Lee and Cho (2007); Gao *et al.* (2004)]. At this point in time no devices combining EO pumps and cell culture have been reported.

2.8 Summary

This chapter supplied the background information required for developing a microfluidic device. A detailed discussion was provided regarding the major transport phenomenon occurring in microflows. This was followed by techniques for designing microfluidic chips through numerical and system modelling, fabricating devices, and characterizing designs by measuring flow fields, temperature fields and electrokinetic properties. A review of micropumps was provided with emphasis on EO pumps. Finally, a summary of microfluidic cell culture discussing the important parameters that must be considered in any chip design. The review also pointed out the lack of applications involving EO pumps in integrated chip designs.

Chapter 3

Experimental Techniques for Design Characterization

The purpose of this chapter is to provide a foundation for the experimental aspect of this thesis. The equipment and procedures used throughout this work are concentrated in this chapter and are referred to frequently through this thesis. This includes techniques for performing flow field visualization using fluorescent microscopy, measuring solution properties, measuring microchannel dimensions and generating pressure driven and electroosmotic flow.

3.1 Fluorescent Flow Field Visualization Methodology

Micro flow visualization is an important technique for analyzing, developing and evaluating microfluidic devices. Several non-invasive imaging techniques have been developed using particle-based, scalar-based and point detection methods [Sinton (2004)]. Although each technique is slightly different, the working principal is essentially the same: the motion of the bulk fluid is inferred from the observed velocity of marked particles. Fluorescent molecules are employed to increase the measured signal due to the small fluid volume in a microchannel. Fluorescence is the process by which molecules emit a photon after they are excited by external electromagnetic radiation. The emitted photons are of lower energy or longer wavelength than the excitation photons. This shift in wavelength, known as the Stokes shift, is the basis of fluorescence microscopy since it permits filtering of the excitation light from the emission light.

The most predominant micro scale flow visualization used in the study of micro flows is micro-PIV. Originally, developed by Santiago *et al.* (1998) and Meinhart *et al.* (1999), micro-PIV has been used extensively to study both pressure driven flow [Meinhart and Zhang (2000)] and electroosmotic flow [Devasenathipathy *et al.* (2002)]. In this method, the particle displacement is cross correlated between two successive images to obtain a velocity vector. The infrastructure and techniques required for micro-PIV are extensive and costly. At the time of this thesis a micro-PIV system was not available for performing detailed micro flow visualization. Instead, several simpler techniques using fluorescence microscopy were applied to monitor the flow field. These methods include particle streak velocimetry (PSV) for visualizing streamlines and particle tracking velocimetry (PTV) for obtaining magnitudes of velocity. Scalar based visualization was also used to visualize the flow of multiple streams. The experimental system and techniques are discussed below beginning with the working solutions.

3.2 Working Solutions

Buffer solutions are often used in biological and chemical processes as they are able to maintain a set pH level even with minor additions of acid or base. In terms of electroosmotic flow, electrolysis at the electrodes generates additional H^+ (anode) and OH^- (cathode) ions that alter the pH level of the surrounding medium. The zeta potential is strongly dependent on the pH level of the solution and any fluctuations may affect the performance of the EO pump. An effective buffer solution can minimize changes in pH and stabilize electroosmotic flow.

For this purpose two buffer solutions were used in the electrode reservoirs. The first is 1XTBE (89mM Tris-Base, 89mM Boric Acid, 1.98mM EDTA, 2.5mM NaOH) which was also used as a working fluid during EO pump testing. TBE was chosen for initial testing of the EO pump since it provided the most stable and repeatable electroosmotic measurements (refer to Chapter 6). However, TBE is often used for cell lyses and was not used for tests with cells. The second solution is a commercial buffer called Bufferall from Sigma Aldrich which contains a combination of Good's buffers (EPPS, HEPES, MOPS) of unknown concentration (proprietary data) and pK_a values of 7.2, 7.55 and 8.0. A combination of buffers at different pK_a is an effective means of suppressing wide pH fluctuation. Good's buffers are chemically stable and are often used in cell culture applications [Good *et al.* (1966)]. Bufferall comes in a 100X concentration and was diluted with ultra pure water (UP water) to a 1X concentration. To obtain a higher buffer capacity 2ug/L $NaHCO_3$ was added and the solution was titrated to pH 7 with 0.1M NaOH (Sigma Aldrich).

3.2.1 Solution Properties

Determining the properties of the working fluid is important to modeling and design. The most important properties in terms of electroosmotic flow are the pH, electrical conductivity and electroosmotic mobility. For measuring pH and conductivity specialized low sample microprobes (MI-407, MI-915, Microelectrodes Inc.) were used in conjunction with an Orion 5Star meter (Thermo Scientific). To insure high accuracy readings the meter was calibrated regularly with standard calibration solutions. Other fluid properties were assumed to be the same as water: density ρ=1000 kg/m^3, viscosity μ=0.001 Ns/m^2, relative dielectric constant ε_r=80, thermal conductivity k=0.6 W/mK. Electroosmotic mobility measurements were performed using the current monitoring technique and a novel Y-channel design developed as part of this thesis (refer to Chapter 6).

3.2.2 Fluorescein Dye

Fluorescein die was used as a scalar based technique for micro flow visualization. In this method, standard reference fluorescein dye (Molecular Probes, Oregon) was added to the working fluid in a small concentration (100µM). The concentration of dye is low enough so that it does not affect the general fluid properties. The absorption maximum of fluorescein is 490 nm and the emission maximum is 513 nm. In addition, fluorescein dye has a diffusion coefficient of 4.37×10^{-10} m^2/s and estimated electrophoretic mobility of -3.58×10^{-8} m^2/Vs [Taylor (2007)]. Fluorescein dye is often used to indirectly visualize the flow of multiple streams within a complex microfluidic network as shown in Figure 3.1.

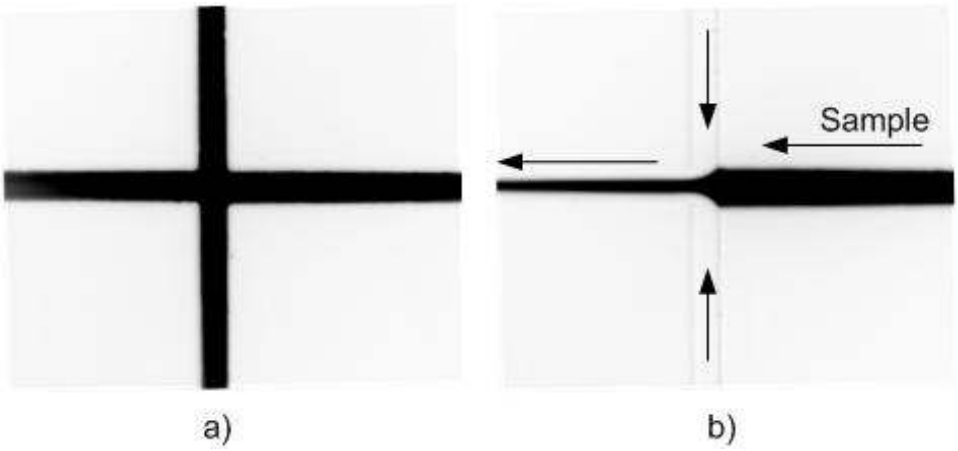

Figure 3.1 Example of the use of fluorescein dye to study hydrodynamic focusing in a cross microchannel design. Images are inverted (black represents fluorescence): (a) Fluorescein dye is added to all streams to show the geometry of the intersection and (b) dye is added only to the sample stream in order to demonstrate the degree of focusing. Images obtained with assistance from Barsam Tabrizi.

3.2.3 Fluorescent Particles

Adding particles to the fluid is an effective method for visualizing the flow field. In this work two particle solutions were used containing polystyrene latex beads with a nominal diameter of 0.2µm and 0.5µm (Fluoresbrite YG, Molecular Probes). The particles are yellow-green fluorescent with an emission wavelength of 441nm and an excitation wavelength of 486nm. The concentration of the stock solution is 2.5% solid material (5.68×10^{12} particles/mL, 3.64×10^{11} particles/mL) and was diluted to 0.0125% in the working solution. If the particle density is too high it is difficult to visualize the particles due to high levels of background noise from out of focus particles. At first the 0.2µm particles were used but these were too difficult to visualize using the current microscope set up. Instead the 0.5µm particles were used for all measurement experiments. However, there is a concern that the particles may affect the flow field since the smallest channel dimension is 2.7µm which eventually leads to partial blockage of the channel.

At the start of an experiment the particle solution was first ultra-sonicated for ten minutes to break up clumped particles and homogenize the solution. In general, the properties of the micro spheres are not well known but experimental observations indicate a strong negative charge [Taylor (2007)]. Hence due to additional electrophoretic forces the motion of the particles does not correlate with the motion of the bulk fluid under electroosmotic flow as discussed in Section 2.2.3. Consequently, velocity measurements in regions of strong electric fields were not considered for quantitative analysis. On the other hand, in purely pressure driven flow the particle velocity represents the fluid velocity since only the drag force is acting on the particle (buoyancy is negligible since particle density is ρ=1.05 kg/m^3) and the relaxation time is small (τ_p=1e-9s) [Santiago *et al.* (1998)].

3.3 Microscopy

Visualization of the fluorescent particles and microchannel dimension measurement was performed with a fluorescent microscope and CCD imaging system as shown in Figure 3.2. The main microscope used is the Olympus GX-71 reflected light inverted microscope. The major components of the microscope include dual lamps (mercury and halogen), filter mount, multiple objectives, filter cubes and CCD camera connected to a computer. Choosing the appropriate objective and lamp is important to capture the desired level of detail. In this work, 5x, 10x and 20x objectives were used. The properties of the objectives are (numerical aperture, working distance): 5x (0.15, 12mm), 10x (0.3, 6.5mm) and 20x (0.46, 3mm). The amount of light gathered decreases with magnification for an epi-illumination microscope. Therefore, the lowest magnification necessary to accomplish the task was always used. The microfluidic chips were fabricated from 1mm glass slides on the bottom and 2.5mm PDMS molds on top. Since observations with the inverted microscope were made through the bottom, the working distance of the objectives was not an issue.

The mercury arc lamp (100W) and the halogen lamp (100W) were both used for illumination. In most cases the halogen lamp was used except for the illumination of the 0.2μm beads where the mercury lamp provided higher fluorescent intensity. Filter cubes consisting of an excitation band pass filter, long pass dichroic mirror and emission long pass filter were used with the fluorescein dye and fluorescent particles. In particular, the BSWM Olympus filter cube which posses the following characteristics: BP450-480 nm excitation, DM 500nm dichroic mirror, and BA 515nm long pass emission filter. To visualize features and channel geometry the microscope was set to bright field illumination.

Images were recorded using a high speed CCD camera. High frame rates are required to track particles and capture sequences of pictures for videos. The monochrome camera accompanying the GX-71 microscope is a Q-Imaging Retiga Exi Mono. The camera image area is 1392 x 1040 pixels or equivalent 8.88 x 6.6 mm area with a progressive scan feature. The image digital image quality is 12 bit with a maximum 10 frames per second frame rate at this specification. With binning (grouping pixels together) the capture speed increases up to 110fps (8x8 binning). In this work, lower 8 bit images were used since the images are qualitatively analyzed and can be easily converted into jpeg and avi files. Accompanying the camera is a custom software program (Image Pro-Plus) to capture the images and perform post image processing. The program is very flexible and allows for intensity line profiling, object tracking, data filtering, image annotation, and spatial measurement.

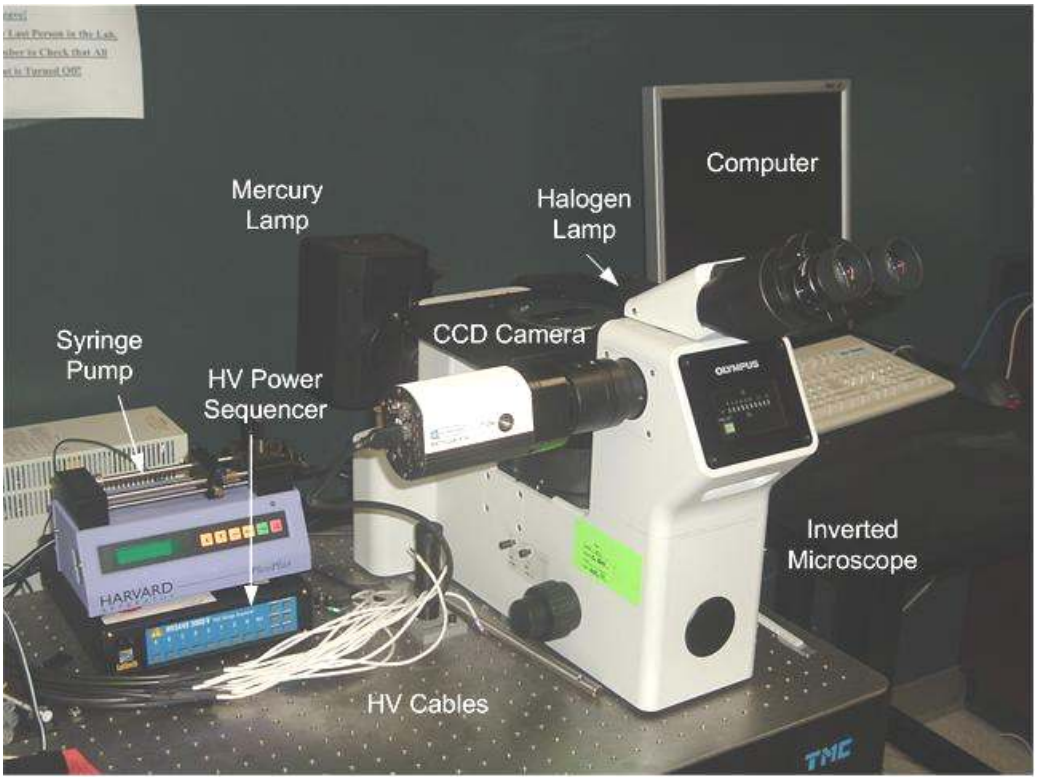

Figure 3.2 Fluorescence microscopy system used for flow visualization and dimension measurements. The system consists of an Olympus GX-71 inverted microscope, CCCD camera, halogen and mercury lamps and computer. Also included are the HV power sequencer and syringe pump.

3.4 Flow control

Both pressure driven and EOF flow control were applied for pumping fluids. Pressure driven flow was achieved with a high precision syringe pump. For EOF control a high voltage sequencer was used to apply the electric field.

3.4.1 Syringe Pump

The syringe pump (11 Plus Syringe Pump, Harvard Apparatus) allows for simultaneous pumping from two syringe but not independent control over each syringe (the progression of the two plungers is tied together through the travelling pusher). The syringe pump can operate in both infuse and withdraw modes as well as constant flow rate or volume dispense. The accuracy of the flow rate is 0.5% and the minimum flow rate is 1.4nL/hr.

The connection between the syringe and the chip is achieved using specialized connectors, valves, unions and other necessary parts (Upchurch Scientific and McMaster-Carr). Further discussion on attaching the connectors to the PDMS chip is provided in Chapter 5. Connecting the tubing to the chip poses some problems as bubbles are often trapped in the connector and eventually make their way into the microchannel. The syringe and tubing was first primed by eliminating all bubbles and then the droplet merging method was used to attach the connectors [Edmond *et al.* (2006)]. Some issues arose with using the syringe pump and tubing. Stiff tubing was found to exert a strong force on the connectors which was then transferred to the flexible PDMS. This tension affected the flow field by distorting the microchannel shape. Consequently, the preference was to use flexible tubing since it did not exert as much tension on the connectors and it was easier to handle.

3.4.2 HV Power supply

The Labsmith HV power sequencer (HVS338-3000) supplies a maximum 3000V differential to eight independently controlled channels. Both negative and positive voltages can be applied through three operational settings: -3000 to 0, -1500 to 1500, and 0 to 3000. Each channel can be manually controlled in real time or programmed to perform a series of executed steps using the Sequence software program. There are four possible channel configurations: applied voltage, applied current, constant power and monitor. The user interface displays the voltage and current simultaneously for all channels; data can be recorded and stored in a text file. In the monitor mode the channel acts as a voltmeter, however, during experiments a small amount of current is still drawn by the channel which leads to slightly false readings of the voltage (i.e. the impedance

of the channel is too low to be an effective voltmeter). For stable operation a minimum of 50uA must be drawn from a channel or the voltage will fluctuate irregularly. HVC cables connected to the back of the HV power sequencer safely route the voltage to the microfluidic chip.

3.5 Chip Holder

During experiments the test chips were placed in a custom made acrylic holder as shown in Figure 3.3. The holder fits a microscope slide sized microfluidic chip. A window was machined in the bottom of the holder for optical access for access with the inverted microscope. An electrical circuit board was attached to the holder to connect directly to the HV power sequencer cables. Up to 8 channels can be connected to the electrical circuit via terminal block (green). The channels are distributed around the chip to the individual terminal blocks (black). Platinum electrodes insulated with Teflon shrink wrap tubing connect the chip to the electrical circuit. A set of switches (red) allow for individual ON/OFF control of the channels. Each of the input channels from the HV power sequencer can be distributed anywhere around the perimeter of the chip. The platinum electrodes can easily be adjusted and repositioned to match the reservoir locations of the test chip. The flexibility of the chip holder proved to be invaluable during experiments since it efficiently organized the HV cables and could be easily fitted to a variety of chip designs.

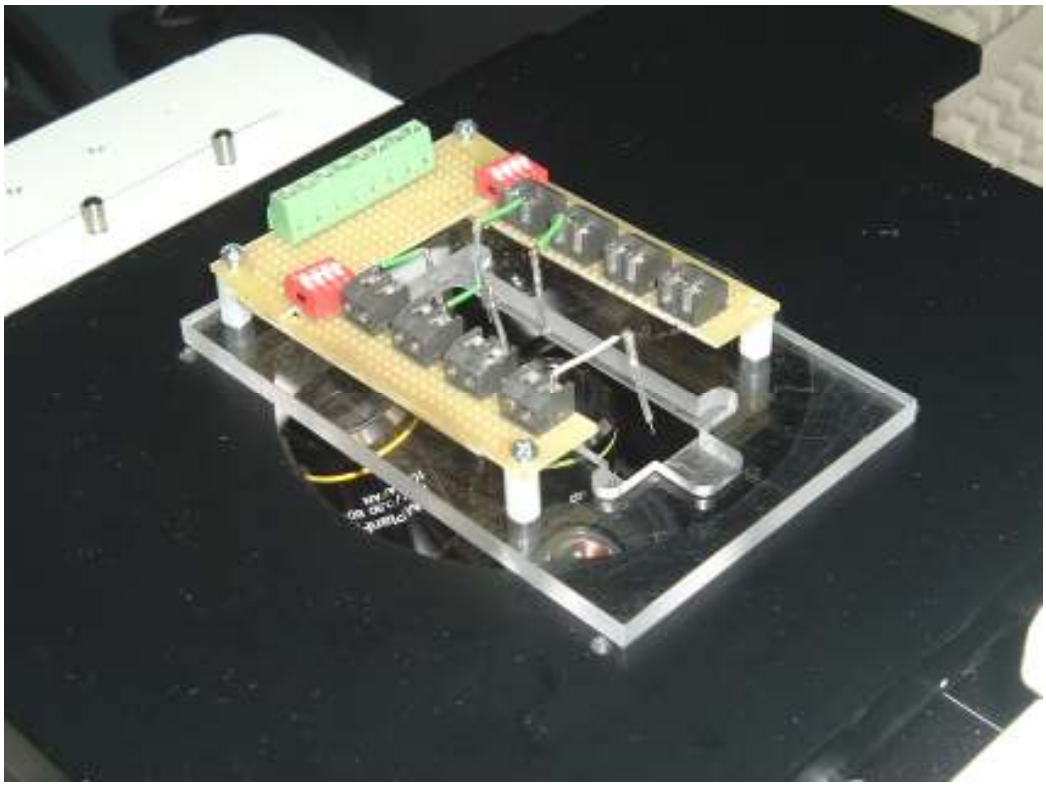

Figure 3.3 Custom chip mount fabricated for the PDMS microfluidic chips and distributing the applied electric potentials from the HV power sequencer.

3.6 Flow Field Visualization

In this work, both scalar and particle velocimetry was used to visualize the flow field. For scalar based visualization fluorescein dye was added to the working fluid and visualized using the microscopy setup outlined in section 3.3. For fluorescein measurements the halogen lamp was used with a typical exposure time of 50ms.

Particle streak velocimetry (PSV) and particle tracking velocimetry (PTV) techniques were applied to obtain qualitative and quantitative measurements of the flow field. PSV involves recording the particle displacement over a period of time (4-5s exposure time) in a single image to obtain a trace of the particles motion. This technique was applied to visualize streamlines of the flow field, examples of pressure driven flow in a T-junction and 90° corner are shown in Figure 3.3. In PTV individual particles are tracked in successive images and the displacement of the particle between images is used to determine the velocity. Here a combination of PSV and PTV was used to determine the velocity of the particles as shown in Figure 3.5. Longer exposure times (100-200ms) were used to generate a streak of the moving particle as this helped isolate moving particles from stationary particles. Velocities were determined using two techniques: (a) measure the streak length and divide by the exposure time, and (b) measure the displacement of the particle and dived by the delay between images. The estimated error for determining the displacement length from the images is ±5%. An additional error comes from the Brownian motion of the particles that creates a random noise in the measurements. The relative error due to Brownian motion can be expressed as [Santiago *et al.* (1998)]:

$$\varepsilon_{BM} = \frac{1}{u}\sqrt{\frac{2D}{\Delta t}} \qquad \textbf{(3.1)}$$

where u is the velocity, D the diffusion coefficient and Δt the time between images. Using an example velocity of 100 μm/s, measurement time of 100ms and D=4.32x10^{-13} m^2/s (0.5μm fluorescent beads) the estimated error is 3%. However, this error can be reduced by averaging the velocity over several particle images ($\varepsilon_T = \varepsilon_{BM} / \sqrt{N}$ where N is the number of images).
In Chapter 7, fluorescent beads are used to determine the average flow rate in EO pumps by measuring the centerline velocity in a pressure driven channel. For all experiments, between 3 to 5 images were taken to determine the centerline velocity, thus the estimated error due to Brownian diffusion is less than 1%.

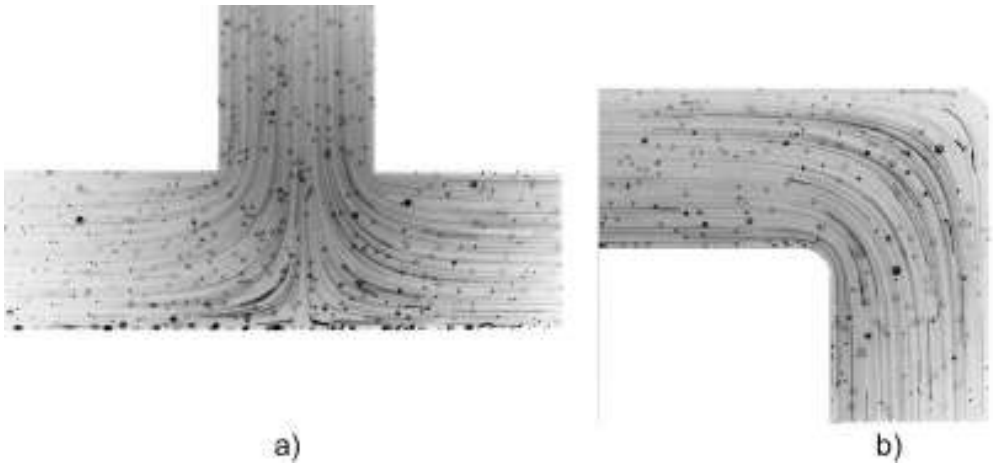

Figure 3.4 Streamline patterns obtained from particle streak velocimetry technique for pressure driven flow in (a) T-junction and (b) corner.

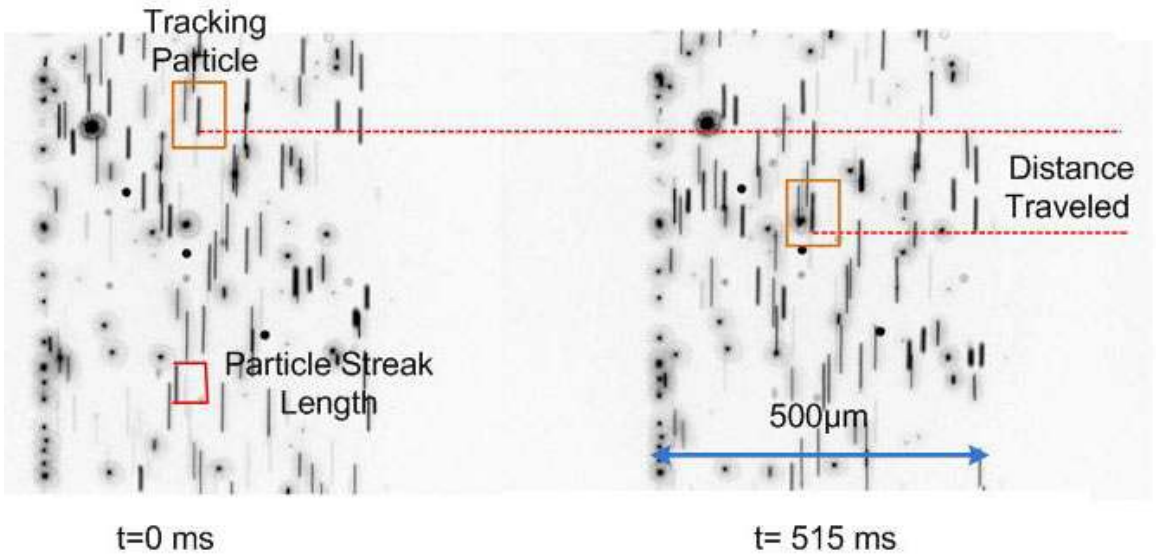

Figure 3.5 Particle tracking combined with particle streak velocimetry to measure flow velocity in a 500µ(w)X100µm(h) channel under pressure driven flow. Exposure time is 200ms and time between images is 515ms. The long exposure time makes it easier to determine which particles are moving. The streak length for the highlighted particle is 32.5µm and the distance traveled for the tracking particle is 84.32µm which corresponds to velocities of 162.5µm/s and 163.5µm/s.

3.7 Channel Dimension Measurement

Knowing the channel dimensions is very important for characterizing the fabrication process and modelling microfluidic devices. Two methods were employed to measure the dimensions of the microchannels from the silicon master. The first method uses a microscope to measure the height and width of the features. Height measurements were performed by focusing on the top and bottom of the features using the GX-71 microscope. A grading on the vertical axis knob was used

to determine the difference between the top and bottom of the structure. It is estimated that this method is accurate to within ±5μm for the 20X objective and ±2μm for the 50X objective. Thus for small structures the 50X objective was used while for the larger structures the 20X. The width of the channel was determined using images from the CCD camera. A calibration for each objective was first performed using a reference micrometer scale.

The dimensions of the channels were also measured using a contact profilometer (SJ-400, Mitutoyo). In this method, a diamond stylus is moved across the surface of the master for a specified distance and the height change of the stylus is recorded. The radius of diamond stylus is 5μm and the horizontal resolution is controlled by the scan speed and length. There is a horizontal broadening factor which is a function of stylus radius and step height of the microchannel. The resolution of the profilometer is 12.5 nm on the 800μm range setting and 1.25nm on the 80μm range setting. Channel dimensions are analyzed and evaluated using SURFPAK-SJ, the SJ-400's roughness analysis software program. Vertical and horizontal cursors define the distance between the top and bottom of the channel profile and the width as shown in Figure 3.6.

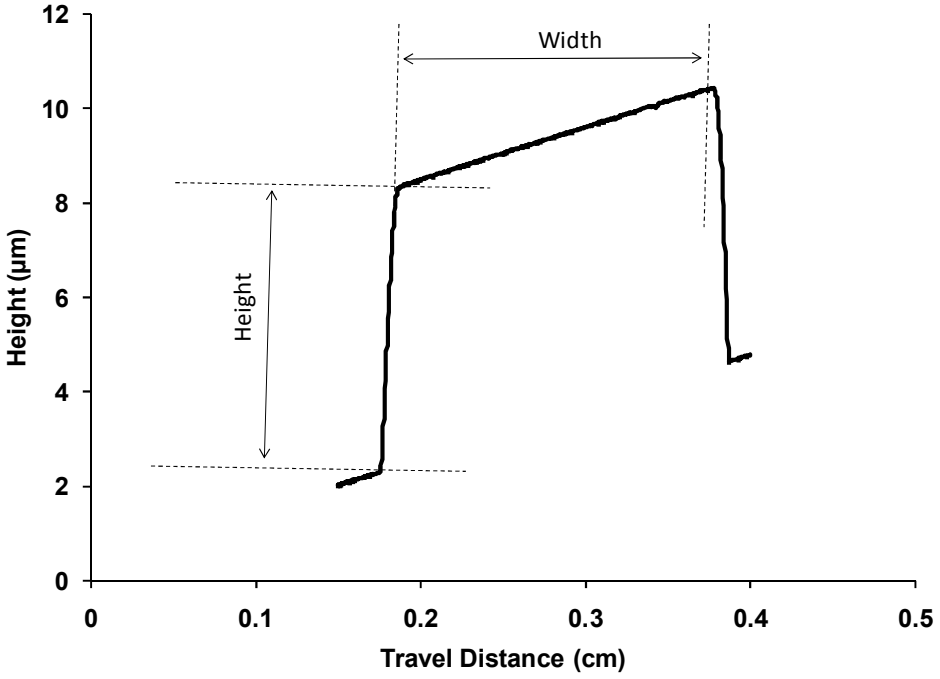

Figure 3.6 Example microchannel profile obtained from the profilometer (SJ-400, Mitutoyo). The angular profile is due to tilting of the silicon wafer caused by bowing.

3.8 Safety

During the course of this thesis safety was of the utmost concern. Special precautions were taken when operating the high voltage power supply and handling hazardous materials during the fabrication process.

3.8.1 High Voltage Safety

Electroosmotic flow requires the application of extremely high voltages which have the potential to cause serious physical harm. When operating the high voltage power supply a short circuit through the body will shock the operator. Fortunately, the high voltage power supply has a built in current limit of 6.5mA which is below the physical limit of paralysis of the muscles at 10mA and more serious heart damage at 50mA. Several precautions were taken to reduce the risk of electrical shock while operating the high voltage power supply. The power supplies were grounded directly to the building infrastructure through the power receptacle. All exposed wires were covered with electrical tape or insulation and a lower current limit (e.g. 1mA) was set when smaller currents were used. In addition, all connectors and reservoirs were fabricated from polypropylene, an excellent electrical insulator, to prevent a short circuit occurring between electrodes.

3.8.2 Chemical Safety

Several chemicals mentioned throughout this thesis are especially hazardous to the operator: SU-8 developer (PGMEA), acetone, PDMS curing agent, trimethylchlorosilane (TCMS), poly(2-hydroxyethyl methacrylate) (HEMA), acrylamide, N-methylenebisacrylamide, 2-dimethoxy-2-phenylacetophenone and 3-(trimethoxysilyl)propyl methacrylate (Bind-Silane). Extreme care should be taken when using TCMS since it is hazardous to the respiratory system and acrylamide since it is a severe neurotoxin easily absorbed through the skin. All the appropriate safety procedures were followed as described in the respective material safety data sheets. This included the use of fume hoods, goggles, gloves, respiratory devices, face shields and lab coats as was specified. In addition, handling equipment (e.g. bottles, tubing, jars) was checked for compatibility with any chemicals that were used.

Chapter 4

Designing Microfluidic Chips using Numerical Methods

The use of numerical simulations during the design process can provide valuable insight into the performance of a microfluidic device. The cost of performing these analyses depends on the level of detail that is desired. Complete 2D /3D models provide valuable insight into the phenomenon of interest but are very costly and are therefore limited to studying isolated regions in a microfluidic network or specific processes. As an alternative, a simplified 1D circuit equivalent model can be developed to capture the behaviour of the entire network. Determining which numerical analysis to use depends on the quality of the information that needs to be extracted. If only the general physical behaviour is required then a 1D model is appropriate. On the other hand, if specific details and local values of velocity, pressure, electric field, concentration, ect. are required then a full 2D/3D model needs to be performed. In this work, both 1-D circuit models for the electric and flow fields and full 2D/3D numerical simulations for electric, velocity, concentration and temperature fields were employed. The details of these methods are presented in this chapter.

4.1 1D Equivalent Circuit Modeling

Simplified 1D or compact models are typically used for analysis and design of global microfluidic networks as these require little computational effort but are still accurate enough to capture the basic phenomena. Such models have been applied to solve the flow field in microfluidic networks under electroosmotic flow [Fletcher *et al.* (2001)] and combined pressure driven/electroosmotic flow [Qiao *et al.* (2002); Chien *et al.* (2002)]. A more complete model developed by Xuan and Li (2004) accounts for variations in the electric and flow field through the EDL as well as the streaming potential generated during pressure driven flow. In their model, Chatterjee and Aluru (2005) included capacitive elements for the EDL in the electric domain and flexible membranes in the fluidic domain. Chatterjee and Aluru (2005) also included chemical reaction and electrokinetic separation modelling to successfully analyze several integrated microfluidic systems published in literature.

These compact models are not without limitations and must be applied with some restrictions. The major assumption is that the electric and flow fields are fully developed in most of the network. This assumption is justified if the channel length is much greater than the channel width (L>>w). The exceptions are regions of 2D or 3D non-uniformity such as intersections and step changes in zeta potential where the complex flow field is not captured by the 1D model. The best way to illustrate the application of the compact model is through an example. For this purpose, consider the double cross network operating under combined EOF/pressure driven flow as shown in Figure 4.1. The network can be decomposed into two equivalent circuits that describe the electric field and the flow field (see Figure 4.1b) which are discussed in more detail below.

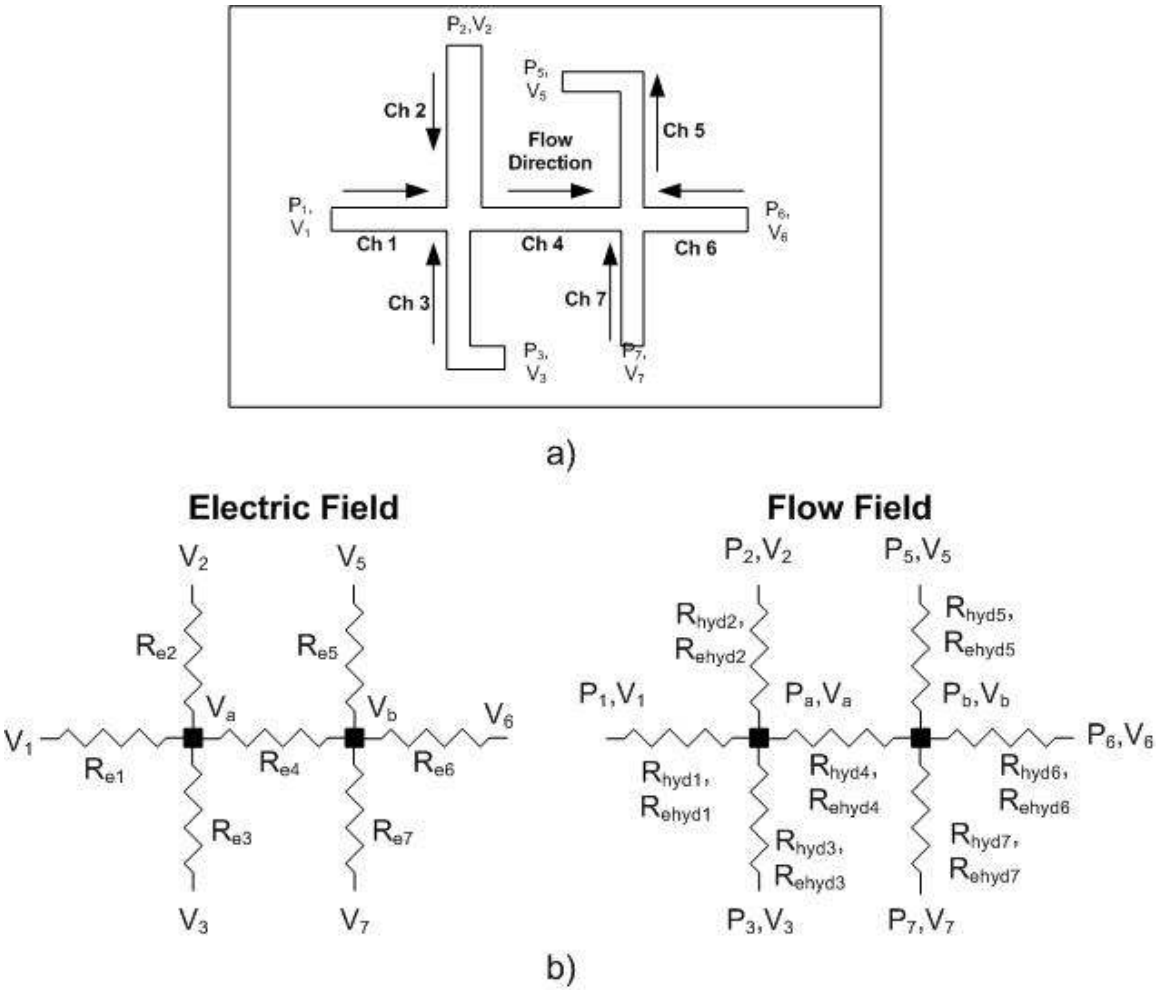

Figure 4.1 Schematic of (a) example double cross microfluidic network under combined EOF/pressure driven flow and (b) the equivalent electric and flow field resistance networks.

Electric Field

When the solution is electrically neutral, the electric potential field is described by:

$$\nabla\left(\lambda_b \nabla\phi\right) = 0 \qquad \textbf{(4.1)}$$

where ϕ is the electric potential and λ_b is the electrical conductivity. For a 1D channel the simplified model results in a linear drop of potential along the channel similar in principal to an electrical resistor. Thus the potential drop is related to the electrical resistance of the channel according to Ohm's law:

$$-\Delta V = IR_e \qquad \textbf{(4.2)}$$

where I is the electric current passing through the channel and R_e is the electrical resistance. For simplicity the variation in bulk conductivity caused by the EDL and the surface conductance of the channel are neglected, although, these terms are important in very small microchannels [Xuan and Li (2004)]. The electrical resistance of the channel is given by the following equation:

$$R_e = \frac{L}{\lambda_b A_c} \qquad \textbf{(4.3)}$$

Where L is the channel length and A_c is the average the cross-sectional area. In a rectangular channel $A_c = h \cdot w$, where h is the channel height and w is the channel width. For a network the solution of the electric field is completed by applying Kirchoff's Law at each node:

$$\sum I = 0 \qquad \textbf{(4.4)}$$

This creates a system of equations that defines the electric network which will yield the electric potential at each node and the current in each channel. Figure 4.1b shows the equivalent electric field circuit for the example network.

Flow Field

The flow field in fully developed microchannels is governed by the continuity equation and the Stokes' equation as discussed in Chapter 2:

$$\vec{\nabla} \cdot \vec{u} = 0 \qquad \textbf{(4.5)}$$

$$0 = -\vec{\nabla} p + \mu \vec{\nabla}^2 \vec{u} + \rho_e \vec{E} \qquad \textbf{(4.6)}$$

Due to the linearity of the two solutions the contributions of pressure driven flow and electroosmotic flow can be evaluated separately. Recall that the electroosmotic flow produces a uniform velocity profile and is represented by the Helmholtz-Smoluchowski slip condition at the wall. The flow rate for EOF is then defined as:

$$Q_{eof} = -\frac{\Delta V}{R_{ehyd}} \tag{4.7}$$

$$R_{ehyd} = \frac{L}{\mu_{eof} A_c} \tag{4.8}$$

where R_{ehyd} is the electro-hydraulic resistance of the channel and μ_{eof} is the electroosmotic mobility. The equation above assumes that the EDL is thin compared to the channel dimensions. When the EDL thickness becomes comparable to the channel dimensions the slip velocity model becomes inaccurate. Models developed by Xuan and Li (2004) and Chatterjee and Aluru (2005) account for the velocity variation in the EDL but use the simplifying Debye-Huckel approximation for the potential distribution in the EDL. This limits the solution to symmetric electrolytes where the zeta potential ζ<25mV. In order to obtain a more detailed solution of the EDL, a numerical solution of the Poisson-Boltzmann equation is required; however, this contradicts the motivation for using a compact model. As an alternative, the concept of an electric double layer displacement thickness, δ^*, developed by Dutta and Beskok (2001) may be applied. The velocity distribution in the EDL results in a mass flow rate defect if the bulk flow is assumed to extend up to the wall. This is analogous to the boundary layer displacement thickness for air flow in ducts. Applying this concept to a rectangular channel the electro-hydraulic resistance becomes:

$$R_{ehyd} = \frac{L}{\mu_{eof}(h-2\delta^*)(w-2\delta^*)} \tag{4.9}$$

Dutta and Beskok (2001) provided solutions for the EDL displacement thickness for symmetric electrolytes without the Debye-Huckel approximation. In their calculations the displacement thickness can be calculated through the ionic energy parameter, α, and the Debye length, λ_d :

$$\alpha = \frac{ez\zeta}{k_b T} \qquad \frac{1}{\lambda_d} = \sqrt{\frac{2n_o z^2 e^2}{\varepsilon_r \varepsilon_o k_b T}} \tag{4.11}$$

where e is the electron charge, z the ion valance, ζ the zeta potential, k_b the Boltzmann constant, T the absolute temperature, ε_r the relative dielectric constant, ε_o the vacuum permittivity and n_o the bulk concentration. Table 4.1 summarizes some values for the ratio of the EDL displacement thickness to the Debye length as a function of the ionic energy parameter.

Table 4.1 Variation of the EDL displacement thickness for a symmetric electrolyte as a function of ionic energy parameter. The equivalent zeta potential is included as a reference.

α	**ζ(mV)**	δ^*/λ_d
1	25.44	0.98635
3	76.33	0.89156
5	127.22	0.7567
7	178.11	0.62702

Note that the EDL displacement thickness is always less than the Debye length and decreases for higher ionic energy parameters (corresponding to increasing zeta potential). In most channels, the zeta potential is less than 100mV, therefore, referring to Table 4.1 the EDL displacement thickness is approximately 80-95% of the Debye length. Thus a conservative estimate for the EDL displacement thickness is to use the Debye length. For complex solutions involving multiple species the Debye length may be too difficult to calculate. As a very rough approximation the solution may be equated to a symmetric electrolyte (KCl) through the bulk conductivity:

$$n_{oEQV} = \frac{\lambda_{fluid}}{2mze} \qquad \textbf{(4.12)}$$

Where n_{oEQV} is the equivalent KCL concentration of the fluid, m is the ionic mobility and λ_{fluid} is the bulk conductivity of the fluid measured with a conductivity meter. From the equivalent concentration the Debye length can be estimated form Eqn.4.9. If the zeta potential is also known (for electroosmotic mobility measurements refer to Chapter 6) the EDL displacement thickness can be estimated from Table 4.1. For example, 1XTBE has a conductivity of λ_{fluid} =0.123S/m and measured zeta potential of ζ=-50mV in PDMS/PDMS channels. Using Eqn.4.12 and Eqn.4.9 the equivalent concentration is 7.95mM and the estimated EDL thickness is 3.43nm. This analysis is crude but can be used to determine whether complete modelling of the EDL is required. In this particular example, the variation of the flow field in the EDL does not need to be considered as

long as the channel dimensions are much larger that the EDL (h>200nm). Throughout this study the EDL is considered to be small compared to the channel height and the slip boundary condition is applied (i.e. electro-hydraulic resistance is defined by Eqn.4.8).

A hydraulic resistance can also be defined for pressure driven flow:

$$Q_p = -\frac{\Delta P}{R_{hyd}} \tag{4.13}$$

where ΔP is the pressure difference along the channel and the hydraulic resistance, R_{hyd}, for a rectangular channel is calculated from [Beebe *et al.* (2002)]:

$$R_{hyd} = \frac{12\mu L}{wh^3}\left[1 - \frac{h}{w}\left(\frac{192}{\pi^5}\sum_{n=1,3,5}^{\infty}\frac{1}{n^5}\tanh\left(\frac{n\pi w}{2h}\right)\right)\right]^{-1} \tag{4.14}$$

This equation applies to low-aspect ratio channels ($w \approx h$) and converges quickly. For high aspect ratio channels ($w >> h$) the equation reduces to:

$$R_{hyd} = \frac{12\mu L}{wh^3} \tag{4.15}$$

The cubed term is always the smaller of the two dimensions (w,h). The overall flow rate in the channel is the sum of the electroosmotic and pressure driven flows:

$$Q = Q_{eof} + Q_p \tag{4.16}$$

$$Q = \frac{\Delta P}{R_{hyd}} + \frac{\Delta V}{R_{ehyd}} \tag{4.17}$$

Applying the conservation of mass to each junction:

$$\sum Q = 0 \tag{4.18}$$

This creates an additional system of equations for the flow field. Combined with the system of equations developed for the electric field the entire electroosmotic/pressure flow field can be calculated. Note that the resistance elements described above can be applied to any irregular shaped channel as the flow rate is always related to the pressure/voltage drop and a form factor:

$$Q_p = -\Delta P f_1, Q_{eof} = -\Delta V f_2, I = -\Delta V f_3 \tag{4.19}$$

The form factor can be obtained analytically for some simple geometries or through numerical simulation for more complex shapes.

The circuits are solved using the nodal analysis technique typically employed in electrical engineering. For example, the system of equation for the network described in Figure 4.1 is:

Electric Field	Flow Field
$V_1 - V_a - I_1 R_{e1} = 0$	$Q_1 - (P_1 - P_a)/R_{hyd1} - (V_1 - V_a)/R_{ehyd1} = 0$
$V_2 - V_a - I_2 R_{e2} = 0$	$Q_2 - (P_2 - P_a)/R_{hyd2} - (V_2 - V_a)/R_{ehyd2} = 0$
$V_3 - V_a - I_3 R_{e3} = 0$	$Q_3 - (P_3 - P_a)/R_{hyd3} - (V_3 - V_a)/R_{ehyd3} = 0$
$V_a - V_b - I_4 R_{e4} = 0$	$Q_4 - (P_a - P_b)/R_{hyd4} - (V_a - V_b)/R_{ehyd4} = 0$
$V_5 - V_b - I_5 R_{e5} = 0$	$Q_5 - (P_5 - P_b)/R_{hyd5} - (V_5 - V_b)/R_{ehyd5} = 0$ **(4.20)**
$V_6 - V_b - I_5 R_{e5} = 0$	$Q_6 - (P_6 - P_b)/R_{hyd6} - (V_6 - V_b)/R_{ehyd6} = 0$
$V_7 - V_b - I_5 R_{e5} = 0$	$Q_7 - (P_7 - P_b)/R_{hyd7} - (V_7 - V_b)/R_{ehyd7} = 0$
$I_1 + I_2 + I_3 - I_4 = 0$	$Q_1 + Q_2 + Q_3 = Q_4$
$I_4 + I_5 + I_6 + I_7 = 0$	$Q_4 + Q_5 + Q_6 + Q_7 = 0$

In general, two types of problems were solved. In the first type of problem the applied voltages are known and the flow rates are to be calculated. For this case a one-way coupling exists and the two systems of equations can be solved seperately. First, the electric field equations are solved and then the voltages are inputted into the flow field to calculate the flow rates. The opposite occurs in the second case, the flow rates are known and the required voltages are to be calculated. For this case the entire system of equations must be solved simultaneously. To solve the system of equations a small program was written in MATLAB to perform the matrix inversion. The circuit network model is used throughout this thesis for the design of the Y-channel electroosmotic mobility measurement chip (Chapter 6), electroosmotic pumps (Chapter 7) and cell culture network (Chapter 8).

4.2 COMSOL MULTIPHYSICS Numerical Models

Erickson (2005) provides a detailed review of the numerical techniques that have been developed for microfluidics along with their application in the design of integrated devices. The major difficulty with performing microfluidic numerical simulations is the large number of different phenomena that must be considered simultaneously in order to truly capture the physical behaviour of a device. Several groups have developed specialized software programs for this

purpose; however, these programs are often designed to solve specific problems and lack the flexibility for rapid numerical prototyping. In addition, developing a code from scratch is an arduous task that requires extensive knowledge of CFD and software programming. In this work numerical modelling was used strictly as a tool to assist in the design of the EO pump and cell culture chip. Thus a commercial modeling program, COMSOL Multiphysics 3.3, was chosen to perform the numerical simulations.

COMSOL Multiphysics (formerly FEMLAB) is a finite element modeling program with an easy to use interface that couples together multiple physical phenomenon through a series of modules. Each module contains the fundamental governing equations and boundary conditions for a specific type of physical phenomenon. Of particular relevance are the modules for solving microfluidic and MEMS problems which couple together fluid flow, electrokinetic flow, mass transport, chemical reactions, electro-magnetism, electrostatics, micro-structure interactions and heat transfer.

Both 2D and 3D models were developed to solve a variety of problems. The development of a model typically consists of three steps. The first step is the pre-processing where the geometry of the computational domain is defined, the mesh is generated, governing equations are specified (through the modules) and boundary conditions are defined. This step requires a good understanding of the physical phenomenon in order to develop an accurate model. For this work the geometry of the microfluidic network is drawn using in-program CAD design tools.
The ease with which the geometry can be dawn and meshed is one of the primary advantages of using a commercial software program. COMSOL uses a triangular (2D) or tetrahedral (3D) unstructured grid mesh to automatically mesh the domain. The mesh can be globally controlled by adjusting free mesh parameter and locally controlled by refining the mesh in areas of high importance such as intersections or regions containing strong gradients. Note that there exists a limit to the mesh density where the computer will run out of available memory. In all the models that were developed the largest mesh that could be solved was used. As mentioned previously, the governing equations and boundary condition are defined through the modules which are discussed in more detail below.

Once the geometry and various parameters are defined the next step is to solve the governing equations. COMSOL MULTIPHYSICS comes with a collection of state of the art solvers for solving both stationary and transient problems. In this work both the linear and non-linear solvers

were used depending on the application. Choosing the appropriate solver requires some knowledge of the mathematics behind numerical modelling. In general, direct solvers were used for 2D models (UMFPACK, SPOOLES, PARADISO) and iterative solvers (GRMES) for larger 3D models where the amount of memory becomes an issue. For problems with coupled governing equations the system was solved simultaneously using a non-linear solver. If the governing equations were not coupled then each module was solved individually in the appropriate sequence to obtain the solution.

The third step is the post-processing where the data is extracted from the model. COMSOL MUTLIPHYSICS provides a variety of visualization tools for analyzing any model quantity or parameter. Plots of the flow field, electric field, temperature field, concentration field, ect. were made for analysis. In addition, flow rates and electric currents were calculated by integrating the velocity and current density along the desired boundary. Before the results were trusted the model was validated by comparing the results to an analytical solution if it was available or to the equivalent 1D circuit model.

The governing equations, boundary conditions, and subdomain setting for the phenomenon considered are provided in the following subsections.

4.2.1 Potential Field

The Conductive Media DC module was used to solve the potential field in the microfluidic network for electroosmotic flow. The governing equation for this model is the potential equation:

$$\vec{\nabla} \cdot \left(\lambda_b \vec{\nabla} \phi\right) = 0 \qquad \textbf{(4.21)}$$

where λ_b is the electrical conductivity and ϕ is the electric potential. Coupling can exist between the potential equation and the temperature field (joule heating) or concentration field (fluid dependent properties) through the bulk conductivity. For electroosmotic flow the electric field values are imported into the flow field calculations through the slip wall boundary conditions.

The boundary condition for the walls of the microchannel is electrical insulation. At the inlets and outlets the applied potential was specified. For any interior boundaries a continuity condition was applied. Within the subdomain the electrical conductivity was entered.

4.2.2 Velocity Field

The Microfluidics Stokes Flow module was used for simulating fluid flow in the microchannel network. The Stokes flow module consists of the Navier-Stokes equations with the inertia terms removed. This assumption is valid since the flow is creeping with a very low Reynold's number (Re<1).

For the Stokes' approximation with a time dependent velocity field the following equations are used:

$$\vec{\nabla} \cdot \vec{u} = 0 \qquad \textbf{(4.22)}$$

$$\rho \frac{d\vec{u}}{dt} = -\vec{\nabla} p + \mu \vec{\nabla}^2 \vec{u} + \vec{F} \qquad \textbf{(4.23)}$$

The major advantage of the Stokes approximation is that a linear solver can be used which reduces the computation time. Pressure boundary condition are applied at the inlet and outlets of the chip (P=0). The electroosmotic boundary condition was applied at the wall for electroosmotic flow with either the mobility of the fluid or the zeta potential selected to define the slip velocity. The electric potential from the Conductive Media DC module was used to determine the electric field in the slip conditions. For interior boundaries a neutral boundary condition was used. The subdomain properties constants associated with the flow field are the density (ρ = 1000 kg/m³), viscosity (μ = 0.001 Ns/m^2), the volume force is set to zero since the electroosmotic wall condition is used instead ($\vec{F}$ = 0). For 2D simulations the shallow depth approximation was applied to simulate the hydraulic resistance effect of the channel depth.

4.2.3 Concentration Field

The concentration field was solved using the Convection/Diffusion Module. The governing equation is

$$\frac{\partial c_i}{\partial t} + \vec{u} \cdot \left(\vec{\nabla} c_i\right) = D_i \vec{\nabla}^2 c_i - \mu_{ep_i} \vec{\nabla}\left(c_i \vec{E}\right) + R_i \qquad \textbf{(4.24)}$$

where c_i is the molar concentration of species i, $\vec{u}$ is the velocity vector, D_i is the diffusion coefficient of the i^{th} species, μ_{ep_i} is the electrophoretic mobility of the i^{th} species, $\vec{E}$ is the applied electric field and R_i is the volumetric rate of generation of the i^{th} species by chemical reaction. The reaction rate for all of the simulations was zero and diffusion coefficients were taken from

literature for the species. The concentration field is coupled to the flow field through the velocity. The boundary conditions are the known sample concentration at the inlets of the channels. For the outflow channels the convective flux boundary condition was applied. An insulation boundary condition was applied to all the channel walls and a continuity boundary condition for all internal boundaries.

4.2.4 Temperature Field

The temperature field at steady state is described by the conservation of energy:

$$\rho c_p \left[\vec{u} \cdot \vec{\nabla} T\right] = \vec{\nabla} \cdot \left(k \vec{\nabla} T\right) + \sigma(T) \vec{E} \cdot \vec{E} \qquad \textbf{(4.25)}$$

where ρ is the density, c_p the specific heat, k the thermal conductivity of the material and $\vec{u}$ is the velocity vector. The electric field required as part of the internal heat generation for joule heating is obtained from the Conductive Media DC Module. Most material properties remain relatively constant over the temperature range considered in microfluidics (25-80ºC) except for the electrical conductivity of the fluid which is temperature dependent. The electrical conductivity of a solution versus temperature is expressed as: $\sigma(T) = \left[1 + \alpha(T - T_o)\right]\sigma_o$, where α is the thermal coefficient and σ_o is the conductivity at the reference temperature T_o. Thermal properties of solutions were approximated as pure water and properties of the other materials (e.g. PDMS, glass) were taken from literature [Erickson *et al.* (2003); Lide *et al.* (1998), Incropera *et al.* (2002)]. The temperature dependent conductivity couples the solution both ways to the Conductive DC module. For convection boundaries the heat flux boundary condition is used and the heat transfer coefficient is specified from the empirical correlations (Nusselt and Rayleigh numbers) and the ambient temperature [Incropera *et al.* (2002)]. On symmetrical boundaries an insulation boundary condition was applied. For internal boundaries a continuity condition was applied.

4.2.5 Coupling of Equations

The governing equations can be coupled together through either the material properties or boundary conditions. To couple two governing equations together in COMSOL the dependent variable from one module is imported into the other. For example, in the case of mass transport the velocity vector from the Stoke's flow module is used to describe the u, v, w velocity components of the convection term in the concentration equation. If one-way coupling exists the modules can be solved seperately in sequence. For two-way coupling the modules can be solved together using a non-linear solver.

4.4 Application of Numerical Models

The two numerical modelling methods described above were used extensively in the design of microfluidic devices. In the subsections two applications are described to demonstrate the performance of these models. The first involves the application of the circuit equivalency model to design hydraulic resistance elements for suppressing undesired pressure driven flow in a microchannel operating under EOF. The second example applies both techniques to study EOF in an expansion channel composed of multiple wall materials. In addition to these models, other models are presented in Chapters 6, 7, and 8.

4.4.1 Undesired Pressure Effects in Microfluidic Systems

In some cases, the magnitude of the undesired pressure driven flow is on the same order as EOF. For instance, consider a standard sized channel 5cm long channel with 100x100μm cross-section. Between the reservoirs there is a 3mm liquid level difference and a meniscus radius difference of 5mm and 3mm (ideal spherical case). Using the equations presented in Section 2.2.2.3 and the 1D equivalency model the pressures generated for water (γ=72.8mN/m) are $\Delta P_H = 29.4\text{Pa}$ and $\Delta P_L = 19.4\text{Pa}$ which corresponds to flow rates of $Q_H = 0.294\,\mu\text{L/min}$ and $Q_L = 0.194\,\mu\text{L/min}$. For comparison, electroosmotic flow for a fluid with ζ=50mV at an applied voltage of 500V is $Q_{EOF} = 0.210\,\mu\text{L/min}$. In this example, the undesired pressure driven flow overpowers EOF negating any control over fluid flow within the chip. Therefore, it is apparent that eliminating the effects of undesired pressure driven flow is essential before implementing EOF on-chip.

The impact of undesired pressure driven flow can be suppressed by adding hydraulic resistance elements to the microfluidic network [Fletcher *et al.* (2001)]. Recall that the hydraulic resistance of a slit microchannel is approximated by:

$$R_{hyd} = \frac{12\boldsymbol{\mu} L}{wh^3} \qquad \textbf{(4.26)}$$

From Eqn.4.26 it is clear that the resistance is highly dependent on the channel height, reducing the channel height will increase the resistance dramatically ($R_{hyd} \propto 1/h^3$). However, reducing the height will also reduce the overall electroosmotic flow rate ($R_{eof} \propto 1/wh$). To keep the same flow rate for the channel the width must be increased proportionally. Under this premise the hydraulic resistance must be a section of channel that is wide and shallow as shown in Figure 4.2. Referring back to the previous example, consider replacing part of the straight microchannel with a 1cm

long hydraulic resistance element. Computations were performed where the height of the resistance element was changed and the ratio of EOF to undesired pressure driven flow was calculated. Figure 4.2b shows the ratio of flow and the corresponding increase in width of the resistance element. The effects of undesired pressure driven flow is largely suppressed ($Q_{L+H}/Q_{EOF} < 5\%$) when the resistance height is approximately 5μm which corresponds to a width of 2mm.

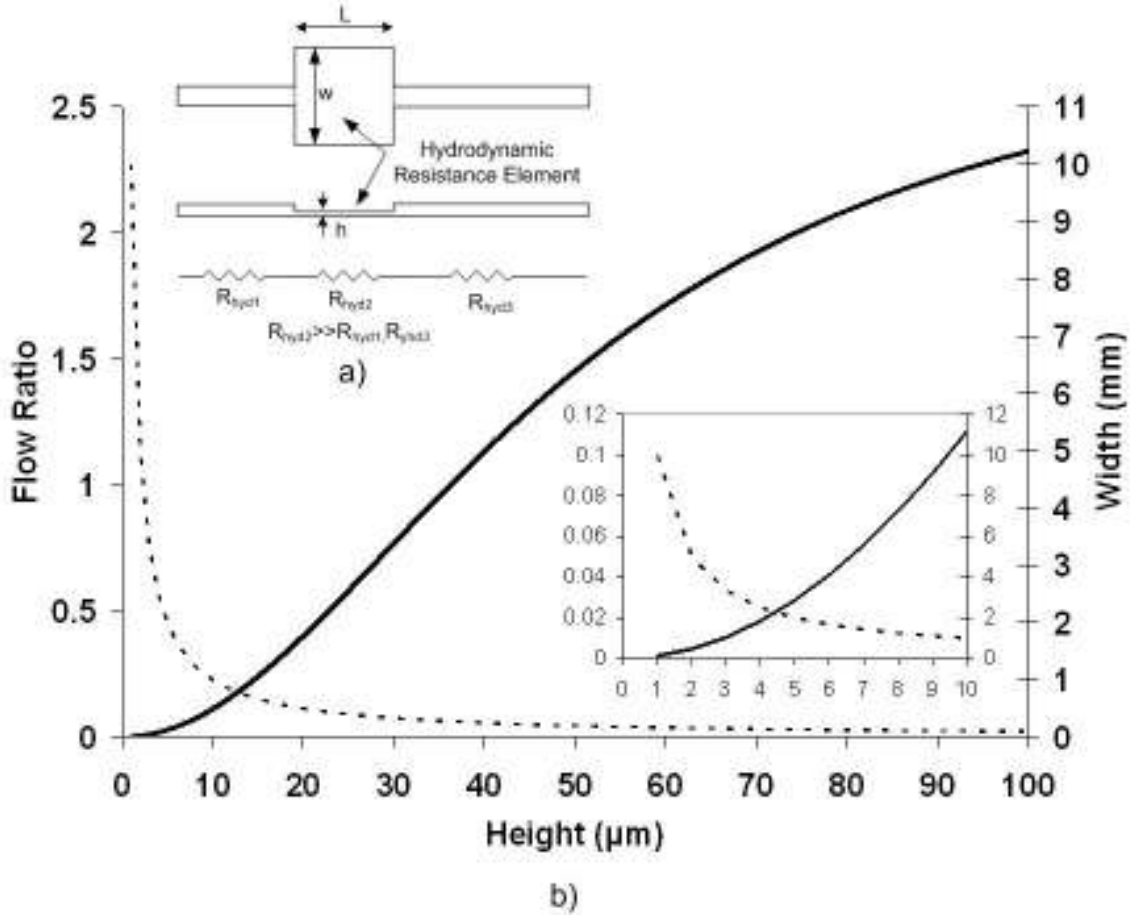

Figure 4.2 (a) Schematic of the hydraulic resistance element incorporated into a straight channel (b) Plot of the ratio of undesired pressure driven flow to EOF flow (solid line) and the corresponding change in hydraulic resistance width (dashed line) for variations in height of the hydraulic resistance. Calculations performed for ΔP=48.8Pa, ΔV=500V, L=5cm, w=100μm, L_{hyd}=1cm.

This analysis shows that microchannels must have an inherently high hydraulic resistance for stable EOF operation. When designing multi-channel networks the effects of external pressure gradients must be taken into account so as to minimize cross flow between channels. As a general rule, channels should be shallow and wide, even when hydraulic resistance elements are included. This fact is incorporated in the design of the EO pumps and the cell culture network as discussed in Chapters 7 and 8.

4.3.2 Expansion Channel with Multiple Wall Materials under EOF

In many microfluidic networks channel size varies throughout the chip. A simple case of changing geometry is an expansion microchannel as shown in Figure 4.3. For a chip made of the same material operating under EOF an equivalent 2D simulation can be performed to determine the flow field without much loss in accuracy. However, a problem arises when the microfluidic chip is made of two different materials, such as PDMS/glass, since the electrokinetic properties of each material may be different. The resulting flow field is actually three dimensional and the velocity profile is no longer uniform.

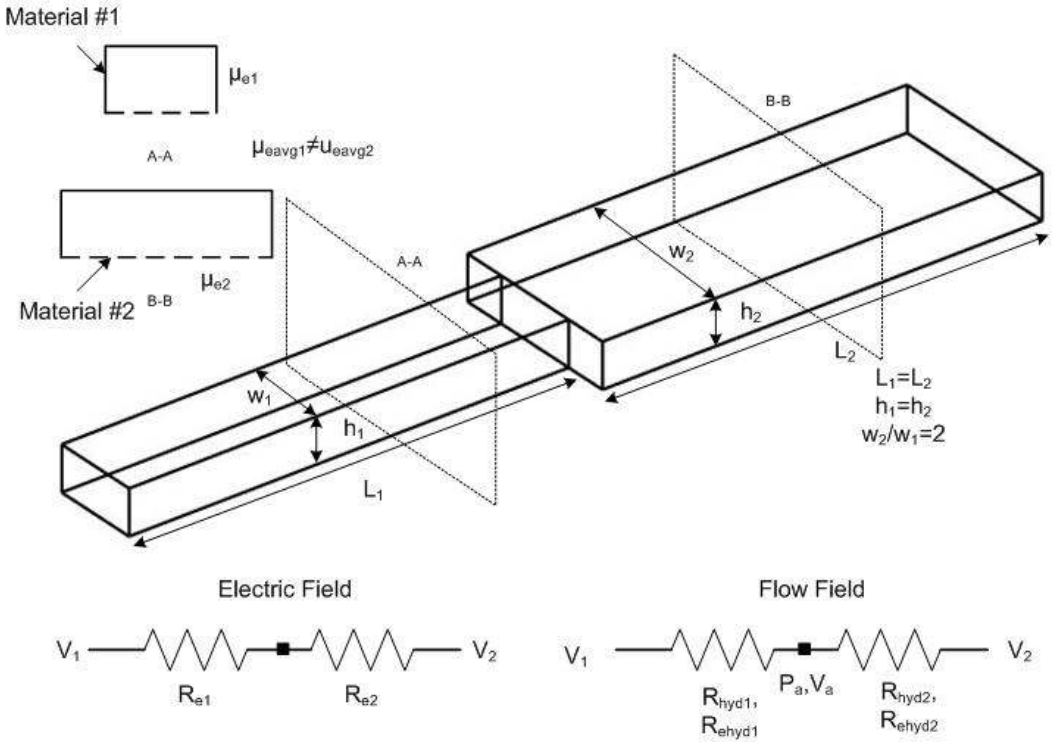

Figure 4.3 Schematic of the expansion channel composed of two different materials. Material 1 composes the top and sides of the channel and Material 2 the bottom. The first material supports a strong EOF, μ_e=7x10^{-8} m^2/(Vs), while the second supports no EOF, μ_e=0 m^2/(Vs)). The equivalent 1D circuit model of the microchannel is included as well.

The average electroosmotic mobility of a composite channel can be approximated by a weighted average of the material properties around the perimeter of the channel [Bianchi *et al.* (2001)]:

$$\mu_{eof_{avg}} = \frac{\sum_{1}^{n} \mu_{eof_i} L_i}{\sum_{1}^{n} L_i} \qquad \textbf{(4.27)}$$

where μ_{eofi} is the electroosmotic mobility over the section of perimeter L_i. For a change in cross sectional area the average electroosmotic mobility between the two sections will be different. This generates an internal pressure gradient that balances out the flow through the channel. Applying the 1D circuit equivalent network the pressure at the intersection and overall flow rate are defined as:

$$P_a = \frac{V_1 R_{e1}}{R_{ehyd1}} \left[\frac{R_{hyd1} R_{hyd2}}{R_{hyd1} + R_{hyd2}} \right] \left[\frac{R_{e1}}{R_{e2}} - \frac{R_{ehyd1}}{R_{ehyd2}} \right] \tag{428}$$

$$Q = \frac{V_1}{R_{ehyd1}(R_{e1} + R_{e2})} \left[R_{e1} - R_{e2} \left[\frac{R_{e1}}{R_{e2}} - \frac{R_{ehyd1}}{R_{ehyd2}} \right] \left[\frac{R_{ehyd1} + R_{ehyd2}}{R_{ehyd2}} \right] \right] \tag{4.29}$$

The geometry considered in this study is a simple microchannel with a 1:2 expansion ratio. The first section of the channel has dimensions of 100µm width, 50µm height and 500µm length. The second section of the channel is 200µm width, 50µm height and 500µm length (see Figure 4.3). The microchannel is composed of two materials: the first material forms the top and sides of the channel (μ_e=7.0x10^{-8} m^2/(Vs)) and the second material forms the bottom of the channel (μ_e=7x10^{-8} m^2/(Vs)). The inlet voltage was set to 10 V and the outlet was grounded ($\vec{E} = 10\text{kV/m}$). Electrical insulation conditions are applied along the channel walls. For the flow field the electroosmotic slip boundary condition is applied along the walls and the electric field is imported from the Conductive Media DC solution. A one-way coupling exists so the electric field is solved first and then the flow field using the iterative GRMES solver.

The equivalent electric mobility for the two sections is calculated as: μ_{e1}=4.67x10^{-8} m^2/(Vs)) and μ_{e2}=4.20x10^{-8} m^2/(Vs)). Because the difference in electro-hydraulic resistance does not match the difference in electrical resistance an induced pressure gradient is generated at the intersection (see Eqn.4.28). The velocity field obtained from the numerical simulation is presented in Figure 4.4. Notice that the velocity is not uniform but varies in the cross section due to the heterogeneous wall condition. The velocity along the bottom wall is zero which matches the imposed no-slip condition. The velocity along the other walls is equivalent to the electroosmotic mobility slip velocity. It is also evident that the flow field varies locally in the immediate vicinity of the intersection but becomes fully developed within one channel width.

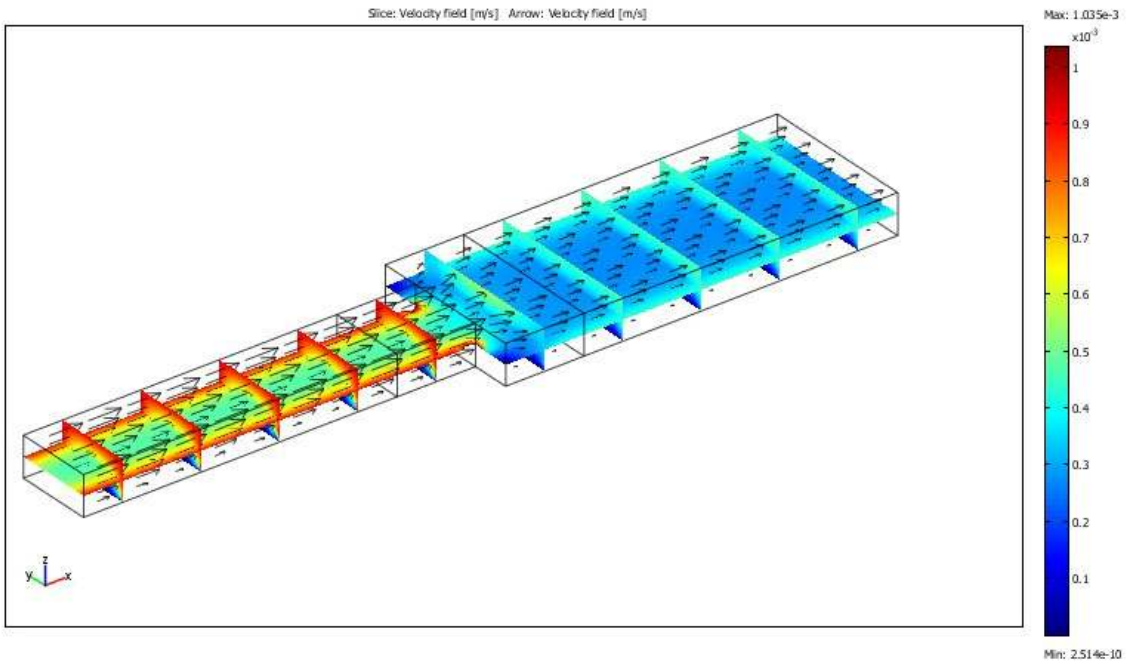

Figure 4.4 A slice plot of the velocity field (m/s) in the expansion channel calculated using COMSOL Multiphysics. An arrow plot is overlaid to show the flow direction.

The flow rate obtained from the numerical simulation is 0.1689μL/min which compares well with the circuit analysis result of 0.1804μL/min. The difference between the two results is only 5.9%. The circuit model also predicts a junction pressure of 0.05Pa (0.058Pa for the simulation), which seems small, however the contribution of pressure driven flow to the total flow rate is still significant (Q_p/Q_t=6.9%). The reason for the discrepancy between the two models is two fold. First, the assumptions made in the compact model are not valid near the expansion where the flow is complex and not fully developed. Secondly, the weighted linear calculation of the average electroosmotic mobility is only a rough approximation. Bianchi *et al.* (2001) showed that this calculation is reasonably accurate to within ~5%. Considering these factors the circuit equivalency model is actually in good agreement with the full 3D simulation. Therefore, it is clear from this analysis that the compact model can effectively predict the flow field in a complex microchannel network with a reasonable degree of accuracy.

4.4 Summary

In this chapter the numerical modelling techniques used to design microfluidic chips were presented. This included a 1D circuit equivalent modelling system as well as full 2D/3D modelling using the commercial software program COMSOL MULTIPHYSICS. These modelling techniques were applied to study two example microfluidic problems. The first study involved the design of hydraulic resistance elements using the circuit equivalent model to suppress undesired pressure driven flow in microchannels. The second problem studied EOF flow in an expansion microchannel made of two different materials. The circuit model was compared with the full simulation results with good agreement. The compact circuit model is an effective design tool and is used extensively in this thesis.

Chapter 5

Techniques Developed for Fabricating Microfluidic Chips: Soft Lithography, Multi Level Fabrication and Fluid Connectors.

This chapter outlines the procedures developed as part of this thesis for fabricating poly(dimethylisiloxane) (PDMS) microfluidic chips using soft lithography techniques. Although soft lithography has been established for over a decade, many published procedures do not include the small details or trade secrets that must be known to successfully fabricate a complete microfluidic chip. At the beginning of this thesis, protocols for fabricating microfluidic chips within the lab were not yet established and without a reliable method of fabricating microfluidic chips it was impossible to progress any further in the design process. Therefore, a lot of time and effort was spent on setting up equipment, optimizing the fabrication process and developing protocols. This chapter presents details of the fabrication process including master fabrication, replica molding and the attachment of chip to world interfaces such as reservoirs and fluid connectors. These microfabrication techniques are used extensively in the following chapters to fabricate EO pump and cell culture chips. Problems that were encountered and their solutions are presented as guidance to future researchers.

5.1 Soft Lithography Overview

Soft lithography is a broad term covering a number of fabrication techniques that use flexible elastomer stamps to construct microstructures [Xia *et al.* (1998); McDonald *et al.* (2000); Duffy *et al.* (1998)]. As it applies to microfluidics, soft lithography is mainly composed of two separate techniques: rapid prototyping and replica molding. Rapid prototyping refers to the fabrication of a master with positive relief microchannel structures using contact photolithography and inexpensive high resolution transparency masks. In replica molding, an elastomer material such as poly(dimethylsiloxane) (PDMS) is cast against the master producing a replica containing the imprinted microchannel network. The mold is then sealed to another substrate, enclosing the channels and completing the chip. PDMS is an excellent material for microfluidics applications as it is optically transparent down to 280nm, chemically inert, biologically compatible, deforms reversibly, produces high accuracy molded features (~1μm) and can be modified easily by several well established surface treatments. In addition, fabricating with PDMS does not require extensive clean room conditions or high temperatures to assemble the chip as is the case for

traditional glass or silicon devices. The time from design to fabrication is often less than one week and costs approximately $10-50/chip compared to several months and thousands of dollars for a custom glass device. Therefore, soft lithography is ideally suited as an inexpensive method for the rapid prototyping of new microfluidic designs.

A typical production process for fabricating a PDMS chip is outlined in Figure 5.1. The first step in the process is to fabricate a reliable master for molding. A negative photoresist, SU-8, is deposited onto a silicon wafer to achieve a desired film thickness by spin coating. The thickness of the film will define the channel height which depends on the type of SU-8 and spin process (e.g. speed, time). Afterwards the wafer is baked on a level hot plate to drive out the solvent and harden the film. Multiple spin coats can be performed to build up the SU-8 layer to almost any desired thickness (>1mm has been achieved). Next, the wafer is placed in a UV exposure system and covered with a photomask containing a negative of the microfluidic design. The assembly is illuminated with UV light (~365nm) where exposed regions undergo photo-polymerization and begin to cross-link. This is followed by a post exposure bake (PEB) which completes the cross-linking process. The process of spin coating, soft bake, exposure and post exposure bake can be repeated for multiple layers to produce multi-level structures. Once the photolithography step is complete the features are developed in a large bath of SU-8 developer. During this process unexposed SU-8 dissolves away leaving behind the positive relief structures. The wafer is then treated with a silanizing agent to assist in the release of the PDMS mold.

Once the master is complete a replica is made by pouring liquid PDMS over the master and then curing it in an oven. Cured PDMS is flexible and easily peels from the master. The mold is trimmed to the desired shape and fluidic access holes are punched. To complete the microfluidic chip the mold is sealed to another substrate (e.g. glass, PDMS, quartz, silicon) either reversibly or irreversibly. For a reversible bond the PDMS will simply seal itself against any smooth surface. This method produces a watertight seal but will only withstand nominal pressures in the microchannels. To obtain an irreversible bond, the PDMS and substrate are exposed to oxygen plasma which alters the surface chemistry. The two substrates are then placed in contact and a permanent bond is formed. Additionally, the plasma treatment transforms the PDMS from hydrophobic to hydrophilic allowing for easy filling of the microchannels. Afterwards reservoir extensions or microfluidic connectors can be attached to the chip, if desired. A more detailed discussion for each step of the fabrication process is given in the following sections.

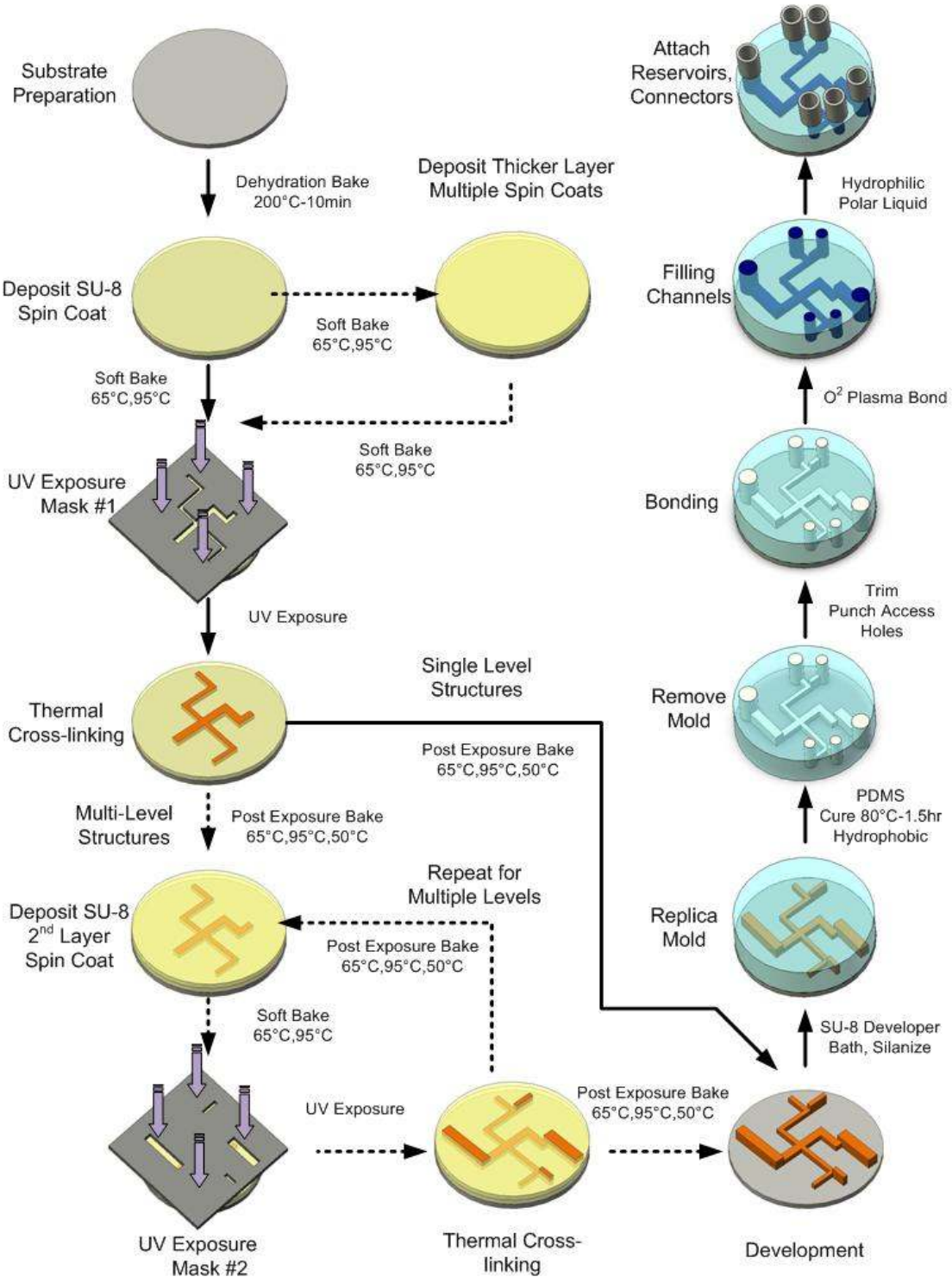

Figure 5.1 Illustration of the procedure for fabricating a microfluidic chip using soft lithography.

5.2 Master Fabrication

The fabrication of a high quality master is certainly the most important part of the soft lithography process. Features defined in the master are directly transferred to the PDMS mold including any defects or imperfections. As well, the durability of the master will determine the amount of molds that can be made. Consequently, a series of experiments were performed to optimize the fabrication of the masters. The procedure included determining the spin coating curves and optimum UV exposure doses for SU-8 2005, 2015, 2025 and 2075. Other aspects were also investigated, including depositing of SU-8 as well as the soft bake and post exposure bake. The photomask used for the exposure tests contains 10 groups of 3 lines with varying thickness (50, 100, 200μm) as shown in Figure 5.2. For each type of SU-8, three wafers were coated at different speeds (1000, 2000, 3000 rpm). A range of exposure doses was applied across the photomask (e.g. 100-600 mJ/cm^2 by 50mJ/cm^2) for each set of lines. After development, the structures were analyzed to determine the thickness of the film and the optimum exposure dose.

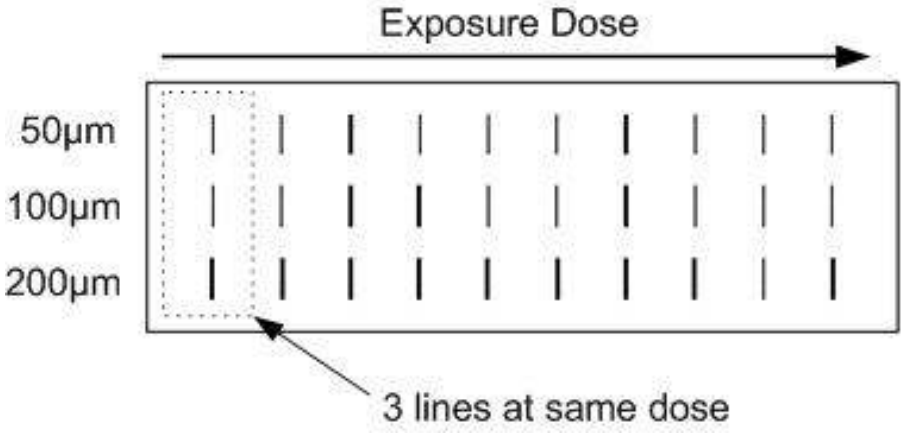

Figure 5.2 Photomask used for calibrating the SU-8 photolithography process.

Height measurements of the SU-8 structures were performed by focusing on the top and bottom of the features through the GX-71 microscope (refer to Chapter 3). A total of five measurements were made at random locations on the wafer not including the edge bead area. The width of the channel was determined using images from the CCD camera. Determining the optimum exposure dose was largely a subjective process. Criteria for a high quality structure included (i) minimal surface pitting (ii) low thermal stress (i.e. cracks, lift-off) (iii) thin edges indicating vertical side walls and (iv) accurate widths. Each structure that remained on the substrate was investigated and the best exposure dose was selected (see Figure 5.3). Data from this calibration is included throughout the following discussion.

Figure 5.3 Example of calibrations results for 100µm channels with SU-8 2005 (7.5µm). Exposure doses of (a) 200 mJ/cm^2 (b) 300 mJ/cm^2 (c) 400 mJ/cm^2 (d) 500 mJ/cm^2 (e) 600 mJ/cm^2 . (a)-(c) show considerable lift off (white features) and poor edge definition, (d) and (e) are nearly optimal but (e) has slightly better characteristics and was considered the optimum exposure dose.

5.2.1 Mask Design

After the numerical and analytical modeling has been finished for a new design the next step is to obtain a mask print. A negative of the microchannel network is drawn using a computer aided design program (AutoCAD). It is good practice to add reference points or an outline of the substrate to the mask for alignment during the exposure step. The design is printed on a transparency made of Mylar or polystyrene film using a high resolution printer. The transparency must be of good quality, low quality films have microscopic bubbles or scratches (see Figure 5.4a) that can be transferred to the SU-8 structures.

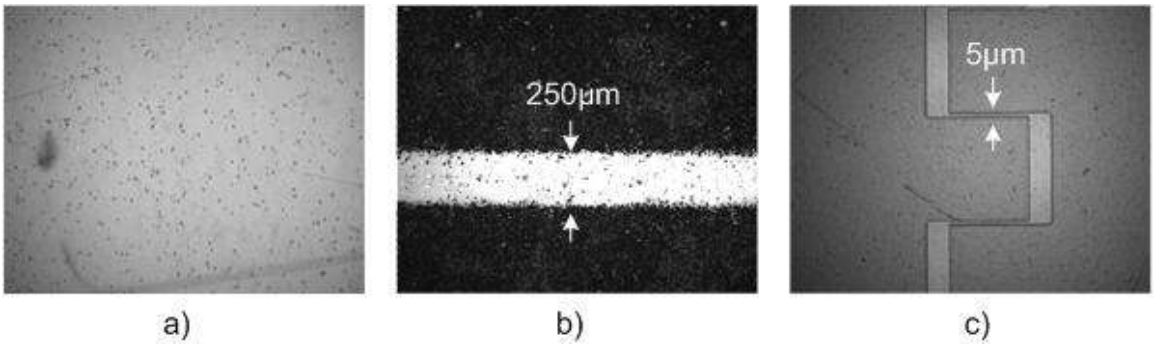

Figure 5.4 Images of the transparency photo masks: (a) bubbles and scratches in the Mylar film (b) photomask printed in house (c) 20000dpi print obtain from CAD/Art Services.

The resolution of the printer determines the smallest microchannel size that can be fabricated. Masks printed in house using a 2400 dpi printer (ScreenWriter4, Xanté) were of poor resolution (microchannels>250μm) and quality as shown in Figure 5.4b. Exposed features were indistinguishable after processing since the ink lacked the opacity to block out all of the UV light. After several attempts to improve the quality of the prints by increasing the ink deposition, the process was eventually abandoned. Instead commercial prints were obtained from two companies with resolutions of 20000dpi (CAD/Art Services, Brandon OR) and 40000dpi (The Photoplot Store, Colorado Springs CO). These companies guarantee a minimum feature size of 12.5μm and 6.0μm respectively; smaller channels down to 5μm were fabricated, though they were not as robust. In addition, approximately 16 microscope slide designs can be printed at once on a single large transparency (8x11"). After receiving the print the designs were protected with a transparent film to prevent scratching and cut out with a paper trimmer. Finished masks were labelled and stored in anti-static bags to prevent damage until they were needed.

5.2.2 Substrate Selection

Microscope slides, rectangular glass wafers and silicon wafers were all used as substrates for the rapid prototyping of masters. Glass slides were first used since they are inexpensive and roughly the same size of the final PDMS chip. However, microscope slides are generally not used for microfabrication because of their low quality. Standard slides have low tolerances and are contaminated with particles, chemical impurities and surface defects. As a consequence, spin coating suffered from numerous defects in the form of pitting and streaking. SU-8 features on glass slides were found to have poor adhesion, often cracking and peeling from the substrate during the development phase. In addition, for thick resists large edge beads would form after spin coating and during soft bake the edge bead would spread into the center of the slide resulting in severe thickness variations across the film. After several months of working with glass slides trying to improve the quality of the masters, only simple designs could be fabricated with low success rates.

As a result, a switch was made to high quality silicon wafers as the preferred substrate for fabricating masters. Silicon wafers have high tolerances (flatness, roughness, thickness), are made in clean room conditions, and are tested thoroughly before shipping (Montco Silicon Technologies, Spring City PA). On one 4" wafer up to three microscope slide sized designs can be fabricated at once, saving valuable time and resources. To accommodate the switchover, tools for handling the silicon wafers were purchased including specialized dipping baskets, tweezers

and transport containers (Entegris, Chaska MN). Glass slides were still used in limited applications for testing new procedures and teaching the fabrication process to others.

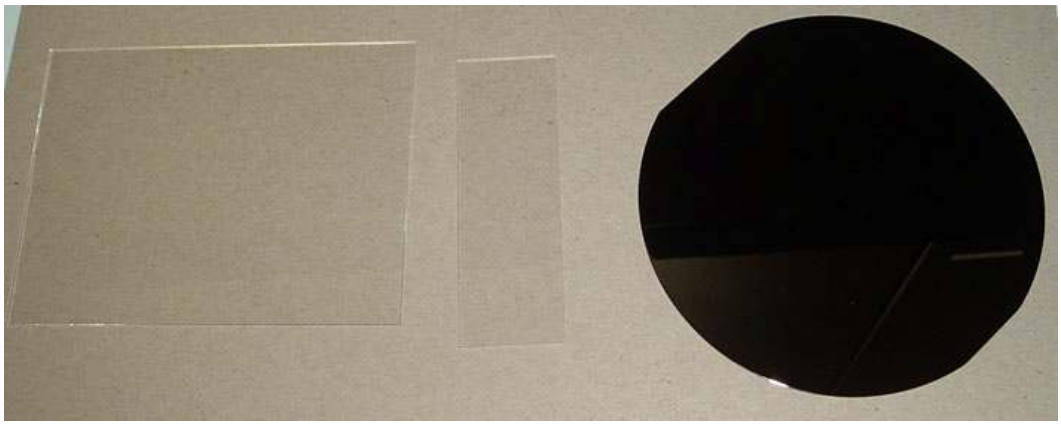

Figure 5.5 Substrates used for master fabrication: 4x3" glass slide, microscope slide, 4" silicon wafer.

5.2.3 Spin Coating

SU-8 is a high contrast negative epoxy photoresist with near UV radiation sensitivity that allows for a broad range of thickness to be obtained in one spin coat (0.5-200μm) [Microchem, Newton MA]. The thickness of the layer depends on the viscosity of the photoresist and the spin speed [Lorenz *et al.* (1998)]. In this work, two versions of SU-8 were purchased and will be referred to as SU-8 XX (old) and SU-8 2XXX (new), where XXX defines the type of SU-8 (e.g. SU-8 25). The new version has several enhanced properties compared to the old version such as improved coating, better adhesion and significantly shorter bake times. Initially, the old version was used but eventually a switch was made to take advantage of the improved characteristics of the new version. Hence the following discussion will focus primarily on the SU-8 2XXX series.

The first step in the spin coating process is to choose the appropriate SU-8 for the desired thickness. Each SU-8 covers a specific range: SU-8 2005: 5-8μm, SU-8 2015: 15-40μm, SU-8 2025: 25-80μm, SU-8 2075: 75-200μm. In the case of overlap, it is better to choose a lower SU-8 since thickness variation across the wafer is less at higher spin speeds [Mata *et al.* (2006)]. If the required SU-8 is not on hand, other versions can be formulated from a thicker stock by diluting it with solvent (cyclopentanone). Each type of SU-8 contains a specified percentage of solids which is provided in the manufacturer's specification sheets. Therefore, a new version can be quickly made by adding enough solvent to match the solid contents of the desired SU-8. This was done to produce small quantities (~20mL) of SU-8 2002 from SU-8 2015. Note that careful measurements are required to obtain repeatable spin coating properties. Measuring out precise

volumes of SU-8 can be difficult because it is highly viscous and sticky. The favoured method of measuring out the SU-8 was to use a mass balance; the volume was then calculated from the density which is also provided by the manufacturer. Afterwards, the appropriate volume of solvent was added. The solution was rigorously shaken for ten minutes and left over night to allow the bubbles generated during mixing to dissolve.

Before spin coating the SU-8 must be decanted from the large shipping bottle into small UV blocking vials (50mL). Decanting the SU-8 makes it easier to handle and prevents the large bottle from being contaminated. It is important to prevent bubble formation by carefully pouring the SU-8 from one bottle into the other. This is especially true for thick resists, such as SU-8 2075, which are very viscous and sticky. After pouring, the bottle threads must be wiped with acetone and a lint free cloth (Kimwipes, Kimberely-Clark) or the SU-8 will dry out and thousand of small particles will fall into the bottle. If this happens, the bottle is contaminated and must be thrown out. The small vial is left to sit for 24hrs so that bubbles formed during pouring will dissolve. For thicker versions this process can take several days. Attempts were made to decrease the debubbling time by heating the vial or by placing it in a vacuum; however, it was determined that too much solvent evaporated during these treatments which changed the viscosity of the SU-8.

Prior to spin coating the substrate must be cleaned and prepared. Cleaning glass slides within the lab using weak acids and bases (1M HCl, 1M NaOH) was found to be insufficient. Consequently, slides were sent to the CIRFE MEMS lab at the University of Waterloo for cleaning using either RCA 2 or Piranha etches to removal all organic materials on the surface. Purchased wafers were of virgin quality and did not require any additional cleaning. SU-8 is hydrophobic and dislikes moist surfaces and humidity [Nordstrëm *et al.* (2004); Microchem], therefore, a dehydration bake is performed to remove all water molecules on the surface: 200C on a hot plate for 10-20min followed by 10 min cool down on a glass Petri dish. The dehydration bake is essential and was found to significantly improve the adhesion of SU-8 structures to the silicon wafer. It is important to let the substrate cool before spin coating so that the viscosity of the SU-8 does not change. Immediately before spin coating the wafer should be cleaned with a blast of nitrogen gas to remove any particles on the surface.

The three hotplates are turned on and allowed to stabilize (95°C, 65°C, 50°C) as shown in Figure 5.8a. The wafer is then placed on the spin chuck and aligned with the centering tool. Misalignment of the wafer can result in uneven coating or worse - the wafer may be thrown off

the chuck. The vacuum pump is turned on and the wafer is held in place against the chuck by suction. The chuck must be handled carefully since any defects or distortions will break the vacuum seal. For glass slides a separate spin chuck was fabricated in house and needs to be used or the slides will be thrown off. A recipe is entered into the spin coater (200 CB, Brewer Science) consisting of the following steps: (a) 0-500 rpm with an acceleration of 100 rpm/s hold for 10-25s (b) 500-**SET** with an acceleration of 300 rpm/s, hold for 30s. In (a) the SU-8 is dispensed and allowed to spread over the wafer while in (b) the **SET** point refers to the final spin speed which will determine the thickness of the layer. The calibration curves obtained through experimentation are presented in Figure 5.6.

Both static and dynamic dispensing was used in this study. For static dispensing the SU-8 is poured carefully from the bottle into the center of the substrate until two-thirds of the wafer is covered. The spin coater is then activated and the thin layer is formed. However, after spin coating a "ring" or "depression" would appear where the initial amount of SU-8 was poured (see Figure 5.7). This depressed region was approximately 20% smaller than the outer region. Surprisingly, the outer region was at the desired thickness. Several variations to the static dispensing method were investigated, such as increasing the spin coating time from 30s to 120s and shortening the time between dispensing and the start of spin coating; however, there was no improvement in the coating. At this moment there is no explanation for this phenomenon, though, it most likely relates to a difference in surface wetability or chemistry that forms while the pool of SU-8 waits to be spin coated.

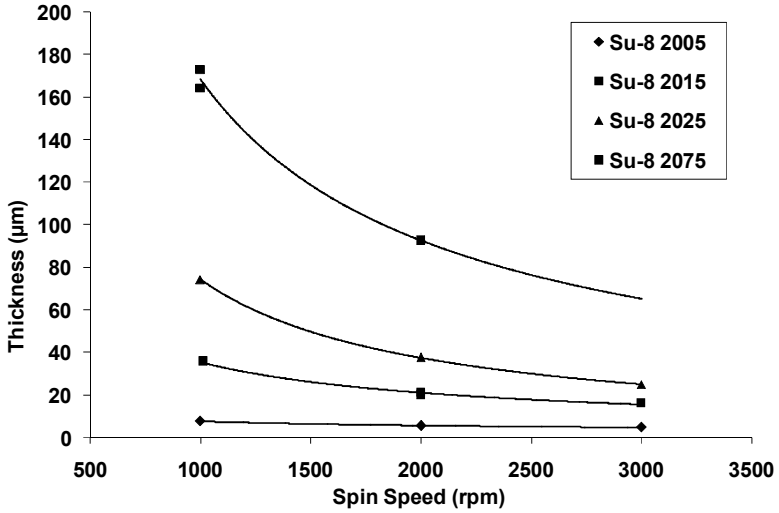

Figure 5.6 Thickness versus spin speed curve for SU-8 obtained during calibration.

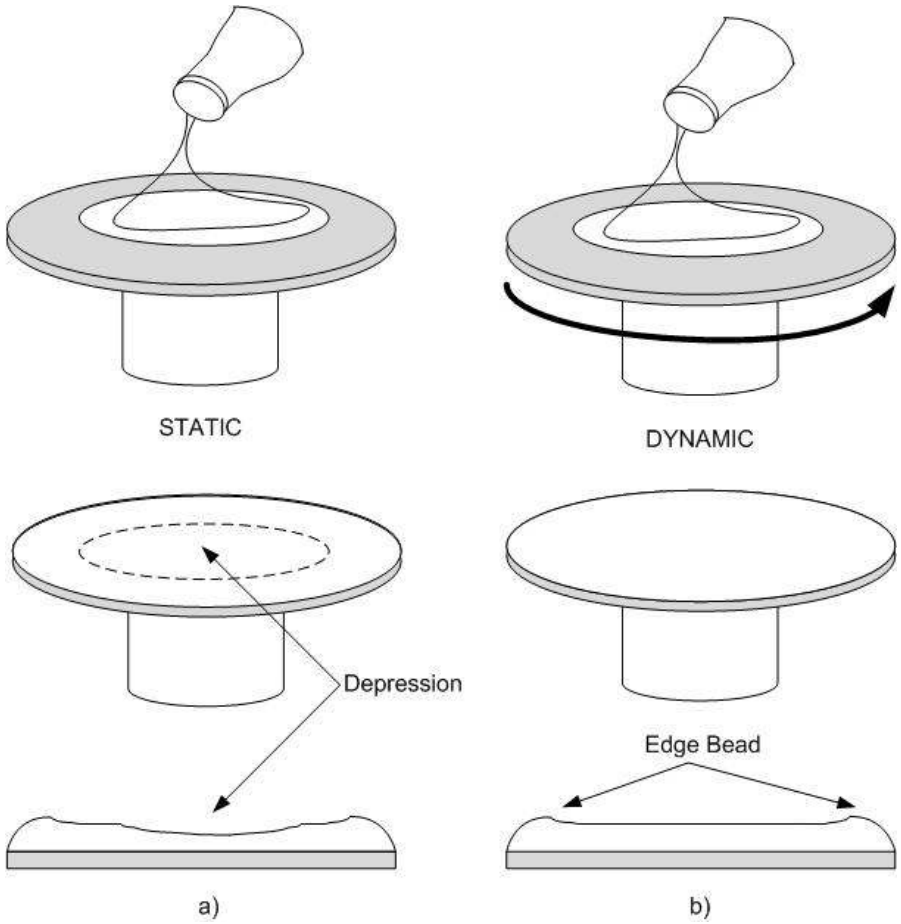

Figure 5.7 Illustration of the spin coating procedure (a) static dispensing (b) dynamic dispensing.

To solve this problem the SU-8 was deposited dynamically. This procedure involves dispensing about 5-7mL of SU-8 while the wafer is spinning at 500 rpm until about 80% of the wafer is covered. As the SU-8 is poured it spreads out at the same time and the crater does not form. Originally the SU-8 was poured from the vial but this requires excellent hand eye coordination in order to keep the flow rate steady and the stream positioned at the center of the wafer. Controlling the height of the bottle over the wafer is critical or the SU-8 will fold upon itself trapping bubbles as it is dispensed. To make the process easier a specialized pneumatic dispensing system was purchase (Ultra 1400, Engineered Fluid Dispensing). The SU-8 is decanted into a UV blocking syringe following the same procedures as before. The bottom of the syringe is capped and a plunger is inserted into the syringe to prevent back flow if the syringe is tilted. The system works the same as a normal syringe but in this case the plunger's progression is controlled by pressurized air through a foot petal trigger (see Figure 5.8).

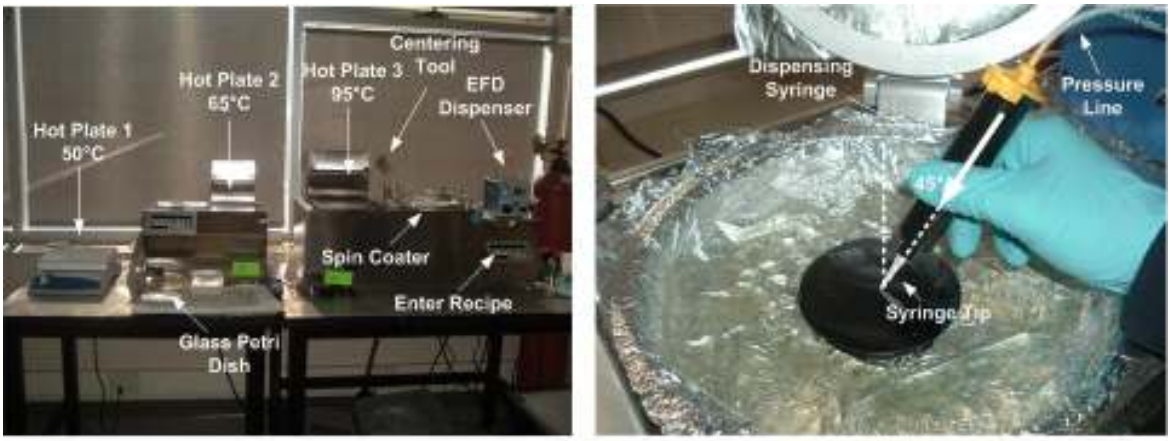

Figure 5.8 Images of (a) the spin coating system and (b) a close up of the dispensing system and technique.

When dispensing, the syringe should be held at a 45° angle and the tip should hover approximately 5mm from the surface of the wafer. The distance varies depending on the type of SU-8, thicker versions should be held closer to the wafer. To assist in the centering of the syringe an additional step was added to the beginning of the spin coating recipe:

1. 0-100 RPM at an acceleration of 300rpm/s for 7s.
2. 0-500 rpm with acceleration of 100 rpm/s hold for 25s
3. 500-**SET** with acceleration of 300 rpm/s and hold for 30s

The time delay allows the user to center the syringe by watching the stream and the rotation of the wafer. A calibration was performed to determine the optimum pressure and tip size for each SU-8 and is summarized in Table 5.1. The addition of the dispensing system greatly increased the quality of spin coating by eliminating costly defects that typically occurred during the dispensing process, more importantly it shortened the learning curve for new operators.

Table 5.1 Suggested components and set up for the pneumatic dispenser (EFD).

SU-8 Type	Dispensing Tip	Pressure (psi)
2005	22g Taper (Blue)	15
2015	18g Taper (Green)	20
2025	18g Taper (Green)	25
2075	14g Taper (White)	30

During the spin coating process a build up of SU-8 occurs at the edge of the wafer. This edge bead is typically 2-3 times higher than the rest of the layer. In the subsequent soft bake, the edge bead will seep into the center of the wafer causing significant thickness variation across the wafer. This effect is more pronounced in thicker versions of SU-8 and can consume two-thirds of the surface. The edge bead can be removed with either the sharp edge of a glass slide or an acetone soaked lint free swab by gently pushing the edge bead off the wafer.

After spin coating the wafer is soft baked at 65°C and 95°C on two hotplates following the times suggested by the supplier. This process hardens the SU-8 layer by driving out the solvent. Convection ovens are not recommended because a skin can form on the resist blocking the evaporating solvent. The wafer must be in good contact with the hotplate so that the evaporation is uniform. For thicker resists it is essential that the hot plate be levelled or the thickness may vary due to SU-8 reflow [Lin *et al.* (2002]. The process summary is:

1. X min @65C (SU-8 dependent, taken from Microchem guidelines)
2. X min @ 95C (SU-8 dependent, taken from Microchem guidelines)
3. 30s to 1min at 65C for a slower cool down. For thicker resists the cool down should be extended to 3-5min.
4. Cool down on glass Petri dish.

The process can be repeated for multiple spin coats, one on top of the other, to achieve any desired thickness.

The majority of defects and imperfections in the master occur during the spin coating process. Surface irregularities in the form of chemical imperfections will cause the SU-8 to recede creating small divots and craters. In a typical spin coat, 5 to 10 of these defects can appear for thinner versions of SU-8. On the other hand, for thicker resists the long soft bake time tends to planarize the layer and smooth out these defects. The most devastating defects are caused by bubble or particles that are trapped during the spin coating process. As the SU-8 is being thrown off the wafer during spin coating these obstacles leave a long streak (1-5cm) in their wake. For designs that occupy a large surface area these types of defects are very difficult to avoid and often ruin the master.

Another source of defects comes from particles, such as dust or lint, that fall on the substrate it is on the hotplate. For a single spin coat these defects do not cause too much trouble since they can be easily avoided by repositioning the mask during the exposure step. However, if another layer is to be spin coated on top, then these particles will create extremely large wakes which are very difficult to avoid. Therefore, it is good practice to protect the wafer with a shield of tin foil while the substrate is being baked. Prior to spin coating the area around the spin coater should be wiped down to remove any dust. Also, leaning over the substrate should be avoided because one of the main sources of lint comes from the operators' clothing. Although clean room conditions are not necessary, a very clean environment does help.

5.2.4 UV exposure and Thermal Cross-linking

UV exposure generates an acid in the SU-8 that cross-links the material making it insoluble to the developer. Choosing the right dose for a given thickness is important in order to fabricate high fidelity structures. If the exposure dose is too low, then the cross-linking will not extend down to the substrate and the features will lift-off. On the other hand, an overdose will create features that are much larger than the mask [Ling *et al.* (2000)]. The calibrated exposure dose that must be entered into the UV exposure system is presented in Figure 5.9. For reference the suggested dose given by Microchem is also presented. The difference in values can be attributed to losses in the UV exposure system between the input and the output dose at the substrate level (Figure 5.10).

The UV system has a radiometer placed immediately outside the collimating lens which records the overall dose and stops the exposure once the set point has been reached. However, the dose at the substrate does not match the dose recorded by the radiometer since there are losses between these two points. Using a radiometer (84410 Photoresist Radiometer, International Light) the dose was recorded at (1) the collimating lens (2) above the vacuum membrane (3) after the vacuum membrane (4) after the mask to determine the actual dose at the substrate level. The measurements showed that there was a 60% transmission of light from (1-2), 80% from (2-3) and 80% from (3-4). Therefore, the total transmittance between the input value and the actual exposure dose is approximately 39% suggesting that the Microchem data should be multiplied by a factor of 2.63. However, the factor obtained from the calibration process is 3.67 because more exposure time is required to remove surface pitting on the structures caused by bubbles in the transparency. Therefore, when stating the exposure dose it is important to account for this system factor. Note for glass substrates the optimum exposure dose in Figure 5.9 needs to be multiplied by 1.5-2X to account for the transparency of the substrate.

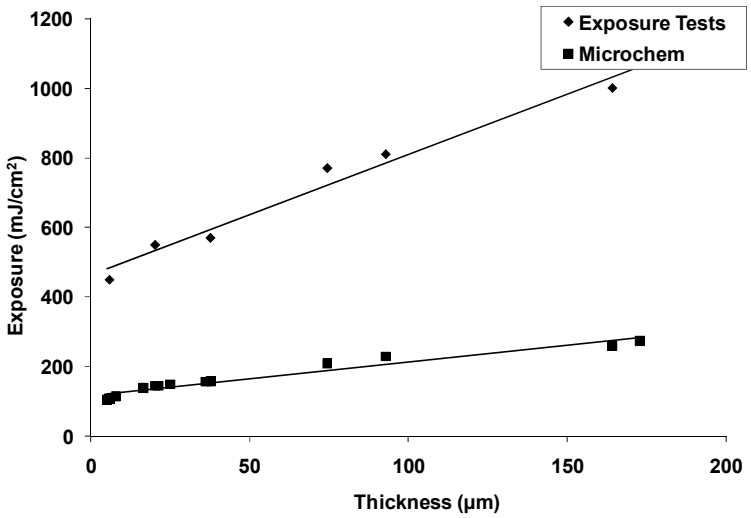

Figure 5.9 Exposure dose for a film thickness that must be entered into the UV exposure system.

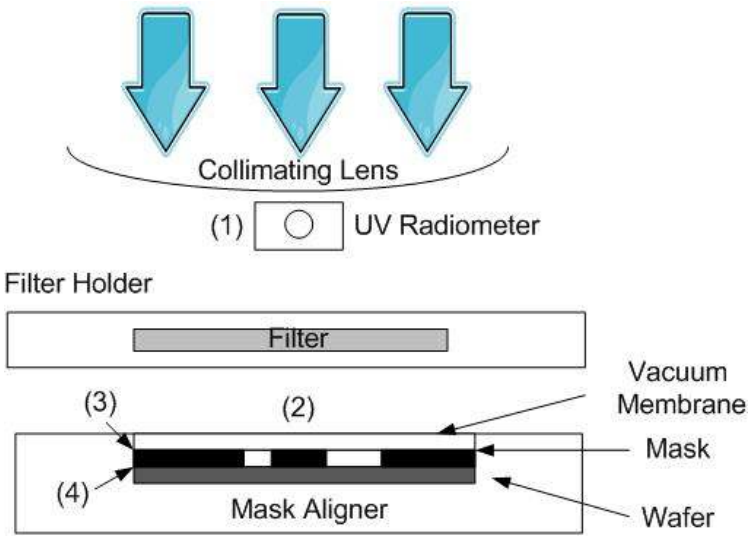

Figure 5.10 Demonstration of loses through the UV assemble measured using a UV radiometer.

Several researchers have reported T-topping of SU-8 of structures if a wideband UV source is used. SU-8 has a high absorption at wavelengths below 350nm causing excessive acid generation in the top of the layer [Microchem]. A solution to this problem is to use an I-line filter that eliminates wavelengths below 350nm. To accomplish this, a high pass filter was purchased with a cut off at 350 nm [Omega Optical, Brattleboro VT]. The transmission spectrum of the filter is shown in Figure 5.11, for comparison, the output spectrum of the UV lamp (1000W Hg(Xe), Newport) is also presented. The filter was mounted in a custom holder to the UV exposure system so that it could be slid into place when needed. As would be expected, the filter adds additional

loses to the UV system. The optimum exposure doses stated before must be multiplied by a factor of 2.72. Tests performed with the filter showed that in fact it worked too well, transferring any defects in the mask such as bubbles, scratches and dust to the SU-8 structures. The only option to solve this problem was to increase the exposure dose dramatically in order to smooth out the defects. Therefore, a decision was made not to use the filter with transparency masks; however, the filter may still be potentially used with high quality emulsion or chrome masks.

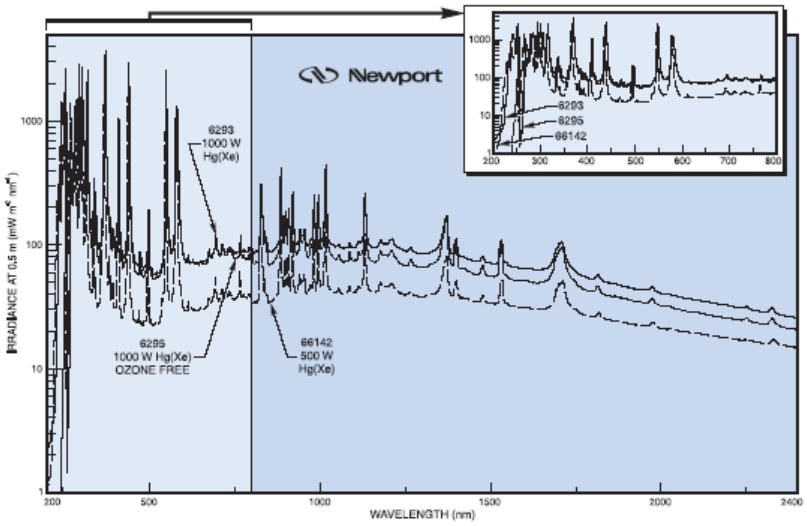

(a)

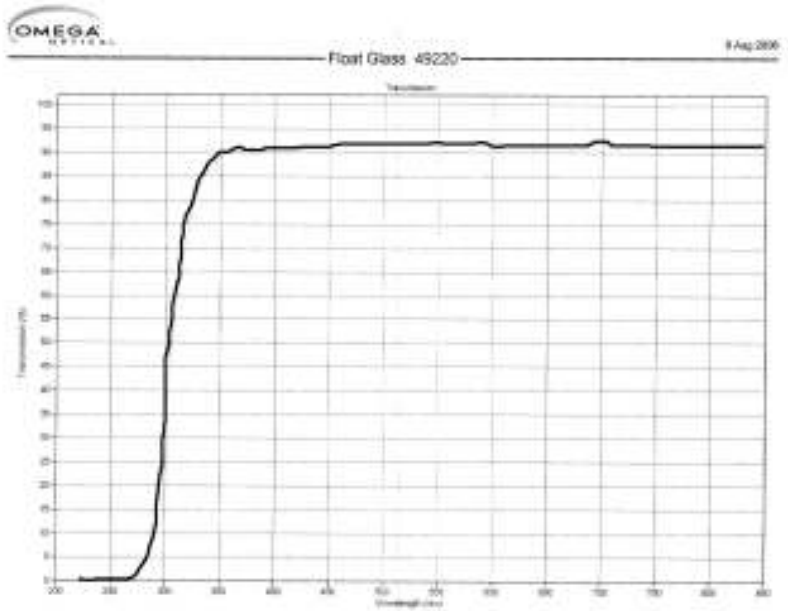

(b)

Figure 5.11 Emission spectrum of (a) UV light source 6295 1000W Hg(Xe) Ozone Free Lamp [Oriel Product Training Manual] (b) transmission spectrum of Float Glass 49220 filter [Omega Optical].

Next, the substrate is put in the mask aligner and the mask is placed over top of the SU-8 layer with the printed side down. The print side can be confirmed by looking at the mask under a microscope. Note that the design will be flipped compared to the CAD drawing. It is imperative that the print side is in contact with the SU-8 or Fresnel diffraction effects will create large structures with negative sloping side walls as shown in Figure 5.12. Fresnel diffraction causes more energy to be distributed to the pattern edges and this effect increases with gap size [Chuang *et al.* (2002)]. Therefore, a vacuum is used to enhance the contact between the mask and SU-8. The optimum vacuum pressure was found to be 3-5psi, larger pressures tended to push the mask into the SU-8 layer. Since the transparency is flexible, it conforms to the shape of the SU-8 layer; however, air bubbles are usually trapped under the mask and may cause non-uniform exposure conditions. For high aspect ratio designs (>5:1), non-uniform exposure doses can produce partial-cross linking and residual stress build up, resulting in deformed structures [Matta *et al.* (2006)]. To obtain better results some researchers have used index matching liquids between the mask and substrate [Yang *et al.* (2005); Chuang *et al.* (2002)]. For thicker resists the exposure should be done in steps, waiting one minute after each dose, as large exposure doses will generate heat in the top layer increasing residual stress.

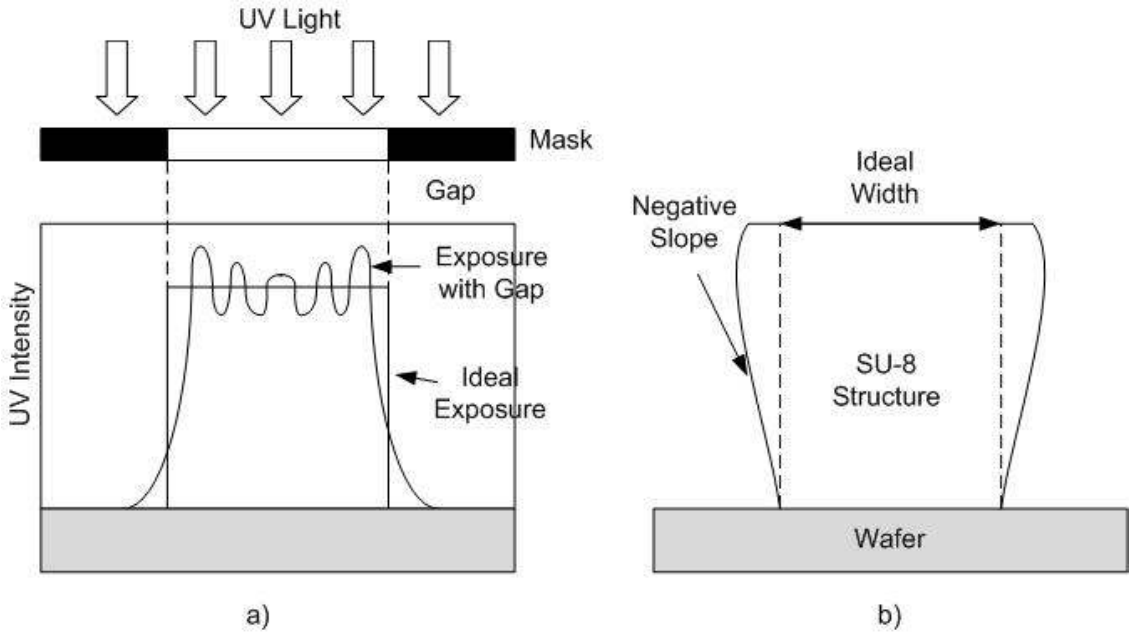

Figure 5.12 Illustration of (a) Fresnel diffraction effect on exposure with gap and (b) resulting structure with negative sloping side walls.

The cross linking process is completed by a post exposure bake (PEB). In general, the process parameters provided by Microchem were followed and are summarized below:

1. X min at 65°C (SU-8 dependent, taken from Microchem guidelines)
2. X min at 95°C (SU-8 dependent, taken from Microchem guidelines)
3. 2 step cool down 30s at 65°C and 30s at 50°C.
4. Final cool down on glass Petri dish for 10 min.

The design usually appears on the silicon wafer after a few minutes on the 95C hot plate. For thicker resists the cool down times should be extended (3-5min). SU-8 and silicon have significantly different coefficients of thermal expansion (CTE): 3.44×10^{-6} 1/K and 52.410^{-6} 1/K [Lorenz *et al.* (1998)]. A gradual cool down is crucial or thermal stress due to the CTE mismatch will cause cracking and possible lift-off of the SU-8 structures as shown in Figure 5.13. The wafer must be allowed to cool back down to room temperature (>1hr) before proceeding to the development step.

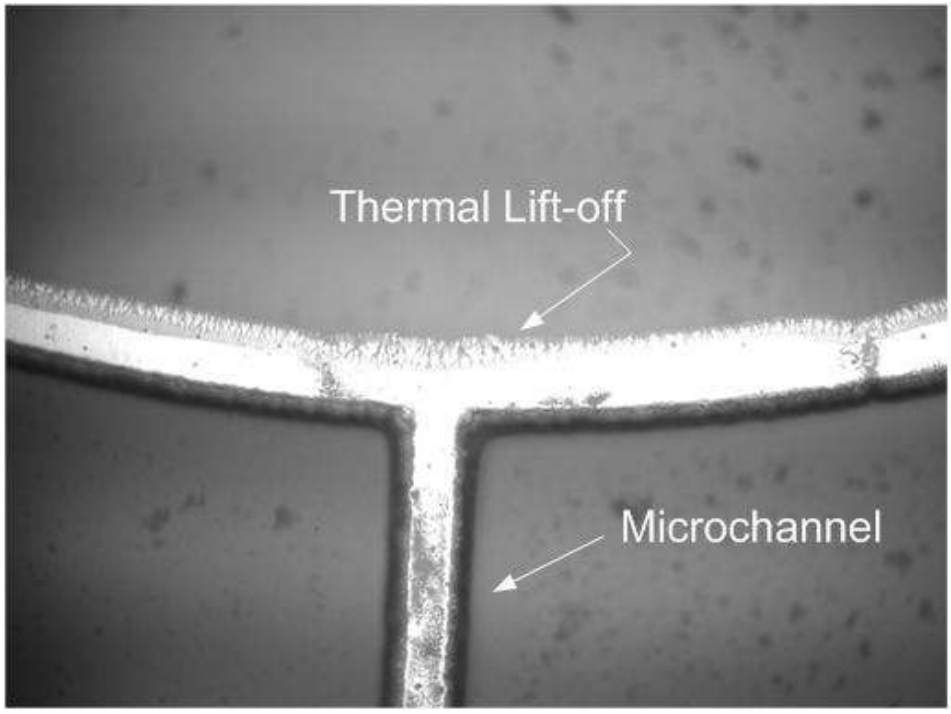

Figure 5.13 Cracking of SU-8 features and lift-off caused by CTE mismatch during cooling.

5.2.5 Development of Features

The development step removes uncross linked SU-8 leaving behind the positive relief structures. The wafer is held in a dipping holder and placed in a large jar (4L) of SU-8 Developer. Slight agitation is provided by gently bubbling nitrogen gas through the solution. Agitation is necessary for complex or high aspect ratio designs to fully develop the structures [Matta *et al.* (2006); Williams *et al.* (2004)]. Qualitatively, extending the development time (>20min) was not found to cause lift-off of the features, though, swelling of the features has been reported as an issue [Liu *et al.* (2004)].

The development times vary with the film thickness and were found to be in good agreement with Microchem specs. After development, the wafer is rinsed with isopropanol. If a white residue appears than the development process is not finished and the wafer is washed with DI water and returned to the SU-8 developer for one minute. The process is repeated until all the structures are fully developed. Then the wafer is washed copiously with DI water and fresh SU-8 developer to remove any residue. Finally, the wafer is washed again with DI water and blown dry with nitrogen. Afterwards the wafer is silanized through vapour deposition with trichloromethylsilane (TCMS) to aid in the release of the PDMS mold. This is done by placing the wafer in a vacuum desiccator with a small open bottle of TCMS for 20-30 minutes. Note TCMS is extremely harmful to the respiratory system and should be handled with care under a fume hood. The complete master is stored in a specialized wafer container until it is needed.

5.3 Multi-Level Fabrication Technique

Multi-level structures of SU-8 can be fabricated by performing multiple photolithographic steps of spin coating and exposure followed by a single development step [Mata *et al.* (2006)]. This technique is useful for creating channel networks with more than one height and is essential in fabricating very thin channels as hydrodynamic resistance elements for suppressing undesired pressure driven flow. The process for each layer is the same (coating/SB/exposure/PEB), where each layer is coated on top of the previous layer. A new mask is required for each structure level and alignment between levels is achieved using fiducials incorporated into the masks. Overlapping structures are built bottom-up where shorter features are fabricated first and taller features last. Mata *et al.* (2006) has used this technique to develop six levels of structures alternating between SU-8 2010 and SU-8 2100 for an overall thickness of 500µm.

This technique was successfully applied using the SU-8 2000 series of resists to fabricate up to four levels of structures. The most direct application of multi level fabrication is the addition of an adhesion layer to the silicon wafer before fabricating additional structures [Carlier *et al.* (2004)]. The adhesion layer is formed by spin coating a thin layer of SU-8 2005 (~5µm) on the substrate, exposing the entire wafer and PEB. This layer creates a buffer for thermal contraction of subsequent structures and reduces cracking and lift-off of the smaller microchannel structures. In fact, the adhesion layer was so successful that it was implemented as a standard protocol for all silicon masters.

The fabrication of multi-level structures posses a number of additional challenges. SU-8 reflow in the unexposed regions of an under layer during PEB creates a wavy surface that can be difficult to spin coat over with thinner resists. For thick resists it is important to remove the edge bead after each spin coat or the size of the edge bead will increase with subsequent coats. More importantly, the edge bead was found to affect the spin coating of upper layers, increasing the thickness above the projected value. Thick or multiple SU-8 layers contain residual stresses causing the wafer to bow. A distorted wafer will have poor contact with the hot plate, resulting in uneven heating, which adds more stress. Therefore, extended cool down times (10-50%) above those mentioned previously for single layer structures are required. For thicker layers, the SB and PEB times need to be extended (~5-10%) to account for thermal loss through the lower layers.

Defects in the first layer can be avoided by moving the design around; however, once the first layer is exposed, the position of subsequent masks is fixed and defects that occur in these layers cannot be avoided. Thus the success rate for multi-level masters is much lower, decreasing with additional layers. Therefore, it is good practice to make three of the same design on one wafer because on average 1 out of 3 designs will contain a detrimental defect. In some cases, when thicker layers are coated over top of thinner structures it is difficult to see these structures and align the mask. To solve this problem the reference points on the thin layer can be highlighted with a permanent marker before spin coating the second layer. It is important to provide a reasonable tolerance (0.5-1mm) in the mask design when aligning by eye. Improved accuracy, down to several microns, can be achieved using a mask aligner; however, this was not attempted in this study. To enhance the durability of the master, epoxy glue (5 minute epoxy, Lepage) is brushed around the edges of the wafer to prevent lift-off of the adhesion layer. Master can be characterized by measuring the dimensions with the contact profilometer (see Section 3.7). Multi-level masters fabricated with the adhesion layer have survived over 30 replications.

5.4 Replica Molding with PDMS

PDMS is cast against the master to obtain a replica of the microchannel design. Typically, a 10:1 base to curing agent ratio is used for the liquid PDMS pre-polymer. To a certain extent, the mechanical properties of PDMS can be controlled by adjusting the mixing ratio; lower ratios such as 5:1 will produce a stiffer PDMS, higher ratios a softer PDMS after curing. Mata *et al.* (2005) demonstrated that the optimum ratio for curing and ultimate tensile strength is 7:1. Each component of the PDMS is weighed out using a mass balance and mixed thoroughly in disposable plastic dish. Mixing traps bubbles in the PDMS which are removed by placing the dish in the vacuum oven and applying a 25psi vacuum for 20 minutes. While waiting, the master is placed in a disposable 5" aluminium weighing dish with the sides curled up to increase the holding capacity. A flexible holding container is necessary or the master might brake when the mold is removed. For the aluminium dish, 40g of PDMS mixture will create a ~2.5mm thick mold. After the mixture is degassed it is poured over the master and degassed again to remove any remaining bubbles caused by the pour. The pressure is equalized and the PDMS is cured at 80C for 1.5-2hrs depending on the amount of PDMS. Longer bake times (>12hrs) were found to improve PDMS plasma bonding and EOF properties as confirmed by others [Eddington *et al.* (2006)].

The cured PDMS designs are then carefully cut and trimmed from the master using a sharp scalpel. To prevent contamination, both sides of the PDMS mold are covered with Saran wrap. Holes are punched with a leather punch (2 to 4.5mm diameter by 0.5mm) at specified points to gain access to the microchannel network. Smaller holes (<1.5mm) are punched using hypodermic needle stubs connected to a syringe. Typically, the hole has an hourglass shape due to the elasticity of PDMS. The punch should start on the design side of the PDMS to assure it is placed in the right position. The punching process generates fine particles in the reservoirs that can enter the network and block the channels. These particles are removed by washing the holes with pressurized water and air. Another method to gain fluidic access is to attach posts to the master and mold the holes directly [Duffy *et al.* (1998)].

5.4.1 Plasma Treatment and Bonding

Sealing the replica mold to a flat surface encloses the microchannels. A reversible seal is provided through Van der Walls forces by simply placing the mold in contact with another flat substrate [McDonald *et al.* (2000)]. Since PDMS is flexible it can seal around any small imperfections in the substrate. In this manner the bond is water tight but cannot withstand pressures greater than 5psi; however, filling the channels is difficult since PDMS is naturally hydrophobic [Fritz *et al.* (1995); Bhattacharya *et al.* (2005)]. To obtain a permanent seal, PDMS and the bonding substrate are oxygen plasma treated before being brought in contact. The treatment is believed to generate silanol groups, $-O_nSi(OH)_{4-n}$, on the surface of the PDMS through the oxidation of methyl groups, $-OSi(CH_3)_20-$ as shown in Figure 5.14 [McDonald *et al.* (1998)]. For PDMS, silicon and glass surfaces a reaction creates covalent siloxane (Si-0-Si) bonds between the two substrates when they are placed in contact. This method can bond PDMS irreversibly to a number of additional materials ($Si0_2$, quartz, silicon nitride) but not to some other polymers (PMMA, polycarbonate) [Duffy *et al.* (1998)]. Materials such as gold and polystyrene which do not contain silicon chemistries can be irreversibly bonded with the combination of an adhesive and plasma bond [Kim *et al.* (2007)].

The presence of the silanol groups renders the PDMS surface hydrophilic so the channels can be easily wetted. In addition, when in contact with a neutral or basic polar liquid the surface produces ionizable groups ($SiOH \leftrightarrow SiO^- + H^+$) that generate a negative zeta potential for EOF. The plasma treated surface is unstable in air and reverts back to its natural hydrophobic state in 1-2hr [Fritz *et al.* (1995); Bhattacharya *et al.* (2005)]. However, the oxidize PDMS can be stabilized by placing it in contact with a polar liquid immediately after treatment [Murakami *et al.* (1998)]. For wetted channels the zeta potential decreases rapidly after surface treatment but stabilizes after several hours (>12hrs). The degradation is believed to be caused by the diffusion of uncross linked low molecular species to the surface of the PDMS through cracks in the silica like layer created by the plasma treatment [Kim *et al.* (2000)]. Plasma treated channels that have been exposed to air can be recharged by treating with 1M NaOH [Ren X. *et al.* (2001)]

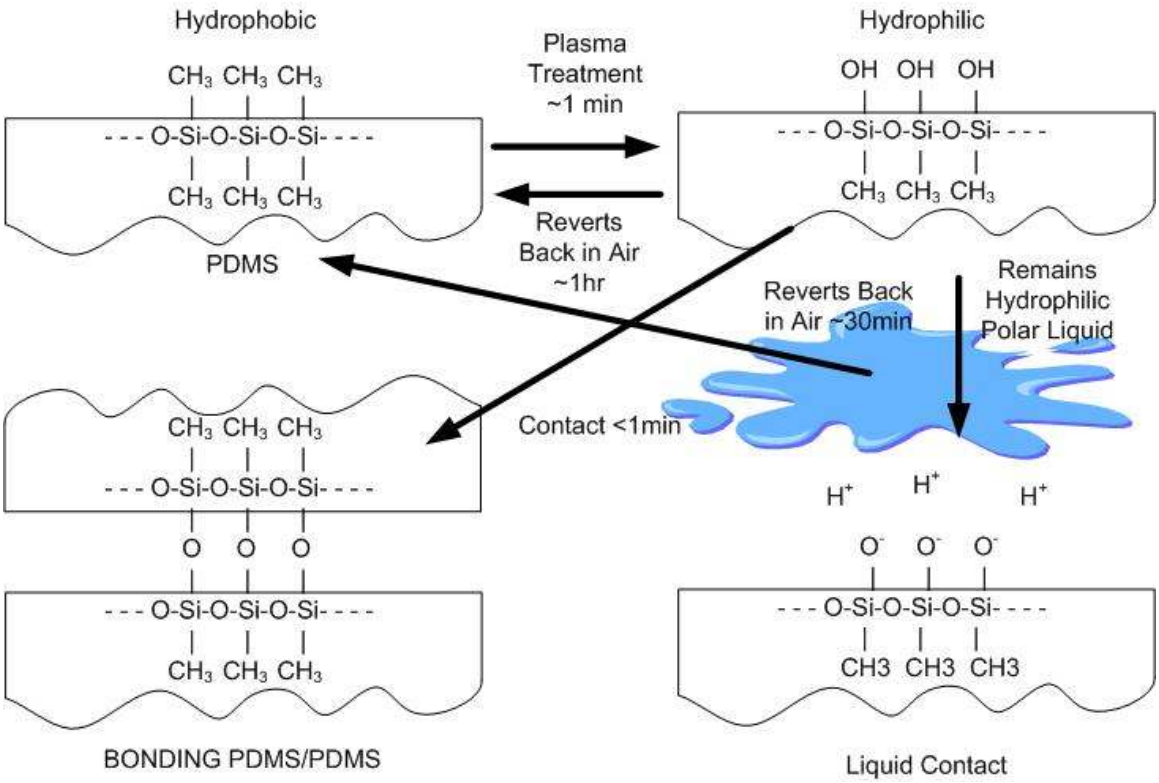

Figure 5.14. Schematic showing the oxidation of PDMS and subsequent bonding and liquid contact phenomenon.

The optimized procedure for bonding PDMS/PDMS and PDMS/glass chips are as follows:

1. Place the mold and substrate in the plasma cleaner with the bonding sides up. (PDC-001, Harrick Plasma)
2. Close the needle valve and turn on the vacuum for 30s.
3. Turn off the vacuum and turn on the plasma on high (29.6W) for 50s.
4. Turn off the plasma and release the vacuum quickly by opening the valve.
5. Take the two pieces and place them in contact immediately (<1 min). The PDMS will self-seal once in contact, however, pinching the sides helps provide gentle pressure.
6. Fill the channels with DI water within 5min and let rest.

The vacuum must be turned off during the plasma treatment or the bond will be very poor. A good bond is achieved within 5 minutes after contact and should be checked by trying to peel the PDMS mold off the substrate. To assure high quality bonds the substrates must be clean and dry. In addition, PDMS that has been cured for extended times was found to have a better bonding quality. It is also known that heating the device after bonding can improve bond strength

[McDonald *et al.* (2002)]. One of the problems with plasma bonding is the short amount of time allotted for aligning the mold on top of the substrate. Possible solutions to this problem is using a few drops of methanol as a lubricant [Jo *et al.* (2000)] or PDMS mortar for PDMS/PDMS bonding [Wu *et al.* (2005)].

Bubbles can get trapped in the network when filling the channels with water. In most cases, these bubbles will dissolve within 1-2 hrs after filling. However, if the bubbles do not dissolve than they can be very difficult to remove after this time. For complex designs where bubbles are trapped easily it is best to remove the bubble soon after filling while the PDMS is still very hydrophilic. This can be done by connecting a syringe to the reservoir (*via* a tubing connector) and generating a vacuum to draw the fluid through the chip. Care should be taken not to collapse shallow channels since they may bond permanently. Another filling method is the channel out gas technique described by Monahan *et al.* (2001). In this method, the chip is submersed in water and the container is placed in a vacuum chamber. The decreased pressure allows the air to escape through the outlet ports of the chip. The authors found that for complex 3D networks with terminated channels this method was superior to filling using strictly capillary action or drawing the fluid with a vacuum. After filling, the reservoirs need to be sealed with tape or Parafilm to prevent evaporation.

5.5 Attaching Fluid Connectors and Reservoirs

Connecting a microfluidic chip to macro components such as tubing, valves, syringes, reservoirs and pumps can be difficult. Several techniques have been developed for fabricating low-dead volume connections with capillaries and tubing [Chiou *et al.* (2004]. A common method is to integrate commercial connectors for High Pressure Liquid Chromatography systems as these components have low dead volumes and are chemically resistant. A variety of such connectors and components (tubing, valves, 3-way couplings) were purchased from Upchurch Scientific (see Figure 5.15).

Several issues arose while trying to attach the connectors to the PDMS chips. Bonding using the adhesive supplied with the connectors requires high temperatures (120C for 1.5hr) while simultaneously clamping the connector to the substrate. The flexibility of PDMS makes it incompatible with this process. Instead the connectors were bonded to a piece of polycarbonate with a small hole (~1mm) drilled through the center. The polycarbonate piece was then glued to the chip *via* a thin layer of PDMS adhesive and cured in the oven for 10 minutes at 80°C. Along

these lines the connector would easily twist off when tightened and leaks would often occur at the glue level. This problem was solved by replacing the PDMS glue with a silicone sealant (PL Silicone Sealant, LePage) which provides a semi-permanent bond to the connector and a permanent bond with the PDMS. In this way the connectors can be removed from the chip and reused. Using this same method cut glass tubes (1/8-1/2”- inner diameter, 0.5-1” length) can also be attached to increase the reservoir volume.

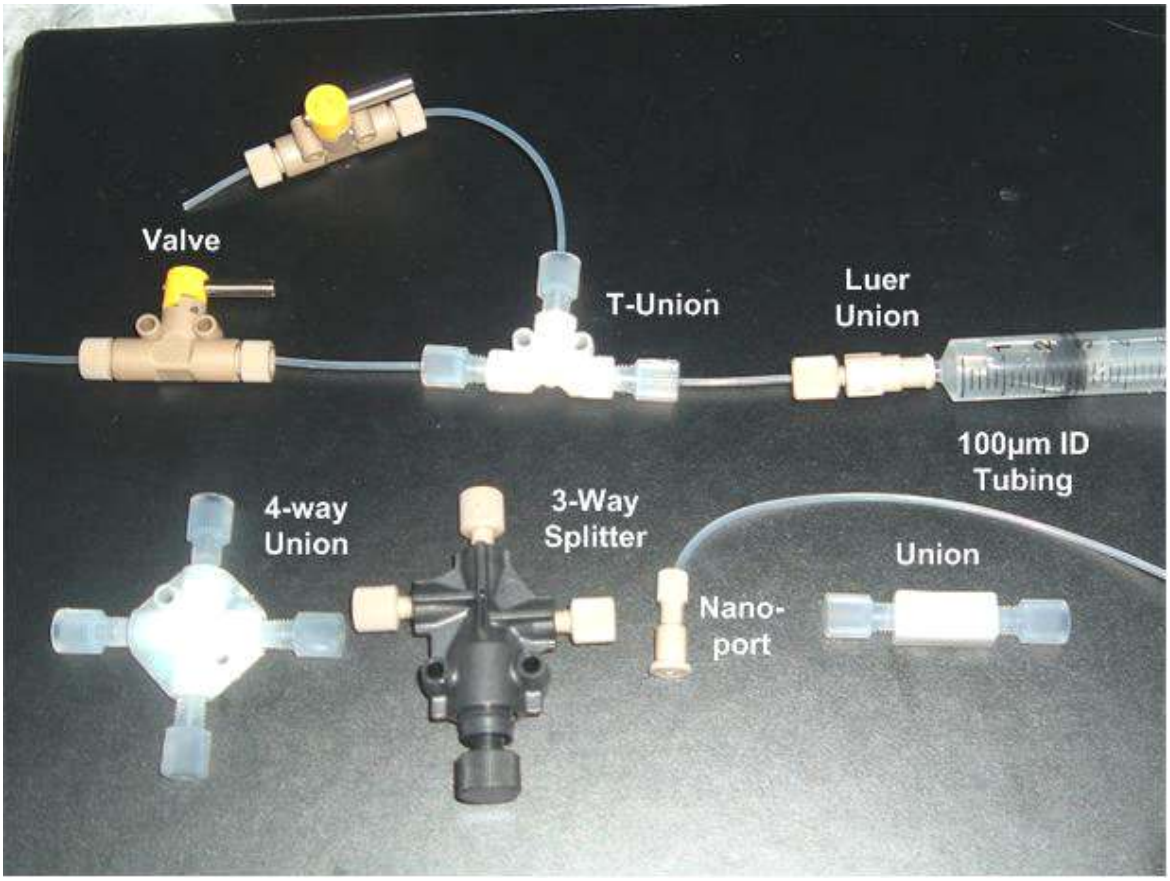

Figure 5.15 Nano-port components (Upchurch Scientific) used for interfacing with external flow network.

The nano-flow connectors do not allow for a direct connection with many standard medical components such as syringes and filters. As an alternative several polypropylene quick turn Luer Lock couplings were purchased for the system (Luer Lock couplings, McMaster-Carr). These standard fittings are inexpensive, approximately $1/20^{th}$ the price of nano-port connectors, autoclavable and require only a quarter turn to connect and disconnect. Nano-port connectors require a full turn or more which can cause the tubing to twist, adding tension to the connector. Female caps were modified by drilling an access hole through the cap and molded to the PDMS

chip using silicone sealant extending the reservoir volume up to 100µL. Flexible tubing can be connected with Male to barb connectors and extra large reservoir (1.5mL) were fabricated with Male to thread connectors attached to polypropylene extensions as shown in Figure 5.16. Matching male caps can be attached to seal the chip when transporting or for long term storage. Tightening the caps can also be used to dissolve bubbles in the chip by increasing the internal pressure. Standard medical components such as filters and syringes can be directly connected to the female connector attached to the chip. These Luer connectors were attached to attach tubing, reservoir extensions, caps and syringe filters to the EO pump and cell culture chips.

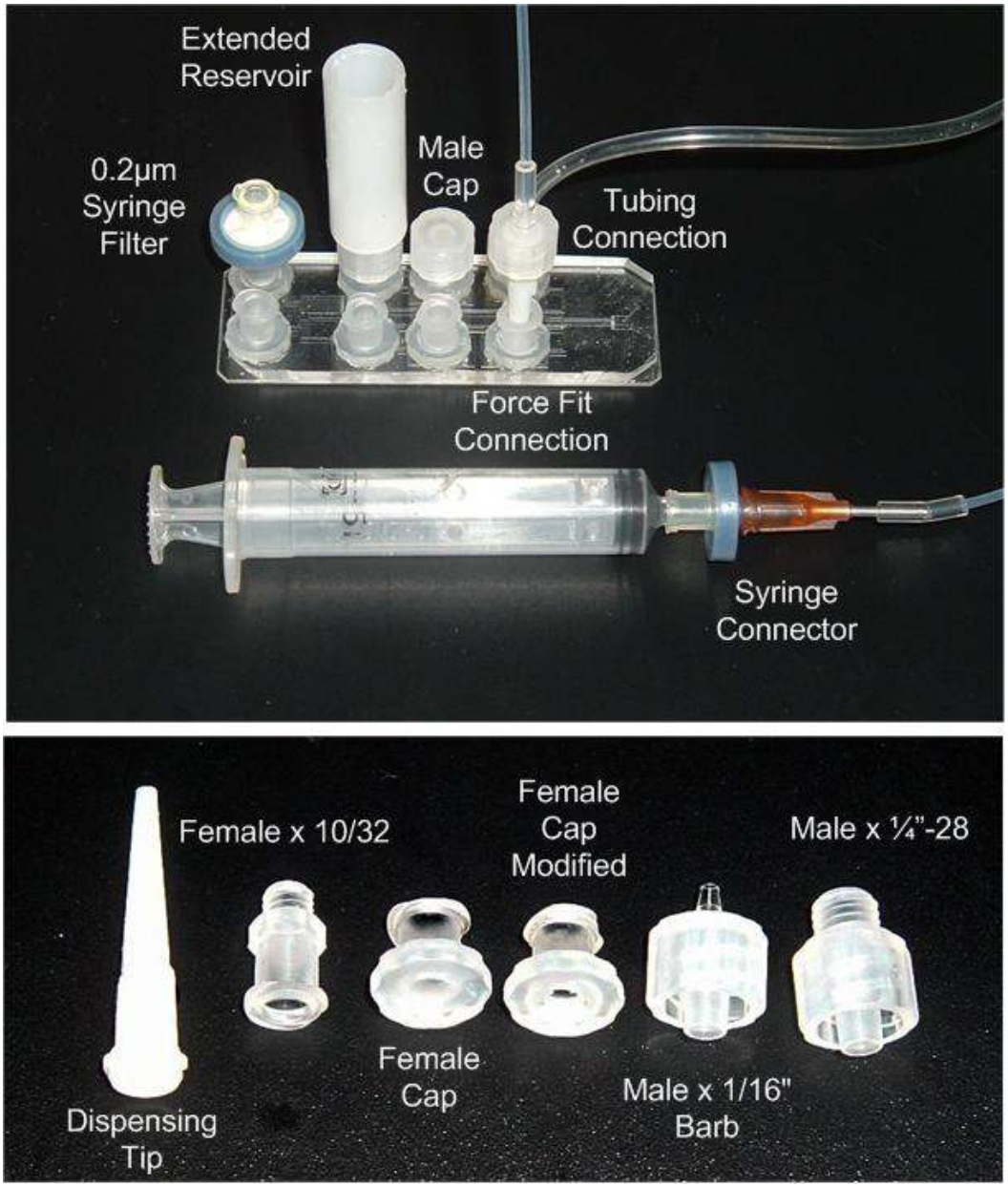

Figure 5.16 Luer type polypropylene components used to interface with PDMS chips.

5.6 Summary

The techniques and procedures developed for fabricating PDMS microfluidic devices at the University of Waterloo microfluidic lab were presented in this chapter. Details of each step in the fabrication process were explicitly described to assist future researchers in the fabrication of new microfluidic chips. The protocols discussed here were used to fabricate the EO pumps and cell culture chips used during this thesis.

Chapter 6

Design and Development of a Novel Y-channel Chip for Electroosmotic Mobility Measurements

To successfully implement EOF in a microfluidic chip requires knowledge of the physical and electrokinetic properties of the working fluid. Some physical properties such as viscosity, dielectric constant and conductivity can be assumed or obtained from literature; however, due to the complex parameters affecting zeta potential it must be measured experimentally. To this end, a system was developed to measure the electroosmotic mobility of various fluids in microchannels using the current monitoring technique and a new Y-channel design. This chapter discusses the design and development of the Y-channel design as well as improvements to the slope method for calculation the electroosmotic mobility and numerical simulations of the displacement process in the Y-channel. Experimental results for various solutions and surface treatments in PDMS/PDMS and PDMS/glass microchannels are also presented. This work was done in partnership with Zeyad Almutairi.

6.1 Details of the Current Monitoring Method

As discussed in Section 2.5.3 several methods have been developed to determine the electrokinetic properties of the liquid/surface interface inside a microchannel. The current monitoring method is one of the most widely implemented techniques for measuring these properties due to its simplicity, accuracy, and low cost [Sze *et al.* (2003)]. In this method, the average electroosmotic velocity is measured by monitoring the electrical current when a similar solution of slightly different concentration replaces another in a single microchannel under EOF. The fundamental of the current monitoring method are presented in Figure 6.1. First, the test solution is pumped by EOF through the microchannel until a steady state is reached by monitoring the current draw. The electric field is then turned off and the solution in one reservoir is replaced with a similar solution of slightly lower concentration. The high voltage power supply is turned back on and under EOF the second solution begins to replace the first in the microchannel. As a result, the current draw changes due to the difference in electrical resistance of the two solutions. Once the second solution completely replaces the first the current plateaus and stabilizes.

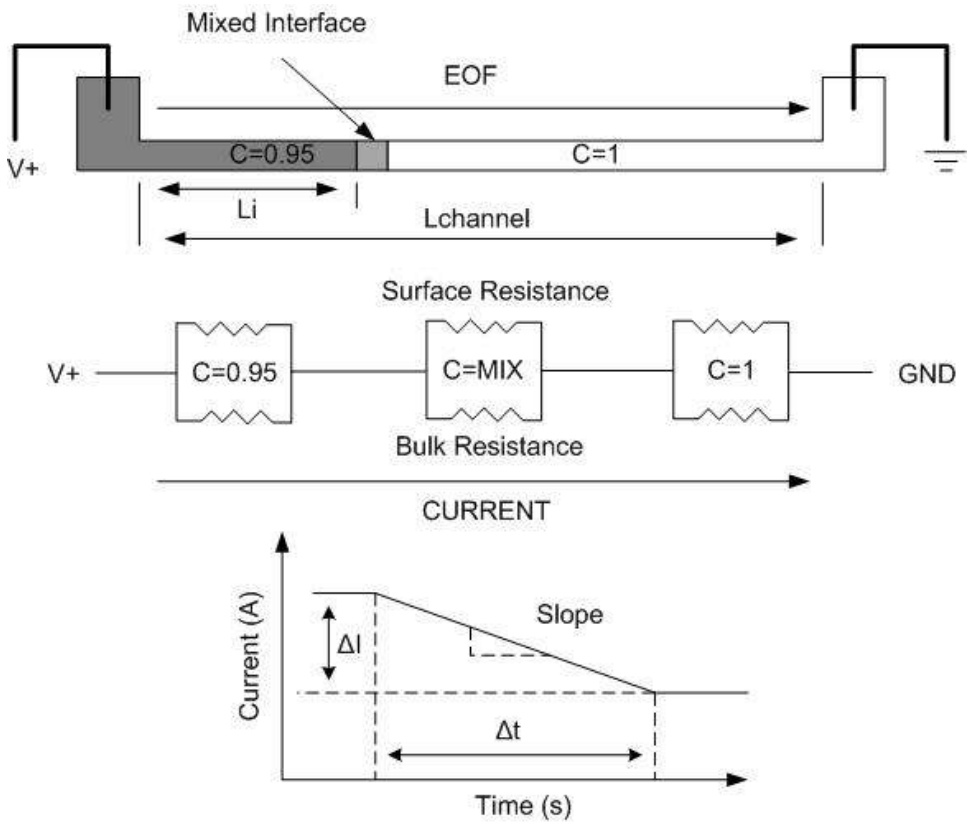

Figure 6.1 A schematic of the current monitoring method for measuring the electroosmotic mobility of a test solution.

For accurate measurements the concentration difference must be kept to a minimum so that the zeta potential and electric field are nearly uniform throughout the microchannel. Typically a 5% difference is used since it provides a measurable current difference without negatively affecting the results [Pittman *et al.* (2003)]. The average electroosmotic velocity can be determined from the displacement time, Δt, and the total channel length, $L_{channel}$:

$$\overline{u}_{eof} = \frac{L_{channel}}{\Delta t} \qquad \textbf{(6.1)}$$

By substituting this value into the Helmholtz-Smoluchowski equation the electroosmotic mobility or zeta potential can be calculated:

$$\overline{u}_{eof} = \mu_{eof} E_x = -\frac{\varepsilon_o \varepsilon_r \xi}{\mu} E_x \qquad \textbf{(6.2)}$$

The major problem associated with the total length method is the ambiguity surrounding the displacement time. Small current fluctuations and gradual transitions due to diffusive mixing of the two solutions at the interface can make it difficult to determine the start and end of the

displacement process. To solve this problem, Ren *et al.* (2003) developed an improved method to determine the zeta potential by using the slope of the current-time relationship. The slope method takes advantage of the fact that for small concentration difference the change in current is linear. In contrast, large differences in concentration cause a non-linear change since the current is inversely proportional to the resistance ($I = V / R_e$). For the former case the slope can be defined by:

$$slope = \frac{\Delta I}{\Delta t} \tag{6.3}$$

The derivation for the electroosmotic mobility from the slope is given as:

$$slope = \frac{\Delta I}{\Delta t}\frac{L_{channel}}{L_{channel}}$$

$$slope = \Delta I \frac{\overline{u}_{eof}}{L_{channel}} \tag{6.4}$$

$$\mu_{eof} = \frac{slope \cdot L_{channel}}{E_x \cdot \Delta I}$$

The zeta potential can then be calculated from the electroosmotic mobility:

$$\zeta = -\frac{\mu\mu_{eof}}{\varepsilon_r \varepsilon_o} \tag{6.5}$$

Under electroosmotic flow the current draw is composed of three parts: the bulk conductivity current, $I_{cond,bulk}$, the surface conduction current, $I_{cond,surf}$, and the convection current created by the fluid motion, $I_{cond,conv}$. The convection current is several orders of magnitude smaller than the two other currents and is often neglected. The total current reduces to:

$$I_{total} = I_{cond,bulk} + I_{cond,surf} = \lambda_b A_c E_x + \lambda_s P_w E_x \tag{6.6}$$

where λ_b is the bulk conductivity of the fluid, λ_s is the surface conductivity, A_c is the cross-sectional area, P_w is the wetted perimeter of the channel and E_x is the applied electric field. To determine the surface conductivity the reservoirs and channel are filled with the same solution and the total current is measured for an applied electric field. The surface conductivity is calculated from Eqn. 6.6 assuming that the bulk conductivity is already known:

$$\lambda_s = \frac{I}{P_w E_x} - \lambda_b \frac{A_c}{P_w} \tag{6.7}$$

Substituting Eqn.6.6 into Eqn.6.4 and assuming that $\Delta\lambda_s = 0$, the electroosmotic mobility can be calculated as:

$$\mu_e = \frac{slope \cdot L_{channel}}{E_x{}^2 A_c (\lambda_{b2} - \lambda_{b1})} \tag{6.8}$$

Therefore, for a single current-time plot two methods are available for analyzing the data to determine the electroosmotic mobility. For well defined start and end points the preferred method of calculation is the total length method since it relies on the measurement of fewer variables thus reducing the expected uncertainty. In the subsequent study both the total length and slope method are used in all experiments. Therefore, a simple current monitoring experiment can provide both the electroosmotic mobility and surface conductivity for the microchannel.

6.2 The Y-Channel Design

After attempting some preliminary experiments using the conventional current monitoring method several issues arose. As mentioned previously, for some fluids it was difficult to determine the start and end times because of the diffuse interface. The data was often scattered and repeatable results could not be obtained. To reduce uncertainties in the measurements and to obtain an average value for the electroosmotic mobility the displacement was repeated for different applied electric fields. This was a very time consuming and tedious process because after each displacement the reservoirs had to be refilled and the electrodes repositioned. Repeated interaction with the equipment may have introduced additional errors in the measurements; more importantly the operator's safety was jeopardized because high voltages are used during the experiments.

To solve these issues a new Y-channel design was proposed that would allow for more accurate measurements and higher throughput. A similar T-channel design has been used for electroosmotic mobility measurements by Liu *et al.* (2001) and Shin *et al.* (2007). Liu *et al.* (2001) used a three reservoirs channel configuration with an integrated conductivity meter at the end of the displacement channel. The meter was used to detect the change in conductivity as one solution displaced another solution. The displacement time is then used to determine the electroosmotic mobility of the fluid. Shin *et al.* (2007) work is based on the fact that confluent flow streams in a T-channel show oscillation under a time-periodic electric field. Two streams of fluid are pumped simultaneous down the main channel, one fluid contains fluorescent die and the other does not. An oscillating electric filed is applied between the two streams and the movement

of the interface is monitored using fluorescent microscopy. The oscillation of the interface is used to determine the electroosmotic mobility of the channel. Both these methods serve as alternatives to measuring the electroosmotic mobility; however, they are more difficult to implement than the current monitoring technique.

The proposed design consists of two side channels attached to the main displacement channel as shown in Figure 6.2. The principal of operation is as follows. First, the reservoirs R1 and R2 are filled with the 100% and 95% solutions and platinum electrodes are connected to the reservoirs by a switch to the high voltage power supply. An electric field is applied between R1→R3 while R2 is left floating and the 100% solution is pumped by EOF down the main channel until it is filled. The electric field is then applied between R2→R3 and the 95% solution is pumped so that the two side channels are filled with each of the fluids and the main channel now contains the 95% solution. The electric field is switched back to R1→R3 and the 100% solution is pumped down the main channel displacing the 95% solution and the current change is recorded. The process is repeated switching back and forth between the two channels. In this way multiple displacements can be obtained quickly without having to refill the reservoirs. In addition, the design creates a well defined interface so that the start and stop times can be easily determined. Figure 6.3 shows the current draw for a typical Y-channel experiment. Notice the sharp start and end transitions of the Y-channel result as well as the quick and repeatable displacements. The Y-channel design also allows for the investigation of long term continuous electroosmotic flow since the solutions do not have to be replaced.

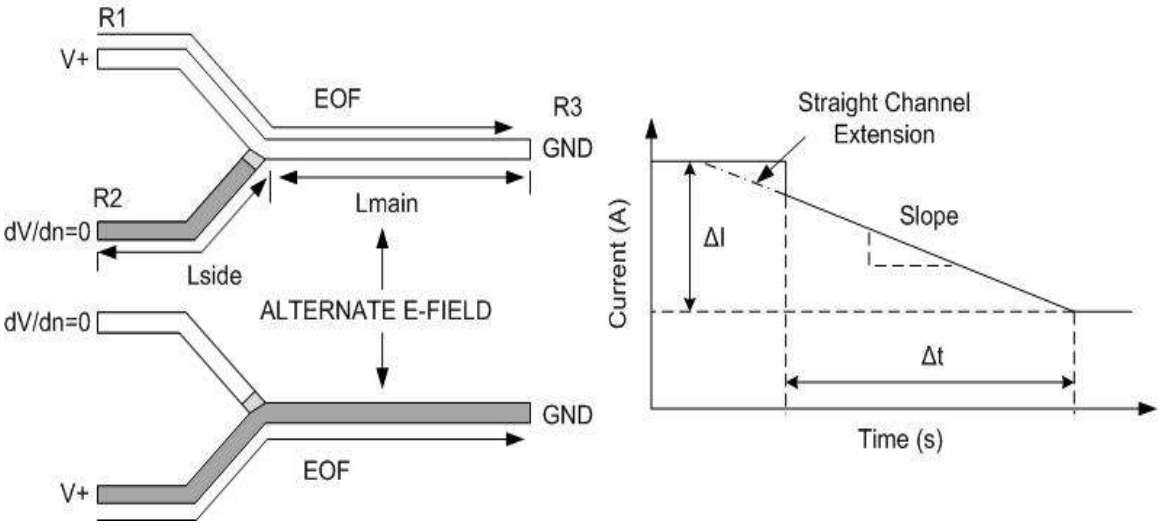

Figure 6.2. A schematic of the principals governing the Y-channel design for performing current monitoring experiments.

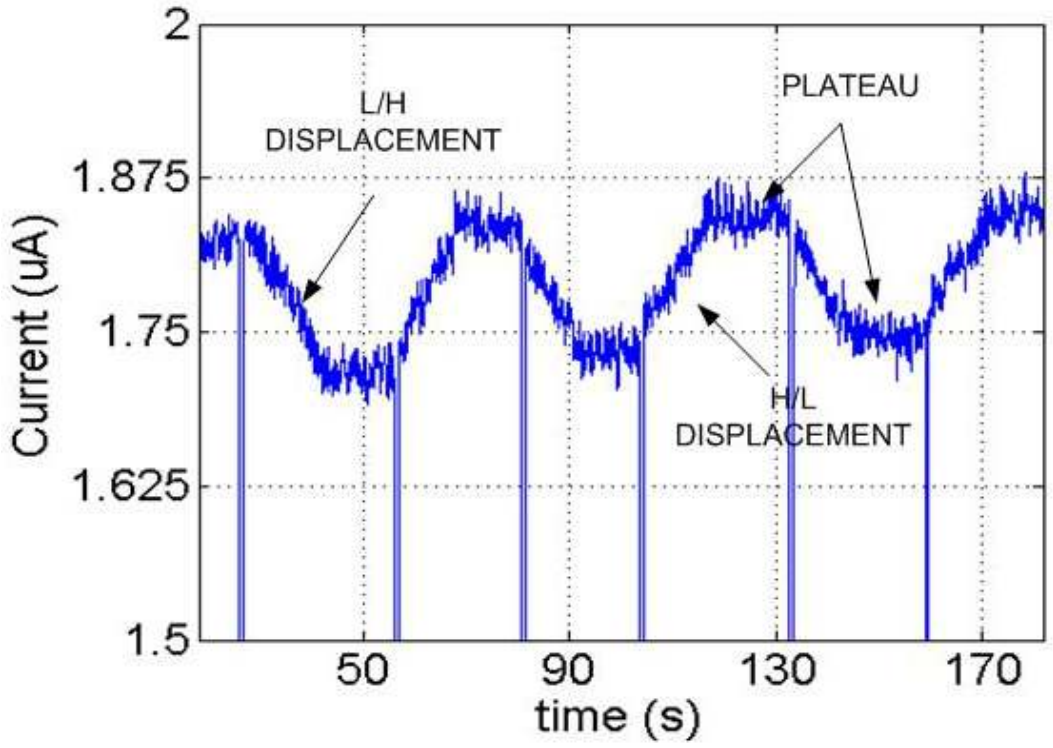

Figure 6.3 Current plot obtained from an experiment with 1mM KCl and the Y-channel design. The current draw falls when the low concentration solution replaces the high (L/H) and vice versa (H/L). Complete replacement of the solution is marked by a plateau in the current.

The current output is identical to the straight channel design except that the displacement process starts with one solution partially through the channel (in Figure 6.2 the straight channel result is represented by the extended dashed line). The equations derived before for calculating the electroosmotic mobility must be slightly altered. For the total length method the electroosmotic mobility is determined by:

$$\mu_e = \frac{L_{main}}{E_x \cdot \Delta t} \tag{6.9}$$

and for the slope method:

$$\mu_e = \frac{slope \cdot (L_{main} + L_{side})}{E_x{}^2 A_c (\lambda_{b2} - \lambda_{b1})} \tag{6.10}$$

where the electric field is now defined as:

$$E_x = -\frac{\Delta V}{L_{main} + L_{side}} \tag{6.11}$$

Details of the Y-channel design are presented in the following section.

6.2.1 Network Geometry and Dimensions

As discussed in Section 2.2.2.3 undesirable pressure driven flow created by differences in hydrostatic and Laplace pressure between the reservoirs can create significant stability problems for EOF. For the current monitoring method undesired pressure driven flow will cause erroneous measurements of the electroosmotic mobility. In order to minimize these effects, the channels were designed to have a large hydrodynamic resistance by decreasing the channel height ($R_{hyd} \propto 1/h^3$). Calculations show that pressure driven flow is largely suppressed if the height of the channel is below 5μm. Although, there exists a lower limit to the channel height; if the EDL thickness is comparable to the channel depth then the Helmholtz-Smoluchowski approximation is invalid [Hunter (1981)]. Typically this only applies to very dilute solutions with large electric double layers such as deionized water which has an EDL thickness of ~300nm. The width of the channel must be chosen so that the current draw can be measured by the experimental system. On the other hand, the width must be limited or large currents will cause significant joule heating and electrolysis. Thus several chips with a range of widths and heights are needed to test the various fluids; choosing the appropriate dimensions depends on the conductivity and estimated EDL thickness of the test fluid.

One of the negative aspects of the Y-channel design is that if the side channels are not the same then the two fluids will experience different electric fields in the main channel. Asymmetry between the side channels may be caused by fabrication defects, channel height irregularities or there may be a partial blockage in one of the channels. By designing short side channels the effects of asymmetry can be suppressed. The total resistance for the displacement process is the sum of the side and main channel resistances. Shorter side channels will have less impact on the total resistance and electric field in the main channel. However, the side channels must still be long enough to suppress pressure driven flow.

A longer main channel will improve the accuracy of both calculation methods. In the case of the total length method the error in determining the displacement time will decrease as the displacement time becomes longer. For example, an error of 1s is less significant if the displacement time is 60s rather than 20s. For the slope method a longer displacement time will result in more data points when determining the slope and thus greater accuracy. Still the length of the middle channel has an upper limit or extremely high voltages will be required to pump the solutions.

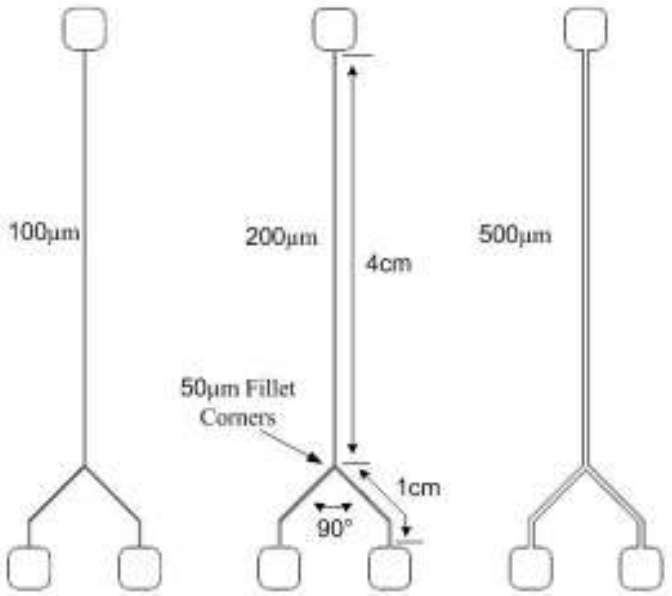

Figure 6.4 Dimensions of the Y-channels used for the current monitoring experiments.

In addition to undesired pressure driven flow, electrolysis at the electrodes can be a major problem for EOF and the current monitoring method [Rodriquez *et al.* (2005)]. This process creates additional H+ and OH- at the electrode reservoirs which changes the pH level and bulk conductivity of the liquid. The ions cause perturbations in the zeta potential, electric field and EDL as well as a steady rise in the background current. Convection within the reservoir creates a heterogeneous mixture of high and low conductivity regions that can enter the channel causing the current draw to fluctuate unpredictably. A solution to this problem is to place the electrodes far from the microchannel entrance and to limit the current draw so that the negative effects can be delayed. To absorb the pH change larger reservoirs are required especially for non-buffered solutions.

After considering all of the above mentioned factors a final design was chosen with dimensions given in Figure 6.4. The main channel length is 4cm and the side channel length is 1cm. The side channels intersect the main channel at a 45° angle and 50μm fillets are applied to the corners in order to eliminate local spikes in the electric field. The channel height was chosen between 5-9μm and the widths 100, 200 and 500μm. For the case of 500μm wide channels a 1cm head difference between reservoirs R1→R2 results in flow rate of 6.25×10^{-3} μL/min. An applied voltage of 1000V between R1→R3 with an electroosmotic mobility of 5×10^{-8} m^2 V^{-1} s^{-1} creates an EOF flow of 1.5μL/min. Thus the error caused by pressure driven flow is only 0.5% of the EOF flow which is

well within the uncertainties expected from the measurement system. The displacement time for this example solution is expected to be 40s and if a 20s stabilization period is added after the displacement, it will take approximately 1minute to perform a displacement. Since the process can be quickly repeated 10 displacements can easily be performed in 10 minutes. For the straight channel design the same number of displacements would take approximately 1hr to complete.

6.2.2 Improvements to the Slope Method

After performing several preliminary experiments a problem was found with the standard slope method of calculating the electroosmotic mobility. Typically the conductivity difference of the two solutions did not match the difference in current draw. For instance, if $\Delta\lambda_b = 5\%$, the actual current difference would often lie between 6-8% resulting in a miscalculation between the slope and current difference in Eqn.6.10. As stated previously, the traditional slope method assumes that the surface conductivity difference is negligible. However, in channels with high surface to volume ratios the surface current can be a significant portion of the overall current (~10-20%) [Arulanandam *et al.* (2000)]. As well, the surface conductivity plays an important role in the streaming potential technique for measuring the zeta potential and should not be neglected. There are also problems with measuring the bulk conductivity since the accuracy of the conductivity probe is only 0.5-1% as stated by the manufacturer. Since the calculations require the measurement of a small difference in conductivity the error introduced into Eqn.6.10 can be quite large (~30%). Furthermore, the conductivity is strongly dependent on temperature (2 %/°C), electrolysis and concentration of ions; therefore, measurements performed prior to the experiments may not represent real time values.

To improve the calculations a suggestion was made to simply reverse the derivation of Eqn.6.10 back a few steps and use the measured current difference at the two plateaus (see figure 6.2). By using the actual current change both the bulk conductivity and the surface conductivity differences in the two solutions will be included. In addition, measuring the current is also more accurate (~0.1%) and sources of errors are eliminated by not including the width and height of the channel in the calculations. The equation below presents the improved current-slope calculation:

$$\mu_{eof} = \frac{slope \cdot (L_{main} + L_{side})}{E_x (I_2 - I_1)} \qquad \textbf{(6.12)}$$

where I_1 and I_2 are the steady current values measured before and after replacement.

6.3 Numerical Modelling of Y-Channel Replacement

Numerical simulations were performed to provide insight into the Y-channel displacement process. First, a simple 1D model was developed to analyze the effect fluid properties have on the current draw and accuracy of the total length and slope methods. Afterwards, a 2D model of the entire Y-channel design created in COMSOL MULTIPHYSICS was used to study the displacement process in more detail. Data from this simulation was compared to the 1D model as well as experimental results.

6.3.1 1D Displacement Model

Several researchers have analyzed the displacement process in a microchannel with varying degrees of complexity. Chien and Helmer (1991) developed a simple 1D model to describe the bulk flow in a microfluidic channel containing two different buffers. However, their model did not account for the diffuse region at the interface or variation in flow through the EDL. Ren *et al.* (2001) presented an extended 1D analysis which included a solution of the concentration profile at the mixed interface and the Poisson-Boltzman equation for the EDL. Numerical results were compared to experimental results for the displacement of several KCl and $LaCl_3$ solutions with good agreement. A 3D model was developed by Shao *et al.* (2006) analyzed the displacement of 10^{-4} M KCl with 10^{-4} M $LaCl_3$ in a 100μm x 200μm channel. Their results show that the displacement process can produce a multi-dimensional flow if the two solutions have very different properties. In fact, the authors found that at the beginning and end of the displacement the fluid re-circulates and flows backwards out of the channel. In another work, Rodriquez *et al.* (2005) simulated the current monitoring process in a straight channel and included changes in pH and bulk conductivity from electrolysis at the electrodes. They found that perturbations to the EOF velocity can be significant (10-30%) even for buffered solutions if small volume reservoirs are used.

Since the goal of this investigation is to determine the general trends of the current monitoring process a simple 1D model was chosen for the Y-channel. An equivalent circuit model as described in Chapter 3 was applied to solve the electric field and the flow field within the channel. The Y-channel is reduced to a single microchannel where the low concentration solution displaces the high concentration solution as shown in Figure 6.5. In the beginning the low concentration solution occupies a portion of the channel equivalent to the side channel length in the Y-channel (L2) while the high concentration solution occupies the main channel (L1). First, the electric field is calculated using Kirchoff's Law and the values are inputted into the flow

model to determine the flow rate in the channel. The average velocity is then used to calculate the displacement of the fluid interface (Li) for a given time interval (Δt). The process is then repeated for the next time-step until the interface has reached the end of the channel. The flow rate, internal pressure at the interface and current draw are outputted and the electroosmotic mobility is back calculated using the total length and slope method. To solve the system of equations a computer program was developed using Matlab. Calculations were performed for the Y-channel design described in section 6.2.1 with a 200μm channel width and 6μm height.

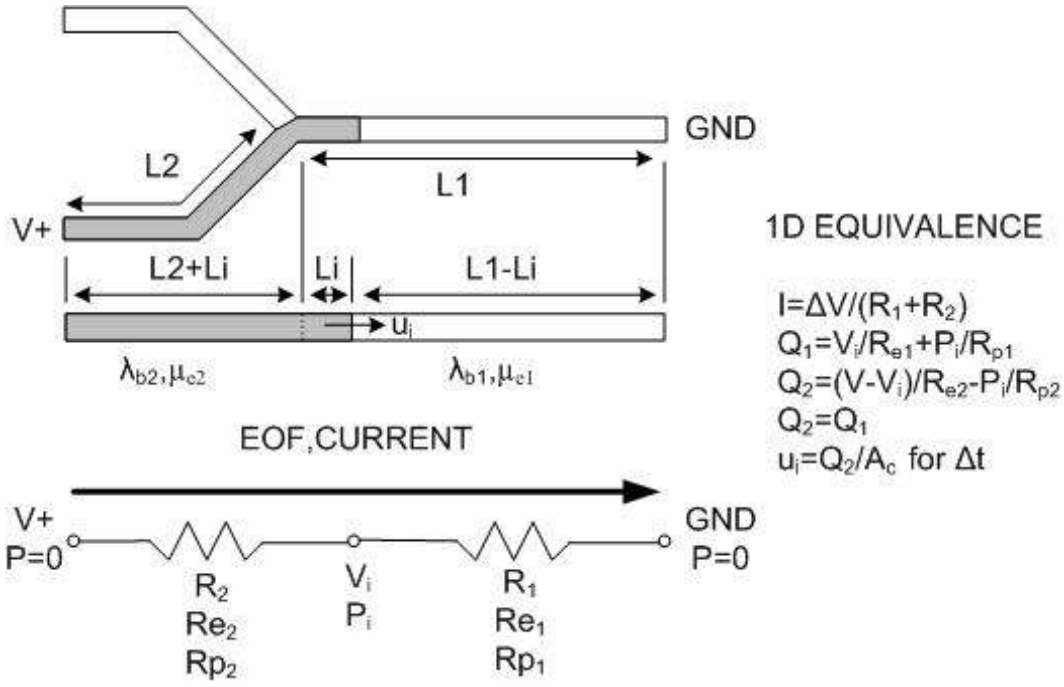

Figure 6.5 Equivalency model used for the 1D analysis of the displacement process in the Y-channel.

The most important parameters affecting the displacement process are the electrical conductivity and electroosmotic mobility. First, we look at varying the electrical conductivity of the displacing solution while keeping the electroosmotic mobilities equal. Figure 6a shows the normalized current draw for 10mM KCl replaced by the lower conductivity solution for different concentration ratios. As expected, the current draw becomes less linear as the conductivity difference becomes larger since the current is inversely proportional to the resistance; nevertheless, the displacement time remains the same for all cases. The reason for this is that although the lower conductivity solution has a greater electroosmotic flow due to the proportionally larger electric field ($\overline{u}_{eof} = \mu_{eof} E_x$) the internal pressure generated at the interface balances out the overall flow. Figure 6b shows the internal pressure at the interface during the displacement process where larger conductivity differences generate greater internal pressure.

Comparing the two calculations methods, the performance of the slope method suffers at higher concentration differences (error~18% for $c_1/c_2 = 0.5$) due to the non-linearity of the current draw while the total length method remains constant (error <1%) as long as the start and end times are well defined.

Alternatively, in the second analysis the conductivity ratio is kept constant at 0.95 while the electroosmotic mobility is varied. Decreasing the electroosmotic mobility of the second solution increases the displacement time and creates a less linear current draw as shown in Figure 6c. This is a consequence of the change in flow rate during the displacement process. As the second solution replaces the first the flow rate decreases to match the EOF of the second solution and reaches a plateau once the displacement process is complete as shown in Figure 6d. The average flow rate during the displacement is approximately the average of the inherent electroosmotic flow rates of the two solutions.

The accuracy of the two calculation methods can be evaluated since the electroosmotic mobility is entered as an input in the model. There exist two possible comparisons for the calculated electroosmotic mobility. The first is to consider the high concentration solution as the "test" liquid whose electroosmotic mobility is desired. The second is to compare the result to the average electroosmotic mobility of the two solutions. Figure 6.7 shows the results for the calculated electroosmotic mobility compared to the former (a, b) and later (c, d). For both methods the error is severe (~30%) for larger electroosmotic mobility differences when comparing to the "test" solution. On the other hand, both methods show good agreement (error <10%, for 50% difference) when comparing to the average electroosmotic mobility. In practical terms, during an experiment the "test" solution properties are unknown so the calculated mobility will represent the average of the two solutions. It should be noted that these results represent a conservative estimate of the error since larger differences in conductivity and electroosmotic mobility will create a complex 2D flow within the channel that is not accounted for in the 1D model. If large internal pressure gradients are generated there may be a leakage flow to the other side channel which will lower the overall flow rate in the main channel. These errors can be limited by ensuring that the conductivity and electroosmotic mobility difference between the two solutions is very small as is already the protocol for the current monitoring method.

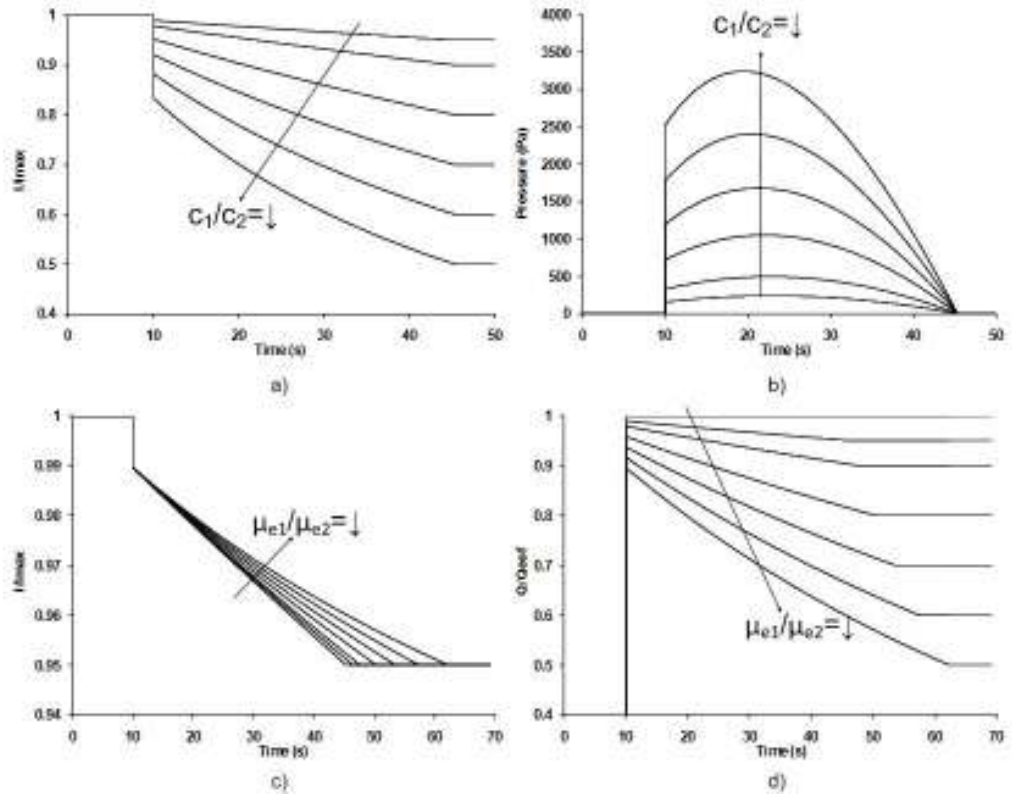

Figure 6.6 1D equivalence model results for the Y-channel model with ζ=-80mV (a) Current draw for concentration ratios (c_2/c_1) 0.95, 0.9, 0.8, 0.7, 0.6, 0.5 with equal electroosmotic mobility between the two solutions. (b) Pressure generated at the interface as it travels through the channel for different concentration ratios. (c) Current raw for a conductivity ratio of (c_2/c_1=0.95) and electroosmotic mobility ratios (μ_{e2}/μ_{e1}) 1, 0.95, 0.9, 0.8, 0.7, 0.6, 0.5. (d) Flow rate through the microchannel during the displacement for different electroosmotic mobility ratios.

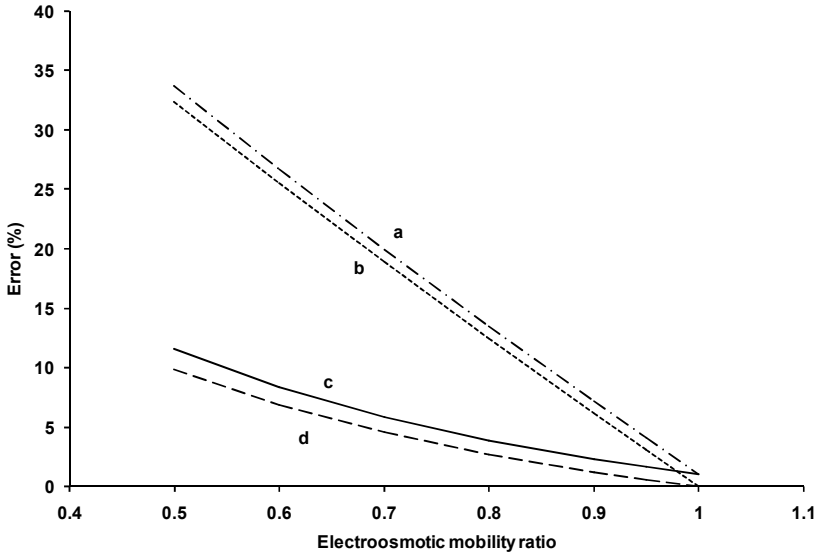

Figure 6.7 Error for calculating the electroosmotic mobility from the current draw for electroosmotic mobility ratios (a) slope method (b) total length method compared to the "test" solution and (c) slope method (b) total length method compared to the average electroosmotic mobility of the two solutions.

6.3.2 2D COMSOL MULTIPHYSICS MODEL

The previous 1D analysis provided valuable insight into the parameters affecting the current monitoring method; however, it was an ideal representation of the displacement process. In reality, the electrokinetic switching and diffuse interface creates a more complex system with 2D non-uniformity that must be analyzed using numerical modeling. To assist in this analysis a model was developed using COMSOL MULTIPHYSICS to simulate an experiment involving the displacement of 10mM KCl with 9.5mM KCl. The entire Y-channel with standard dimension described previously was used as the domain. Temporal solutions of the concentration, electric and flow field were calculated simultaneously because of extensive coupling between the equations. The electric field is coupled to the concentration through the bulk conductivity, the flow field is coupled to the electric field through the EOF slip boundary condition and the concentration is coupled to the flow field through convection. Refer to Chapter 3 for an in depth discussion of the governing equations and boundary conditions used in the simulations.

Physical properties of the KCl solution were taken from literature and the zeta potential was assumed to be the same for both fluids [Masliyah (1994)]. Initially a portion of one side channel (R2) was filled with the lower conductivity solution (c_2=0.95) and the rest of the channels were filled with high conductivity solution (c_1=1). To simulate priming of the chip, 1000V was applied to R2 while R1 was kept floating and c_2 replaced c_1 in the main channel. The simulation ran for 100s until the concentration at the outlet of the main channel, R3, was equal to c_2. The applied potential conditions were then switched between R1 and R2 so that c_1 replaced c_2 in the main channel and ran for 80s completing the priming step. The next switch represents a true current monitoring displacement in the Y-channel.

Figure 6.8 shows a time lapse of the concentration field at the Y-channel intersection during the displacement process. At t=0s the mixed interface is relatively small, ~0.5mm in length, and extends into the side channel. The protrusion increases the apparent length of displacement. Progression of the interface into the side channel depends on the diffusion properties of the fluid as well as the time between switching. To account for this effect when performing calculations a 0.1% error (~400μm) was added to the displacement length.

As the interface passes through the intersection it becomes stretched and distorted. This effect is known as electrokinetic dispersion and is caused by the 2D electric field at the intersection. Near the inside corner the electric field is stronger resulting in higher EOF along the inside wall

compared to the outside wall as shown in Figure 6.9. The difference in EOF elongates the interface as it moves through the intersection resulting in a more diffuse and larger interface region inside the main channel. At t=5s the interface has passed the intersection and the mixing region is now ~9mm long and continues to grow as it moves down the channel. The diffuse interface makes it difficult to resolve the displacement time.

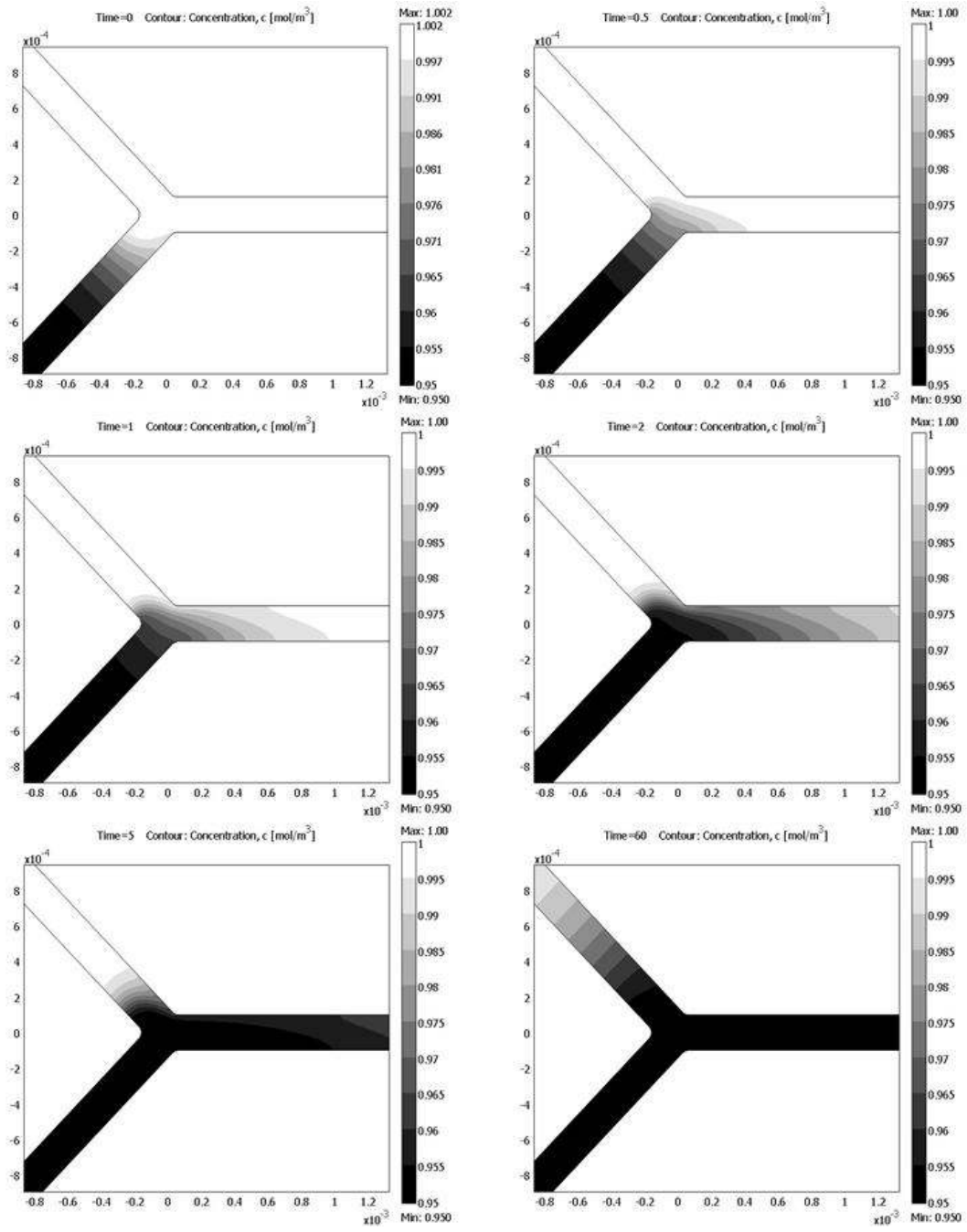

Figure 6.8 Time-lapse contour plot of the concentration at the intersection for the numerical simulation during the displacement process at times (t=0, 0.5, 1, 1.5, 2, 5, 60s). The low concentration solution (dark) replaces the high concentration solution (light).

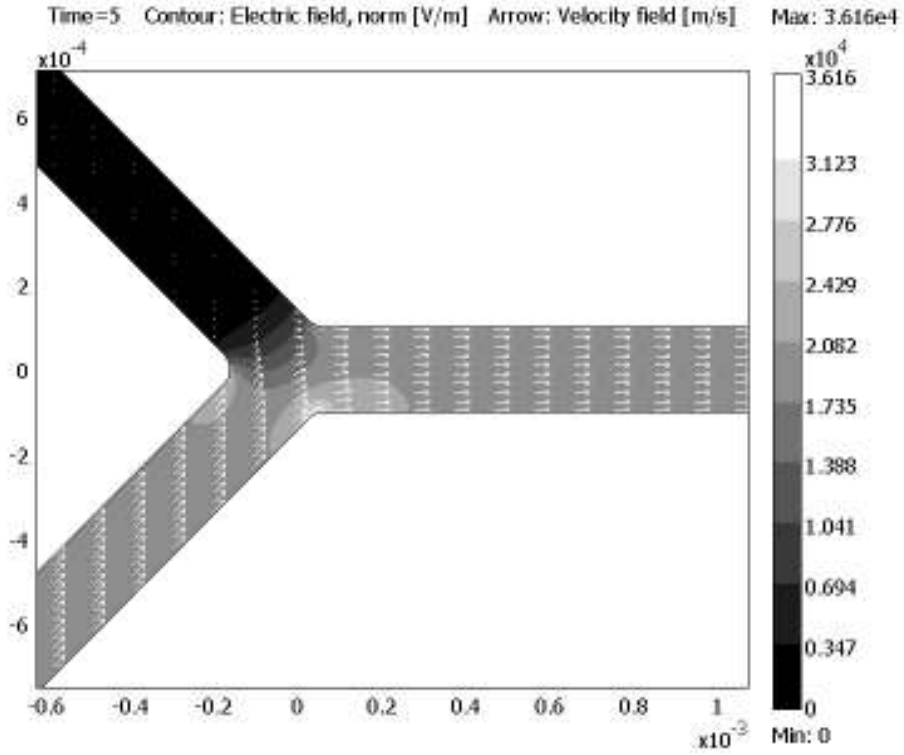

Figure 6.9 Contour plot of the electric field and arrow plot of the velocity field at the intersection for the numerical simulation during at t=5s. A strong electric field appears near the inside corner of intersection.

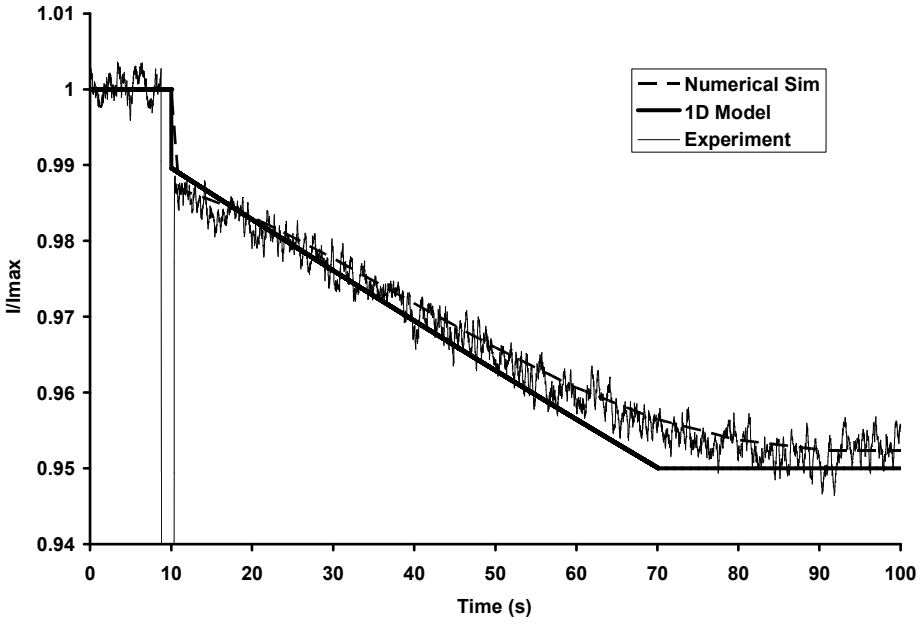

Figure 6.10 Current draw plots for 10mM KCl ($D=2x10^{-9}m^2/s$, ζ=-47mV) from the 1D model, numerical simulation and experimental results. Experimental results obtained for 10mM KCl in PDMS/PDMS chip with HEMA treatment, measured zeta potential from analysis ζ=-47mV.

The current draw from the numerical simulation was compared to the ideal case of the 1D model and experimental results obtained for 10mM KCl (ζ=-47mV) as shown in Figure 6.10. Surprisingly, the experimental and numerical models show excellent agreement which verifies the accuracy of the 2D model. Indeed the model is able to pick up the current variation at the beginning of the displacement process as the interface passes through the intersection (t=10-15s). As expected, the diffuse interface creates a very gradual transition at the end of the displacement. By looking at the chart one might estimate the displacement process to end somewhere between 70 and 90s. Comparing this to the ideal 1D model which the calculations are based on the error can be as large as 30%. In fact experimental results with KCl showed a lot of scatter within a single test when calculating the electroosmotic mobility. However, for many other fluids experiments produced well defined start and end points and the results were repeatable. The reason for this is unclear but may be explained by the fact that K^+ and Cl^- ions are very mobile and possess relatively high diffusion coefficients ($D_i = 2x10^{-9} m^2 / s$). The other solutions may contain more complex molecules that have lower diffusion coefficients; less diffusion will result in a smaller initial interface region and a smaller amount spreading during the displacement process. This analysis does show that more work can be done to optimizing the Y-channel design using numerical simulations.

6.4 Experimental Setup and Methods

In the following sections the experimental setup, fabrication and experimental methods are briefly discussed. For a more detailed description refer to Zeyad Almutairi master's thesis.

6.4.1 Fabrication of Test Chips

PDMS chips were fabricated using standard soft lithography techniques and fabrication process described in Chapter 3. In order to accommodate the various solutions to be tested, several silicon masters were fabricated with various channel heights and widths. Table 6.1 summarizes the dimensions of all masters available for the experiments. Measurements of the channel width and height represent the average value for each channel obtained from a profilometer. These dimensions are important in the subsequent analysis of the current monitoring data using the equations stated in section 6.2.

PDMS molds were fabricated from the masters via replica molding. Unless otherwise stated the standard procedure was to mix PDMS in a 10:1 ratio and to plasma treat for 40s before bonding. For PDMS/glass chips the mold was bonded to a thoroughly cleaned microscope slide. In the case

of PDMS/PDMS chips, the channel mold was bonded to PDMS coated slides that were fabricated by spin coating 1mL of PDMS (10:1) at 3000 rpm to achieve a 30μm layer. After bonding, ultra pure water was introduced into the channels and cut glass tubes were then molded over the fluidic access holes to extend the reservoir volume to 1.45 mL (the total channel volume is about 0.27μL). The filled channels were left for two days to allow for the zeta potential to stabilize before performing an experiment. A photograph of the complete chip is provided in Figure 6.11.

Table 6.1 Channel dimensions of all silicon masters used in fabricating Y-channel chips for electroosmotic mobility measurements. Right to left refers to the three designs fabricated on one master when the main channel of the Y-channel design is pointing away from the observer.

Master No.	Channel	Avg. Width (μm)	Avg. Height (μm)
Y-500-2	Right	483.75	9.002
	Middle	482.50	9.175
	Left	483.75	9.008
Y-500-3	Right	489.00	7.095
	Middle	492.00	7.120
	Left	489.00	7.100
Y-200-1	Right	193.00	10.400
	Middle	191.75	10.200
	Left	193.75	10.500
Y-200-2	Right	192.00	5.940
	Middle	192.50	5.800
	Left	193.00	5.715
Y-200-3	Right	193.00	7.000
	Middle	190.00	7.090
	Left	193.75	6.910
Y-100-1	Right	94.75	5.729
	Middle	94.00	5.813
	Left	95.50	5.736
Y-100-2	Right	93.25	7.316
	Middle	93.62	7.373
	Left	95.50	7.268

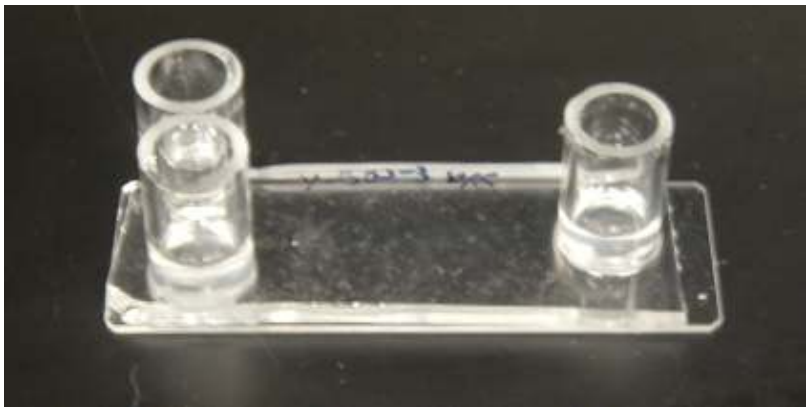

Figure 6.11 Photography of a complete PDMS/glass Y-channel chip used for current monitoring experiments.

6.4.2 Experimental Set up

A schematic of the experimental setup is presented in Figure 6.12. A high voltage power supply (SL10, Spellman) is connected to an electrical circuit containing a switch that distributes the applied voltage via platinum wires to the reservoirs. The electrical switch is used to quickly alternate the applied voltage between the two reservoirs R1, R2 while R3 is kept grounded. A custom chip holder was built to attach the electric circuit and to fix the microfluidic chip in place. A 12V fan was setup beside the holder in order to maintain a stable chip temperature during experiments. Current and voltage data was outputted from the high voltage power supply to a DAQ and recorded by a custom designed LabView program. The LabView program provides real time output of the current draw and voltage and allows the user to start and stop recording at any time. Raw data from the high voltage supply is first filtered before it is displayed on the interface; recorded data is outputted to a text file for subsequent analysis.

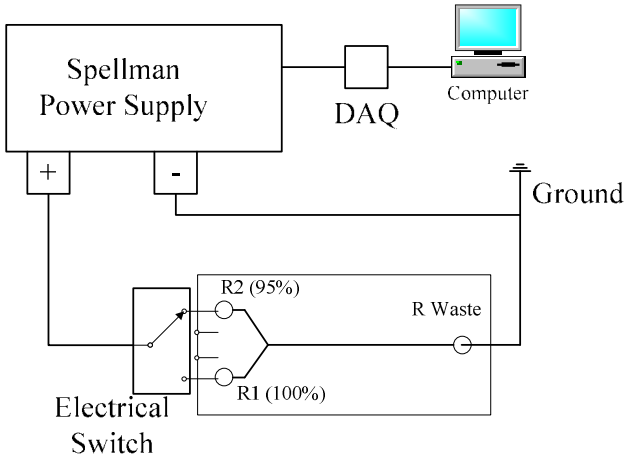

Figure 6.12 Schematic of the experimental setup for the Y-channel current monitoring experiments, courtesy Zeyad Almutairi.

6.4.3 Experimental Procedure

The first step in performing an experiment is to determine the appropriate master for fabricating the test chip. The electrical conductivity of the test solution is measured using the conductivity meter and probe and the expected current draw is then calculated using the following equation:

$$I = \frac{V}{R_e} = \frac{V \cdot A_c \cdot \lambda_b}{L} \qquad \textbf{(6.13)}$$

Dimension from the masters supplied in Table 6.1 are inputted into the above equation until the current draw falls between 2-10uA for the applied potentials. Once the master is chosen a chip is fabricated using the methods described in section 6.3.1. Two solutions of the test liquid are then prepared carefully with a concentration difference of 5%. Any fluids stored in the refrigerator must be brought back to room temperature before testing. Immediately before an experiment the electrical conductivity and pH of the two solutions in the bottles and in the reservoirs was recorded. All data pertaining to the fabrication of the chip, experiment and fluids was recorded in a specific data sheet for the experiment.

Prior to starting the experiment symmetry between the two side channels was verified. This was done by first filling all the reservoirs with the high conductivity solution and monitoring the current draw from each channel (R1→R3 and R2→R3). Under ideal conditions the monitored current was identical in either direction of the electric field validating that the chip was defect free. The three reservoirs were then filled with new solutions where R1 and R3 contained the high concentration solution, and R2 was filled with the lower concentration solution. The experiment started by applying a voltage to (R1→R3) until a steady state was reached indicating that the high conductivity solution had fully replaced the fluid in the straight portion of the Y-channel. The voltage difference was then applied in the second configuration (R2→R3) by changing the electrical switch direction. The lower concentration solution was then pumped through the channel displacing the high concentration solution and the current changed accordingly. The full replacement of the solutions in the channel was recognized by reaching a new steady state. Several displacements were performed by repeating the process for a single applied voltage. After a set of switches was completed the temperature, pH, and electrical conductivity of the solutions in each reservoir was recorded. The experiment was then repeated for the next applied voltage. A typical experiment for a solution involved 4 switches at 4 different applied voltages for a total of 16 measurements.

6.4.4 Data Analysis and System Errors

To analyze the data a custom Matlab program was written. After importing the raw data and master dimensions a GUI allows the user to select each displacement for further analysis as shown in Figure 6.13. Each region of the displacement process (pre-injection, post-injection, displacement) is defined by entering the start and stop times. In the pre and post injection times the current difference is determined by averaging the data points within that region. In the displacement region a linear regression is applied to determine the slope and to calculate the electroosmotic mobility using the two calculation methods. This process is repeated for subsequent displacements. Note that the first few displacements are ignored since the chip is being primed and the displacement length is not well defined. An error analysis is also included in the program to account for bias and precision uncertainties in the measurements. Typical uncertainties in the calculations lie between 4-6%. A final GUI then appears which provides a summary of the calculated zeta potential, electroosmotic mobility and surface conductivity for each displacement. The user can then select which data sets to keep and output to a text file.

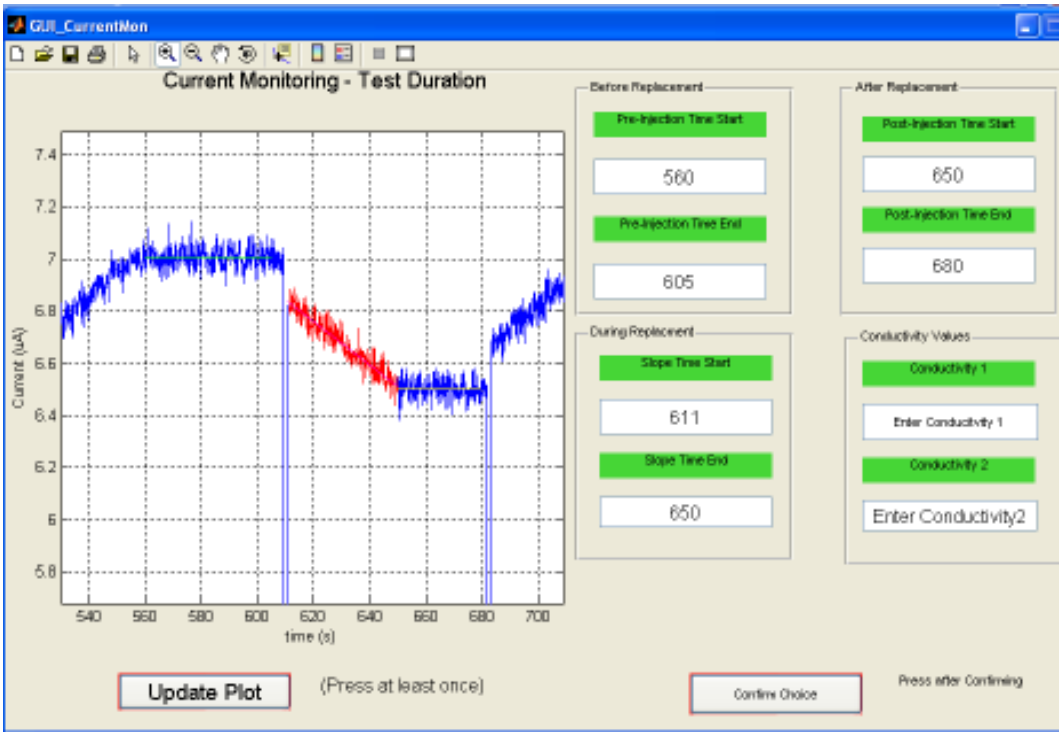

Figure 6.13 Matlab GUI used to analyze the current monitoring data. The user selects the pre, post and displacement times for analysis.

6.5 Experimental Results

Experiments were performed with the Y-channel design to determine the electroosmotic mobility of a variety of fluids and surface treatments. Tests were conducted to verify the performance of the Y-channel design by imaging the switching process. Measurements obtained from the Y-channel were validated by comparing with corresponding straight channel measurements and data obtain from literature. Afterwards experiments were performed on a variety of fluids relevant to bio and chemical analysis in microfluidic systems. In addition several surface treatments were investigated to improve the electroosmotic mobility of PDMS for the EO pump design.

6.5.1 Visualization of Switching Process

Fluorescence microscopy was used to visualize the switching process by adding fluorescein dye (10mM) to 1X TAE. Images were taken at the intersection as the fluid in R2 (non-dyed) replaces the fluid in R1 (dyed) for an applied potential of 1000V as shown in Figure 6.14. Prior to switching (t=0s), the dye interface extends approximately 250μm into the other side channel. After the electric field is switched the displacing fluid travels primarily along the inside wall and the interface is stretched diagonally because of the asymmetric electric field. Comparing the experimental results with the numerical results of Section 6.3.2 the progression of the interface in both cases is similar but there is less diffusion in the experiment results. This can be attributed to the fact that fluorescein possesses a diffusion coefficient ($D=4.6x10^{-10}m^2/s$) one order of magnitude lower than KCl. In addition, fluorescein is negatively charged and is therefore influenced by the applied electric field. Consequently, the dye movement may not accurately represent the actual progression of the KCl interface and the results should be considered qualitatively. This is especially true in monitoring the progression of the interface down the main channel since the velocity was found to be only 50% of the anticipated value from current monitoring measurements. The images verify that that the switching process is successful and the fluids are effectively displaced in the main channel.

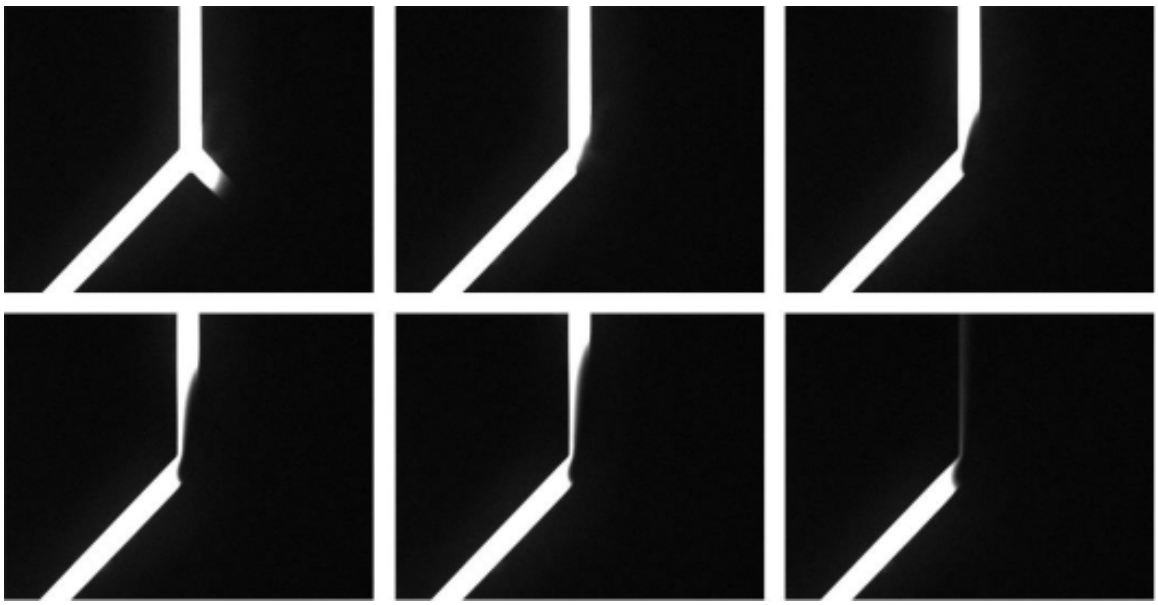

Figure 6.14 Time-lapse images of the displacement process with 100µM fluorescein dye added to 10mM KCl solution for an applied potential of 1000V. Images are taken at approximately t=0, 400m, 600ms, 1s, 2s, 10s after the switch.

6.5.2 Validation of the Y-channel Design

In order to validate the measurements obtained with the Y-channel design, results were compared to published data obtained using conventional straight microchannel designs. Directly comparing results is not easy since the fabrication techniques used by other researchers are often unknown or do not match the methods used in this study. This is especially true of plasma treatment since most published results do not include the exact dose or treatment time. Furthermore, it is well known that PDMS quickly loses the surface charge generated during the treatment eventually reverting back to its natural hydrophobic state. During this process the electroosmotic mobility of the surface can decrease significantly in the first few hours after treatment. Consequently, it is important to know the time between treatment and testing to perform a valid comparison.

The work produced by Venditti *et al.* (2006) provided the closest comparison in terms of fabrication methods and measurement techniques. This group used the current monitoring method to measure electroosmotic properties in both PDMS/PDMS and PDMS/glass chips. Straight channel chips with comparable dimension to the Y-channel (300µm W x 8µm H) were fabricated using soft-lithography techniques. In fact, much of the fabrication equipment and testing apparatus is the same (i.e. plasma equipment, high voltage supply). Table 6.2 summarizes the comparison between the results obtained by Venditti *et al.* (2006) and those obtained using the Y-channel chip. Also included is a comparison of 50mM $NaHCO_3/Na_2CO_3$ measurements taken

using a straight channel and Y-channel in the lab. There is good agreement between results over all cases which validates that the Y-channel design can produce reliable measurements with a good degree of accuracy.

Table 6.2 Comparison of electroosmotic mobility measurements obtained with the Y-channel design and those published by Venditti *et al.* (2006). For 50mM $NaHCO_3/Na_2CO_3$ the reference value refers to a straight channel measurement obtained internally.

Solution (channel type)	**Reference ζ (mV)**	**Y-Channel ζ (mV)**
50mM $NaHCO_3/Na_2CO_3$ (PDMS/glass)	-59.12 *	-56.79
1mM KCl (PDMS/Glass)	-88.32	-92.26 ± 4.63
10mM KCl (PDMS/Glass)	-54.84	-49.89 ± 1.45
1X TE (PDMS/Glass)	-68.13	-66.09 ± 3.67
1X TBE (PDMS/Glass)	-48.05	-49.19 ± 1.30

6.5.3 Results for Various Solutions and Surface Treatments

A number of different solutions relevant to the microfluidics community were considered for testing. These solutions included simple electrolytes, buffers for DNA electrophoresis applications [Dia *et al.* (2003); Stellwagen *et al.* (2000)], cellular analysis and cell culture [Kim *et al.* (2007), Khademhosseini *et al*. (2005)]. Furthermore, the influence of the substrate material on electroosmotic mobility measurements was measured by testing solutions in both PDMS/PDMS and PDMS/glass chips. The results are presented in Figure 6.15 where zeta potential values represent the average result of all experiments for a particular solution. In some cases, as many as 80 displacements were analyzed for a single solution. Calculations by both methods are typically in good agreement with each other; however, the slope method tends to predict slightly higher zeta potentials. As expected, solutions with higher concentrations of ions have lower zeta potentials, for example, the zeta potential of 1mM KCl and 10mM KCL is ζ~85mV and ζ~50mV respectively. This point is further enhanced by considering 1XPBS which contains a high salt content (137mM NaCl) and has a zeta potential of ζ~20mV.

In hybrid microchannels, such as PDMS/glass channels, the heterogeneous wall properties of the channel create a non-uniform velocity profile under EOF. To a certain degree the average electroosmotic mobility of the hybrid channel can be estimated as the weighted average of the properties of the two different materials [Bianchi *et al.* (2001)]. In terms of the current monitoring method, the flow rate through the channel can be approximated by the average electroosmotic mobility; however, the 3D velocity profile will distort the interface increasing the transition time at the start and end of the experiment. This effect becomes more prominent as the difference in electroosmotic mobilities increases. In experiments with PDMS/PDMS and PDMS/glass chips measurements for both substrates were similar for all solutions. This may indicate that the surface of plasma treated PDMS closely resembles that of glass which agrees with results published by Ren *et al*. (2001). Although, Venditti *et al.* (2006) and Spehar *et al.* (2003) documented lower zeta potentials in PDMS/PDMS devices as compared to PDMS/glass devices. The reason for this discrepancy is unclear but probably stems from differences in fabrication of the PDMS most notably in the curing time of PDMS and plasma treatment of the glass substrate.

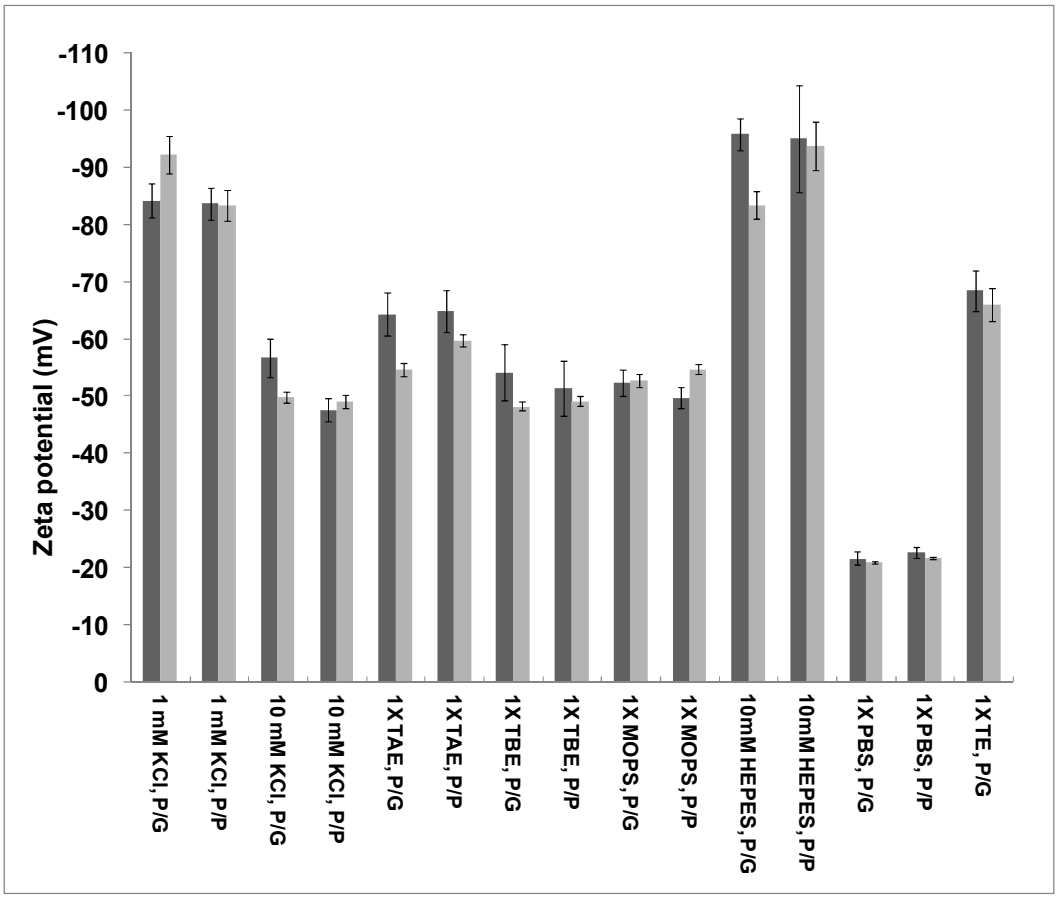

Figure 6.15 Zeta potential measured using the Y-channel design for various fluids in PDMS/PDMS (P/P) and PDMS/glass (P/G) chips. Dark columns are for calculations using the slope method and light the total length method. Error bars represent a 90% confidence level.

Surface conductivity calculations were performed during all experiments but the results were found to be inconclusive. The reason for this is that the present measurement system does not posses the sensitivity required to measure the current draw accurately. The internal ammeter on the high voltage supply has an accuracy of 0.1% PP or an equivalent ±10uA error which essentially nullifies any low current measurements. To overcome this problem a high accuracy picoammeter was purchased to replace the internal ammeter in the measurement system; however, experiments with the picoammeter were not finished prior to the completion of this thesis.

6.6 Recommendations

Future work should focus on improving the design of the Y-channel through numerical simulation. Particular focus is needed on designing the intersection to minimize the amount of electrokinetic dispersion as the interface passes through the intersection. Surface conductivity measurements with the new picoammeter and Y-channel design ought to be completed in order to further characterize the electrokinetic properties of each fluid/surface pairing. Finally, it is recommended that additional solutions be continuously tested in order to develop a database of fluid properties that can be used in the development of future microfluidic designs.

Chapter 7

Design, Fabrication and Operation of Electroosmotic Pump

In this chapter, the design and fabrication of the electroosmotic pump (EO pump) developed as part of this thesis are described. Utilizing 1D-circuit equivalency modelling an integrated EO pump was designed to achieve high flow rates for pumping cell culture solutions. The soft lithography fabrication techniques developed in Chapter 5 are used to build the EO pump. Two types of pumps were developed based on commercial ion exchange membranes and *in situ* fabricated gel membranes. Fabrication techniques for both these designs are presented within this chapter. The performance of the pumps was characterized to determine the flow rate for an applied current. Several issues encountered with the fabrication and operation of the pumps is discussed and resolutions are presented. The final design achieved at the end of the development process was incorporated in the subsequent microfluidic network for cell culture.

7.1 Background

This section provides a brief review of the background and principals for the use of EO pumps in cell culture. There are two commonly used pumping methods for microfluidic chips which are pressure driven flow and electroosmotic flow (EOF). Most microfluidic chips previously developed for cell culture applications use a single syringe pump to provide pressure driven flow [Kim *et al.* (2006); Hung *et al.* (2005); Wu *et al.* (2006)]. Although pressure driven flow has been successfully applied in this area, there are several disadvantages. For independent control of multi-media solutions multiple syringes must operate in unison which can be difficult to attain. In addition, valving and switching with an external pressure network has a much longer reaction time due to the dead volume of the components and elastic nature of the tubing and PDMS microchannels. Thus it is difficult to obtain fine spatial and temporal control of the fluid within the microchannel network.

As discussed in Chapter 2, EOF pumping is a compact method of pumping fluids in microfluidic chips where flow rate and direction can be accurately controlled by simply manipulating applied voltages at the reservoirs. However, EOF cannot be directly applied to cell culture applications as it affects the microenvironment surrounding a cell. For instance, the high electric field typical of EOF may cause electroporation creating tiny pores in the cell membrane and allowing for foreign

mater to enter the cell [Weaver (1995)]. In addition, joule heating can be problematic since many cells require a stable temperature to survive (e.g. mammalian cells require 37°C). Furthermore, attached cells may experience a higher than normal shear stress which may alter their morphology.

These problems can be solved by utilizing the advantages of EOF in electroosmotic pumps (EO pumps). These pumps generate an induced pressure driven flow from EOF flow. EO pumps provide pulse free flow, almost instant flow control, and precise movement of minute volumes of fluid (μL-pL). The integration of EO pumps on-chip also opens up the possibility of multi-fluid control on the chip without valves. Most importantly, with EO pumps applying an electric field through the cell region can be avoided while still maintaining the advantages of EOF flow.

7.2 Planar EO Pump Fundamentals

A detailed description of the theoretical and operation of planar EO pumps has been previously provided by Chen and Santiago (2002). Therefore, this section will only provide a review of the fundamentals for EO pump design. Consider the simplified schematic of a planar EO pump shown in figure 7.1. This configuration will be referred to as the 1-electrode-channel (1-EC) EO pump. A membrane connects the side channel containing the electrode reservoir to the main flow channel. This membrane allows for an electrical connection with the working fluid but prevents any fluid flow to the side channel. An electric field is applied between the inlet of the pump and the membrane channel generating EOF flow in CH 1. Consequently, a pressure builds up at the end of the electric field which then pumps the fluid down the outlet channel, CH 2.

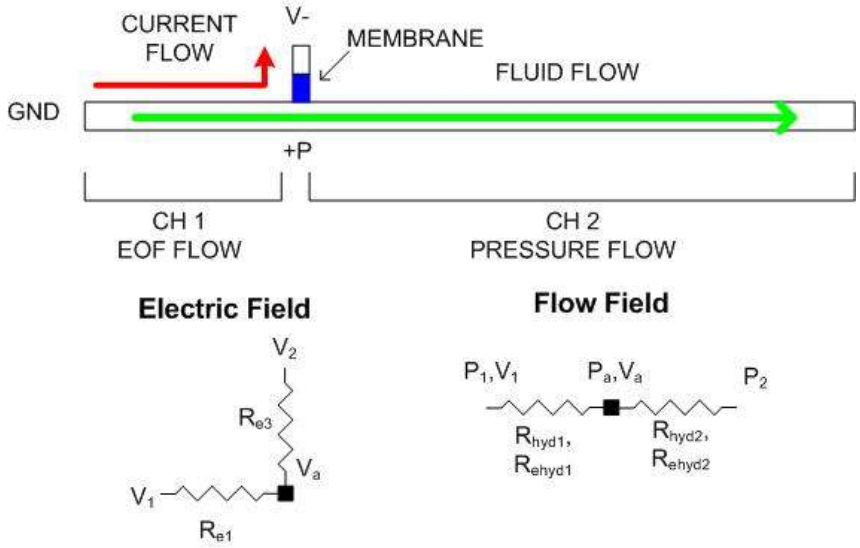

Figure 7.1 Schematic of the 1-EC pump design describing the electrical and flow fields.

Applying the 1-D circuit equivalency model to the network the flow rate is given as (calculations available in Appendix A):

$$Q = \frac{(V_1 - V_a)}{R_{ehyd1}} \left(\frac{R_{hyd1}}{R_{hyd1} + R_{hyd2}} \right) \tag{7.1}$$

In these calculations it is assumed that the EDL is thin compared to the smallest channel dimension.

One of the disadvantages of the 1-EC design is that one of the electrodes is placed in the fluid reservoir that contains the working fluid. Electrolysis will occur in this reservoir changing the properties of the solution such as pH and electrical conductivity. This will effect the operation of the pump since the zeta potential is pH dependent. A solution to this problem is the 2-EC design shown in figure 7.2 which contains two membrane channels and effectively isolates the electrodes from the working solution delaying or preventing any electrolysis effects.

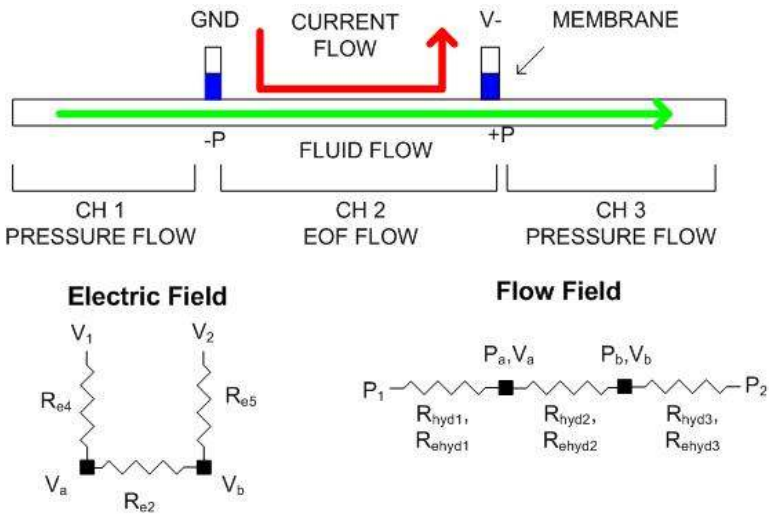

Figure 7.2 Schematic of a 2-EC EO pump design describing the electric and flow fields.

Again an electric field is applied in a limited region of the pump generating EOF flow (CH2). Due to continuity an internal pressure is generated which draws fluid *via* a vacuum into CH1 and drives the fluid *via* positive pressure out CH3. The fluid flow in CH2 is actually a combination of EOF flow and back pressure flow. By placing the cell chamber in the inlet region (CH1) the electric field will be separated from the cells. As well, the medium will first flow over the cells and through the EO pump eliminating any changes in the medium as it experiences EOF. Therefore, this configuration will allow for the integration of EO pumps within a microfluidic cell culture chip.

The flow field equations for the design are (calculations are provided in Appendix B):

$$Q = \frac{(V_a - V_b)}{R_{ehyd2}}\left(\frac{R_{hyd2}}{R_{hyd1} + R_{hyd2} + R_{hyd3}}\right) \quad \textbf{(7.2)}$$

$$R_e = \frac{L}{\mu_e wh},\ R_p = \frac{12\mu L}{wh^3} \quad \textbf{(7.3)}$$

To achieve a high flow rate for low voltages the EOF flow carrying channel must have a high hydraulic resistance compared to the inlet and outlet channels (CH1, CH3) but a low electroosmotic resistance. This is accomplished by designing an EOF flow channel that is short, wide and very shallow [Chen and Santiago (2002); Brask (2003)]. In addition, the side channels should be large so that they have a low electrical resistance which will minimize the electric field losses in these channels. The maximum efficiency of a planar EO pump can be approximated by the following equation (derived in Appendix B):

$$\eta = 3\left(\frac{\mu}{\lambda_b}\right)\left(\frac{\mu_{eof}}{h_{eof}}\right)^2 \quad \textbf{(7.4)}$$

As the equation above shows, the efficiency is largely tied to the working fluid through the viscosity, electrical conductivity and electroosmotic mobility. Typical efficiencies of EO pumps are lower than 1%. The ideal solution for an EO pump is one with a low electrical conductivity and high electroosmotic mobility suggesting the use of very low concentration electrolytes or pure water. However, these conditions are not met with cell culture solutions. Cell culture medium is saline based containing high ionic concentrations (e.g. 0.1M NaCl) which magnify the problems associated with EO pumps:

- reduced pumping rate due to the low zeta potential of the liquid/surface interface requiring higher electric fields to obtain modest flow rates,
- significant joule heating due to the high electrical conductivity of the solution,
- large amounts of electrolysis at the electrodes which changes the properties of the solutions (pH, bulk conductivity) reducing stability and long term operation of the pump,
- polarization and bubble formation causing instability in the applied electric field

All the challenges discussed above are coupled together during operation making the evaluation of EO pumps in cell culture even more difficult. Methods that were used to resolve these issues are presented throughout this chapter.

7.3 Fabrication of EO Pumps

The main difficulty in fabricating integrated EO pumps on-chip is incorporating the membrane system which separates the electrode from the working solution. Many stand alone EO pumps use commercial ion selective membranes [Brask *et al.* (2005); Liu *et al.* (2003); Wang *et al.* (2006)]; however, integrating these membranes into a PDMS chip is quite difficult due to swelling and sealing issues. In this work several attempts were made to integrate these membranes into the PDMS device with little success. The methods tried and problems encountered are discussed in Section 7.2.2. Due to this failure a different method was used involving the fabrication of gel salt bridges inside the microchannel network using a photo-polymerization technique [Takamura *et al.* (2003)]. Greater success was achieved with this method and the fabrication details are presented in Section 7.2.3.

7.3.1 General Fabrication Notes

All masters were fabricated using the multi-level techniques previously described in Chapter 5. As well, standard soft-lithography techniques for building the EO pump chips were followed. Surface modifications to the PDMS channels were attempted and are discussed in more detail in Section 7.7. Dimensions stated in the following sections were obtained by measuring the masters using a contact profilometer.

7.3.2 Ion Exchange Membrane

Integrating a commercial ion exchange membrane reliably into a PDMS device is a challenging task. The main difficulty is sealing the membrane to the PDMS because these membranes tend to increase in size substantially (10-30%) when wetted [DuPont Fuel Cells]. Since PDMS is a flexible material it is unable to withstand the expansion and leaks form around the membrane. Still several attempts were made to integrate commercial ion exchange membranes into PDMS a device. The details of the processes attempted are described below.

The ion selective membrane used for this application is Nafion (N-115, Fuel Cell Store) which is a cation selective membrane typically used in fuel cell applications. Circular pieces were punched from the film using a hole punch. In the first attempts the membrane was bonded directly over the reservoir using PDMS as a mortar for sealing (see Figure 7.3). Afterwards the entire mold was bonded to the glass substrate and filled with water following the usual soft lithography fabrication procedure. However, several issues arose with this method. First, when using the mortar the PDMS would often coat the membrane eliminating any electrical connection with the fluid.

Second, when filling the microchannel a small air bubble would be trapped under the membrane (see Figure 7.3) which would also cut off any electrical connection. Several methods were attempted to remove the trapped bubble by vacuum degassing or high pressure pumping, however, none of these methods worked consistently. If by chance the bubble was removed, the mortar was still not able to withstand the swelling of the membrane.

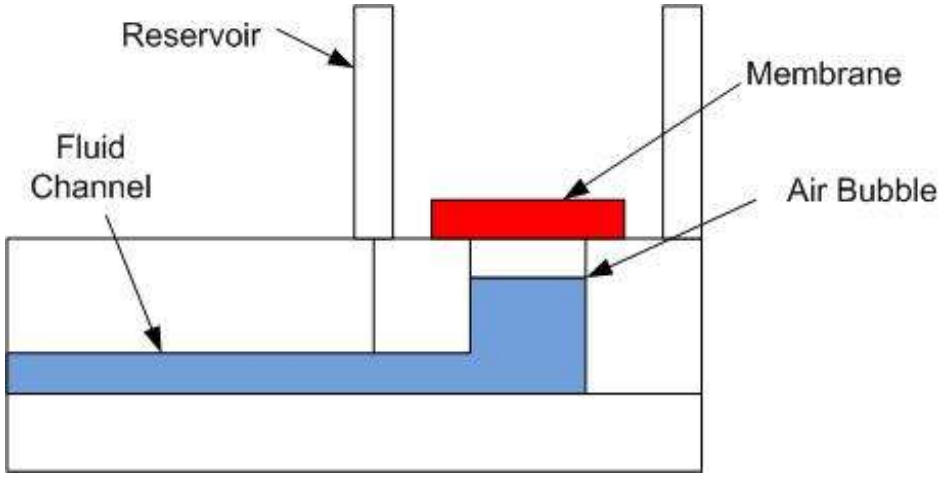

Figure 7.3 Diagram of Nafion membrane fabrication. Membrane is placed over top of the reservoir connecting to the microchannel. During this process a bubble would often get trapped under the membrane eliminating any electrical connection with the fluid below.

In response to these problems, two additional methods were tried to bond the membrane over the reservoir: double sided tape and plasma bonding. Of these methods plasma bonding provided the most consistent results and produced a strong (but not permanent) bond with the PDMS. Additional measures were also taken to reduce the amount of bubble entrapment. Smaller holes were punched (<1mm) using a Luer needle stub for the membrane reservoir. This decreased the wetting surface of the membrane so there was less overall swelling and increased the bonding surface. In addition, the fabrication procedure was slightly altered. The Nafion membranes were soaked in DI water for 24hrs to allow the membranes to fully swell. The PDMS microchannel mold was bonded to the substrate and filled with water making sure that the membrane hole was filled to the top so as to reduce the possibility of trapping a bubble. Next, the membrane was removed from the water and dried with nitrogen followed by air plasma treatment for 25s. The Nafion was bonded over top of the reservoir assuring that the membrane made contact with the liquid in the reservoir. During this step the Nafion must be laid down slowly in a rolling motion to assure no air is trapped. Afterwards a reservoir was molded overtop of the membrane. In general, the success rate for fabricating a membrane was 30% and since two membranes are needed for one EO pump the overall success rate is actually quite low.

Several of these membrane devices were tested using 1-EC and 2-EC configurations. Upon operating these devices an interesting phenomena was observed. Due to the flexibility of the membrane the devices were affected by undesired pressure driven effects. For instance, a difference in liquid level heights between the two membranes would cause a pressure difference that would deflect the membrane. This resulted in pressure driven flow into or out of the electrode channel. This effect was most evident in the transient operation of the pump during start up and shut down. Using fluorescent visualization with beads added to the solution the flow field was monitored during these transient points. Figure 7.4 presents a schematic of the flow phenomenon during these times. Initially the pump is turned off and there is no flow. Then the electric field is applied between the two membrane reservoirs. During the first 30s the majority of the incoming fluid actually travels into the membrane channel. This causes the membrane to deflect until a force balance is reached between the pressure in the microchannel and the membrane tension. After a short time a steady state is reached and the incoming fluid travels as expected down the EOF channel (CH2) and through the outlet (CH3). Alternatively, when the power is turned off the membrane relaxes and induces flow out of the membrane channel and back into the inlet. In essence, the membrane acts as a fluidic capacitance element which causes a time delay in the response of the EO pump. Therefore, for quick switching or changes in applied electric field the membrane pump will have a slow response that must be considered during operation. Due to the fabrication and operational difficulties the Nafion based EO pump was abandoned and more focus was put towards the gel based design.

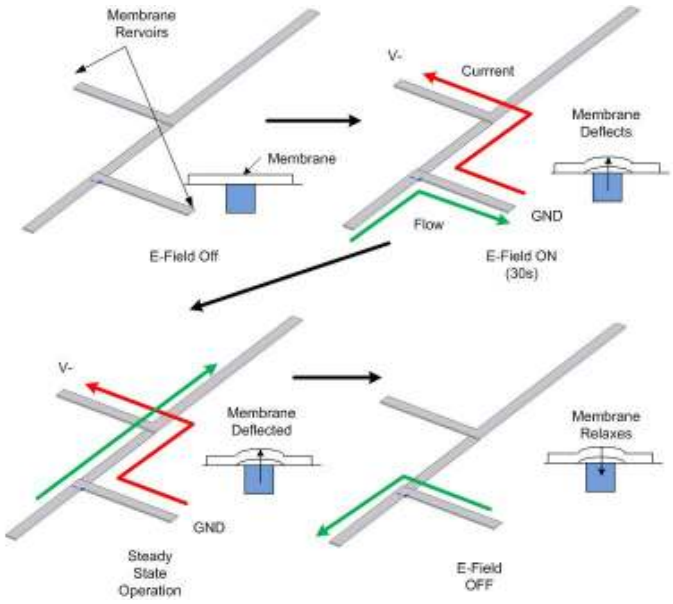

Figure 7.4. Schematic of the transient operation of Nafion/PDMS EO Pump device.

7.3.3 Gel Salt Bridge

The gel salt bridge was fabricated within the microchannel network following the general procedures outlined by Takamura *et al. (*2003) and Kohlheyer *et al.* (2006), as presented in figure 7.5. Takamura *et al.* (2003) used this technique to develop several types of EO pumps in glass chips. Brask *et al.* (2003 1, 2003 2) performed a numerical analysis of these pumps and found their performance to be much lower than the experimental results provided by Takamura *et al.* (2003) at higher pressures. One of the possible explanations was leakage around the gel due to poor sealing. To improve the fidelity of the gels used in this work an additional treatment was applied to help covalently bond the gel matrix to the PDMS channel wall. The procedure is as described below and is presented in figure 7.5.

After bonding, the chip is filled with a Bind Silane solution containing 0.4% (v,v) Bind-Silane (3-(trimethoxysilyl)propyl methacrylate, Sigma Aldrich) , 0.4% (v,v) acetic acid (ph 3.5). The treatment promotes bonding between the polyacrylamide gel (PAA) and the PDMS microchannel wall [Zeng *et al.* (2006); Kohlheyer *et al.* (2006); Sigma Aldrich]. The plasma treatment is actually required as a precondition to bonding the Bind-Silane to the PDMS. The plasma treatment creates silanol groups on the PDMS which provide reaction sites for the Bind-Silane molecule. Bind-Silane is a bifunctional molecule that participates in the PAA reaction and creates a bond between the PAA gel and PDMS/glass. The treatment increases the mechanical stability of the gel and eliminates voids between the gel and microchannel wall.

Immediately after treatment a solution of 18% acrylamide, 3% N-methylenebisacrylamide and 3% 2-dimethoxy-2-phenylacetophenone (Sigma Aldrich) in isopropanol (IPA) is flushed through the chip. Regions where the gel is to be located are masked off with tape on the underside of the chip. The chip is then placed on the microscope stage and the regions are exposed using the Xe(Hg) burner through the 20x objective lens. The photo-polymerization was monitored *in situ* with the CCD camera until it was complete. Each gel salt bridge area was fabricated individually since only one gel area could fit in the field of view. Flood exposure with the UV exposure system was also tried but this resulted in exposure outside the desired areas. A photograph of a complete gel within the EO pump is shown in figure 7.6.

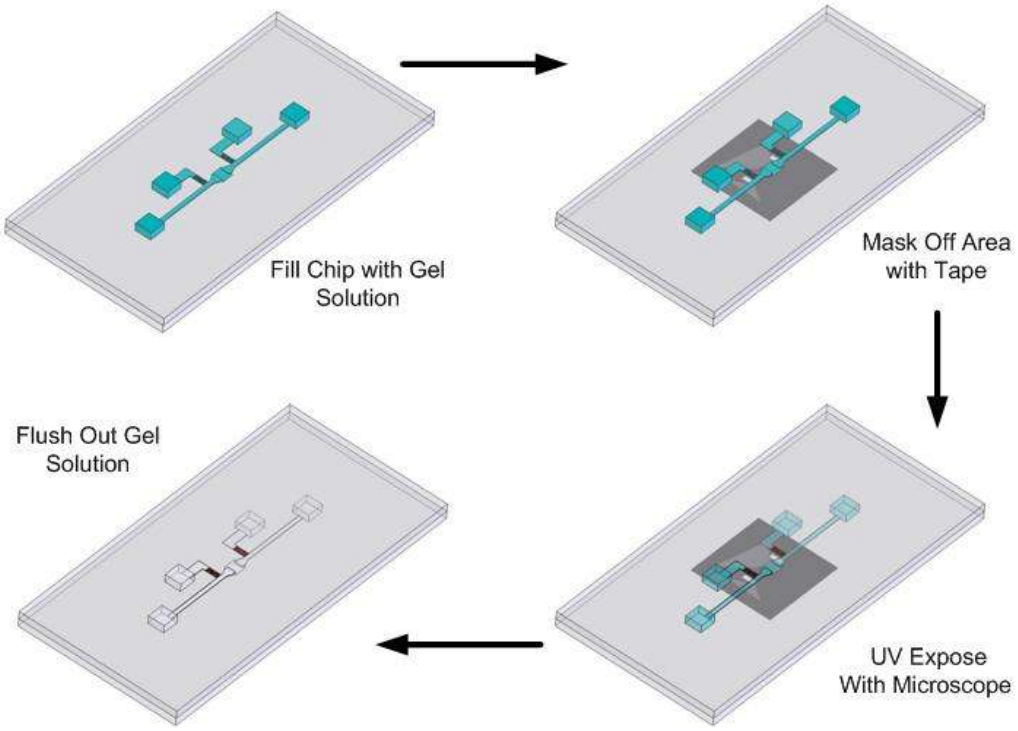

Figure 7.5 Diagram of the procedure for fabricating gel salt bridges within the microchannel network.

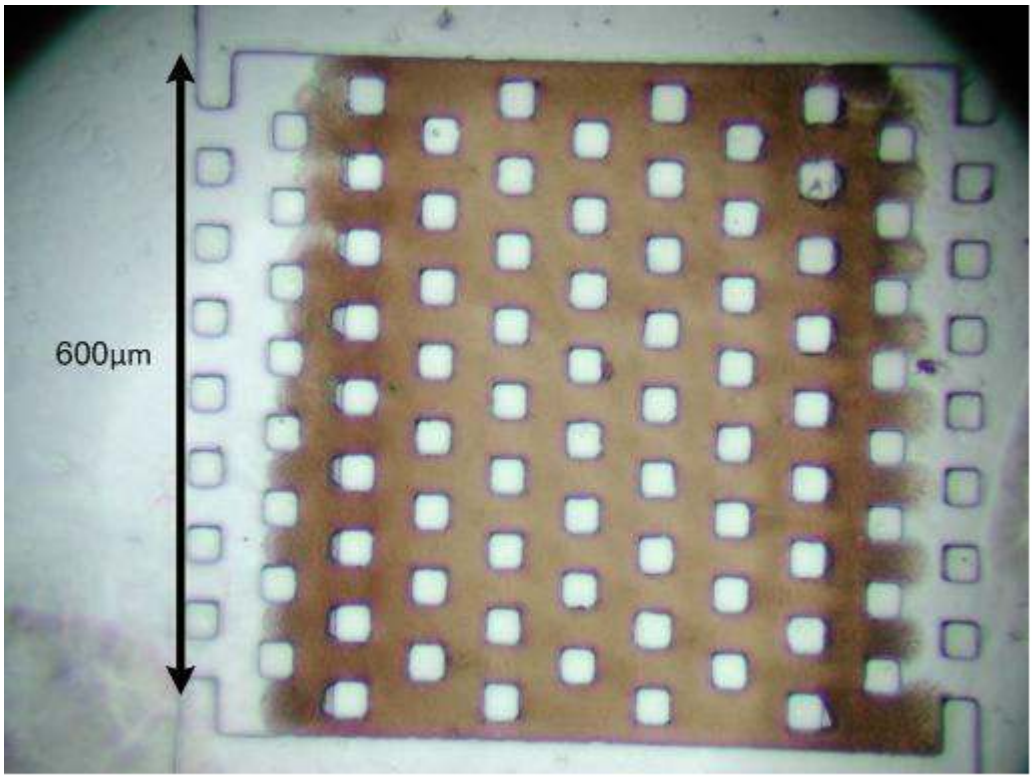

Figure 7.6 Phase contrast image of gel salt bridge integrated into the chip using a photopolymerization technique. PDMS posts in the mold help anchor the gel when exposed to high pressure differentials.

Afterwards the chip is flushed with 10% (v,v) IPA solution using the syringe pump to remove residual monomer. A total of 1mL (~200 channel volumes) of 10% IPA solution is pumped at 20µL/min. The IPA solution penetrates through the gel and washes out any residual uncross linked monomer. The chip is subsequently flushed at 10uL/min with 0.5% NaOH solution to remove residual Bind-Silane attached to the channel walls [Kohlheyer *et al.* (2006)]. This is followed by another flushing with ultra pure water. The total amount of liquid flushed through the system is approximately 1.5-2mL Modified female Luer type connectors were then attached to the PDMS as discussed in Chapter 5.

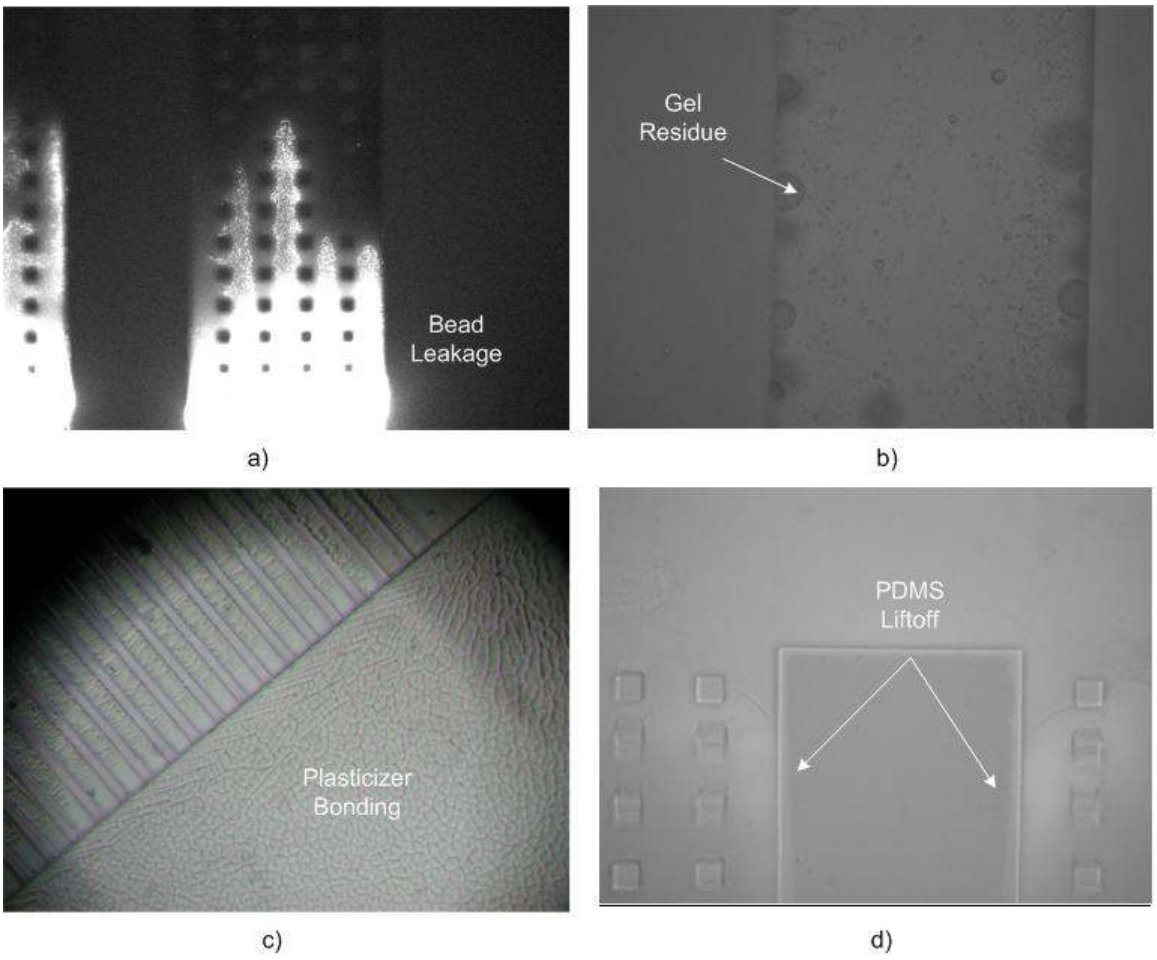

Figure 7.7. Fabrication issues with the gel salt bridge fabrication (a) poor gel to PDMS bonding without Bind-Silane treatment (b) gel solution residue left behind due to insufficient flushing (c) plasticizer residue from Tygon tubing covalently bonded to the PDMS surface (d) PDMS lift-off from glass substrate after flushing with 10%NaOH (v/w).

The fabrication process described above was optimized through several iterations. Some of the problems encountered during this process are shown in Figure 7.7. At first, the Bind-Silane treatment was not incorporated into the fabrication process which resulted in gels with poor fidelity. Without the Bind-Silane treatment the gel was not anchored to the PDMS and the gel would move under an applied electric field. Also, a gap was created between the gel and PDMS which allowed for leakage around the gel as shown in Figure 7.7a. The figure shows fluorescent beads penetrating over and under the gel during EO pump operation. Once the Bind-Silane treatment was incorporated no bead penetration was seen. As well, insufficient flushing would leave behind gel residue in the channel as shown in Figure 7.7b. This problem was solved by extending the flushing time. Tygon (R-1305) tubing was initially used to connect the syringe to the device. After several fabrication attempts peculiar "spider web" features were seen on the surface of the PDMS microchannels (see Figure 7.7c). It turned out that the tubing is incompatible with several alcohols such as isopropanol and ethanol. These alcohols extract the plasticizer which makes the tubing flexible. During flushing the extracted plasticizer was deposited into the device and bonded with the PDMS surface. To solve this problem the Tygon tubing was replaced with chemically inert Teflon tubing. In addition, a strong base solution (10% NaOH w/v) was initially used to remove residual Bind-Silane. However, it was found that this strong base solution degraded the PDMS/glass bond and caused leakage around the channels and gels as shown in Figure 7.7d. Consequently, the solution was diluted to 0.5% and this problem did not appear.

7.4 Flow Rate Measurements

The flow rate of the pumps was measured using particle velocimetry as discussed in Chapter 3. Five successive images were taken at the mid channel height in a location where there was only pressure driven flow. The maximum velocity of a number of beads was calculated using the tracking option in the software and this process was repeated for several sets of images. This velocity represents the centerline flow velocity and was used to estimate the flow rate through the equation for Poiseuille flow between parallel plates:

$$Q = \frac{3}{2} V_{\max} wh \qquad \textbf{(7.5)}$$

In actuality, the flow is not ideally Poiseuille flow since the aspect ratio of the pressure driven channel is ~1:6; however, this calculation serves as a reasonable approximation. Additionally, there are other errors that occur in the measurement. Most notably, determining which particles

are traveling along the centerline is quite difficult. Therefore, the estimated error of the flow rate measurements is 5-10%.

7.5 Design Iterations

Testing and evaluation of several iterations of the EO pump design were required before successful and repeatable operation was achieved. These modifications focused on improving the flow rate and the fabrication process. As part of the design process numerical simulations and 1D models were developed to provide guidance. Characteristics of each design are presented in the following subsections

7.5.1 Preliminary Designs 1-EC and 2-EC

The first design developed are the 1-EC and 2-EC channel designs as presented in Figure 7.8. These designs were initially used to test the fabrication and operational procedures of the EO pumps. Both designs contained an EOF section that is 5mm long, 500µm wide and 5µm high. The inlet and outlet channel height is 75µm in order to reduce the hydrodynamic resistances and improve the overall flow rate as determined by Eqns. 7.1 and 7.2. Other relevant dimensions are provided in Figure 7.8. In addition, these designs were used to validate the 1D modeling presented in Section 7.1 by comparing the numerical results with experimental data. To this end experiments were performed with 1X TBE (gel salt bridge design) and the flow rate versus applied current trend was determined for the two pumps as shown in Figure 7.9. Notice that for both pump design configurations the performance is similar. Furthermore, there is good agreement between the experimental results and the 1D model which validates their use an effective design tool for planar EO pumps. As discussed by Brask (2003) the 1D model provides good results when the ratio between inlet/outlet channel depth and EOF channel depth ratio is less than 30%. If the ratio is comparable, then there will be large losses in pressure and electric field at the junction between the inlet/outlet channel and the EOF channel. In the following design, the ratio of all chips lies between 5%-7%, thus the 1D model should be valid.

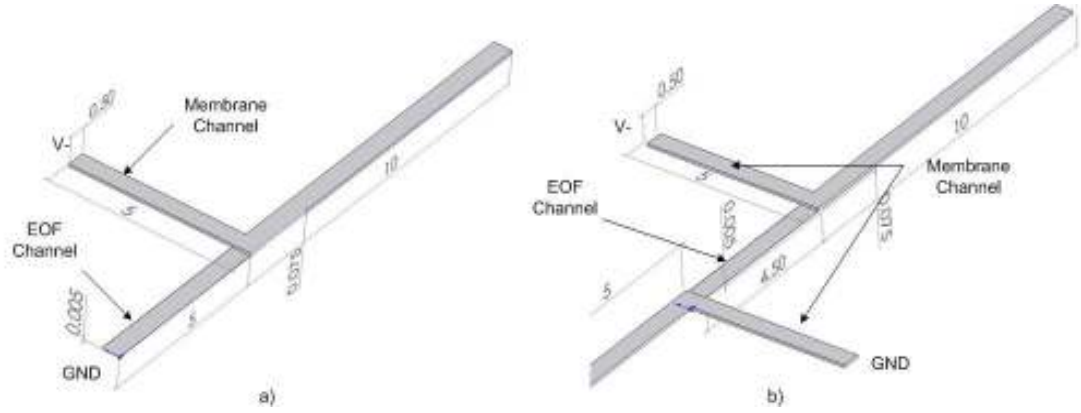

Figure 7.8 3D models of the 1-EC and 2-EC pump designs initially fabricated and tested.

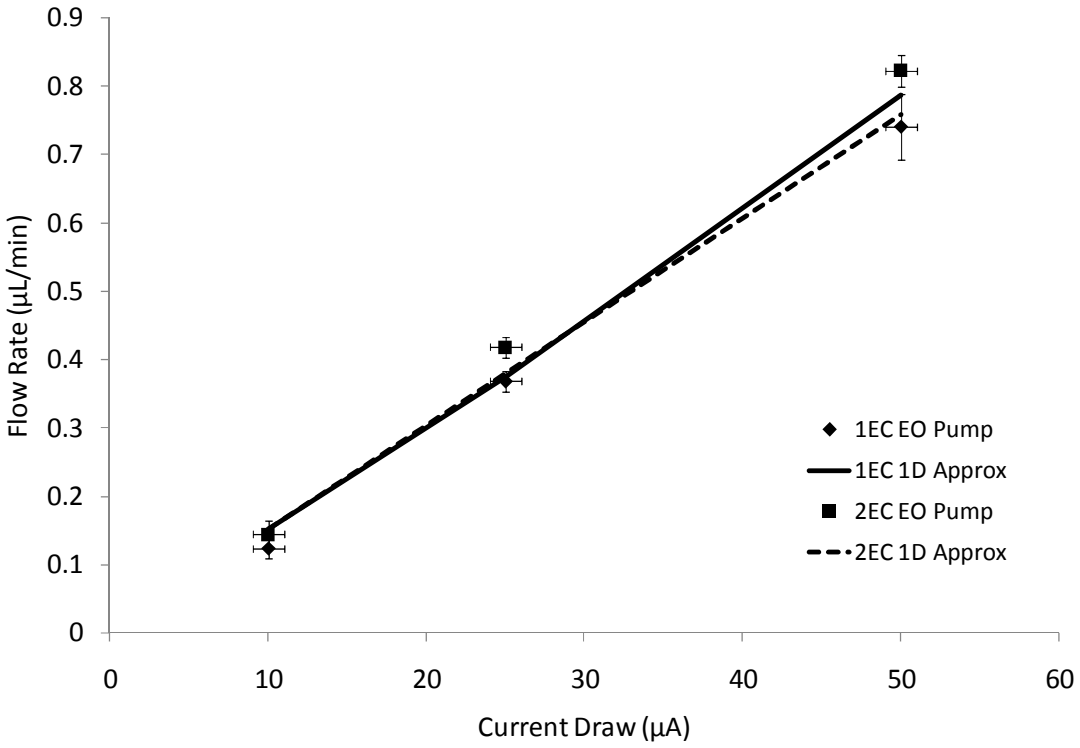

Figure 7.9 Comparison of the flow rate vs. current draw for the 1-EC and 2-EC pump designs (1X TBE working fluid with gel salt bridge) compared with approximations from the 1D models presented in Appendix A and B. Dimensions measured with profilometer: EOF channel 500µm W and 5.8µm H and fluid properties λ_b=0.13 S/m and ζ=47mV.

7.5.2 1st Generation EO Pump

Using the findings of the 1-EC and 2-EC pumps a new design was fabricated as shown in Figure 7.10. The figure also includes actual images of the fabricated pump in PDMS. To increase the flow rate over the previous designs a wider (1.0mm) EOF flow region was included. The electrode channels were shortened and brought closer together to reduces losses in the electric

potential in these channels. Posts were added to the gel region to increase the mechanical stability. A tapered was included in the channel up to the EOF region to reduce losses in the flow field and electric field caused by sudden expansions/contractions. Figure 7.11 shows the numerical simulation of the electric field in the EO pump. One notices that the electric field is not uniform in the EOF channel which will cause additional losses. As well, fabricating the EO pump was difficult since the wide and shallow EOF channel would sag or even collapse due to the flexibility of PDMS. Several preliminary tests were performed with this pump design but a new design was quickly developed to solve the collapsing issue.

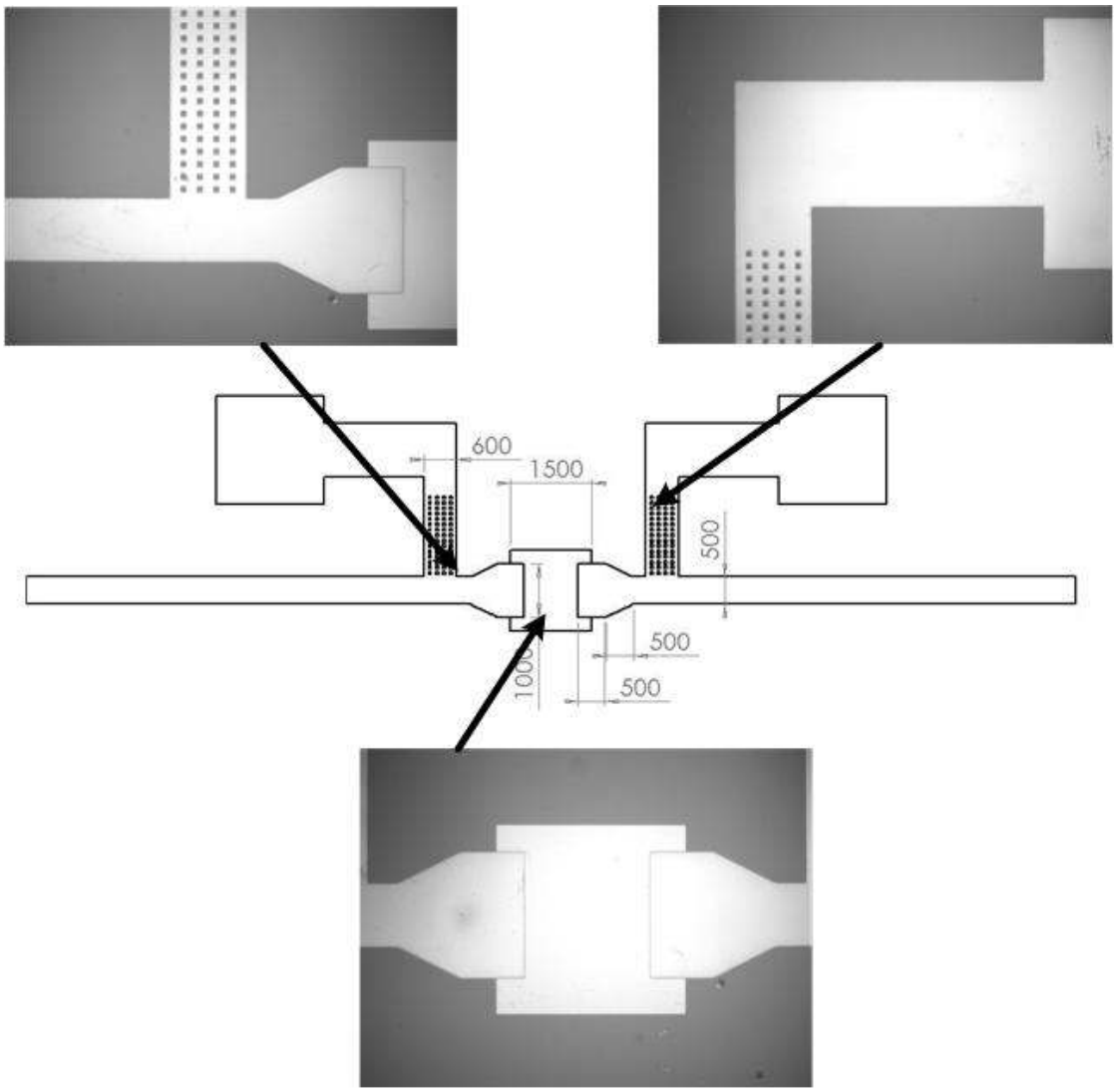

Figure 7.10 Diagram of the 1st generation EO pump designed. Also included are images of the PDMS microchannel mold in various regions of the pump.

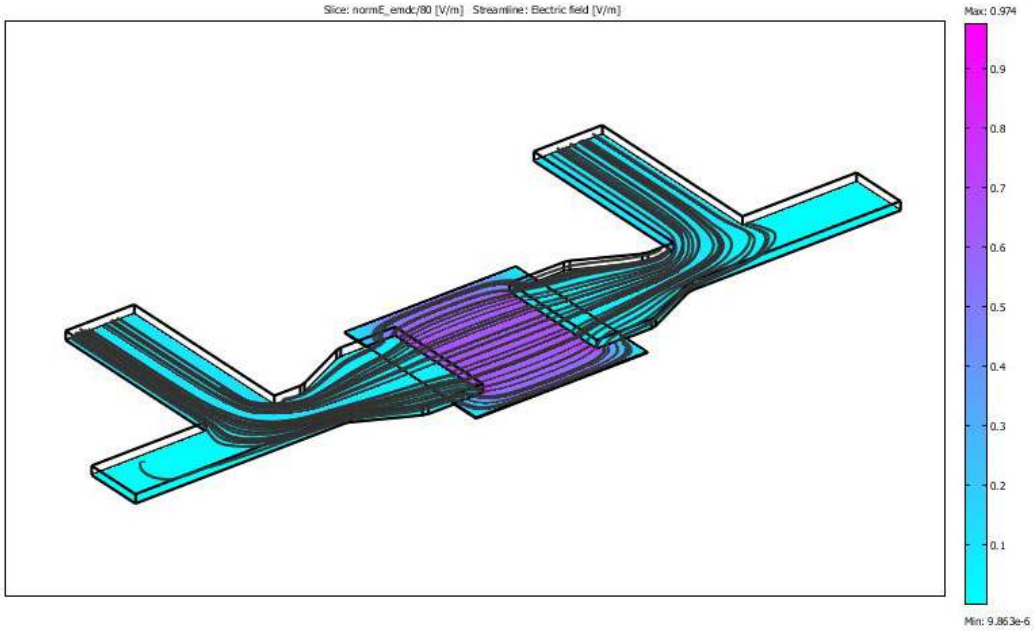

Figure 7.11 Numerical simulation result of the normalized electric field as a surface plot along with streamlines for the 1st generation EO pump. Gel posts were left out of the model in order to simplify the meshing.

7.5.3 2nd Generation EO Pump

In the 2nd generation design the single EOF channel was replaced with ten 100µm channels in parallel to reduce the amount of sagging as shown in Figure 7.12. In addition the electrode channels were rearranged to lay directly in-line with the EOF channels. This reduced any electrical field losses caused by the 90° bend in the 1st generation design. As shown in Figure 7.13 the electric field through the EOF channels is uniform. However, a negative of this design is that high flow rates could not be achieved without applying strong electric fields due to the narrow width of the EOF region.

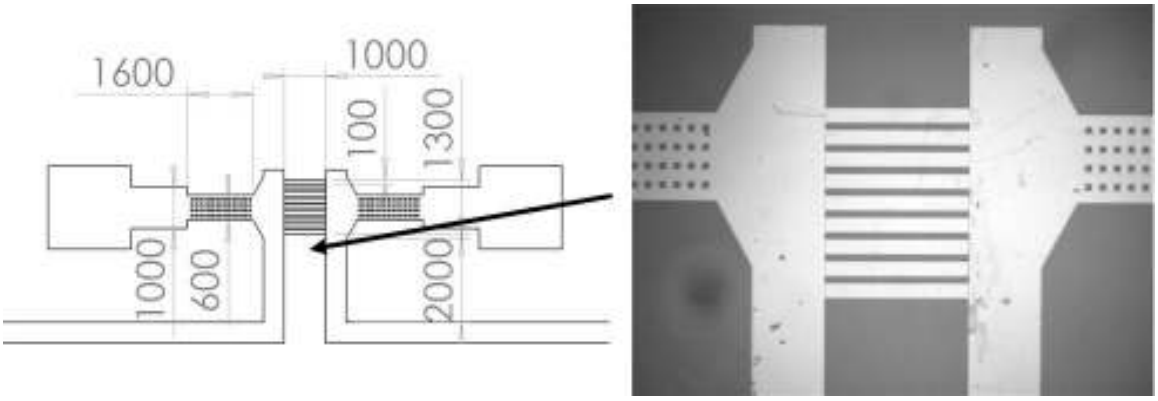

Figure 7.12 Diagram of the 2nd generation EO pump design with inset showing the fabricated network in PDMS.

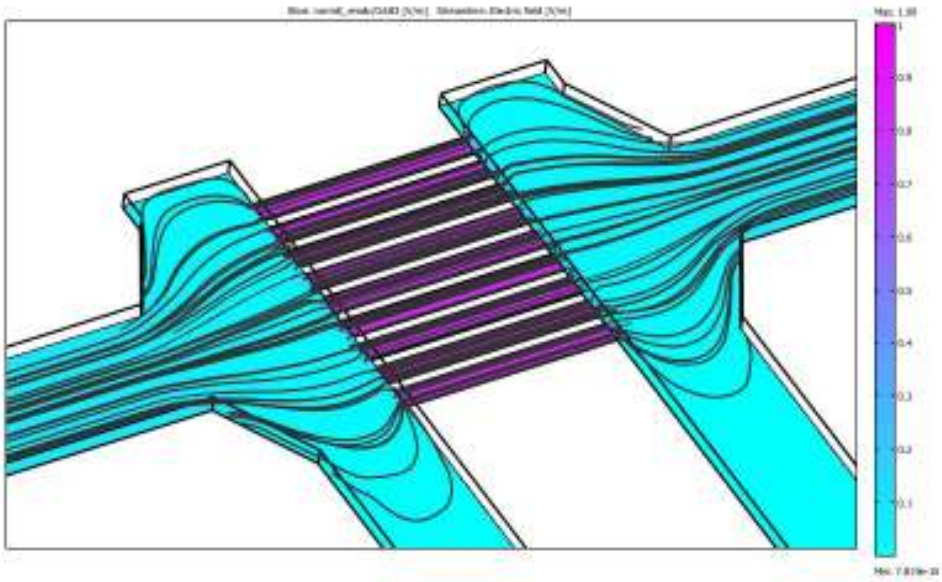

Figure 7.13 Numerical simulation result of the normalized electric filed and streamlines for the 2nd generation EO pump design.

7.5.4 3rd Generation EO Pump

Using the 1D models developed previously a new generation pump was design with specific criteria for pumping the cell culture media. The pump, shown in Figure 7.14, contains 35 parallel 100μm channels, which is a 3.5X increase in the effective EOF region width. To provide a uniform electric field the single gel salt bridge separating the electrode reservoir was replaced with four evenly distributed gel regions. As shown in Figure 7.15, the electric field is uniform throughout the EOF region with this configuration.

Additional 3D numerical simulations were performed to study the flow field in the 3rd generation design. Due to symmetry within the EO pump, one half of the pump was modeled as shown in Figure 7.16. In addition, several features were not included such as the gel regions to reduce the complexity of the model. The flow field within the pump is shown in Figure 7.16b. The flow is evenly distributed through the EOF channels but there is a linear decrease in the velocity in the inflow region of the pump. In the inlet channel there is purely pressure driven flow as can be seen by the parabolic flow field. The pressure distribution in the inflow region is also relatively uniform indicating that there is only a small amount of pressure loss.

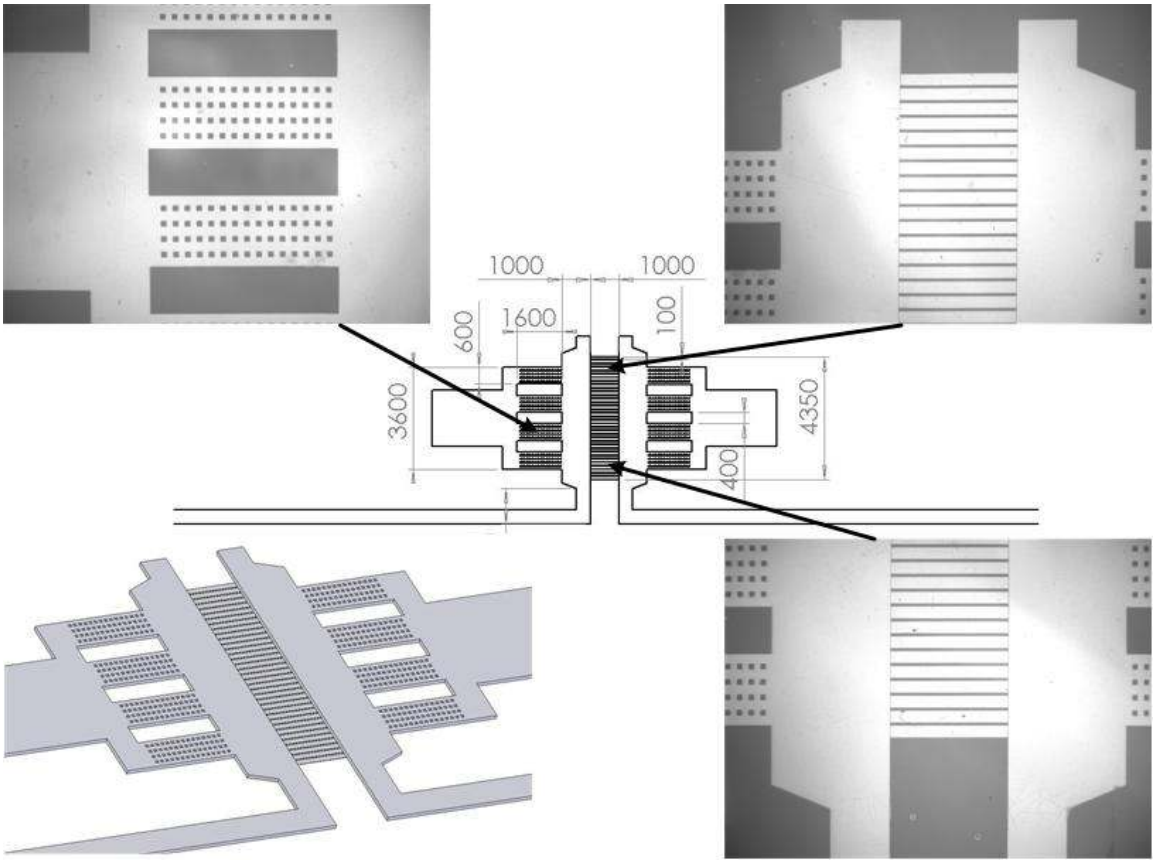

Figure 7.14 Diagram of the 3rd generation EO pump design with insets showing the fabricated network in PDMS.

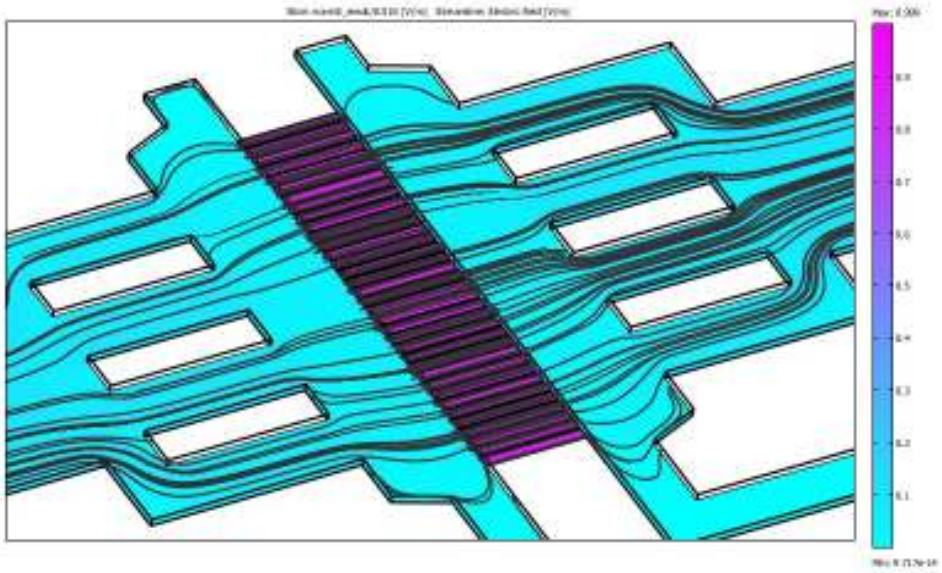

Figure 7.15 Numerical simulation result of the normalized electric filed and streamlines for the 3rd generation EO pump design.

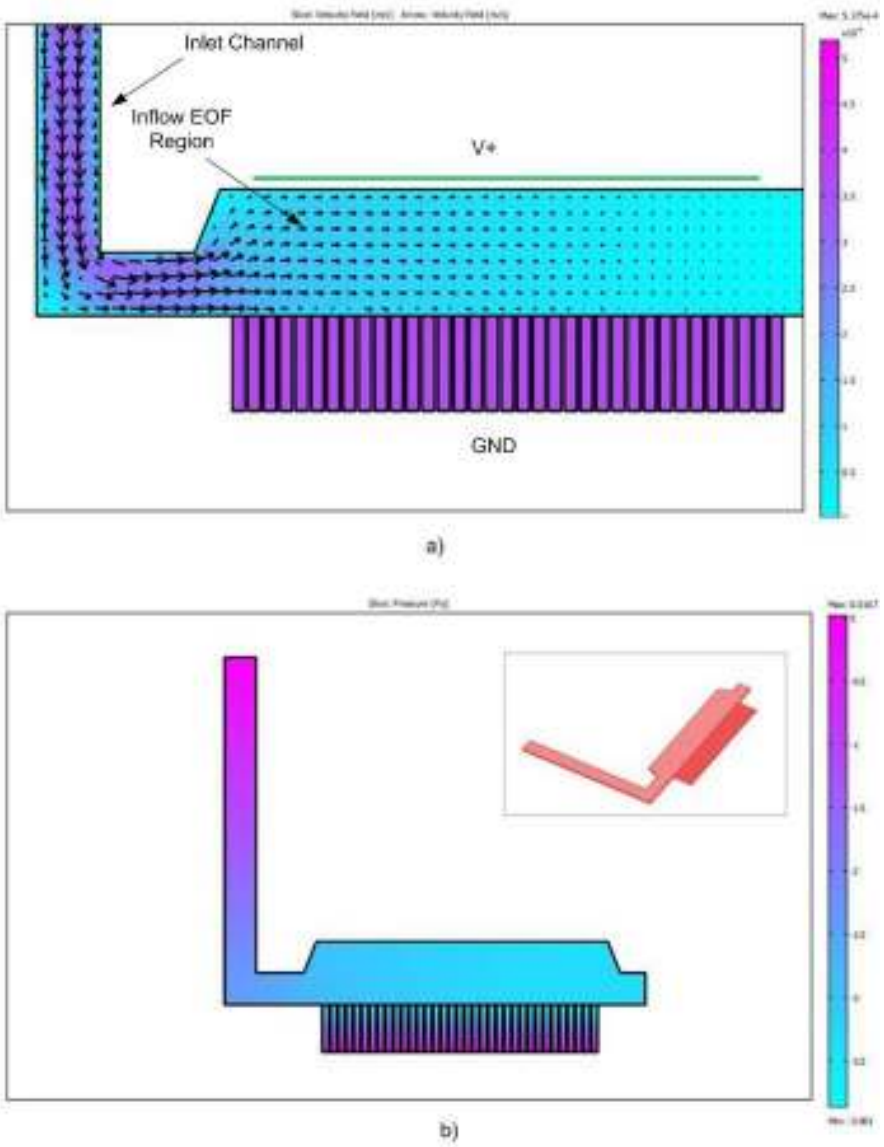

Figure 7.16 Numerical simulation results of the 3rd generation EO pump design (a) flow field with arrow plot indicating the flow direction (b) pressure field within the EO pump.

To validate the 3D numerical model and 1D circuit model the flow rate calculations for 1XTBE were compared with experimental results. The results are summarized in Table 7.1 for two applied currents. Analyzing the results one can see that the flow rates predicted by the two models are in excellent agreement, again signifying that the simpler 1D model is sufficient for modelling purposes. Comparing the predicted results with experimental values there is also good agreement with only a small error at the higher applied current probably due to uncertainties in measurement at the higher flow rate.

Table 7.1 Comparison of experimental (Exp), 3D numerical results (Num. Model) and 1D circuit analysis results for 1XTBE with the 3rd generation pump design.

Current (μA)	Flow Rate (μL/min)		
	Exp	Num. Model	1D Model
68	1.098±0.055	1.088	1.096
140	2.08±0.11	2.24	2.257

7.5.5 4th Generation EO Pump

In the final pump design only small changes were made to the previous design as shown in Figure 7.17. First, two inlet channels were added to the pump in order to add an additional degree of symmetry in the design. The goal was to reduce some of the pressure losses that occurred in the previous design. As well 70 EOF channels 50μm wide were used to further reduce any sagging of these channels. The gel regions were shortened and the posts were redistributed in a staggered arrangement to increase the mechanical stability of the gel. The width of the gel regions was reduced to fit better in the field of view of the 20X objective. The overall size of the pump is quite small, approximately 1cm x 2.5 cm in size. On one microscope slide four of these pumps can be comfortable fabricated and operated allowing for multi-fluid control in a small space.

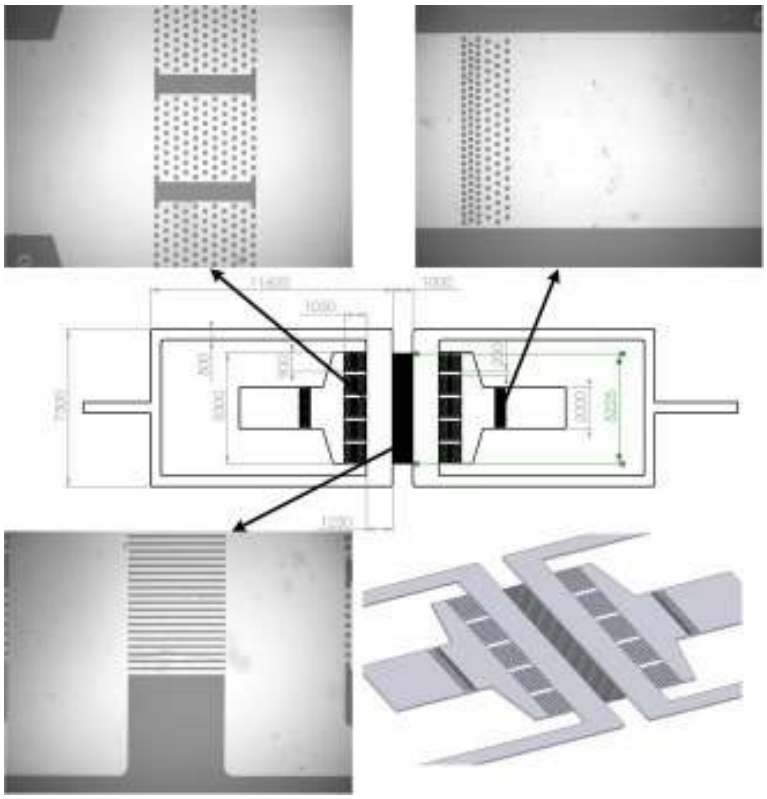

Figure 7.17 Diagram of the 4th generation EO pump design with insets showing the fabricated network in PDMS.

A 3D numerical model was also developed for the 4th generation design as shown in Figure 7.18. Only one-quarter of the pump was modeled due to duel symmetry along both axes. The flow field within the pump is shown in Figure 7.18a. The flow field is evenly distributed along the EOF region and there is less pressure drop in the inflow region (see Figure7.19b). This design was chosen as the design to be implemented in the cell culture network and will be the focus of further discussion.

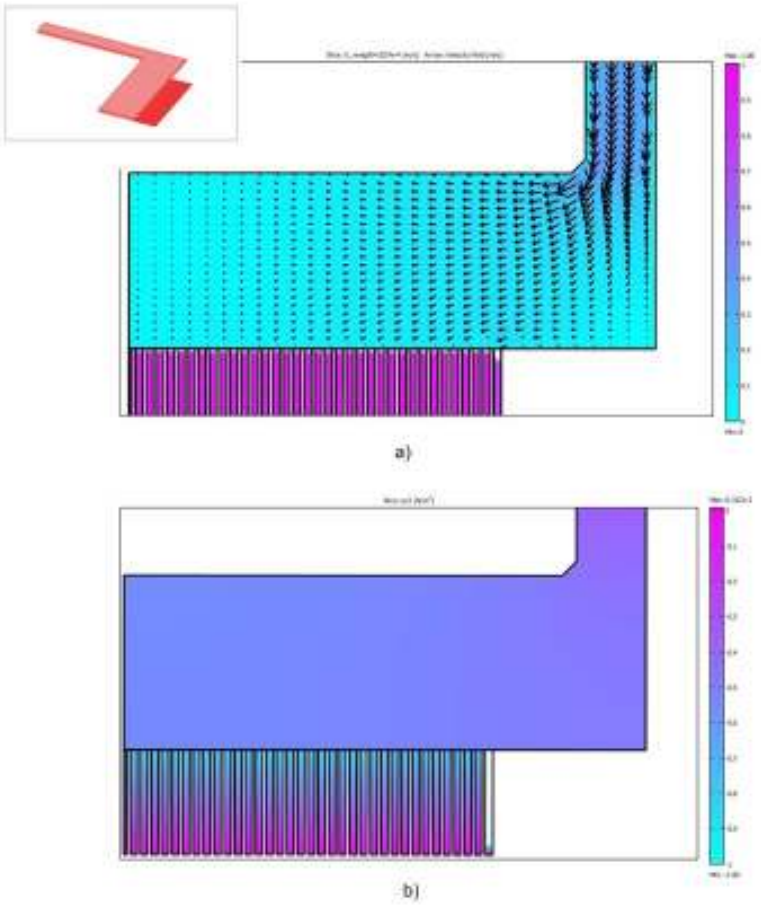

Figure 7.18 Numerical simulation results of the 3rd generation EO pump design (a) flow field with arrow plot indicating the flow direction (b) pressure field within the EO pump.

7.6 Further Design Evaluation

The following subsections focuses on the design evaluation of the 4th generation EO pump. This includes discussions on the techniques and methods used to suppress the problems associated with using EO pumps with high concentration solutions. Details of the flow rate performance of the pump are provided, as well as electrolysis, joule heating and transport phenomenon effects.

7.6.1 Network Dimensions of Master

The uniformity of the channel features and the information of the actual channel height are very important for reliable operation of EOF pumping, therefore, these parameters were measured and used in pump design and operation. The mean channel heights are 2.78μm (0.2 S.D, n=6) for the EOF channel and 80.2μm (2.0 SD, n=10) for the inlet /outlet channels and electrode regions.

7.6.2 Flow Rate Measurements

In the previously presented experimental results the working fluid and the electrode reservoir fluid were the same. However, L15ex posses a small buffering capacity so that the pump would only be able to run for at most 30 minutes. In order to increase the operating time the electrode reservoir solutions were replaced with well buffered solutions: 1XTBE and Bufferall. The flow rate curves for these two combinations are shown in Figure 7.19. The results show a linear trend for the flow rate versus applied current as would be expected from Eqn. 7.2. The preferred combination is L15ex+Bufferall since it shows better flow rate performance. More importantly, Bufferall is biocompatible and is often used to add buffering capacity to cell culture media. The solution contains three types of Good's buffers at different pKa so that the solution is able to absorb pH changes over a wider range. In all subsequent experiments with cells the performance curve presented here was used to determine the applied flow rate.

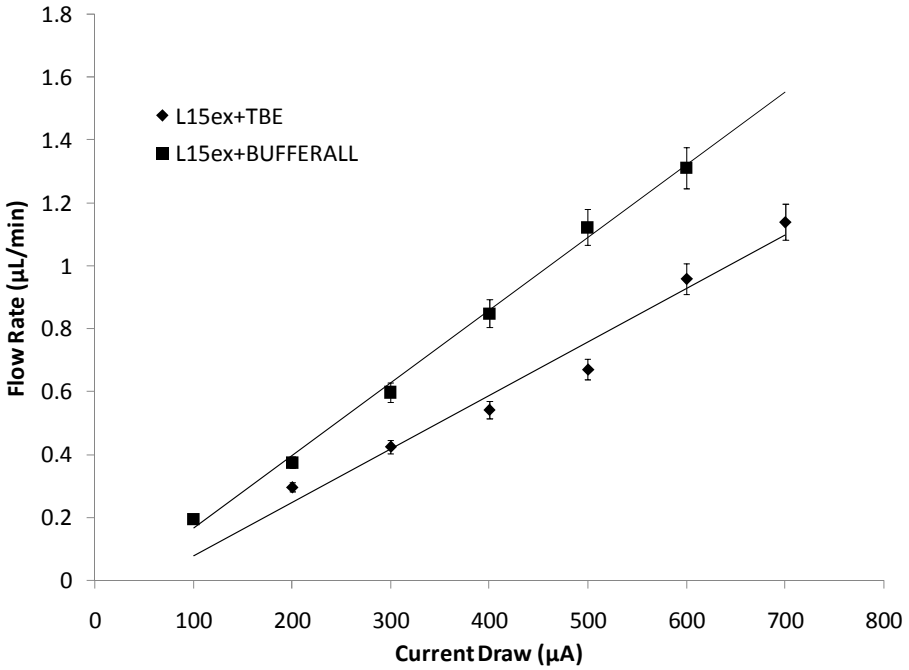

Figure 7.19 Flow rate measurements of the 4th generation EO pump with L15ex and buffers in the electrode reservoir 1XTBE and Bufferall refer to Chapter 3 for details on these solutions.

7.6.3 Electrolysis Effects

Electrolysis problems have been reduced by using well buffered solution and large reservoirs (2mL) for the electrodes. These reservoir extensions were attached to chip as discussed in Chapter 5. The large volume of the fluid is required to absorb the electrolysis affects and limit pH changes. An estimate of the depletion time is given as [Brask *et al.* (2005)]:

$$\tau_{dep} = \frac{c v_{res} F}{I} \qquad \textbf{(7.6)}$$

where, F is Faradays constant, v_{res} is the reservoir volume (2mL), I is the electric current (500μA) and c the buffer concentration (100mM). With these values the depletion time is approximately 10.7 hrs which is still much lower than conventional cell culture perfusion requirements of 1-7 days. Once the buffer is depleted significant changes in pH will occur at the reservoirs resulting in changes to the zeta potential and flow. Therefore, the buffer needs to be replaced prior to this time and this limits the continuous operation of the chip.

One possible method of extending the operation life of the pump past the depletion of the buffer is to use ion selective membranes rather than gel salt bridges. Brask *et al.* (2005) reported that the use of anion exchange membranes greatly extends the operation of the pump by eliminating acid transport to the working fluid. However, through investigation, it has been found that integrating commercial ion exchange membranes into PDMS chips can be difficult due to swelling of the membrane and the flexibility of the PDMS (see Section 7.2.2). Further investigation into different buffers would also be a viable route for improving the operating time of the pump. The gel salt bridge help reduce electrolysis effects by compartmentalize the electrodes from the working fluid which delays the mass transport of H^+ and OH^- into the fluid [de Jesus *et al.* (2005)].

Another negative aspect of the electrolysis reaction is the consumption of the buffer as water is decomposed into hydrogen and oxygen gas. During long term operation the buffer liquid level will continuously drop and eventually the electrode will loose contact with the fluid. This process also generates small bubbles on the electrodes causing perturbations in the electric field. Polarization of the electrodes was also witnessed during the experiments. Polarization consists of activation polarization caused by an inhibition in the electrochemical reaction through the electric double layer and concentration polarization caused by an inhibition of mass transport of the reacting species. This means that the overall electrical resistance increases so the applied voltage

must increase as well to maintain a constant current. To solve these problems the pumps were operated in a constant current mode rather than constant voltage. In this way the electric field applied across the EOF channels would remain the same since it is assumed that the above mentioned effects act as a series resistance in the electrical network. Additionally, the current is intrinsically related to the flow rate as the flow rate and current are proportional to each other:

$$Q = \frac{\Delta V}{R_{ehyd}} = \frac{IR}{R_{ehyd}} = I\left(\frac{\mu_{eof}}{\lambda_b}\right) \qquad \textbf{(7.7)}$$

Therefore, the stability of the pump will improve by running it in a constant current mode.

7.6.4 Joule Heating

Joule heating can be a serious problem for EO pumps operating under high current and high voltages. The typical power consumption for the EO pumps tested ranges between 100 to 400mW. A 2D numerical simulation of the cross-section of the EO pump at the EOF channels was performed as shown in Figure 7.19. Three cases were studied: (1) the chip is placed on a large metal surface which acts as a heat sink and provides a room temperature on the bottom of the chip (2) the bottom surface is in partial contact with the heat sink (h=200 W/m^2K) (3) the chip is suspended so there is only free convection flow on the bottom surface (h=10 W/m^2K). In all these cases the top surface is assumed to be under free convection with h=10 W/m^2K. The current draw for this simulation is 500μA for L15ex (λ_b=1.1 S/m) for a power consumption of 0.24 mW.

Analyzing these cases, the maximum temperature (T=60°C) occurs for the third case where the chip is well insulated as compared to the other cases. Measurements performed during experiments with a thermocouple placed overtop of the EOF region recorded a temperature of 31°C compared to a 22°C room temperature. This result compares well with the second simulation where the internal temperature at the EOF region is 40°C. However, these measurements were performed as the chip was suspended overtop of the inverted microscope which does not represent actual operation. In reality, the chip will be placed on a flat surface and the conditions will mimic the first case where there is only a small increase in temperature (T=27°C).

Joule heating can actually have a positive effect on pump performance since it decreases the viscosity of the fluid and increases the flow rate [Brask (2003)]]. Although, joule heating should be avoided for cell culture applications since most cells require strict temperature control. Joule heating can be reduced by using a narrow but wide EOF pumping region so as to decrease the

current density; however, this will always be an issue unless higher zeta potentials can be achieved. A forced convection cooling (i.e. a fan) is a simple option to reduce joule heating effects, particularly for long-time operation purposes. If joule heating is affecting pump performance a deviation from the linear current versus flow rate curve is expected. However, this was not the case with experiments, so it is assumed that joule heating effects are negligible. In future work, further investigation into the internal temperature using fluorescent based laser induced thermometry would be useful.

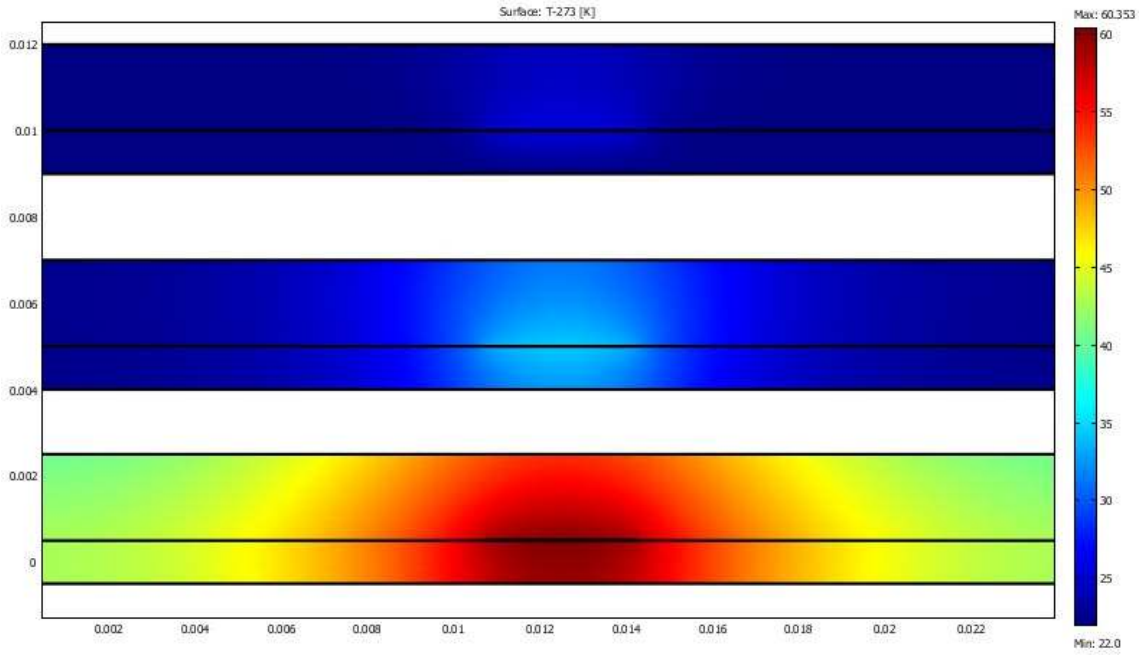

Figure 7.20 Numerical simulation (2D) of PDMS/glass chip with EOF channels under joule heating. The dimensions of the channel are 3.5mm and 2.7µm. The joule heating is entered as a volumetric heating for 500µA for L15ex λ_b=1.1 S/m, where the temperature coefficient is 2%/°C. Three cases were studied: (top) top surface h=10 W/m^{2}K, bottom T=22°C, (middle) top surface h=10 W/m^{2}K, bottom h=200 W/m^{2}K and (bottom) top surface h=10 W/m^{2}K, bottom h=10 W/m^{2}K

7.6.5 Transport Phenomenon in with Gel

In a typical experiment, the pH will change in the electrode reservoir (Bufferall) from an initial value of 7 to a pH = 6.5 and pH = 8 in the anode and cathode reservoir, respectively, after 5 hours of operation. After 14hrs of operation the anode would be at a pH=3 and the cathode pH=13. In addition, the pH was monitored at the inlet and outlet (L15ex) of the chip. The inlet of the chip experiences no change in pH after long-term pumping. On the other hand, the outlet can experience changes of pH from pH=7 to pH = 7.4 after pumping. This indicates that there is some species transport between the buffer in the electrode reservoirs and the working fluid. This may

be caused by several possible modes of transport through the gel including leakage of the buffer around the gel, electroosmotic flow of the buffer through the gel, or convection/diffusion of the species through the gel [Hill (2006)].

To test this hypothesis further, an experiment was performed where 1XTBE (pH=8) was place in the electrode reservoirs and L15ex (pH=7) was pumped continuously at 10μL/min through the network using a syringe pump. No electric field was applied during this tested. The experiment ran for 30min and the pH at the outlet of the pump was measured to be 7.7. This shows that even without possible electrokinetic effects, through convection and diffusion alone there is species transport through the gel. In fact, applying the 1D circuit models to predict flow rates for the TBE+L15ex and Bufferall+L15ex combination results in serious under predictions. The most probable explanation is that the mass transport through the gel has a significant effect on the pump performance. This effect can be plainly seen in the two different operation curves for 1XTBE and Bufferall as shown in Figure 7.19. It is believed that the transport of ions in and out of the electrode reservoir changes the zeta potential of the EOF channel which creates the two distinct curves. This also justifies placing the cell culture chamber in the inlet stream of the EO pump so that the fluid flowing over the cells will not experience any property changes. According to these results a more complete model that includes species transport needs to be developed. The development of a complete model that accounts for the mass transport would be of extreme value to future designs.

7.7 Improvements to Pump Performance

As mention before, the main difficulty with applying EOF pumps to cell culture solutions is the high salt content (~100mM NaCl for example) they typically contain. The high concentration has double negative effects in increasing the electrical conductivity and lowering the zeta potential. Due to the low zeta potential, higher electric fields are required to pump the fluid which in turn results in larger currents that contribute to joule heating in the channel and electrolysis at the electrodes. In this study, Many efforts were made to maximize the amount of flow rate for the given medium (L15-ex). First, attention was paid to the design of the EO pumps to maximize the flow rate. This was accomplished by fabricating 35 parallel channels that produce a large hydrodynamic resistance but a lower electroosmotic resistance.

Second, surface modifications were attempted to improve the zeta potential and thus the flow rate. Tests were performed to measure the zeta potential of L15ex using the Y-channel design

described in Chapter 6. Table 7.2 summarizes the measurements of L15ex under several conditions. For standard L15ex solution (λ_b= 11280 μS/cm) which contains only the essential salts for cellular stability the zeta potential was measured to be ζ=-18.96±0.45mV. A more complete cell culture medium of L15ex with 10%FBS added for feeding had a slightly higher electrical conductivity of λ_b= 12790 μS/cm but a substantially lower zeta potential of ζ=-10.17±0.72 mV (μ_e= 0.81±0.05 x10^{-8} $m^2V^{-1}s^{-1}$). The decrease in apparent zeta potential is most likely due to the higher viscosity of FBS. Note that in the calculations of zeta potential from the electroosmotic mobility the viscosity and dielectric constant values of DI water were used. However, this may not be an appropriate assumption in the case of complex solutions where additional tests should be performed to determine the relevant properties of the solution before calculating the zeta potential.

Table 7.2 Results of current monitoring experiments for: (a) L-15ex at 21 °C, PDMS/PDMS channel, (b) 50 % L-15ex at 24.4°C, PDMS/PDMS channel, (c) L15ex with 10%FBS at 24.3 °C, PDMS/glass, (d) L15ex 10%FBS at 45 °C , PDMS/glass. Results courtesy Zeyad Almutari.

Solution	Substrate	Zeta Pot. (mV)
L-15ex (a)	P/P	-18.96±0.45
50 % L-15ex (b)	P/P	-27.70±0.90
L15ex 10%FBS (c)	P/G	-10.17±0.72
L15ex 10%FBS (d)	P/G	-14.27±0.13

Diluting the L15ex to 50% results in a decrease of the electrical conductivity to λ_b= 6690 μS/cm and an increase in the zeta potential to ζ=27.70±0.90mV. The 50% reduction in conductivity and 46% increase in zeta potential results in a roughly four times improvement of pump performance. As mention before, the main difficulty with using cell culture solutions with EO pumps is that they contain a high concentration of salt which has double negative effect of increasing the electrical conductivity and lowering the zeta potential. Accordingly, higher electric fields are required to pump the fluid which in turn produces larger currents causing substantial joule heating in the channel and electrolysis at the electrodes. The option of using a diluted version of L15ex for the EO pump chip was considered by testing the survival of RT gill cells in solutions of 75%, 50%, and 25% L15ex as discussed in Chapter 9. In addition, to decreasing the salt content there also exists the possibility of including additives to the working fluid that may improve the overall EO pump performance [Reichmuth *et al.* (2003)]. However, since the goal of this study is to explore the possibility of utilizing EO pumps for cell culture an effort was made to try and keep

as many aspects of the chips operation the same as the conventional cell culture method. For this reason, a decision was made not to modify the cell culture solution but to look at other possible methods of increasing the electroosmotic mobility and EO pump performance.

It is well known that at elevated temperatures the electroosmotic mobility of a fluid increases primarily due to the change in viscosity. In addition, there is evidence that for some liquid/surface combinations the zeta potential is also temperature dependent [Venditti *et al.* (2006)]. To investigate this point further experiments were performed with L15ex+10%FBS at 45ºC by placing the Y-channel chip inside an incubator (SI-950, UVP). The chip and solutions were allowed to reach steady state by monitoring the temperature with a thermocouple. The measured electroosmotic mobility at 45 ºC nearly doubled to μ_e= 1.471±0.67 x10^{-8} $m^2 V^{-1}s^{-1}$ which equates to a zeta potential of ζ=-14.27±0.13mV using temperature corrected fluid properties. Comparing to the room temperature measurement the increase in electroosmotic mobility and zeta potential is about 81% and 40% respectively. This trend generally agrees with the results presented by Venditti *et al.* (2006) where the zeta potential was established to increase with temperature for KCl solutions. Stronger temperature dependence was found for higher concentrations of KCl (e.g. 0.9%/ ºC for 10mM KCl). Extrapolating this trend it seems reasonable that L15ex will show even stronger temperature dependence (~2.67%/ºC) due its high salt content.

This discussion suggests that a viable option for increasing EO pump performance for difficult solutions is to heat the incoming fluid. In fact heating the perfusion medium to 37ºC is already a prerequisite for microfluidic mammalian cell culture [Kim *et al.*(2007)] and may be accomplished by embedding micro heaters into the microfluidic chip using a variety of techniques [de Mello *et al*. (2005); Futai *et al.* (2006); Stangegaard *et al.* (2006)]. Further investigation into using micro heaters was not pursued during this study since the fabrication techniques and methods were not available; however, this method of improving EO pump performance is a viable option that should be considered in future work. Instead an effort was made to improve the electroosmotic mobility of PDMS through surface modification [Pallandre *et al* (2006); Makamba *et al.* (2003)].

These techniques involve either the bulk modification of the PDMS by including pre-polymer additives [Luo et al. (2006)], surface modification of the microchannels [Bodas *et al.* (2007); Liu *et al*. (2000); Slentz *et al.* (2002); Hu *et al.* (2002); Hu *et al.* (2003); Hu *et al.* (2004); Roman *et al.* (2005); Roman *et al.* (2006)] or including additives to the working fluid [Won Ro *et al.* (2002); Badal *et al.* (2002)]. The goal of each surface treatment varies depending on the specifics

of the application. In the case of PDMS chips for capillary electrophoresis applications reducing adsorption of analytes and increasing the stability of EOF is extremely important to obtain repeatable and reliable results. Examples of other important criteria include stability of EOF over large pH ranges, increasing the length of hydrophobic recovery of PDMS after plasma treatment and suppressing or increasing EOF flow. In this study the main goal was to improve the electroosmotic mobility of the PDMS for the EO pump design. Since plasma treatment is already part of the fabrication process for PDMS chips the mobility of plasma treated PDMS is considered the base for which the performances of the surface treatments are to be compared.

The first surface modification to be considered involved grafting 2-hydroxy ethyl methacrylate (HEMA) to the surface of PDMS using procedures reported by Choi *et al.* (2003) and Bodas *et al.* (2006,2007). Both groups reported improved electroosmotic mobility and hydrophylicity after treatment. In the former case the PDMS microchannel is treated by infusing HEMA or placing the PDMS mold within a HEMA bath and grafting by heating the solution. In the second case, HEMA is spin coated on to the PDMS mold and is then plasma treated to complete the grafting. Note that in both cases the PDMS molds are first plasma treated in order to activate the surface so as to open up potential bonding sites. Several experiments were performed following the methods presented by the two groups which included some modifications to the procedures to try and improve the process. The most successful treatment procedure was:

- Plasma treatment for 40 s of the PDMS channel.
- Placing the PDMS mold in a 65 C HEMA bath for 6 hrs.
- Rinsing in a 40 C DI water bath.
- Drying the channel in a 45 C oven.
- Plasma treatment for 40 s and bonding the chip to the substrate.

This treatment generated hydrophilic PDMS even if the mold was not plasma treated again for bonding. Microfluidic channels could be filled with water several days after treatment indicating a sustainable hydrophilic surface which agrees in general with the results of Bodas *et al.* However, current monitoring tests with various solutions including L15ex showed no improvement over standard plasma treated PDMS and further work was not continued.

It has been established that the hydrophobic recovery of PDMS after plasma treatment is due to the migration of lower molecular weight (LMW) oligmers from the bulk to the surface [Fritz *et al.* (1995)]. These LMW species are either uncross linked PDMS or residual cross linking agent left over from the curing process and removal of these LMW species will extend the

hydrophylicity of plasma treated PDMS. The simplest method of removing the LMW species is to complete the cross linking reaction by extending the bake time. Eddington *et al.* (2006) performed studies to this effect and found that thermally aged PDMS remained hydrophilic for more then 2 weeks. However, bake times of 7-14 days were required which is impractical for rapid prototyping of new designs. As an alternative, the LMW species can be removed through chemical extraction. PDMS molds placed in certain organic solvents exhibits a large amount of swelling. The process removes LMW species from the bulk PDMS which manifests as a reduction in weight (~5%). Vickers *et al.* (2006) developed an extraction process composed of three main steps:

- Cured PDMS (2hrs 80°C) is placed in a triethylamine bath for 2hrs.
- Then in an ethyl acetate bath for 2hrs.
- Then in an acetone bath for 2hrs.

This is followed by drying the PDMS at 65 C and washing copiously with DI water. In experiments with PDMS the average reduction in weight was 4%. Analysis of the PDMS mold under a microscope showed no changes in the dimensions of the channels. Extracted PDMS showed very good hydrophilic properties and channels could still be filled after one week. Vickers *et al.* (2006) provided mobility measurements for cases of native PDMS, extracted PDMS without plasma treatment, and extracted PDMS with plasma treatment. They found the electroosmotic mobility to increase in that order; however, data for only plasma treated PDMS was not provided as a comparison. Therefore, it is unknown if their extraction process actually improves the electroosmotic mobility over standard plasma treated PDMS. Consequently, experiments were performed with KCl and TBE solutions but there was no improvement in the mobility.

The benefit of sustained hydrophilic channels should not be underestimated since it greatly increases the fidelity of PDMS microfluidic devices. Devices that remain hydrophilic do not have to be filled with water making them easier to transport and store. Although the surface treatments were unsuccessful valuable information was obtained. The concept of extracted PDMS was used in the fabrication of PDMS chips for cell culture. To improve the biocompatibility and hydrophylicity PDMS molds were cured for 12-24 hrs rather than the conventional 2 hrs. This resulted in microchannels that were easy to fill with less bubbles being trapped and stronger bonds.

7.8 Summary and Recommendations

In this chapter the fabrication and design of integrated planar EO pumps in PDMS was presented. Two types of pumps were developed, one based on the integration of a commercial ion exchange membrane and the other on the fabrication of *in situ* gel salt bridges. In the end the ion exchange device was abandoned due to severe problems with integrating the membranes on-chip due to swelling and sealing issues. Several designs using the gel salt bridges were developed and tested through numerical and experimental work. Based on the final design the flow rate characteristics of the pump were presented for electrode buffer/working fluid combinations of L15ex+1XTBE and L15ex+Bufferall. The L15ex+Bufferall combination was chosen due to the superior pump performance and biocompatibility with cells. Several issues that exist with pumping high conductivity solutions such as L15ex were presented and discussed with respect to the final pump design. These issues include electrolysis, joule heating, and species transport through the gel. Solutions for these problems were discussed in terms of pump design and operation. Additionally, methods for improving the pump performance were also investigated. This included designing the pump to maximize the flow rate and attempting to modify the surface of PDMS to increase the electrokinetic properties. Other methods such as decreasing the ion concentration of the solution and increasing the temperature were considered. However, none of these improvements were implemented due to unsatisfactory results.

There are several recommendations that should be considered in another iteration of the EO pump design. To improve the flow rate characteristics other surface modifications should be considered as well as the possibility of using high surface charge polymer monoliths to replace the parallel EOF channels. For stability and operation time other buffers should be considered as well as the integration of anion exchange membranes to allow the pump to operate past the buffer depletion time.

Chapter 8

Microfluidic Network for Cell Culture with Integrated EO Pumps

The 4th generation EO pump described in the previous chapter was integrated into a larger microfluidic network for medium perfusion with cells. Three potential modes of operation for the device are presented: (i) the EO pumps operate as primary sources of fluid flow (ii) an external source provides the main flow and the EO pumps regulate the flow to the cells (iii) the EO pumps injection fluid into the main stream. A 1D circuit equivalency analysis was performed to quantify the characteristics of the network under these modes. Fluorescent visualization which demonstrates the network operating under these three modes is also presented.

8.1 Cell Culture Microfluidic Network

Figure 8.1 shows a schematic of the microfluidic device developed for incorporating the EO pumps into a cell culture network. Two cell chambers are connected in series with their own individual EO pump. An intersecting channel connects the two EO pump channels to each other and to another inlet channel. The shallow channels of the EO pumps serve to suppress external pressure driven flow from liquid level differences and meniscus differences (Laplace pressure) in the exit pump reservoir (R4,R5) and the cell chamber (R2,R3) . Similarly, the channel connecting the two cell chambers is also of high resistance (equal to the EO pumps) to prevent undesired cross flow between the low resistance chambers (R1, R2, R3). A photograph of the microfluidic network in PDMS is shown in Figure 8.2.

The cell chambers were designed to have the same surface area as a conventional 96 well plate. The tapered inlet/outlets provide a more uniform velocity field across the cell area (rectangular portion). The calculated shear stress in the cell current chamber is minimal (0.3 dynes/cm^2) and will not affect the cells under normal flow rates (0-50μL/min). Filters in the chambers (25μm spacing) prevent cells from entering the EO pump during seeding. Since the primary motivation of this work is to explore the possibility of using EO pumps with cell culture not much effort was spent on optimizing the perfusion chamber. Ideally, a well design chamber should provide nearly uniform mass transport and control of the microenvironment [Kim *et al.* (2007)]. In future iterations, numerical simulations should be performed to assess the nutrient delivery within the cell chamber [Hung *et al.* (2005)].

The chip was fabricated using the techniques described in Chapters 5 and 7. There are three different channel heights in the network: EOF channels (2.7μm), intersecting channel (5.1μm) and the other channels (80.2μm). The dimensions were measured using the methods explained in Chapter 3. This required the fabrication of a three level master with successive overlapping features. The fabrication procedure for creating the master and fabricating the gel electrodes is provided in Appendix C.

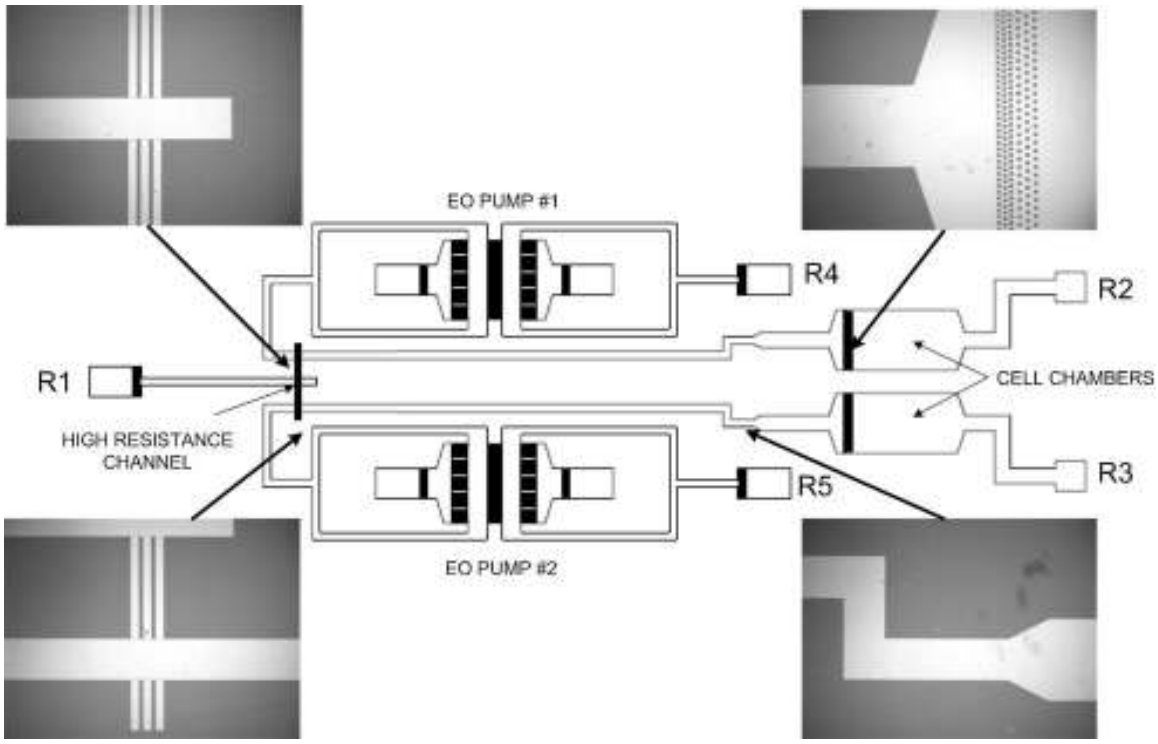

Figure 8.1 Schematic of the microfluidic network design with integrated EO pumps used for cell culture experiments. Insets show the fabricated design at specific location in the network.

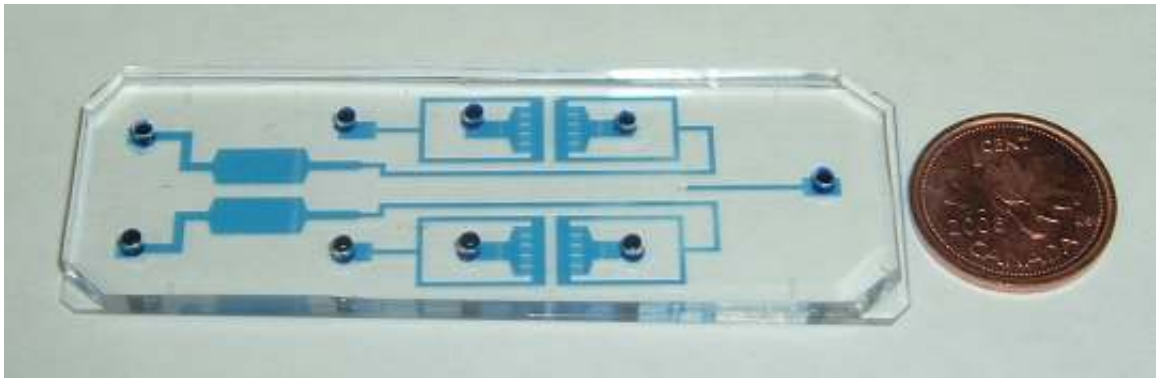

Figure 8.2 Fabricated chip PDMS with dye solution added to the channels to illuminate the microfluidic network.

8.2 Operation Modes of Network

An attractive feature of the microfluidic network design is its flexibility. There exists three potential configurations where the EO pumps are utilized to control the flow to the cell chambers (refer to figure 8.3). In the first configuration, shown in figure 8.3a, the two EO pumps are used to directly pump the fluid through the cell chamber. The flow is from R2 → R4 and R3 →R5. As mentioned before, placing the pump downstream from the cells avoids passing the fluid first through the pump and then the cells. Therefore, the cells experience a slightly negative pressure (a few Pascals) since they are on the inlet side of the EO pump. As well, the electrode near the cell chamber is set to ground (GND) and the other to negative voltage (-V). In this way the cells do not experience an abnormally high voltage. The high resistance channel connecting the two pumps allows them to operate independently without affecting the flow to the other chamber.

In the second configuration (see figure 8.3b) flow from an external pressure driven source such as a syringe pump provides constant flow over the cells (R1→R4, R1→R5). Due to symmetry between the two sides of the network the flow will split equally between the cell chambers. In addition, little flow will be lost to the EO pump channels due to their high hydrodynamic resistance. If the EO pumps are operating in the same manner as the previous configuration, then the flow will be diverted away from the cell chamber and down the EO pump channels. This provides the possibility of dynamically regulating flow to the cells from a single source without the need for integrating valves on-chip.

In the third configuration (see figure 8.3c) the EO pumps operate in the opposite direction as before. The pump can operate continuously or periodically to dispense small amounts of fluid into the main stream. In continuous operation a gradient generator can be added to create concentration gradient across the cells. This design can be used to study the effects of factor concentration on cells. Park *et al.* (2007) demonstrated such a device with a single cell chamber using an osmotic pump (flow generated by a concentration difference across a membrane). However, their pump was not integrated on-chip and only provides flow in one direction. Alternatively, the system can be used periodically to inject a discrete amount of steroid in the fluid. A mixer would have to be placed prior to the cell chamber to insure a uniform concentration. The benefit of using the EO pump over on-chip valves is that the time response is nearly instantaneous and the fluid can be pumped in either direction with volume control down to several nano-litres. Furthermore, the network can be expanded in parallel to increase the amount of cell culture chambers and EO pumps.

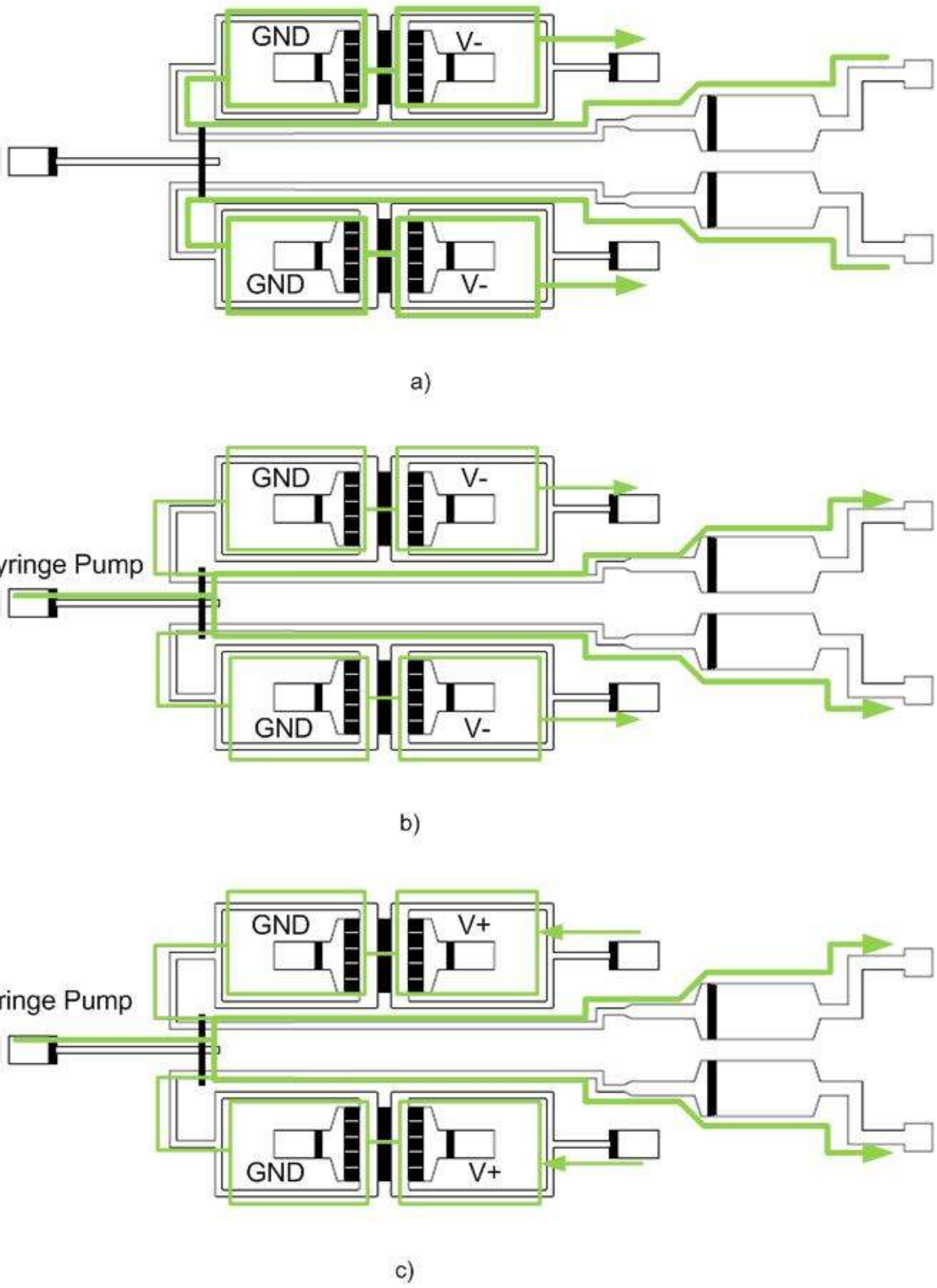

Figure 8.3 The possible operational modes for the microfluidic network (a) EO pump operates independently (b) EO pumps regulate flow from another principal source to the cell culture chambers (c) EO pumps inject fluid continuously or discretely into the main fluid flow.

8.3 1D Circuit Equivalency Network Analysis

To determine the operational conditions of the microfluidic network we can apply the 1D circuit analysis described in Chapter 4. The equivalent circuit for the network is presented in Figure 8.4.

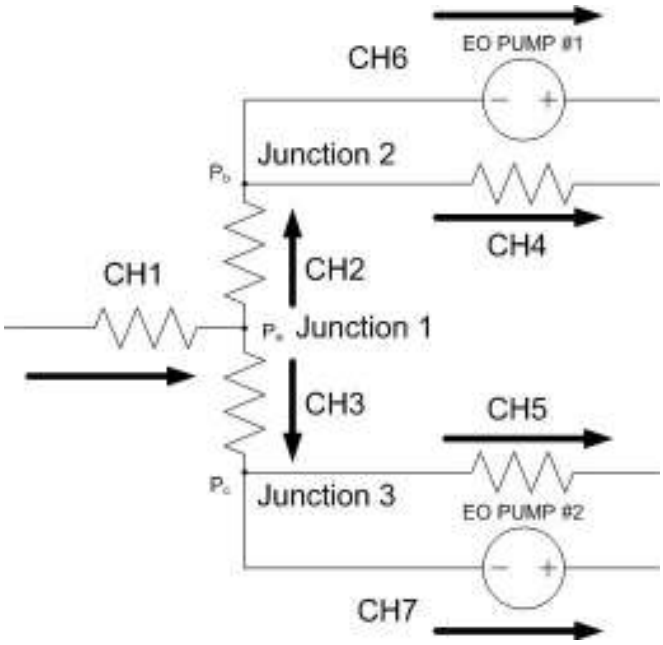

Figure 8.4 1D circuit equivalent network of the microfluidic cell culture chip with two EO pumps.

The system of equations that describe the flow network are:

$$Q_1 = \frac{(P_1 - P_a)}{R_{hyd1}} \quad \textbf{(inlet channel)}$$

$$Q_2 = \frac{(P_a - P_b)}{R_{hyd2}} \quad \textbf{(branch channel)}$$

$$Q_3 = \frac{(P_a - P_c)}{R_{hyd3}} \quad \textbf{(branch channel)}$$

$$Q_4 = \frac{(P_a - P_b)}{R_{hyd4}} \quad \textbf{(cell chamber channel)}$$

$$Q_5 = \frac{(P_a - P_c)}{R_{hyd5}} \quad \textbf{(cell chamber channel)}$$

$$Q_6 = \frac{P_b}{R_{hyd6}} + \frac{G_{EOP\#1}}{R_{hyd6}} I_{EOP\#1} \quad \textbf{(EO Pump \#1 channel)}$$

$$Q_7 = \frac{P_c}{R_{hyd7}} + \frac{G_{EOP\#2}}{R_{hyd7}} I_{EOP\#2} \quad \textbf{(EO Pump \#2 channel)}$$

$$\begin{aligned} Q_1 &= Q_2 + Q_3 \\ Q_2 &= Q_4 + Q_6 \\ Q_3 &= Q_5 + Q_7 \end{aligned} \quad \textbf{(8.1)}$$

Where R_{hyd} is the hydrodynamic resistance of the channel as described in Chapter 4, I_{EOP} is the constant current applied to operate the pump and G_{EOP} is a geometric factor of the EO pump which can be derived from the network analysis for the pump (see Section 7.2) and is given as:

$$G_{EOP} = \frac{R_{hyd\_EOF} R_{e\_EOF}}{R_{ehyd\_EOF}} \quad \textbf{(8.2)}$$

where the resistances refer to the EOF channels in the EO pump. Using the above set of equations the three operation modes of the network are analyzed.

Operation Mode #1

In this mode the two pumps are operating independently without an external flow source. Since the intersecting channels (CH2, CH3) are of high resistance compared to the cell culture channels (CH4, CH5) the two pumps are essentially isolated from each other. Solving the system of equations where $Q_1 = 0, Q_2 = 0, Q_3 = 0$, the flow rate to the two chambers is given as:

$$Q_4 = -\frac{G_{EOF\#1}}{R_{hyd6} + R_{hyd4}} I_{EOF\#1} \quad \textbf{(8.3)}$$

$$Q_7 = -\frac{G_{EOF\#3}}{R_{hyd5} + R_{hyd7}} I_{EOF\#2} \quad \textbf{(8.4)}$$

The negative sign indicates that the fluid flow will be opposite to the direction in Figure 8.4. Recall that the EO pumps will draw the fluid first through the cell chamber before the EO pump.

Operation Mode #2

In the second operation mode there is an additional source of fluid flow from a syringe pump and the two EO pumps serve as regulators that control the flow rate to the cell culture chambers. Here the syringe pump acts as a constant flow rate source and not as a constant pressure source, therefore, the incoming flow (Q_1) must be specified. In addition, the desired flow to the two cell chambers is also known. Under these conditions there are only nine unknowns: P_a, P_b, P_c, $I_{EOP\#1}$, $I_{EOP\#2}$, Q_2, Q_3, Q_6, Q_7 and one equation is lost since Q_1 is known.

Using the equations for junctions 2 and 3 ($Q_1 = Q_2 + Q_3, Q_2 = Q_4 + Q_6$) to solve for the internal pressures P_b, P_c :

$$P_b = \left(\frac{P_a}{R_{hyd2}} - \frac{G_{EOP\#1}}{R_{hyd6}} I_{EOF\#1} \right) \left(\frac{R_{hyd2} R_{hyd4} R_{hyd6}}{R_{hyd2} R_{hyd4} + R_{hyd2} R_{hyd6} + R_{hyd4} R_{hyd6}} \right) \tag{8.5}$$

$$P_c = \left(\frac{P_a}{R_{hyd3}} - \frac{G_{EOP\#2}}{R_{hyd7}} I_{EOF\#2} \right) \left(\frac{R_{hyd3} R_{hyd5} R_{hyd7}}{R_{hyd3} R_{hyd5} + R_{hyd3} R_{hyd7} + R_{hyd5} R_{hyd7}} \right) \tag{8.6}$$

Applying the equation at junction 1 to solve for P_a:

$$Q_1 = \frac{P_a - P_b}{R_{hyd2}} + \frac{P_a - P_c}{R_{hyd3}} \tag{8.7}$$

Subbing in the results for P_a and P_b into the equation and assuming a symmetric geometry between the two sides of the network:

$$\begin{aligned} P_a &= \frac{R_{hyd2}}{2(1 - K_f)} \left[Q_1 - \frac{G_{EOP}}{R_{hyd6}} K_f (I_{EOP\#1} + I_{EOP\#2}) \right] \\ K_f &= \frac{R_{hyd4} R_{hyd6}}{R_{hyd2} R_{hyd4} + R_{hyd2} R_{hyd6} + R_{hyd4} R_{hyd6}} \end{aligned} \tag{8.8}$$

Looking closely at K_f and recalling that the hydrodynamic resistance of the cell culture channel is much smaller than the intersection channel and EO pump ($R_{hyd4} <<< R_{hyd2}, R_{hyd6}$) so that $K_f \to 0$ and the equation reduces to:

$$P_a \cong \frac{R_{hyd2} Q_1}{2} \tag{8.9}$$

Which more importantly means that even with the pumps operating: $Q_2 \cong Q_3 \cong Q_1 / 2$. This is due to the high resistance of the intersection channel which isolates the pumps from each other. Solving for the electrical currents required to achieve the desired flow rates to the chambers:

$$I_{EOP\#1} = \left(\frac{Q_1}{2} - Q_4 \right) \frac{R_{hyd6}}{G_{EOP\#1}} \tag{8.10}$$

$$I_{EOP\#2} = \left(\frac{Q_1}{2} - Q_5 \right) \frac{R_{hyd7}}{G_{EOP\#2}} \tag{8.11}$$

Thus, we have a solution for the operation conditions of the EO pumps. The flow rates drawn by the pumps are given as:

$$Q_6 = \frac{G_{EOP\#1} I_{EOP\#1}}{R_{hyd6}} \quad \textbf{(8.12)}$$

$$Q_7 = \frac{G_{EOP\#2} I_{EOP\#2}}{R_{hyd7}} \quad \textbf{(8.13)}$$

Looking at these equations an important condition exists for specifying the flow rates to the cell chambers, $0 < Q_4 < Q_1 / 2$, or the EO pumps will not be drawing fluid from the main stream but adding to it.

Operation Mode #3

In the operation mode #3 the EO pump is adding injecting another fluid in to the main stream. Therefore, the derivation is the same as for mode #2 but now the specified flow rate to the cell chamber must meet the condition: $Q_4 > Q_1 / 2$. The critical condition for stopping flow to the cell chamber is given as:

$$I_{EOP\#1} = \frac{R_{hyd6}}{G_{EOP\#1}} \frac{Q_1}{2} \quad \textbf{(8.14)}$$

Therefore, the critical operating conditions of the network have been determined using the 1D network analysis.

8.4 Visualization of Network Operation Modes

Fluorescent flow field visualization was performed to demonstrate the network operating under the three modes described previously in Section 8.2. Figure 8.5 shows the location of interest on the microfluidic network which is at the junction of the EO pump channel, cell culture chamber channel and intersecting channel. To demonstrate the operational modes a series of videos were captured using the visualization set up described in Chapter 3. The following discussion contains a description of the videos for reference. The videos are provided with this thesis as supplementary data and are referred to as Appendix D, E and F.

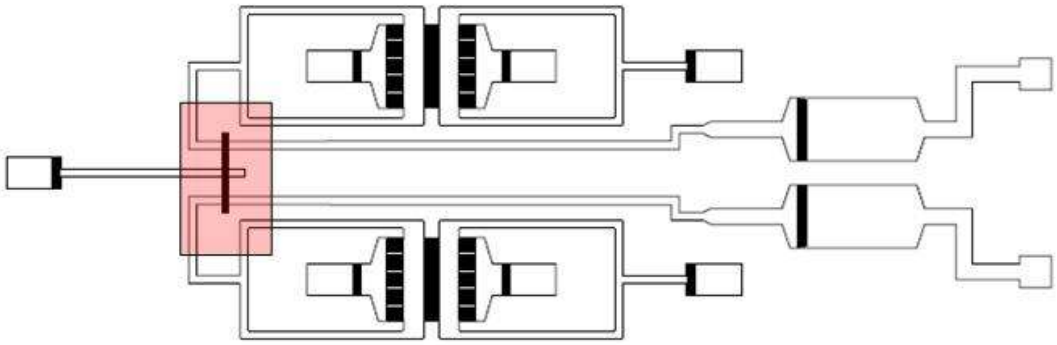

Figure 8.5 Location in the network where the videos were taken during experiments.

Movie #1: Diverting flow to the cell chamber with the EO pump (Appendix D)

Note that this video was taken with the 3rd generation pump so the network dimensions are slightly altered but the overall geometry is similar. This video demonstrates the EO pump diverting flow away from the cell chamber. The location is at the junction between the intersecting channel and the EO pump/cell culture chamber as shown in Figure 8.6. The channel that extends to the left of the image wraps around and becomes the bottom channel which leads to the inlet of the EO pump.

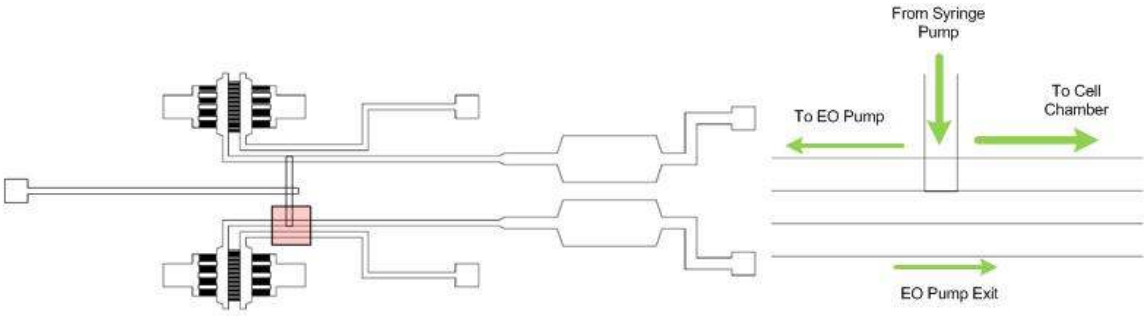

Figure 8.6 Field of view of video #1. On the right a close up of the network geometry in the video indicating the flow direction and locations of the EO pump and cell chamber channels.

A syringe pump is used to provide a constant flow rate to the cell culture chamber at 1μL/min. The EO pump is already turned on at 100μA (0.25μL/min) and is drawing a small flow rate from the main flow. At the 8s mark the pump is set to 200μA (0.5μL/min) and the flow splits equally between the two channels. Again at the 12s mark the pump is set back to 100μA and the flow rate to the EO pump decreases accordingly. This video shows that with the integrated EO pumps dynamic control of the flow rate to the cell culture chambers is possible.

Movie #2: EO pump operation has no affect on other pump (Appendix E)

The purpose of this video is to show that the two pumps are effectively isolated from each other. The system is in the second operation mode and the field of view in the video is shown in Figure 8.7. At first only the syringe pump is operating and the focus is on the left junction. The camera pans across the intersecting channel to the opposite junction to demonstrate that the flow is symmetric. Then the camera pans back to the other junction and the left EO pump is turned on so that the flow rate changes in the left cell chamber. Again the camera pans to the right side to show that there is no noticeable difference in the flow rate while the left EO pump is operating which confirms the results from the 1D network analysis.

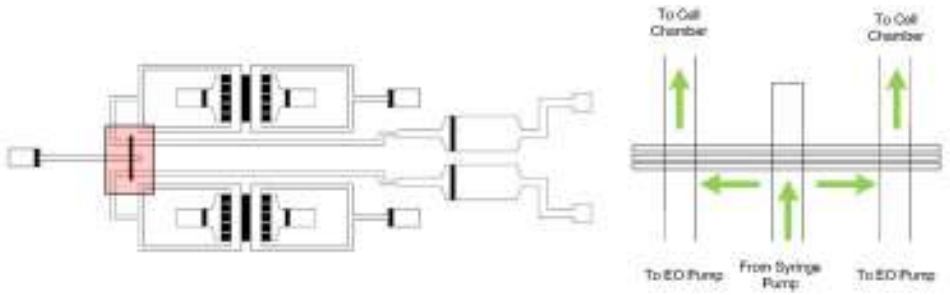

Figure 8.7 Field of view of video #2. On the right a close up of the network geometry in the video indicating the flow direction and locations of the EO pump and cell chamber channels.

Movie #3: EO pump injection into main stream (Appendix F)

This video demonstrates the third network configuration where the EO pump is used to inject fluid into the main stream. The incoming flow from the syringe pump contains 100μM fluorescein dye while the fluid from the EO pump does not. Initially the EO pump is turned off and the flow travels toward the cell chamber. At the 2s mark, the EO pump is turned on briefly to inject a small sample of non-dyed fluid into the mainstream which then travels towards the cell chamber. This video demonstrates the quick response of the EO pump in both continuous and intermittent flow control.

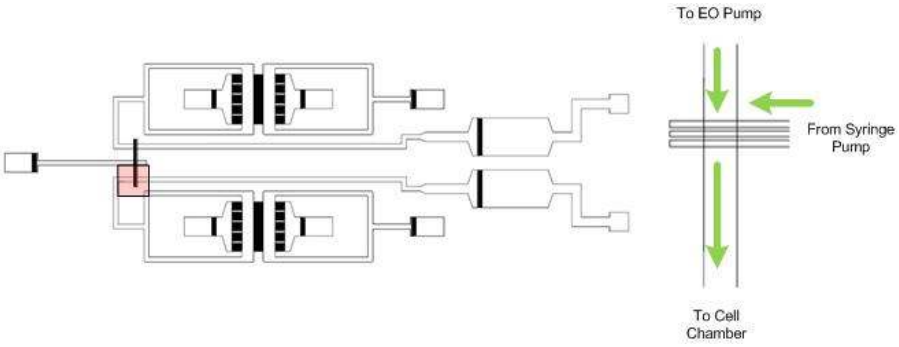

Figure 8.8 Field of view of video #3. On the right a close up of the network geometry in the video indicating the flow direction and locations of the EO pump and cell chamber channels.

8.5 Summary

In this chapter the novel microfluidic network with integrated EO pumps was presented. The design and evaluation of this network was provided with a detailed analysis using a 1D circuit equivalency model. Three potential modes of operation were presented in which the EO pumps act as (i) primary sources of fluid flow (ii) secondary sources of flow manipulation with an external source providing the main flow and (iii) continuous or intermittent injectors of small amounts of fluid. Experimental results in the form of videos demonstrate the operation of the network under these conditions. As discussed in Chapter 7 the operation of the EO pump is limited to about 10-20hrs of continuous operation. Since perfusion times range between 1-7 days for cell culture the first operation mode may not be feasible at this point in time. However, the EO pumps may still operate in the two other modes at periodic time intervals. In the following work with cells only the first operation mode was tested as this represents the worst case scenario.

Chapter 9

Testing of the EO pump Cell Culture Chip

The purpose of this work is to investigate the possibility of using EO pumps on-chip to control fluid flow in a microfluidic cell culture chip. The EO pumps and cell culture network described in Chapters 7 and 8 were experimentally tested by culturing rainbow trout gill cells. Performing these experiments required additional techniques to be developed primarily concerning sterilization of the chip and maintaining sterility outside the bio hood while imaging cells. The procedures for sterilizing the chip, seeding the cells and setting up the perfusion system are discussed within this Chapter. Results are presented for cell culture with continuous perfusion using the integrated EO pumps as the primary flow source.

9.1 Cell Culture Experimental Setup

The following discusses the rainbow trout gill cells, experimental set up and procedures used for testing the microfluidic chip. Working with cells requires expertise in biology and cell culture which was provided by Dr. Lucy Lee at Sir Wilfred Laurier University (Waterloo, Canada). The procedures and techniques described below were developed with assistance from Dr. Lee's students Jackie Beitz, Mary Rose Bufalino and Bounmy Inthavong. All experiments with cells were performed at Dr. Lee's lab.

9.1.1 Cell Line: RT-gill W1

Gill cells were chosen for this initial investigation since their culture requirements are not as demanding compared to mammalian cells. Gill cells (RT-gill W1) do not require incubation or CO_2 regulation and are thus easier to handle during experiments. The RT-gill W1 cell line [Bols *et al.* (1994)] was initiated from primary cultures of rainbow trout gill cells maintained in L-15 medium (Sigma Aldrich) supplemented with 10% fetal bovine serum (FBS). Cells were maintained in a non-vented 75 cm^2 polystyrene tissue culture flasks at room temperature (22 °C) and passaged when 90% confluent. At the time of this thesis the RT-gill W1 cells were passaged over 85 times. The perfusion medium for culture of RT-gill W1 cells was L15-ex (136mM NaCl, 5mM KCl, 1.6mM $MgSO_4$, 2.1mM $MgCl_2$, 1.26mM $CaCl_2$, 1.3mM Na_2HPO_4, 0.36mM KH_2PO_4, 5mM Galactose, 6.7mM Pyruvate). This solution contains the basic salts for cell survival and was obtained from the Dr. Lucy Lee at Wilfred Laurier University. All solutions were first filtered using a 0.2μm pore syringe filter before they entered a microfluidic chip.

9.1.3 Imaging System

For cell imaging during the experiments an inverted phase contrast microscope (Nikon Eclipse TE300) with epifluorescence attachment was used. Phase contrast microscopy is a contrast-enhancing technique that allows for imaging of transparent specimens such as living cells. The technique employs an optical mechanism to translate contrast differences into changes in amplitude, which can then be visualized. Images and videos of the cells and microfluidic network were taken with a digital camera (Nikon coolpix 990). A TV monitor connected to the camera projected the image for more detailed viewing.

9.2 General Experimental Procedure

The overall experimental procedure is described as a schematic presented in Figure 9.1. Below, a brief overview of the experimental procedure will be provided, more detailed discussions are provided in subsequent sections. The procedure for setting up the chip for a cell culture experiment is as follows:

1. First sterilize the chip and peripheral components before any cellular work can be done. After sterilization, the chip and components are only handled inside a bio hood.
2. Before cells can be seeded, a solution is flushed through the chip which promotes cell attachment to the glass substrate of the microfluidic device.
3. The chip is placed inside a refrigeration overnight to complete the surface modification.
4. The next day the attachment solution is flushed out with fresh culture medium
5. A suspension of cells-in-media is obtained from a standard culture flask. The cell solution is then injected into the chip.
6. The cells are allowed to attach to the glass substrate in static conditions for several hours.
7. Afterwards, unattached cells are flushed out with fresh culture medium.
8. The chip is then prepped for the perfusion experiment with the EO pumps. To maintain sterility outside the bio hood during the experiment a specialized bottle system is attached to the chip. The chip is then placed in a custom made chip holder which is place on the microscope stand. Electrodes are inserted into the EO pump reservoirs and the system is set to a specified current.

During experiments the cells are monitored continuously using the digital camera and imaging system. Images were taken periodically during the experiment to determine cell viability. The time period from the start of fabricating a new chip to completing an experiment was 4-5 days. Perfecting the experimental procedures took several iterations and the detailed proceedings are discussed in the subsequent sections.

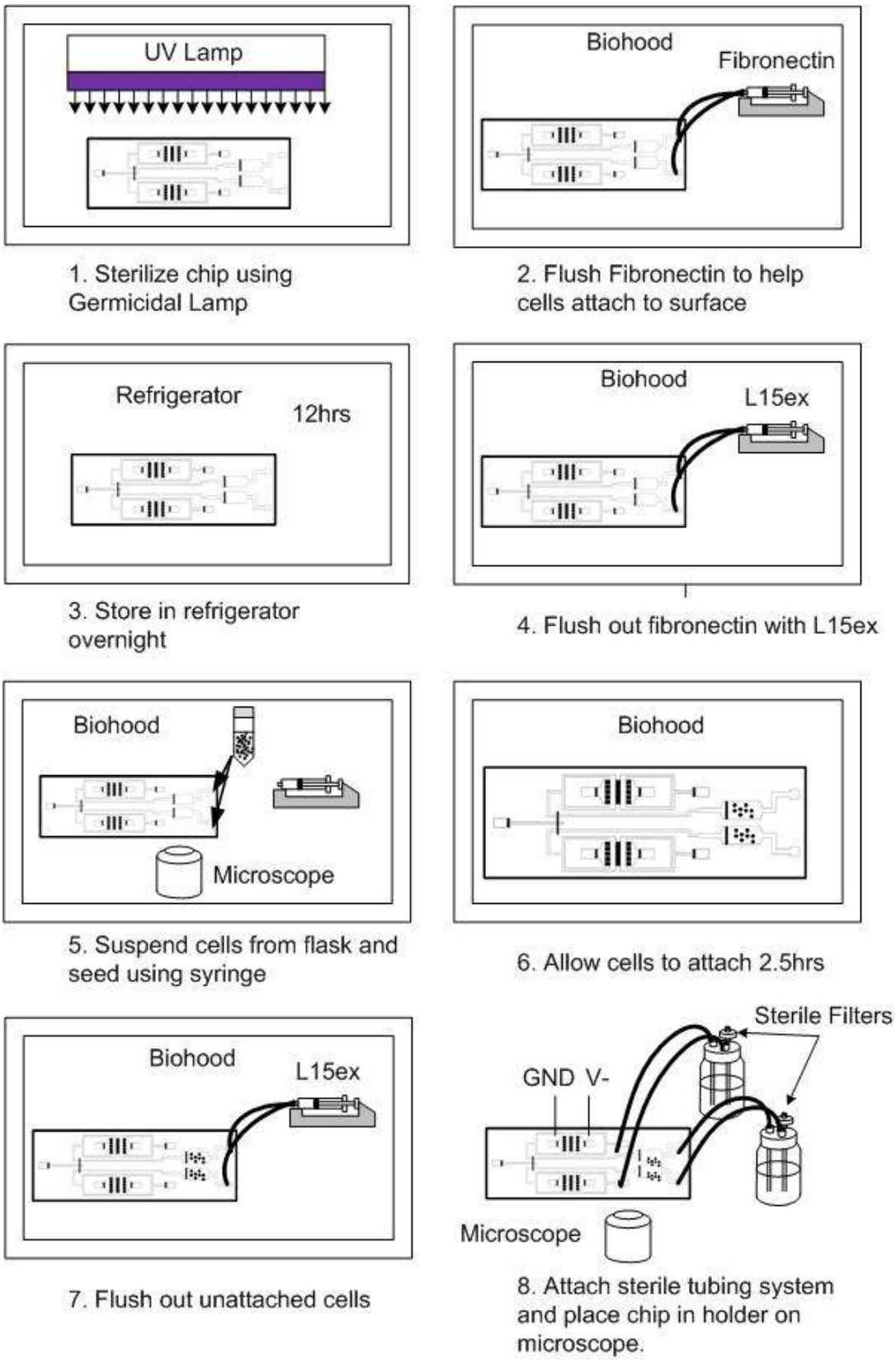

Figure 9.1 Schematic of the procedure for setting up the microfluidic chip for cell culture.

9.2.1 Sterilization of Chip

Effective sterilization of the chip and peripheral components is essential for performing long term cell culture. There are a variety of techniques available for sterilizing components such as autoclaving, washing with 70% ethanol, chemical sterilization with ethylene oxide gas and irradiation with UV light [Kim *et al.* (2007)]. In this work a combination of sterilization methods were used to sterilize the PDMS chip and other components.

The most effective sterilization technique is autoclaving which exposes the components to high temperature pressurized steam (120°C) for a prolonged period of time (15-30min) in order to eliminate transmissible agents such as viruses and bacteria. As one might expect, the melting point of the material must be above the autoclave temperature for this method to work. Many common plastics do not fall into this category, so when purchasing plastic components it is important to check that the component can be autoclaved. In this work, all components used with the microfluidic chip such as tubing, bottles, caps, and Luer connectors were verified to be compliant with autoclave procedures (Omnifit, McMaster-Carr). Prior to starting an experiment all peripheral components were placed in sterilization bags and autoclaved at 121°C, 15psi for 30 minutes.

Although PDMS itself is able to withstand autoclave conditions, the PDMS/glass chip was not autoclaved for two main reasons. First, it was believed that the high thermal stress during heating and cooling may destroy the PDMS/glass bond and more importantly the PDMS/gel bond. In addition, the gel is mainly composed of poly(acrylamide) which possesses an insufficiently low melting point of 84°C. As well, the autoclave treatment would also evaporate all of the liquid inside the microchannels. From experience, refilling channels that have evaporated is very difficult since the PDMS tends to revert back to a hydrophobic state. As a result, two other sterilization methods were attempted to sterilize the PDMS chip: flushing with 70% ethanol and UV irradiation.

The first method that was tried involved flushing the chip with a 70% solution of ethanol following the procedures outlined by Kim *et al.* (2005). The principal of this technique is to flush the ethanol solution for 30 minutes at high pressure to simultaneously sterilize the chip and dissolve any bubbles in the microchannels. Afterwards, the microchannels are flushed continuously for several hours with culture medium to remove any residual ethanol solution. This procedure is typically done overnight, the day before starting experiments with cells. When this

method was applied to the EO pump cell culture chip several problems were encountered. Due to the high hydrodynamic resistance of the EO pumps and intersecting channels the flow rate from the syringe pump was limited to 10μL/min in order to prevent lift-off of the PDMS channels. Since the EO pumps have a higher hydrodynamic resistance than the cell chamber channels very little ethanol solution would pass through the pumps. Therefore, each channel had to be flushed separately (EO pump→cell culture chamber, plus the inlet channel) with ethanol solution followed by the culture medium. Furthermore, at least one thousand channel volume flushes were required to guarantee that the ethanol solution was removed; consequently, the process was very time consuming. In addition, there was another unexpected negative effect of flushing the chip with ethanol. During flushing the gel salt bridges would shrink and recede from the PDMS walls and support posts as shown in Figure 9.2. This phenomenon occurs when the polymer gel is in contact with a poor solvent, in this case ethanol, as opposed to a good solvent such as isopropanol which the gel is originally dissolved in [Iwatsubo and Shinbo (2001)]. Once the chip is refilled with water the gel swells and returns to its previous form; however, the PDMS-gel bonds have been broken and the risk of leakage around the gels increase. From this discussion it is clear that an alternative method of sterilization was required for the EO pumps.

To this end sterilization through irradiation using a UV germicidal lamp (SI-950 Incubator, UVP) was adopted. In this method, the chip was placed 5cm below a UV germicidal lamp for 3 hours. PDMS is transparent down to 240nm allowing for UV sterilization of the microchannels through the top of the layer of the chip [McDonald and Whitesides (2002)]. After the chip was sterilized it was kept in a sterilization bag which was only opened inside a bio hood for further handling. No adverse effects were found in terms of the gel or PDMS.

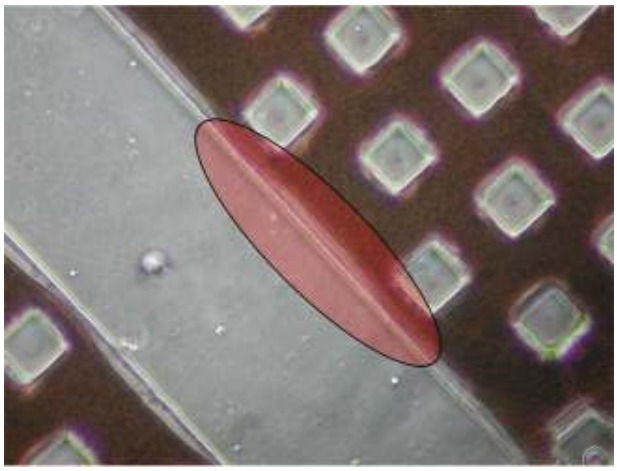

Figure 9.2 Gel shrinking and separation (highlighted red) from the PDMS wall caused by flushing the chip with 70% ethanol solution for sterilization.

9.2.2 Cell Seeding

Cell seeding involves infusing a cell suspension into the cell culture chamber through the outlet reservoirs of the chamber channels. The major challenge with this method is to control the cell density and to ensure that the cells attach to the substrate so that they are not washed away during perfusion. In general, most cells do not attach very well to glass and require an intermediate molecule such as a protein or peptide immobilized on the surface for attachment [Kim *et al.* (2007)]. To create these strong anchoring sites the glass surface must be modified. There is also a limited amount of time for the cells to attach before nutrients are depleted in the cell chamber. Consequently, cells in a microfluidic perfusion system must attach more quickly than in standard cell culture flasks so surface modification is critical.

To help in the seeding of cells into the chamber two surface treatments were used in this work. In the first treatment, a solution of Poly-D-lysine hydrobromide 0.1% (w/v) (P7280, Sigma Aldrich), was flushed through the chip for 30 minutes to promote cell attachment. However, after several attempts to attach the cells without success a different treatment was tried. In the second treatment, a solution (1mg/1mL of sterile water) of fibronectin (F-4759, Sigma Aldrich) was infused into the cell chambers. Fibronectin solution is able to treat unmodified glass substrates as well as surface activated PDMS (UV or plasma treatment) [Toworfe *et al.* (2004)].

This treatment was implemented by placing a small amount of fibronectin solution in the outlet reservoir of the cell chamber channel. A sterile air filled syringe was attached to the reservoir via tubing and a Luer connector. The solution was carefully infused into the cell chamber by hand for several minutes. The process was then repeated for the other cell chamber. Afterwards, all of the outlets on the chip were capped to maintain a sterile environment and the chip was placed in a refrigerator (4°C) overnight. In the mourning, the solution was flushed out with L15ex using the syringe pump at 10μL/min for 1hr. This method proved to work best for attaching the RT-gill W1 cells. Note that patterned seeding of the cells is also possible by locally modifying the substrate through a variety of techniques such as microcontact printing [Khademhosseini *et al.* (2004)] and laminar flow patterning [Takayama *et al.* (1999)]. Both of these techniques could be incorporated in the fabrication of the EO pump microfluidic chip to obtain spatially controlled adhesion.

A cells-in-media suspension was made from the cell culture flask and the number of cells was counted on a hemocytometer with an approximate cell density of 5x106 cells mL-1. Lower seeding densities were found to retard attachment due to the absence of suitable cell-cell contacts.

A small volume (100µL) of the cells-in-media suspension was placed in the outlet reservoir of the two cell chamber channels. Two air filled sterile syringe with tubing and Luer connectors were attached to the reservoirs and 0.2µm syringe filters were placed at all other exposed reservoirs to maintain a sterile environment outside the bio hood. The chip was placed on the phase contrast microscope and the cells were loaded by hand while visualizing the movement with the digital camera. Once the cells had completely filled the cell chamber the syringe was left on and the cells were allowed to attach in a static environment for 2.5 hours. Afterwards, the chip was placed back in the bio hood and unattached cells were flushed out using the syringe pump.

9.2.3 System for Maintaining a Sterile Environment

Maintaining a sterile environment within the microfluidic network is critical once the chip is brought outside the bio hood. The reservoirs of the chip cannot simply be left open to atmosphere as bacteria and viruses may enter the chip. To maintain sterility during the perfusion experiment a closed loop system was developed as shown in figure 9.3. The inlet/outlets of the EO pumps were connected *via* tubing to bottles with specialized bottle caps (00932T-2, Onmifit). These caps have Luer ports integrated into the cap and allow for direct connection into the bottle by force fitting hard wall tubing through the ports. Each cap has three available ports. Two of these ports were used to connect tubing through the port and into the bottle containing the medium. On the other port a 0.2µm syringe filter was attached to maintain a sterile environment and to keep the bottles at atmospheric pressure. The caps and bottles were autoclaved prior to performing an experiment.

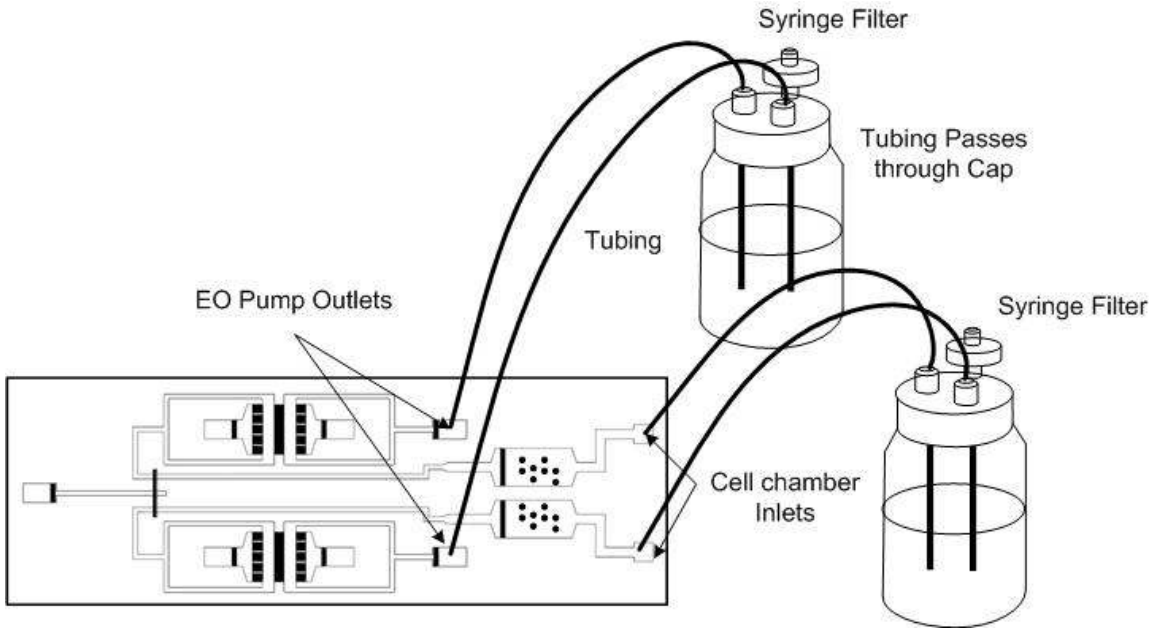

Figure 9.3 System for maintain sterile microfluidic network outside the bio hood using specialized bottles and caps for the reservoirs.

To fill the tubing a syringe was attached to the filter and the bottle was pressurized with air to push the fluid out the tubing. Once the tubing was filled, the connectors were attached using a drip method to prevent bubble entrapment. One bottle was connected to the outlets of the EO pumps and the other to the inlets of the cell chamber channels. The liquid level in both bottles was the same in order to prevent any flow due to a head difference. In addition, the bottle volume was large (30mL) so that there was little change in height during perfusion. Once the system was connected the chip (and bottles) could be moved outside the bio hood and onto the microscope for visualization.

9.2.4 Perfusion Setup

After the sterilization setup was complete the chip was placed in the custom made acrylic holder and placed on top of the microscope stand. Extended reservoir connections were attached to the electrode reservoirs and filled with Bufferall solution. Platinum electrodes were placed in the reservoir approximately 1cm into the solution. A picture of the complete experimental setup for perfusion is shown in Figure 9.4. Tape was used to temporarily secure the holder to the microscope platform. The image also shows the sterile bottle reservoir system attached to one side of the chip. One of the main problems with the experimental setup is that the phase contrast object comes from the top of the microscope and the Luer connectors sometimes block out the field of view. In addition, the tubing connected to the bottle must be flexible or there will be excessive tension on the chip and the tubing may get in the way of the microscope.

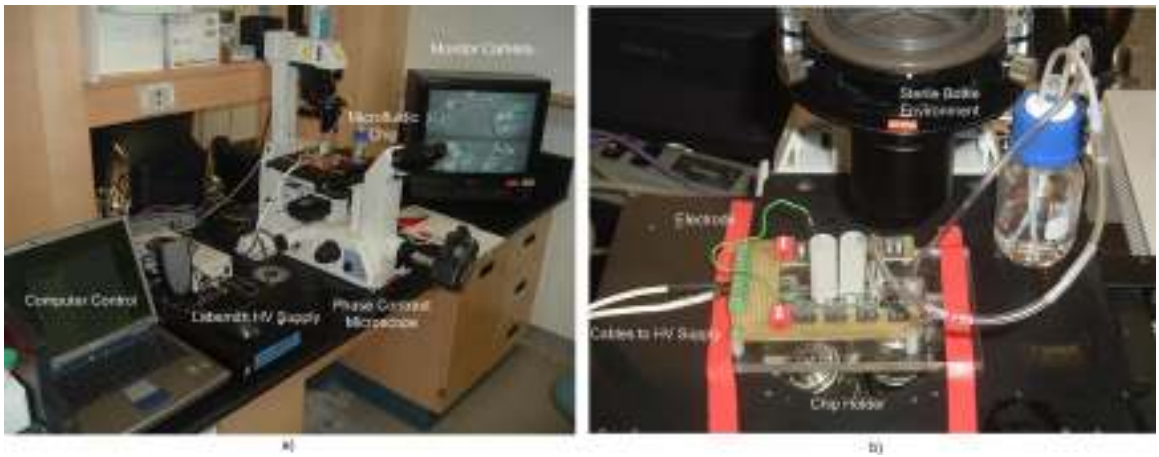

Figure 9.4 Experimental setup of the chip on the phase contrast microscope for EO pumping with the microfluidic chip showing (a) the laptop, HV supply and microscope (b) a close up of the microscope, microfluidic chip, holder and sterile bottle system.

9.3 Experimental Results

Results are presented for cell culture of RT-gill cells in diluted solutions of L15ex in order to exploring the possibility of using lower salt solutions for the EO pumps. As well, experiments with the EO pump cell culture microfluidic chip are presented.

9.3.1 Low Concentration Culture with Cells

To investigate the possibility of using lower salt solutions for medium perfusion with the EO pumps a test was performed to examine the viability of RT-gill cells in conditions of 50% and 25% diluted salts. RT-gill W1 cells were plated in a 6 well plates and left for 1 day with standard culture medium L15ex+10%FBS. On the next day the medium was replaced: 2 wells were set to the control with 100%L15ex, 2 wells to 50% and 2 wells to 25%. The cells were then imaged at 0, 3 and 7 days to study morphological changes. The results are summarized in Figure 5.9. Cells in the severely diluted solution (25%) were unable to withstand the osmotic pressure imbalance and died (see 7days results. Many cells were able to survive in 50% solutions but some changes in morphology were seen. Consequently, a decision was made not to use lower salt solutions as the negative effect on the cells is too large.

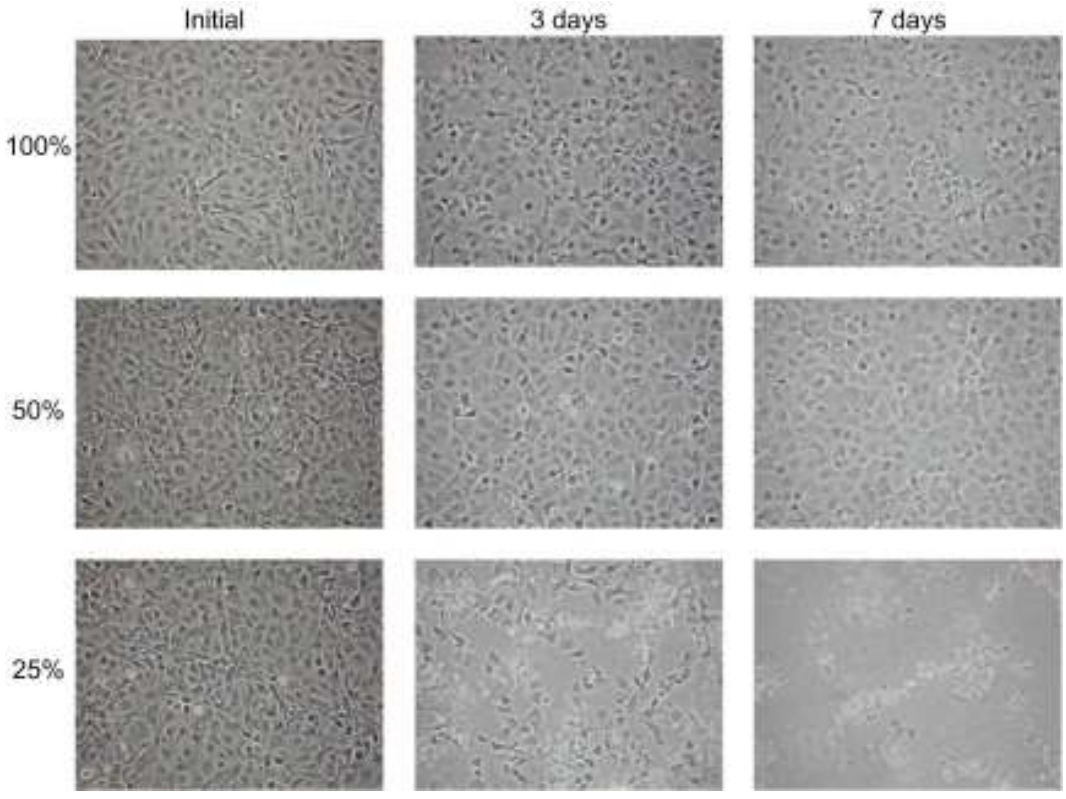

Figure 9.5 Phase contrast images during the osmolarity test with RT-gill W1 cells. Cells were subject to various concentrations of L15ex (100%, 50%, 25%) over a 7 day period. Courtesy Jackie Bietz.

9.3.2 On-chip Perfusion with EO pumps

Since this study is an exploratory investigation into using EO pumps for cell culture applications, the results presented here are largely qualitative. Recall that the main purpose of this work is to verify that EO pumps are able to provide continuous perfusion while eliminating the negative effects of EOF as discussed in Chapter 7. To this end a series of experiments were performed to test the viability of EO pumps.

In this set of experiments the chip was operated only in mode #1, where only the EO pumps are used as pumping sources. This configuration represents the worst case scenario for EO pump operation, as opposed to modes 2 and 3 where a syringe pump provides the main source of flow. For this experiment the chip was prepared following the procedures outline in the previous sections.

For cell culture purposes, seeding cells and attaching them to the substrate is the first step in the experiment. A video (Seeding_cells_in_chamber.avi) of the cells being flowed into the chamber is attached with this thesis (Appendix G). The video shows the cells in suspension being transported with the fluid into the cell chamber. One notices that the cells do not pass individually but a grouped together in larger clusters. Although a single cell may be small (5-10µm) a cluster of cells is quite large (10-200µm in diameter) and may clog the microchannel. To prevent this from happening the exit channel in the cell chamber was designed to be large (1mm W x80µm H). In addition, the filters (25µm) added to the cell culture chamber are not able to block out single cells but are effective in stopping the movement of the more common clusters.

Figure 9.6 shows attachment of cells on the glass substrate after seeding. The first image (figure 9.6a) was taken just after the cells were infused into the cell chamber. The second image (figure 9.6b) shows the cells after 2.5hrs of static culture. Notice that most of the cells have spread and attached to the substrate surface. The attachment of cells is useful meter for cell viability in the microenvironment but is not a definite indicator for all situations. In general, cells that are "happy" with the microenvironment prefer to immobilize and attach to the surface rather than to remain in suspension. For instance, healthy cells in a standard cell culture flask that are 90% confluent are shown in Figure 9.4c. Comparing this image to the cells in the microfluidic chamber, it is evident that the cells in the microfluidic chamber are effectively seeded.

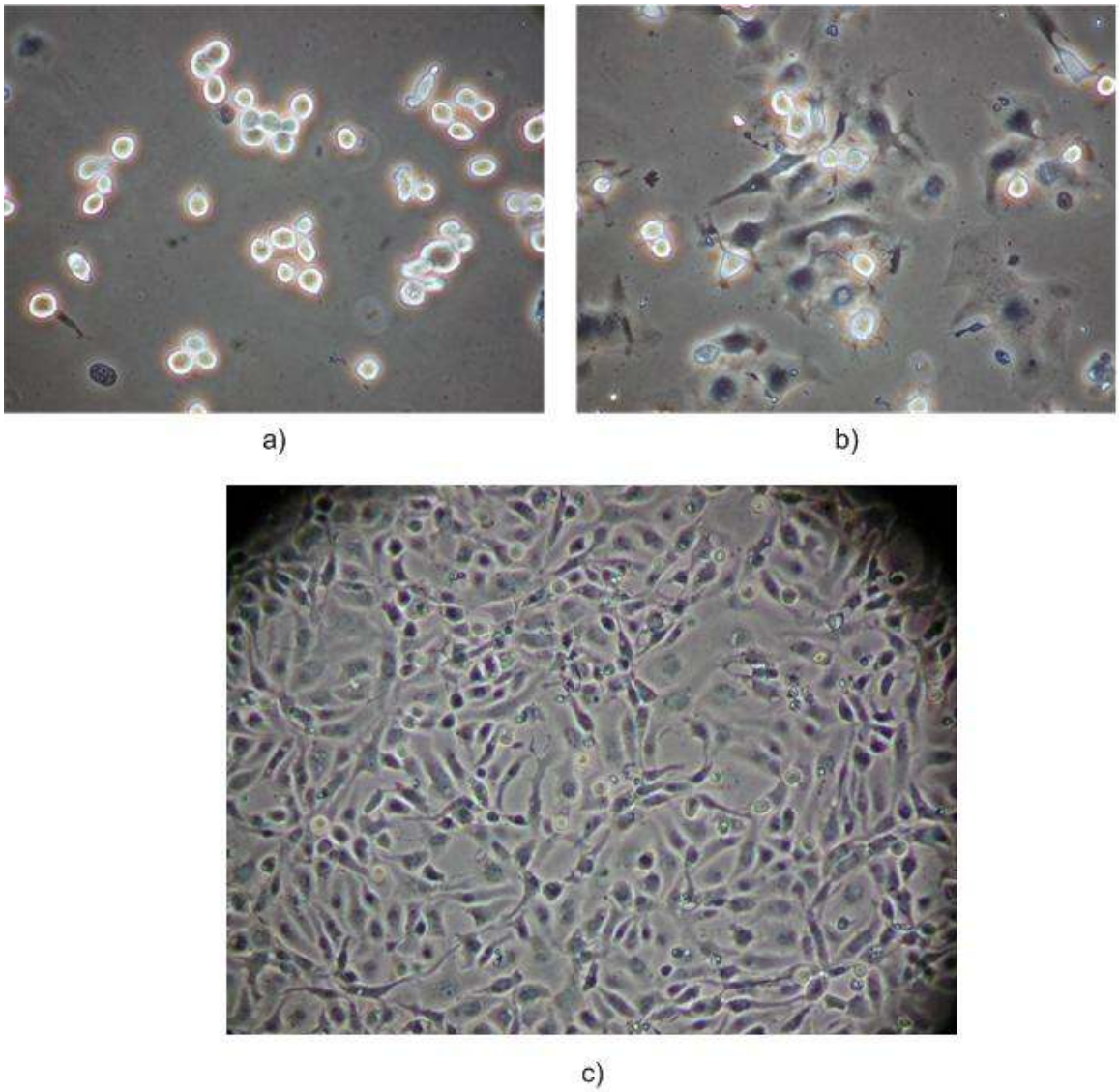

Figure 9.6 Phase contrast images of cells in the chamber (a) immediately after infusing cells into the chamber and (b) 2.5 hrs later cells have mostly attached to the fibronectin coated glass substrate and (c) cells seeded in a conventional static cell culture flask for comparison. The small black areas in the cell are the nucleus.

After the cells were seeded in the cell chamber the EO pumps were turned on and set to 300μA (~0.5μL/min). A combination of L15ex and Bufferall was used as the perfusion medium and reservoir buffer. During perfusion several groups of cells were imaged at several time intervals from the beginning of perfusion. The pump was operated continuously, overnight, for 18hrs using the setup described in the previous sections. The operation time is greater than the expected buffer depletion. This experiment was performed twice on separate days with different chips. The results for both cases were similar and are presented below.

Successive images of a single group of cells in the chamber at different times (t=0, 2, 5, and 18 hrs) are shown in figure 9.7. Comparing the images from times 0-5 hrs, the cells are still alive and actually continue to spread out onto the glass surface. This is most noticeable by comparing images t=0 to t=5 in figure 9.7. The rate of spreading is not as dramatic as would be expected if the cell culture medium contained feeding solution such as FBS. During this time period there is not indication that the cells are negatively affected by the EO pump. Therefore, it can be concluded that a stable microenvironment for cell culture was created. However, in the last image (t=18hrs) the cells are receding from the surface indicating the first stages of possible cell death. The reason degradation in cell vitality is explained by considering the pump performance during the later stages of the experiment.

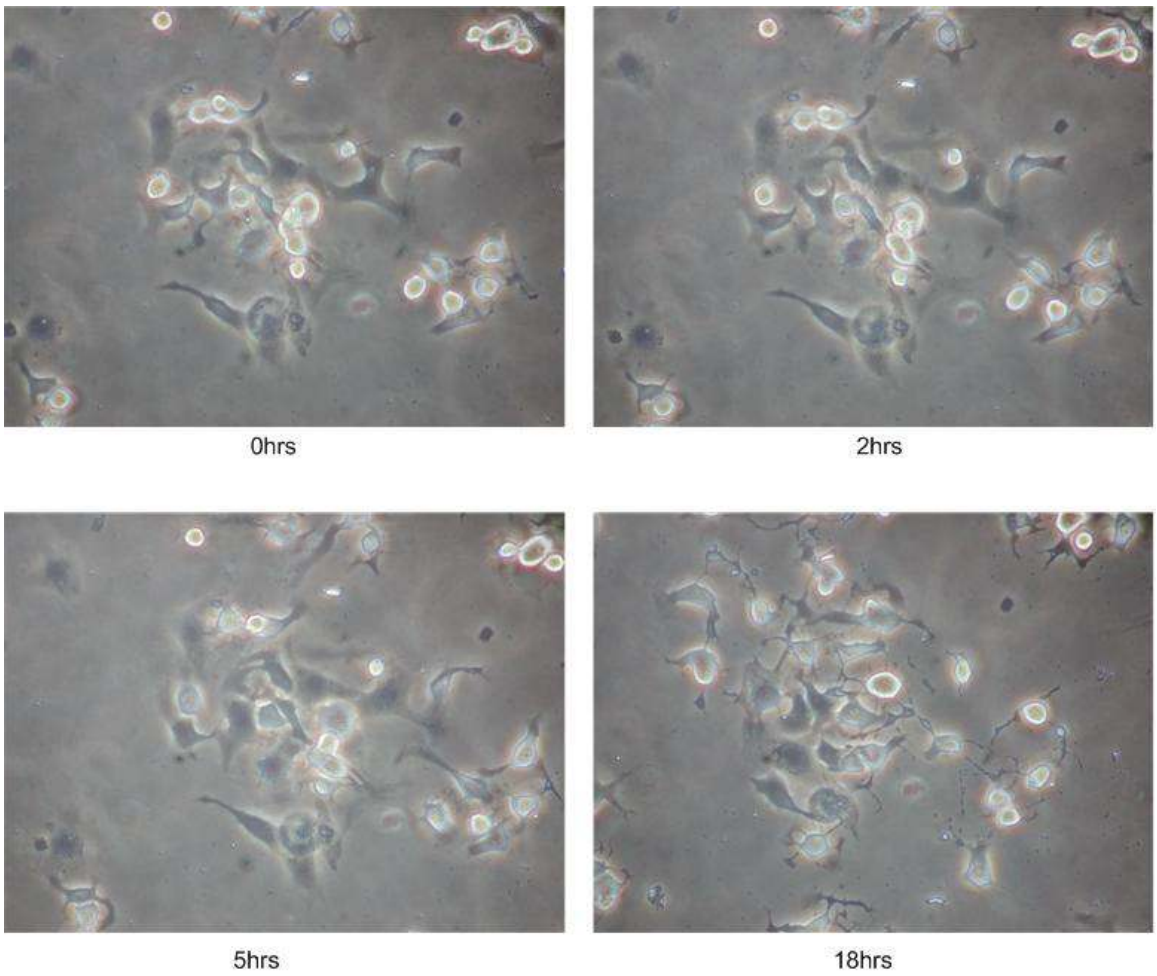

Figure 9.7 Phase contrast images of cells while EO pump perfusion was applied with L15ex medium. The same group of cells was photographed at several time intervals after starting perfusion (a) 0hrs (b) 2 hrs (c) 5hrs and (d) 18hrs.

The applied voltage trace during the experiment is shown in figure 9.8. Recall that the EO pumps operate in a constant current mode so that the voltage is regulated accordingly. Looking closely at the voltage plot we see that the voltage is very stable for the first six hours of operation. However, after this time the voltage begins to increase dramatically until at eight hours the voltage drops down to zero. The increase in applied voltage is caused by electrolysis, most notably bubble formation around the electrodes and polarization. During this time the pump is still operating at the set flow rate. The sudden drop in the voltage at 8hrs indicates that the electrode looses contact with buffer solution causing the HV power supply to shut off. The reason the electrode loses contact is that the electrolysis reaction consumes water in the electrode reservoirs, slowly lowering the liquid level, until eventually one of the electrodes looses contact with the buffer.

Therefore, the cells at the end of the experiment (t=18hrs) were without medium perfusion for nearly ten hours. In a microfluidic cell chamber, the microenvironment volume is small and to prevent build up of waste secreted from the cells continuous perfusion is required. If the waste is not removed the cells are “unhappy” and will begin to detaching from the surface. This explains the decrease in cell vitality at 18 hours. This demonstrates that operational lifetime is one of the limitations of using EO pumps as a primary source of fluid flow. One way to compensate for this is to replenish the buffer solution every 6 hrs, however, this is not practical for long-term culture. Before further experiments are performed a next iteration in the design process is needed to extend the operational time of the EO pumps

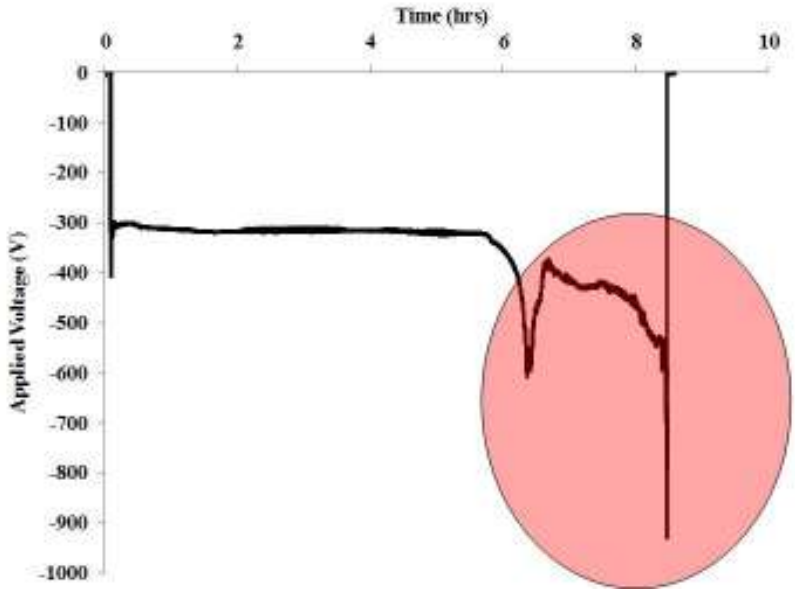

Figure 9.8 Voltage plot of EO pump during cell culture test. Highlighted area shows the drastic increase in applied voltage caused by electrolysis effects.

9.4 Conclusions and Recommendations

Although the EO pump operating time is still less than the perfusion time required for cell culture (1-7 days), the experimental results show that a relatively stable cell culture environment was provided which validates that:

- the risk of high electric fields passing through the cells was eliminated by using integrated EO pumps while still retaining the benefits of EOF.
- through effective design using the 1D circuit analysis high conductivity solutions could be pumped at flow rates required for cell culture.
- electrolysis effects were somewhat suppressed allowing for effective pump operation over a prolonged period of time.
- operating the pump in a constant current mode increased the stability of the pump and maintained a constant flow rate

In the future, continued improvements to the EO pump design will extend the operating time and increase the feasibility of using integrated EO pumps for cell culture. These improvements should focus on increasing electroosmotic flow and reducing or containing electrolysis effects as discussed in Chapter 7. Improving the design of the cell chambers would be useful for future culturing applications as well as modifications to the culture procedure, specifically seeding and sterilization. Additional, experiments with the microfluidic device operating in the two other modes described in chapter 8 should also be performed.

Chapter 10

Conclusions and Recommendations

This chapter provides a summary of the work presented including contributions of this thesis and recommendations for further work.

10.1 Contributions of this Thesis

Continuous perfusion microfluidic devices have the ability to recreate this microenvironment and offer the advantages of increased fluid and media control, reduced consumption of reagents, continuous monitoring of cells and the potential for massively parallel experiments. A number of microfluidic cell culture systems that provide medium perfusion with gas exchange and temperature regulation have been developed. Most microfluidic chips for cell culture applications use pressure driven flow as a major pumping method where syringe pumps are typically used to provide a single source of flow. These designs have a rigid microchannel system where flow is fixed to each chamber and is regulated with off-chip valves. This type of system does not allow for effective and accurate control of the fluid flow needed for dynamic biological studies where small samples of drugs (nL) may need to be injected periodically or continuously.

Electroosmotic flow is another commonly used means for controlling fluids in microfluidic devices. EOF is a compact method where flow rate and direction can be accurately controlled by simply manipulating applied voltages at the reservoirs of the microchannels. The temporal response of EOF is on the order of tens of milliseconds. EOF has been applied in microfluidics for transporting cells in microchannel networks, though, not for cell culture for a variety of reasons. Mostly notably the high electric fields typically used in EOF are hazardous to the cells as they will cause electroporation of the cell membrane; as well, joule heating, electrolysis and the high shear stress for attached cells are also problems. The advantages of EOF can still be realized by utilizing electroosmotic pumps (EO) which generate pressure driven flow from EOF. With EO pumps the electric field is isolated from the cells. EO pumps posses several features that are valuable for dynamic applications including pulsed free flow, almost instant flow control, reversible operation and precise movement of minute volumes of fluid (μL-pL). The integration of internal pumps onto the chip also opens up the possibility of multi-fluid control without valves or external pumps. The purpose of this work was to investigate the possibility of combining on-chip EO pumps with a PDMS cell culture network.

As part of this work, the fabrication of PDMS chips using soft lithography techniques was developed at the University of Waterloo Microfluidics and Biochip Lab. Protocols were established for fabricating the master, PDMS mold and attaching fluidic connectors (Chapter 5). This included a system calibration for spin coating, UV exposure and bake times for the masters, plasma treatment and bonding for the PDMS, and the implementation of nano-flow connectors and components for pressure driven flow. In addition, procedures were established for fabricating multi-level structures. The fabrication techniques established in Chapter 5 were used extensively in the development of the EO pump cell culture chip.

To effectively incorporate EOF flow into a microfluidic application, the electroosmotic mobility for the microchannel/liquid must be well known. Thus a system based on the current monitoring technique was setup to perform the measurements. This included the development of a new Y-channel design that provides substantial improvement over the traditional straight channel design. The channel was designed and evaluated using numerical simulations conducted with COMSOL Multiphysics as well as compact circuit models to study the displacement process (Chapter 4). Several aspects were taken into consideration during the design including the suppression of undesired pressure driven flow, electrolysis, and joule heating. The Y-channel design shows a superior ability in generating sharp start and end times for displacement compared to the traditional straight channel configuration. In addition, more displacements can be performed in a shorter period of time increasing the accuracy of the measurements. Measurements made by the Y-channel were first validated by comparing with several straight channel measurements published in literature with excellent agreement. The Y-channel was then used to measure the electroosmotic mobility of a number of solutions relevant to the microfluidics community in order to develop a database for later reference. The Y-channel was also applied to measure the properties of L15ex used for cell culture and testing the effect of several surface treatments in an attempt to increase EO pump performance (Chapter 8).

By using an EO pump rather than EOF we can take advantage of the benefits EOF without physically harming the cells due to the high electric field that is required for EOF. Two types of EO pumps were developed based on the integration of commercial ion exchange membranes and the fabrication of *in situ* gel salt bridges. Only the later was successfully used for the EO pumps, since the former had several fabrication issues that could not be overcome such as swelling and sealing. As part of this work a fabrication procedure was developed for the gel salt bridges. This procedure improved the mechanical stability of the gels by binding them to the PDMS

microchannel walls. The pumps were fabricated using soft-lithography techniques and multi-level with multi-level (4) structure masters (Chapter 5). Using a combination of full 3D modeling and 1D equivalent circuit modelling a number of EO pumps were designed using the gel salt bridge concept (Chapter 7). Each iteration of the design provided improvements in fabrication and overall performance. The final design shows excellent uniformity of the electric field in the EOF region of the pump, as well as high flow rate and the suppression of undesired pressure driven flow.

The EO pumps were tested with several combinations of fluids including the cell culture medium L15ex and two buffers 1XTBE and Bufferall. Through experimentation the flow rate versus applied current was determined by fluorescence visualization (Chapter 3). As well, interesting issues involving mass transport through the gels was raised, which may warrant further study. To improve stability, the EO pumps were operated in a constant current configuration as this eliminated problems associated with bubble generation and polarization. Electrolysis was accounted for by using large electrode reservoirs with well buffered solutions such as Bufferall. Both of these methods helped prolong the operation of the pump. Improvements to the flow rate were also attempted through various surface modifications of the PDMS; however, none of these attempts were successful.

The pumps were integrated into a new perfusion cell culture chip (Chapter 8). The design and operation of the network was done using 1D circuit modeling (Chapter 3). Undesired pressure driven flow was suppressed by using an intersecting channel with a high hydrodynamic resistant. This helped stabilize the operation of the chip, and isolated the two EO pumps from each other. The flexibility of using EO pumps on-chip was demonstrated by the three potential modes of operation for the pumps. In the first mode, the EO pumps act as primary sources of fluid flow to the cell chambers. In the second and third modes, the EO pumps are secondary sources of fluid flow, manipulating the incoming stream from a syringe pump by directing fluid away from the chambers (mode 2) or injecting fluid into the main stream (mode 3). Since the EO pumps can operate both as flow rate valves and pumps they have an added flexibility which simple vales do not. The pumps were operated with the ground electrode towards the cells so there was no applied potential in the cell chambers. Experiments with fluorescence visualization were presented to show the operation of the microfluidic chip in the three main modes.

Experiments with cells were performed in order to validate that EO pumps coupled with cell culture is feasible (Chapter 9). Rainbow trout gill cells (RT-gill W1) were cultured in the microfluidic network using only the EO pumps as the primary source of perfusion. Several issues were solved pertaining to these experiments including the problems of sterilization the chip and improving cell attachment to the substrate. A system was also developed for maintain a sterile environment for the cells outside of the bio hood. A series of tests were performed where the RT-gill W1 cells were seeded and then perfused with L15ex for a prolonged period of time. Images taken during the experiment show that there are no ill effects on the cells while the EO pump is operating. However, continuous pumping lasted only for 8 hours before instabilities in the pump caused by electrolysis stopped perfusion. Although, the results are preliminary and qualitative, it has been shown that EO pumps can be incorporated into a cell culture perfusion system; however, more work still needs to be done to investigate the impact on cells.

10.1 Recommendations for Extension of Work

The work done as part of this thesis can be thought of as a first step in an overall design process. The next iteration in the design will require several improvements to the EO pumps and cell culture network. The major recommendations for continuing this project are described below.

Integrated EO Pump

Improvements to the EO pump can be broken down into two parts: increasing the overall flow rate and suppressing electrolysis effects. To improve the flow rate of the pump the electroosmotic mobility must be significantly increased. Any improvement will have a significant effect on performance by decreasing the current draw and thus the effects of electrolysis. These improvements will most likely require the use of surface treatments to modify the PDMS EOF channels and will require the co-operation of researchers from chemistry to assist in the development of such treatments. There also exists the possibility of using high surface charge polymer monoliths fabricated within the chip using photopolymerization. Polymer monoliths are similar to the gels currently used in this study but contain small pores (1-5μm) that would replace the shallow EOF channel. Again assistance from researchers in chemistry is vital. Although improvements to the flow rate will help, the majority of research effort should be put towards improving the overall stability and operating time of the EO pumps. Investigating additional buffers that could absorb electrolysis effects for a longer period of time would be a first step in this process. However, this method will never completely solve the long-term stability issues. A more probable solution is the use of anion exchange membranes to prevent the transport of

unwanted ions as suggested by Brask *et al.* (2004). Although there are several issues with integrating membranes that must be solved (swelling, sealing ect.). If these improvements cannot be achieved than the EO pump run time should be limited. The EO pumps may then be used as drug injectors or flow control valves and not as primary sources of fluid flow.

Cell Culture Network

In all cases, experiments with cells should be continued in order to determine the impact of EO pumps on cells. More design work is needed for the cell culture chamber to assure uniform seeding of the cells and perfusion of soluable factors. As well, improvements to the overall network design and operation would be beneficial. For instance, simplify the seeding of cells, perfusion set up and sterilization system. Finally, to achieve complete independent culture outside of the incubator, systems for maintaining temperature and gas exchange must be developed for mammalian cells.

References

Abgrall, P., Gué, A.M. (2007) "Lab-on-chip technologies: making a microfluidic network and coupling it into a complete microsystem-a review." Journal of Micromechanics and Microengineering, 17, R15-R49.

Andersson, H., van den Berg, A. (2004) "Microfabrication and microfluidics for tissue engineering: state of the art and future opportunities." Lab on a Chip, 4, 98-103.

Applegate, R.W., Squier, J., Vestad, T., Oakey, J., Marr, D.W.M., Bado, P., Dugan, M.A., Said, A.A. (2006) "Microfluidic sorting system based on optical waveguide integration and diode laser bar trapping." Lab on a Chip, 6, 422-426.

Arulanandam, S., Li, D. (2000) "Determining ζ potential and surface conductance by monitoring the current in electro-osmotic flow." Journal of Colloid and Interface Science, 225, 421-428.

Badal, M.Y., Wong, M., Chien, N., Salimi-Moosavi, H., Jarrison, D.J. (2002) "Protein separation and surfactant control of electroosmotic flow in poly(dimethylsiloxane)-coated capillaries and microchips." Journal of Chromatography A, 947, 277-286.

Bahrami, M., Yovanovich, M.M., Culham, R. (2006) "Pressure Drop of Fully-Developed, Laminar Flow in Microchannels of Arbitrary Cross-Section." Journal of Fluids Engineering, 128, 1036-1044.

Beebe, D.J., Mensing, G.A., Walker, G.M. (2002) "Physics and Applications of Microfluidics in Biology." Annual Review of Biomedical Engineering, 4, 261-286.

Bedekar, A.S., Wang, Y., Krishnamoorthy, S. (2006) "System-Level Simulation of Flow-Induced Dispersion in Lab-on-a-Chip Systems." IEEE Transactions on Computer-aided Design of Integrated Circuits and Systems, 25, 294-303.

Bello, M.S. (1996) "Electrolytic modification of a buffer during a capillary run." Journal of Chromatography A, 744, 81-91.

Bhatai, S.N., Balis, U.J>, Yarmush, M.L., Toner, M. "Effect of cell-cell interactions in preservation of cellular phenotype

Bhattacharya, S., Datta A., Berg, J.M., Gangopadhyay, S. (2005) "Studies on surface wettability of poly(dimethyl)siloxane (PDMS) and glass under oxygen-plasma treatment and correlation with bond strength." Journal of Microelectromechanical Systems, 14, 590-597.

Bianchi, F., Wagner, F., Hoffmann, P., Girault, H.H. (2001) "Electroosmotic Flow in Composite Microchannels and Implications in Microcapillary Electrophoresis Systems." Analytical Chemistry, 73, 829-836.

Bodas, B., Khan-Malek, C. (2006) "Formation of more stable hydrophilic surfaces of PDMS by plasma and chemical treatments." Microelectronic Engineering, 83, 1277-1279.

Bodas, B., Khan-Malek, C. (2007) “Hydrophilization and hydrophobic recovery of PDMS by oxygen and chemical treatment-An SEM investigation.” Sensors and Actuators B, 123,368–373.

Böhm, S., Björn, T., Olthuis, W., Bergveld, P. (2000) “A closed-loop controlled electrochemically actuated micro-dosing system.” Journal of Micromechanics and Microengineering, 10, 498-504.

Bols, N.C., Barlian, A., Chirino-Trejo, M., Caldwell, S.J., Goegan, P., Lee, L.E.J. (1994) “Development of a cell line from primary cultures of rainbow trout, Oncorhynchus mykiss (Walbaum), gills.” Journal of Fish Diseases, 17, 601–611.

Boxshall, K., Wu, M.H., Cui, Z., Cui, Z., Watts, J.F., Baker, M.A. (2006) “Simple surface treatments to modify protein adsorption and cell attachment properties within a poly(dimethylsiloxane) micro-bioreactor.” Surface and Interface Analysis, 38, 198-201.

Braschler, T., Metref, L., Zvitov-Marabi, R., van Lintel, H., Demierre, N., Theytaz, J., Renaud, P. (2007) “A simple pneumatic setup for driving microfluidics.” Lab on a Chip, 7, 420-422.

Brask, A., Goranovic´, G., Bruus, H. (2003) “Theoretical analysis of the low-voltage cascade electro-osmotic pump.” Sensors and Actuators B, 92, 127–132.

Brask, A., Kutter, J.P., Bruus, H. (2005) “ Long-term stable electroosmotic pump with ion exchange membranes.” Lab on a Chip, 5, 730–738.

Breur, E.K.S. Micro- and Nano-Scale Diagnostic Techniques. Springer Verlag, New York, NY.

Butler, M. (2004) “Animal Cell Culture and Technology: The Basics. Garland Science/BIOS Scientific Publishers, Oxon, UK.

Carlier, J., Arscott, S., Thomy, V., Fourrier, J.C., Caron, F., Camart, J.C., Druon, C., Tabourier, P. (2004) “Integrated microfluidics based on multi-layered SU-8 for mass spectrometry analysis.” Journal of Micromechanics and Microengineering, 14, 619-624.

Castellanos, A., Ramos, A., Gonzalez, A., Green, N.G., Morgan H. (2003) “Electrohydrodynamics and dielectrophoresis in microsystems: scaling laws.” Journal of Physics D: Applied Physics, 36, 2584-2597.

Chakrabarty, K., Zeng, J. (2006) Design Automation Methods and Tools for Microfluidics-Based Biochips. Springer, Dordrecth, Netherlands.

Chang, D.C., Chassy, B.M., Saunders, J.A., Sowers, A.E. (1992) Guide to Electroporation and Electrofusion. Academic Press, Inc. San Diego, CA.

Chatterjee, A.N., Aluru, N.R., (2005) “Combined Circuit/Device Modeling and Simulation of Integrated Microfluidic Systems.” Journal of Microelectromechanical Systems, 14, 81-95.

Chen, C.H., Santiago, J.G. (2002) “A planar electroosmotic micropump.” Journal of Microelectromechanical Systems, 11, 672-683.

Chen, L., Ma, J., Guan, Y. (2004) "Study of an electroosmotic pump for liquid delivery and its application in capillary column liquid chromatography." Journal of Chromatography A, 1028, 219-226.

Chen, L., Wang, H., Ma, J., Wang, C., Guan, Y. (2005) "Fabrication and characterization of a multi-stage electroosmotic pump for liquid delivery." Sensors and Actuators b, 104, 117-123.

Chien, R.L., Bousse, L. (2002) "Electroosmotic pumping in microchips with nonhomogeneous distribution of electrolytes." Electrophoresis, 23, 1862-1869.

Chien, R.L., Helmer, J.C. (1991) "Electroosmotic properties and peak broadening in field-amplified capillary electrophoresis." Analytical Chemistry, 64, 1354-1361.

Chin, C.D., Linder, V., Sia, S.K. (2007) "Lab-on-a-chip devices for global health: Past studies and future opportunities." Lab on a Chip, 7, 41-47.

Chiou, C.H., Lee, G.B. (2004) "Minimal dead-volume connectors for microfluidics using PDMS casting techniques." Journal of Micromechanics and Microengineering, 14, 1484-1490.

Cho, B.S., Schuster, T.G., Zhu, X., Chang, D., Smith, G.D., Takayama, S. (2003) "Passively driven integrated microfluidic system for separation of motile sperm." Analytical Chemistry, 75, 1671-1675.

Choi E.S. Yang S.Y, "Improvement of electroosmotic flow characteristics in poly(dimethylsiloxone) channels via long life chemical surface modification", 7th international conference on miniaturized chemical and biomedical analysis system, 2003, CA.

Chou, H.P., Unger, M.A., Quake S.R. (2001) "A Microfabricated Rotary Pump." Biomedical Microdevices, 3,323-340.

Chuang, Y.J., Tseng, F.G., Lin, W.K. (2002) "Reduction of diffraction effect of UV exposure on SU-8 negative thick photoresist by air gap elimination." Microsystem Technologies, 8,308–313.

Crabtree, H.J., Cheong, E.C.S., Tilroe, D.A., Backhouse, C.J. (2001) "Microchip Injection and Separation Anomalies due to Pressure Effects." Analytical Chemistry, 73, 4079-4086.

Dai, J., Ito, T., Sun, L., Crooks, R.M., (2003) "Electrokinetic Trapping and Concentration Enrichment of DNA in a Microfluidic Channel." Journal of American Chemical Society, 125, 13026-13027.

Davis, J.M. (2002) Basic Cell Culture. Oxford University Press, Oxford, UK.

de Jesus, D.P., Brito-Neto, J. G.A., Richter E.M., Angnes, L., Gutz, I.G.R., do Lago, C.L. (2005) "Extending the Lifetime of the Running Electrolyte in Capillary Electrophoresis by Using Additional Compartments for External Electrolysis." Analytical Chemistry, 77, 607-614.

de Mello, A.J., Habgood, M., Lancaster N.L., Welton, T., Wootton R.C.R. (2004) "Precise temperature control in microfluidic devices using Joule heating of ionic liquids." Lab Chip, 4, 417-419.

de Mello, A.J. (2006) "Control and detection of chemical reactions in microfluidic systems." Nature, 442, 394-402.

Devasenathipathy, S. Santiago, J.G., Takehara K. (2002) "Particle tracking techniques for electrokinetic microchannel flows." Analytical Chemistry, 74, 3704-3713.

Devasenathipathy S., Santiago, J.G. (2003) "Electrokinetic Flow Diagnostics" Micro- and Nano-Scale Diagnostic Techniques (Chapter 3). Springer Verlag, New York, NY.

Dittrich, P.S., Tachikawa, K., Manz, A. (2006) "Micro Total Analysis Systems. Latest Advancements and Trends." Analytical Chemistry, 78, 3887-3908.

Duffy, D.C., McDonald, J.C., Shueller, O.J.A., Whitesides, G.M. (1998) "Rapid Prototyping of Microfluidic Systems in Poly(dimethylsiloxane)." Analytical Chemistry, 70,4974-4984.

Dunphy, K.A., Karnik, R.N., Trinkle, C. (2005) "Analysis of governing parameters for silver-silver chloride electrodes in microfluidic electrokinetic devices." Microscale Thermophysical Engineering, 9:199–211.

Duong, T.N.T., Cheang, H.N., Ghista, D.N., Liu, A.Q. (2006) "Stable and High-Volume Electroosmotic Transport for Microfluidic Chip." Emerging Technologies-Nanoelectronics, 2006 IEEE Confererence, 237-240.

Dutta, P., Beskok, A. (2001) "Analytical Solution of Combined Electroosmotic/Pressure Driven Flows in Two-Dimensional Straight Channels: Finite Debye Layer Effects." Analytical Chemistry, 73, 1979-1986.

Dutta, P., Beskok, A., Warburton, T.C. (2002) "Numerical Simulation of Mixed Electroosmotic/Pressure Driven Microflows." Numerical Heat Transfer Part A, 41, 131-148.

Eddingtion, D.T, Puccineli, J.P., Beebe, D.J. (2006) "Thermal aging and reduced hydrophobic recovery of polydimethylsiloxane." Sensors and Actuators B, 114, 170-172.

El-Ali, J., Sorger, P.K., Jensen, K.F. (2006) "Cells on chips." Nature, 442, 403-411.

Erickson, D. (2005) "Towards numerical prototyping of labs-on-chip: modeling for integrated microfluidic devices." Microfluid Nanofluid, 1, 301-318.

Erickson, D., Li, D., Werner, C. (2000) "An Improved Method of Determining the ζ –Potential and Surface Conductance."Journal of Colloid and Interface Science, 232, 186–197.

Erickson, D., Li, D. (2002) "Influence of Surface Heterogeneity on Electrokinetically Driven Microfluidic Mixing." Langmuir, 18, 1883-1892.

Erickson, D., Li, D., (2004) "Integrated Microfluidic Devices." Analytica Chimica Acta, 507, 11-26.

Erickson, D.; Sinton, D.; Li, D. (2003) “Joule heating and heat transfer in poly(dimethylsiloxane microfluidic systems.” Lab on a Chip, 3, 141-149.

Fletcher, P.D.I., Haswell S. J., Zhang X. (2001) “Electrical currents and liquid flow rates in micro-reactors.” Lab on a Chip, 1, 115-121.

Fredrickson, C.K., Fan, Z.H. (2004) “Macro-to-micro interfaces for microfluidic devices.” Lab on a Chip, 4, 525-533.

Fritz, J.L., Owen, M.J. (1995) “Hydrophobic recovery of plasma-treated polydimethylsiloxane,” The Journal of Adhesion, 54:1, 33-45.

Fu, R., Xu, B., Li, D. (2006) “Study of the temperature field in microchannels of a PDMS chip with embedded local heater using temperature-dependent fluorescent dye.” International Journal of Thermal Sciences, 45, 841–847.

Futai, N., Gu, W., Songa, J.W., Takayama, S. (2006) “Handheld recirculation system and customized media for microfluidic cell Culture.” Lab Chip, 6, 149–154

Gao, J., Yin, X.F., Fang, Z.L. (2004) “Integration of single cell injection, cell lysis, separation and detection of intracellular constituents on a microfluidic chip,” Lab on a Chip, 4, 47–52.

Garcia, C.D., Liu., Y., Anderson, P., Henry, C.S. (2003) “Versatile 3-channel High-Voltage Power Supply for Microchip Capillary Electrophoresis.” Lab on a Chip, 3, 324-328.

Geshke, O., Klank, H., Telleman, P. (2004) Microsystems Engineering of Lab-on-a-Chip Devices. Wiley-VCH, Weinheim, Germany.

Ghosal, S. (2002) “Effect of Analyte Adsorption on the Electroosmotic Flow in Microfluidic Channels.” Analytical Chemistry, 74, 771-775.

Ghosal, S. (2004) “Fluid mechanics of electroosmotic flow and its effect on band broadening in capillary electrophoresis.” Electrophoresis, 25, 214-228.

Gomez-Sjoberg, R., Leyrat, A.A., Pirone, D.M., Chen, C.S., Quake, S.R. (2007) "Versatile, Fully Automated, Microfluidic Cell Culture System," Analytical Chemistry, 79, 8557-8563.

Griffiths, S.K., Nilson, R.H. (2005) “The efficiency of electrokinetic pumping at a condition of maximum work.” Electrophoresis, 26, 351-361.

Gu Y., Li, D. (2000) “The ζ-Potential of Glass Surface in Contact with Aqueous Solutions.” Journal of Colloid Interface Science, 226, 328-339.

Haeberle, S., Zengerle, R. (2007) “Microfluidic platforms for lab-on-a-chip applications.” Lab on a Chip, 7, 1094-1110.

Harrison, D.J., Manz, A., Fan, Z., Ludi, H., Widmer, H.M. (1992) “ Capillary Electrophoresis and Sample Injection Systems Integrated on a Planar Glass Chip.” Analytical Chemistry, 64, 1926-1932.

Harrison, M.A., Rae, I.F. (1997) “General techniques of cell culture.” Cambridge University Press, UK.

Hasselbrink, E.F., Kirby, B.J. (2004) “Zeta potential of microfluidic substrates: 1. Theory, experimental techniques, and effects on separations.” Electrophoresis, 25, 187–202.

Hasselbrink, E.F., Kirby, B.J. (2004) “Zeta potential of microfluidic substrates: 2. Data for Polymers.” Electrophoresis, 25, 203-213.

Hartshorne, H., Backhouse, C.J., Lee, W.E. (2004) “Ferrofluid-based microchip pump and valve.” Sensors and Actuators B, 99, 592-600..

Heo, Y.S., Cabrera, L.M., Song, J.W., Futai, N., Tung, Y.C., Smith, G.D., Takayama, S. (2007) “Characterization and Resolution of Evaporation-Mediated Osmolality Shifts That Constrain Microfluidic Cell Culture in Poly(dimethylsiloxane) Devices.” Analytical Chemistry, 79, 1126-1134.

Ho, C.M., Tai, Y.C. (1998) “Micro-Electro-Mechanical-Systems (MEMS) and Fluid Flows.” Annual Review of Fluid Mechanics, 30, 579-612.

Hohreiter, V., Wereley, S.T., Olsen, M.G., Chung, J.N. (2002) “Cross-correlation analysis for temperature measurement.” Measurement Science and Technology, 13, 1072-1078.

Hu, J.S., Chao, C.Y.H. (2007) “A study of the performance of microfabricated electroosmotic pump.” Sensors and Acuators A, 135, 273-282.

Hu, S., Ren, X., Bachman, M., Sims, C.E., Li, G.P., Allbritton, N.L. (2002) “Surface Modification of Poly(dimethylsiloxane) Microfluidic Devices by Ultraviolet Polymer Grafting.” Analytical Chemistry, 74,4117-4123.

Hu, S., Ren, X., Bachman, M., Sims, C.E., Li, G.P., Allbritton, N. (2003) “Cross-linked coatings for electrophoretic separations in poly(dimethylsiloxane) microchannels.” Electrophoresis, 24, 3679–3688.

Hu, S., Ren, X., Bachman, M., Sims, C.E., Li, G.P., Allbritton, N.L. (2004) “Surface-Directed, Graft Polymerization within Microfluidic Channels.” Analytical Chemistry, 76,1865-1870.

Huang, L., Wang, W., Murphy, M.C., Lian, K., Ling, Z.G. (2000) “LIGA fabrication and test of a DC type magnetohydrodynamic (MHD) micropump.” Microsystem Technology, 6, 235-240.

Hung, P.J., Lee, P.J., Sabounchi, P., Lee, L.P. (2005) “Continuous Perfusion Microfluidic Cell Culture Array for High-Throughput Cell-Based Assays,” Biotechnology and Bioengineering, 89, 1-8.

Hung, P.J., Lee, P.J, Sabounchi, P., Aghdam, N., Lin, R., Lee, P.L. (2005) “A novel high aspect ratio microfluidic design to provide a stable and uniform microenvironment for cell growth in a high throughput mammalian cell culture array.” Lab on a Chip, 5, 44–48.

Hunter, R. J. (1981) Zeta Potential in Colloid Science: Principles and Applications, Academic Press, New Yourk, NY.

Incropera, F.P., DeWitt, D.P. (1990) Fundamentals of heat and mass transfer. Wiley, New York.

Incropera, F.P; DeWitt D.P. (2002), Fundamentals of Heat and Mass Transfer Fifth Edition, John Wiley and Sons.

Iwatsubo, T., Shinbo, T. (2001) "Measurement of liquid composition change inside polymer gels shrinking in liquid mixture." Journal of Macromolecular Science Part B, 6, 1017-1028.

Jackson, D.J., Naber, J.F., Roussel Jr., T.J., Crain, M.M., Walsh, K.M., Keynton, R.S., Baldwin, R.P. (2003)"Portable High-Voltage Power Supply and Electrochemical Detection Circuits for Microchip Capillary Electrophoresis." Analytical Chemistry, 75, 3643-3649.

Jeong, O.C., Park, S.W., Yang, S.S., Pak J.J. (2005) "Fabrication of a peristaltic PDMS micropump." Sensors and Actuators A, 123-124, 453-458.

Jeong , O.C., Yang, S.S. (2000) "Fabrication and test of thermopneumatic micropump with a corrugated p+ diaphragm." Sensors and Actuators A, 83, 249-255.

Jo, B.H., Van Lerberghe, L.M., Motsegood, K.M., Beebe, D.J. (2000) "Three-Dimensional Micro-Channel Fabrication in Polydimethylsiloxane (PDMS) Elastomer." Journal of Microelectromechanical Systems, 9, 76-81.

Kane, B.J., Zinner, M.J., Yarmush, M.L., Toner, M. (2006) "Liver-specific Functional Studies in a Microfluidic Array of Primary Mammalian Hepatocytes." Analytical Chemistry, 13, 4291-4298.

Khademhosseini, A., Suh, K.Y., Jon, S., Eng, G., Yeh, J., Chen, G.J., Langer, R. (2004) "A Soft Lithographic Approach To Fabricate Patterned Microfluidic Channels." Analytical Chemistry, 76, 3675-3681.

Khademhosseini, A., Yeh, J., Eng, G., Karp, J., Kaji, H., Borenstein, J., Farokhzadf, O.C., Langer, R. (2005) "Cell docking inside microwells within reversibly sealed microfluidic channels for fabricating multiphenotype cell arrays." Lab Chip, 5, 1380-1386.

Khandurina, J., McKnight, T.E., Jacobson, S.C., Waters, L. C., Foote, R.S., Ramsey, J.M., (2000) "Integrated System for Rapid PCR-Based DNA Analysis in Microfluidic Devices." Analytical Chemistry, 72, 2995-3000.

Kim D.S., Lee, S.H., Ahn, C.H., Lee, J.Y., Kwon, T.H. (2006) "Disposable integrated microfluidic biochip for blood typing by plastic microinjection moulding." Lab on a Chip, 6, 794-802.

Kim, J., Chaudhury, M.K., Owen, M.J. (2000) "Hydrophobic Recovery of Polydimethylsiloxane Elastomer Exposed to Partial Electrical Discharge." Journal of Colloid and Interface Science 226, 231–236.

Kim J.H., Kang, C.J., Kim, Y.S. (2004) "A disposable polydimethylsiloxane-based diffuser micropump actuated by piezoelectric-disc." Microelectronic Engineering, 71, 119-124.

Kim, L., Toh, Y.C., Voldman, J., Yu, H. (2007) "A practical guide to microfluidic perfusion culture of adherent mammalian cells." Lab Chip, 7, 681–694.

Kim, L., Vahey, M.D., Lee, H.Y., Voldman, J. (2006) “Microfluidic arrays for logarithmically perfused embryonic stem cell culture.” Lab Chip, 6, 394–406.

Koh, W.G., Pishko, M.V. (2006) “Fabrication of cell-containing hydrogel microstructures inside microfluidic devices that can be used as cell-based biosensors.” Analytical and Bioanalytical Chemistry, 385, 1389-1397.

Kohlheyer, D., Besselink, A.J., Schlautmann, S., Schasfoort, R.B. (2006) “Free-flow zone electrophoresis and isoelectric focusing using a microfabricated glass device with ion permeable membranes.” Lab on a Chip, 6, 374–380.

Kopp, M. U.; Mello, A. J.; Manz, A. (1998) “Chemical Amplification: Continuous-Flow PCR on a Chip.”Science, 280, 1046-1048.

Kovarik, M., Torrence, N.J., Spence, D.M., Martin, R.S. (2004) “Fabrication of carbon microelectrodes with a micromolding technique and their use in microchip-based flow analyses.” Analyst, 129, 400–40.

Lacey, M.E., Webb, A.G., Sweedler, J.V. (2000) “Monitoring Temperature Changes in Capillary Electrophoresis with Nanoliter-Volume NMR Thermometry” Analytical Chemistry, 72, 4991-4998.

Laser, D.J., Santiago J.G. (2004) “A review of micropumps.” Journal of Micromechanics and Microengineering, 14, R35-R64.

Leclerc, E., Sakai, Y., Fujii, T. (2004) “Microfluidic PDMS (Polydimethylsiloxane) Bioreactor for Large-Scale Culture of Hepatocytes.” Biotechnology Progress, 20, 750-755.

Lee, D.W., Cho, Y.H. (2007) “A continuous electrical cell lysis device using a low dc voltage for a cell transport and rupture.”Sensors and Actuators B, 124, 84–89.

Lee, J.N., Park, C., Whitesides, G.M. (2003) “Solvent Compatibility of Poly(dimethylsiloxane)-Based Microfluidic Devices.” Analytical Chemistry, 75, 6544-6554.

Lee, P.J., Hung, P.J., Rao, V.M., Lee, L.P. (2005) “Nanoliter Scale Microbioreactor Array for Quantitative Cell Biology.” Biotechnology and Bioengineering, 94, 5-10.

Lemoff, A.V., Lee, A.P. (2003) “An AC Magnetohydrodynamic Microfluidic Switch for Micro Total Analysis Systems.” Biomedical Microdevices, 5, 55-60.

Li, D. (2004) Electrokinetics in Microfluidics, Elsevier Academic, San Diego, CA.

Lide, D.R. ed. (1998) CRC Handbook of Chemistry and Physics: 79th edition, CRC-Press.

Lin C.H., Lee G.B., Chang B.W., Chang, G.L. (2002) “A new fabrication process for ultra-thick microfluidic microstructures utilizing SU-8 photoresist.” Journal of Micromechanics and Microengineering, 12, 590-597.

Liu, J., Cai B., Zhu, J., Ding, G., Zhao, X., Yang, C., Chen, D. (2004) “Process research of high aspect ratio microstructure using SU-8 resist.” Microsystem Technologies, 10, 265–268.

Liu, S., Pu, Q., Lu, J.J. (2003) “Electric field-decoupled electroosmotic pump for microfluidic devices.” Journal of Chromatography A, 1013, 57–64.

Liu, Y., Fanguy, J.C., Bledsoe, J.M., Henry, C.S. (2000) “Dynamic Coating Using Polyelectrolyte Multilayers for Chemical Control of Electroosmotic Flow in Capillary Electrophoresis Microchips.” Analytical Chemistry, 72, 5939-5944.

Liu Y., Wipf D., and Henry C. (2001) "Conductivity detection for monitoring mixing reactions in microfluidic devices", Analyst, 126, 1248–1251.

Lorenz, H., Landon, M., Renaud, P. (1998) “Mechanical Characterization of a New High-Aspect-Ratio Near UV-Photoresist.” Microelectronic Engineering, 41/42, 371-374.

Lu, H., Koo, L.Y., Wang, W.M., Lauffenburger, D.A., Griffith, L.G., Jensen, K.F. (2004) “Microfluidic Shear Devices for Quantitative Analysis of Cell Adhesion.” Analytical Chemistry, 76, 5257-5264.

Luo, Y., Huang, B., Wu, H., Zare, R.N. (2006) “Controlling Electroosmotic Flow inPoly(dimethylsiloxane) Separation Channels by Means of Prepolymer Additives.” Analytical Chemistry, 78,4588-4592.

Macka, M., Andersson, P., Haddad, P.R., “Changes in Electrolyte pH Due to Electrolysis during Capillary Zone Electrophoresis.”Analytical Chemistry, 70, 743-749.

Madou, M. Fundamentals of Microfabrication. CRC Press (2000)

Makamba, h., Kim, J.H., Lim, K., Park, N., Hahn, J.H. (2003) “Surface modification of poly(dimethylsiloxane) microchannels.” Electrophoresis, 24, 3607–3619.

Masliyah, J.H. (1994) Electrokinetic Transport Phenomena, AOSTRA, Edmonton, AB.

Mata, A. Fleischman, A.J., Roy, S. (2005) “Characterization of Polydimethylsiloxane (PDMS) Properties for Biomedical Micro/Nanosystems.” Biomedical Microdevices, 7, 281-293.

Mata, A., Fleischman, A.J., Roy, S. (2006) “Fabrication of multi-layer SU-8 microstructures.” Journal of Micromechanics and Microengineering,16, 276-284.

Martin, B.M. (1994) Tissue Culture Techniques: an introduction. Birkhauser, Boston, MA.

McDonald, J.C., Duffy, D.C., Anderson, J.R., Chiu, D.T., Wu, H., Schueller, O.J.A., Whitesides, G.M. (2000) “Fabrication of Microfluidic Systems in Poly (dimethylsiloxane).” Electrophoresis, 21, 27-40.Journal of Micromechanics and Microenginering, 16, 276–284.

McDonald, J.C., Whitesides, G.M. (2002) “Poly(dimethylsiloxane) as a Material for Fabricating Microfluidic Devices.” Accounts of Chemical Research, 35, 491-499.

Meinhart, C.D., Werely, S.T., Santiago, J.G. (1999) “PIV measurements of a microchannel flow. “ Experiments in Fluids, 27, 414-419.

Meinhart, C.D., Zhang, H. (2000) “The flow structure inside a micorfabricated inkjet printhead.” Journal of Microelectromechanical Systems, 9, 67-75.

Melin, J., Quake, S.R. (2007) “Microfluidic Large-Scale Integration: The Evolution of Design Rules for Biological Automation.” Annual Revue of Biophysics and Biomolecular Structures, 36, 213–31.

Min, J.Y., Kim, D., Kim, S.J. (2006) “A novel approach to analysis of electroosmotic pumping through rectangular-shaped microchannels.” Sensors and Actuators B, 120, 305-312.

Monahan, J., Gewirth, A.A., Nuzzo, R.G. (2001) “A Method for Filling Complex Polymeric Microfluidic Devices and Arrays.” Analytical Chemistry, 73, 3193-3197.

Moorthy, J. Khoury, C., Moore, J.S., Beebe, D.J. (2001) “Active control of electroosmotic flow in microchannels using light.” Sensors and Actuators B, 75, 223-229.

Morf, W.E., Guenat, O.T., de Rooij, N.F. (2001a) “Partial electroosmotic pumping in complex capillary systems: 1. Principles and general theoretical approach.” Sensors and Actuators B, 72, 266-272.

Morf, W.E., Guenat, O.T., de Rooij, N.F. (2001b) “Partial electroosmotic pumping in complex capillary systems Part 2: Fabrication and application of a micro total analysis system (μTAS) suited for continuous volumetric nanotitrations.” Sensors and Actuators B, 72, 273-282.

Murakami, T., Kuroda, S., Osawa Z. (1998) “Dynamics of polymeric solid surfaces treated with oxygen plasma: effect of aging media after plasma treatment.” Journal of Colloid and Interface Science, 2002, 37-44.

Neumann, E., Sowers, A.E., Jordan, C.A. (1989) Electroporation and Electrofusion in Cell Biology. Plenum Press, New York, NY.

Nguyen, N.T., Huang, X.Y., Chuan, T.K. (2002) “MEMS-micropumps: a review.” Transactions of ASME Journal of Fluids Engineering, 124,384-392.

Nguyen, N.T., Werely, S.T. (2002) Fundamentals and Applications of Microfluidics. Artech House, Inc. Norwood, MA.

Nguyen, N.T., White, R.M. (1999) “Design and optimization of an ultrasonic flexural plate wave micropump using numerical simulation.” Sensors and Actuators A, 77, 229-236.

Nguyen, N,T., Wu, Z. (2005) “Micromixers-a review.” Journal of Micormechanics and Microengineering, 15, R1-16.

Nordstrëm, M., Marie, R., Calleja, M., Boisen, A. (2004) “Rendering SU-8 hydrophilic to facilitate use in micro channel fabrication,” Journal of Micromechanics and Microengineering, 14, 1614-1617.

Oh, K.W., Ahn, C.H., (2006) “A review of microvalves.” Journal of Micromechanics and Microengineering, 16, R13-R39.

Olsson, A., Enoksson, P., Stemme, g., Stemme, E. (1997) “Micromachined flat-walled valveless diffuser pumps.” Journal of Micorelectromechancial Systems, 6, 161-166.

Oosterbroek, R.E., van den Berg, A. (2003) Lab-on-a-Chip Miniaturized Systems for (Bio)Chemical Analysis and Synthesis. Elsevier, Amsterdam, Netherlands.

Oriel product training manual: spectral irradiance, Newport Oriel, October 9, 2007.

Pallandre, A., de Lambert, B., Attia, R., Jonas, A.M., Viovy, J.L. (2006) "Surface treatment and characterization: Perspectives to electrophoresis and lab-on-chips." Electrophoresis, 27, 584–610.

Pan, T., McDonald, S.J., Kai, E.M., Ziaie, B. (2005) "A magnetically driven PDMS micropump with ball check-valves." Journal of Micromechanics and Microengineering, 15, 1021-1026.

Park, J.Y., Hwang, C.M., Lee, S.H., Lee, S.H. (2007) "Gradient generation by an osmotic pump and the behavior of humanmesenchymal stem cells under the fetal bovine serum concentration gradient." Lab on a Chip, 7, 1673–1680.

Paul P.H., Garguilo, M.G., Rakestraw, D.J. (1998) "Imaging of Pressure- and Electrokinetically Driven Flows through Open Capillaries." Analytical Chemistry, 70, 2459-2467.

Pennathur, S., Santiago, J.G. (2005) "Electrokinetic Transport in Nanochannels. 1. Theory." Analytical Chemistry, 77, 6772-6781.

Pittman, J.L., Henry, C.S., Gilman, S.D. (2003) "Experimental Studies of Electroosmotic Flow Dynamics in Microfabricated Devices during Current Monitoring Experiments." Analytical Chemistry, 75, 361-370.

Powers, M.J., Janigian, D.M., Wack, K.E., Baker, C.S, Stolz, D.B., Griffith, L.G. (2002) "Functional Behavior of Primary Rat Liver Cells in a Three-Dimensional Perfused Microarray Bioreactor." Tissue Engineering,8, 499-513.

Probstein R.F. (1994) Physiochemical Hydrodynamics. An Introduction. New York, John Wiley & Sons, Inc.

Qiao, R., Aluru, N.R. (2002) "A compact model for electroosmotic flows in microfluidic devices." Journal of Micromechanics and Microengineering, 12, 625-635.

Reichmuth, D.S., Chirica, G.S., Kirby, B.J. (2003) " Increasing the performance of high-pressure, high-efficiency electrokinetic micropumps using zwitterionic solute additives." Sensors and Actuators B, 92, 37–43.

Ren, L., Li, D., Qu, W. (2001) "Electro-Viscous Effects on Liquid Flow in Microchannels."Journal of Colloid and Interface Science , 233, 12–22.

Ren, L.Q., Escobedo-Canseco, C., Li, D. Q. (2001) "Electroosmotic flow in a microcapillary with one solution displacing another solution." Journal of Colloid Interface Science, 242, 264 – 271.

Ren, L.Q., Escobedo-Canseco, C., Li, D. Q., (2002) "A New Method of Evaluating the Average Electro-Osmotic Velocity in Microchannels." Journal of Colloid Interface Science, 250, 238 – 242.

Ren, X., Bachman, M., Sims, C., Li, G.P. Allbritton, N. (2001) “Electroosmotic properties of microfluidic channels composed of poly(dimethylsiloxane).” Journal of Chromatography B, 762, 117-125.

Richter, M., Linnemann, R., Woias, P. (1998) “ Robust design of gas and liquid micropumps.” Sensors and Actuators A, 68, 480-486.

Rodriguez, I., Chandrasekhar, N. (2005) “Experimental study and numerical estimation of current changes in electroosmotically pumped microfluidic devices.” Electrophoresis, 26, 1114–1121.

Roman, G.T., Hlaus, T., Bass, K.J., Sellhammer, T.G., Culbertson, C.T. (2005) “Sol-Gel Modified Poly(dimethylsiloxane) Microfluidic Devices with High Electroosmotic Mobilities and Hydrophilic Channel Wall Characteristics.” Analytical Chemistry, 77,1414-1422.

Roman, G.T., McDaniel, K., Cristopher, C.T., (2006) “High efficiency micellar electrokinetic chromatography of hydrophobic analytes on poly(dimethylsiloxane) microchips.” Analyst, 131, 194–201.

Ross, D., Gaitan, M., Locascio, L.E. (2001) “Temperature Measurement in Microfluidic Systems Using a Temperature-Dependent Fluorescent Dye” Analytical Chemistry, 73, 4117-4123.

Samy, R., Glawdel, T., Ren, C.L. (2007) “A Novel Method for Microfluidic Whole-Chip Temperature Measurement Using Thin-Film PDMS/Rhodamine B.”Analytical Chemistry, accepted in Oct., 2007.

Santiago, J.G., Werely S.T., Meinhart, C.D., Beebe, D.J., Adrian, R.J. (1998) “A particle image velocimetry system for microfluidics.” Experiments in Fluids, 25, 316-319.

Shao, Z., Ren, L.C., Schneider, G.E. (2006) “A 3D electrokinetic flow structure of solution displacement in microchannels for on-chip sample preparation.” Journal of Micromechanics and Microengineering Applications, 16, 589-600.

Shackman, J.G., Dahlgren, G.M., Peters, J.L., Kennedy R. T. (2005) “Perfusion and chemical monitoring of living cells on a microfluidic chip,” Lab on a Chip, 5, 56–63.

Shin. S, Kang. I, and Cho Y. (2007) "A new method to measure zeta potentials of microfabricated channels by applying a time-periodic electric field in a T-channel", Journal of Colloids and Surfaces,294 , 228-23.5

Sia, S.K., Whitesides, G.M. (2003) “Microfluidic devices fabricated in poly(dimethylsiloxane) for biological studies.” Electrophoresis, 24, 3563-3576.

Sinton, D., Escobedo, C., Ren, L., Li, D. (2002) “Direct and Indirect Electro-osmotic Flow Velocity Measurements in Microchannels.” Journal of Colloid and Interface Science, 254, 184-189.

Sinton, D. (2004) “Microscale flow visualization.” Microfluid Nanofluid, 1, 2-21.

Sinton, D., Ren, L., Li, D. (2002) “Visualization and numerical modelling of microfluidic on-chip injection processes.” Journal of Colloid and Interface Science, 260, 431–439.

Slentz, B.E., Penner, N.A., Regnier, F.E. (2002) “Capillary electrochromatography of peptides on microfabricated poly(dimethylsiloxane) chips modified by cerium(IV)-catalyzed polymerization.” Journal of Chromatography A, 948, 225–233.

Spehar, A-M., Koster, S., Linder, V., Kulmala, S., de Rooij, N.F., Verpoorte, E., Sigrist, H., Thormann, W. (2003) “Electrokinetic Characterization of Poly (dimethylsiloxane Microchannels.” Electrophoresis, 24, 367-3678.

Stangegaard, M., Petronis, S., Jørgensen, A.M., Christensen, C.B.V., Dufva M. (2006) “A biocompatible micro cell culture chamber (mCCC) for the culturing and on-line monitoring of eukaryote cells” Lab Chip, 6, 1045–1051.

Stellwage, N.C., Bossi, Al, Gelfi, C., Righetti, P.G. (2000) “DNA and Buffers: Are There Any Noninteracting, Neutral pH Buffers?” Analytical Biochemistry, 287, 167-175.

Stone, H.A., Stroock, A.D., Ajdari, A. (2004) “Engineering Flows in Small Devices: Microfluidics Toward a Lab-on-a-Chip.” Annual Revue Fluid Mechanics, 36,381–411.

Studer, V., Pepin, A., Chen, Y., Ajdarib, A. (2004) “An integrated AC electrokinetic pump in a microfluidic loop for fast and tuneable flow control.” Analyst, 129, 944-949.

Squires, T.M., Quake S.R. (2005) “Microfluidics: Fluid physics at the nanolitre scale.” Reviews of Modern Physics, 77, 977-1026.

Sze, A., Erickson, D., Ren, L., Li, D. (2003) “Zeta-potential measurement using the Smoluchowski equation and the slope of the current–time relationship in electroosmotic flow.” Journal of Colloid and Interface Science, 261, 402-410.

Tabeling, P. (2005) Introduction to Microfluidics, Oxford University Press, Newyork, NY.

Takamura, Y., Onaoda, H., Inokuchi, H., Adachi, S., Oki, A., Horiike, Y. (2003) “Low-voltage electroosmosis pump for stand-alone microfluidics devices.” Electrophoresis, 24, 185–192.

Takayama, S., McDonald, J.C., Ostuni, E., Liang, M.N., Kenis, P.J.A., Ismagilov, R.F., Whitesides, G.M. (1999) “Patterning cells and their environments using multiple laminar fluid flows in capillary networks.” Proceedings of the National Academy of Sciences USA, 96, 5545–5548.

Taylor, J. K. (2007) The Design and Evaluation of a Microfluidic Cell Sorting Chip. M.A.Sc thesis, University of Waterloo.

Toepke, M.W., Beebe, D.J. (2006) “PDMS absorption of small molecules and consequences in microfluidic applications.” Lab on a Chip, 6, 11484-1486.

Tourovskaia, A., Figueroa-Masot, X., Folch, A. (2005) “Differentiation-on-a-chip: A microfluidic platform for long-term cell culture studies.” Lab Chip, 5, 14–19.

Toworfe, G.K., Composto, R.J., Adams, C.S., Shapiro, I.M., Ducheyne, P. (2004) "Fibronectin adsorption on surface-activated poly(dimethylsiloxane) and its effect on cellular function." Journal of Biomedical Materials Research Part A,3, 449-461.

Tripp, J.A., Svec, F., Frechet, J.M.J., Zeng, S., Mikkelsen, J.C., Santiago, J.G. (2004) "High-pressure electroosmotic pumps based on porous polymer monoliths." Sensors and Actuators B, 99, 66-73.

Tsai, N.C., Sue, C.Y. (2007) "Review of MEMS-based drug delivery and dosing systems." Sensors and Actuators A, 134, 555–564.

Tseng, F.G. (2006) "Nano/micro fluidic Systems: Design, Characterization, and Biomedical Applications." Nanomechanics of Materials and Structures, 109-119.

Unger,M. A., Chou, H., Thorsen, T., Scherer, A., Quake, S. R. (2000) "Monolithic microfabricated valves and pumps by multilayer soft lithography." Science, 288, 113–116.

Venditti,R., Xuan, X., Li, D. (2006) "Experimental characterization of the temperature dependence of zeta potential and its effect on electroosmotic flow velocity in microchannels." Microfluid Nanofluid, 2, 493-499.

Vickers, J.A., Caulum M.M., Henry, C.S. (2006) "Generation of Hydrophilic Poly(dimethylsioxane) for High-Performance Microchip Electrophoresis." Analytical Chemistry, 78, 7446-7452.

Vilkner, T., Janasek, D., Manz, A. (2004) "Micro Total Analysis Systems. Recent Developments." Analytical Chemistry, 76, 3373-3386.

Vollmer, A.P., Probstein, R.F., Gilbert, R. Thorsen T. (2005) "Development of an integrated microfluidic platform for dynamic oxygen sensing and delivery in a flowing medium." Lab on a Chip, 5, 1059-1066.

Vozzi, G., Flaim, C., Ahluwaliaa, A., Bhatia, S. (2003) "Fabrication of PLGA scaffolds using soft lithography and microsyringe deposition." Biomaterials, 24, 2533-2540.

Vunjak-Novakovic, G., Freshney, R.I. (2006) Culture of Cells for Tissue Engineering. John Wiley and Sons, Hoboken, NJ.

Walker, G.M., Beebe, D.J. (2002) "A Passive Pumping Method for Microfludic Devices." Lab Chip, 2, 131-134.

Walker, G.M., Ozers, M.S., Beebe, D.J. (2002) "Insect Cell Culture in Microchannel." Biomedical Microdevices, 4, 161-166.

Walker, G.M., Zeringue, H.C., Beebe, D.J. (2004) "Microenvironment design consideration for cellular scale studies." Lab on a Chip, 4, 91-97.

Wang, B., Chen, L, Abdulali-Kanji, Z., Horton, J.H., Oleschuk, R.D. (2003) "Aging Effects on Oxidized and Amine-Modified Poly(dimethylsiloxane) Surfaces Studied with Chemical Force Titrations: Effects on Electroosmotic Flow Rate in Microfluidic Channels." Langmuir 2003, 19, 9792-9798

Wang, P., Chen, Z., Chang, H.C. (2006) "A new electro-osmotic pump based on silica monoliths." Sensors and Actuators B, 113, 500–509.

Wang, Y., Bedekar, A.S., Krishnamoorthy, S., Siddhaye, S.S., Sundaram, S. (2007) "System-level modeling and simulation of biochemical assays in lab-on-a-chip devices." Microfluid Nanofluid, 3, 307-322.

Wang, Y., Lin, Q., Mukherjee, T. (2006) "Composable Behavioral Models and Schematic-Based Simulation of Electrokinetic Lab-on-a-Chip Systems." IEEE Transactions on Computer-aided Design of Integrated Circuits and Systems, 25, 259-273.

Weaver JC. 1995. Electroporation Theory: Concepts and Mechanisms. In: Nickoloff JA, editor. Electroporation Protocols for Microorganisms. Totowa, New Jersey: Humana Press. p 1-26.

Werner, C., Zimmermann, R., Kratzmuller. (2001) "Streaming potential and streaming current measurements at planar solid/liquid interfaces for simultaneous determination of zeta potential and surface conductivity."Colloids and Surfaces A: Physicochemical and Engineering Aspects, 192, 205–213.

White, F. M. (1974) Viscous Fluid Flow, McGraw-Hill, New York, NY.

White, F.M. (1999) Fluid Mechanics, 4th Edition, McGraw-Hill, New York, NY.

Williams, J.D., Wang. W. (2004) "Using megasonic development of SU-8 to yield ultra-high aspect ratio microstructures with UV lithography." Microsystem Technologies, 10, 694–698.

Won Roo, K., Lim, K., Kim, H., Hahn, J.H., (2002) "Poly(dimethylsiloxane) microchip for precolumn reaction and micellar electrokinetic chromatography of biogenic amines." Electrophoresis, 23, 1129–1137.

Wong, P.K., Wang, T.H., Deval, J.H., Ho, C.M. (2004) "Electrokinetics in Micro Devices for Biotechnology Applications." IEEE/ASME Transactions on Mechatronics, VOL. 9, NO. 2.

Wu, H., Huang, B., Zare, B.N. (2005) "Construction of microfluidic chips using polydimethylsiloxane for adhesive bonding." Lab Chip, 5, 1393-1398.

Wu, M.H., Urban, J.P., Cui, Z., Cui, Z.F. (2006) "Development of PDMS microbioreactor with well-defined and homogenous culture environment for chondrocyte 3-D culture." Biomed. Microdevices, 8, 331–340.

Xia, Y., Whitesides, G.M. (1998) "Soft Lithography" Annual Review of Material Science, 28, 153-184.

Xuan, X., Li, D. (2004) “Analysis of electrokinetic flow in microfluidic networks.” Journal of Micromechanics and Microengineering, 14, 290-298.

Xuan, X., Xu, B., Sinton, D., Li, D. (2004) “Electroosmotic flow with Joule heating effects.” Lab on a Chip, 4, 230-236.

Xue, Z., Qiu, H. (2005) “Integrating micromachined fast response temperature sensor array in a glass microchannel.” Sensors and Actuators A, 112, 189-195.

Yan, D., Nguyen, N.T., Yang, C., Huang, X. (2006) “Visualizing the transient electroosmotic flow and measuring the zeta potential of microchannels with a micro-PIV technique.” Journal of Chemical Physics, 124, 021103.

Yang, R., Wang, W. (2005) “A numerical and experimental study on gap compensation and wavelength selection in UV-lithography of ultra-high aspect ratio SU-8 microstructures.” Sensors and Actuators B, 110, 279–288.

Yao, S., Myers, A.M., Posner, J.D., Rose, K.A., Santiago, J.G. (2006) “Electroosmotic Pumps Fabricated From Porous Silicon Membranes.” Journal of Microelectromechanical Systems, 15, 717-727.

Yao, S.H., Hertzog, D.E., Zeng, S.L., Mikkelsen, J.C., Santiago, J.G. (2003) “Porous glass electroosmotic pumps: design and experiments.” Journal of Colloid and Interface Science, 268, 143-153.

Yao, S.H., Santiago, J.G. (2003) “Porous glass electroosmotic pumps: theory.” Journal of Colloid and Interface Science, 268, 133-142.

Yi, C., Li, C.W., Ji, S., Yang, M. (2006) “Microfluidics technology for manipulation and analysis of biological cells.” Analytica Chimica Acta, 560, 1-23.

Zeng, H.E.; Li, H.F.; Wang, X.; Lin, J.M., 2006, “Development of a gel monolithic column polydimethylsiloxane microfluidic device for rapid electrophoresis separation,” Talanta ,69, 226–231.

Zeng, S.L., Chen C.H., Mikkelsen, J.G., Santiago, J.G. (2001) “Fabrication and characterization of electroosmotic micro pumps.” Sensors and Actuators B, 79, 107-114.

Zhang, C., Xu, J., Ma, W., Zheng, M. (2006) “PCR microfluidic devices for DNA amplification.” Biotechnology Advances, 24, 243-284.

Zhang, Y., Gu, X.J., Barber, R.W., Emerson, D.R. (2004) “An analysis of induced pressure fields in electroosmotic flows through microchannels.” Journal of Colloid and Interface Science, 276, 670–678.

Zhu, X., Chu, L.Y., Chueh, B., Shen, M., Hazarika, B., Phadke N., Takayama, S. (2004) “Arrays of horizontally-oriented mini-reservoirs generate steady microfluidic flows for continuous perfusion cell culture and gradient generation.” Analyst, 129, 1026-1031.

Appendix A: Circuit Equivalency Analysis 1-EC EO Pump

The circuit equivalency model was applied to solve the flow rate in the 1-EC EO Pump design. A diagram of the 1-EC EO Pump is provided in figure A.1.

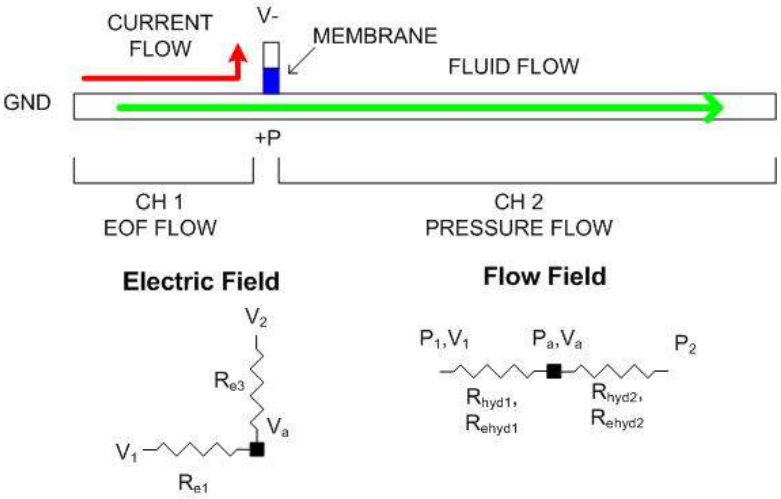

Figure A.1 Schematic of the 1-EC pump design describing the electrical and flow fields.

Appling the electric field component of the 1D model:

$$I = \frac{V_1 - V_2}{R_{e1} + R_{e2}} \tag{A.1}$$

Where the junction voltage V_a is therefore:

$$V_a = V_1 - I\left(\frac{R_{e1}}{R_{e1} + R_{e3}}\right) \tag{A.2}$$

Applying the flow field component of the 1D model:

$$Q_1 = \frac{(V_1 - V_a)}{R_{ehyd1}} - \frac{P_a}{R_{hyd1}} \tag{A.3}$$

$$Q_2 = \frac{P_a}{R_{hyd2}} \tag{A.4}$$

Since $Q_2 = Q_1$ due to continuity:

$$\frac{P_a}{R_{hyd2}} = \frac{(V_1 - V_a)}{R_{ehyd1}} - \frac{P_a}{R_{hyd1}} \quad \textbf{(A.5)}$$

Rearranging the above equation to solve for the junction pressure:

$$P_a = \frac{(V_1 - V_a)}{R_{ehyd1}} \frac{R_{hyd1} R_{hyd2}}{R_{hyd1} + R_{hyd2}} \quad \textbf{(A.6)}$$

Subbing back into A.4 the flow rate can be found:

$$Q = \frac{(V_1 - V_a)}{R_{ehyd1}} \left(\frac{R_{hyd_1}}{R_{hyd1} + R_{hyd2}} \right) \quad \textbf{(A.7)}$$

Therefore the performance of the pump can be evaluated from equation A.7.

Appendix B: Circuit Equivalency Analysis 2-EC EO Pump

The circuit equivalency model was applied to solve the flow rate in the 2-EC EO Pump design. A diagram of the 2-EC EO Pump is provided in figure B.1.

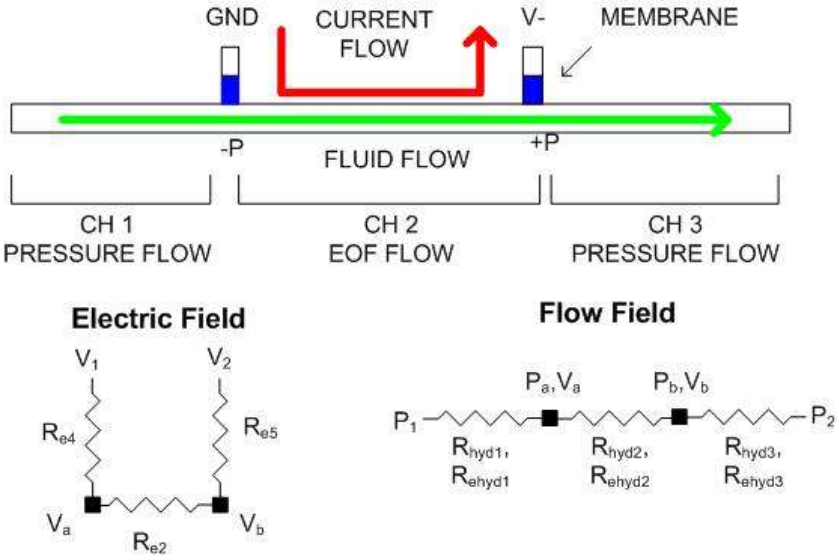

Figure B.1 Schematic of the 2-EC pump design describing the electrical and flow fields.

Appling the electric field component of the 1D model:

$$I = \frac{V_1 - V_2}{R_{e4} + R_{e2} + R_{e5}} \tag{B.1}$$

Where the junction voltages V_a and V_b are:

$$V_a = V_1 - I\left(\frac{R_{e4}}{R_{e4} + R_{e2} + R_{e5}}\right) \qquad V_b = V_1 - I\left(\frac{R_{e4} + R_{e2}}{R_{e4} + R_{e2} + R_{e5}}\right) \tag{B.2}$$

Applying the flow field component of the 1D model:

$$Q_1 = -\frac{P_a}{R_{hyd1}} \tag{B.3}$$

$$Q_2 = \frac{(V_a - V_b)}{R_{ehyd2}} - \frac{(P_b - P_a)}{R_{hyd2}} \tag{B.4}$$

$$Q_3 = \frac{P_b}{R_{hyd3}} \tag{B.5}$$

Since $Q_1 = Q_2 = Q_3$ due to continuity, the junction pressures are:

$$P_a = -\frac{(V_a - V_b)}{R_{ehyd2}}\left(\frac{R_{hyd1}R_{hyd2}}{R_{hyd1} + R_{hyd2} + R_{hyd3}}\right) \tag{B.6}$$

$$P_b = -P_a\left(\frac{R_{hyd3}}{R_{hyd1}}\right) \tag{B.7}$$

Subbing back the flow rate can be found:

$$Q = \frac{(V_a - V_b)}{R_{ehyd2}}\left(\frac{R_{hyd2}}{R_{hyd1} + R_{hyd2} + R_{hyd3}}\right) \tag{B.8}$$

Therefore the performance of the pump can be evaluated from equation B.8. The efficiency of an EO pump is described by the following equation developed by Chen and Santiago (2002):

$$\eta = \frac{\dot{W}_{P,\max}}{VI} \tag{B.9}$$

where $\dot{W}_{P,\max}$ is the maximum pressure work output of the pump which is given as:

$$\dot{W}_{P,\max} = 3(Lhw)\mu\left(\frac{\mu_{eof}}{D}\frac{V}{L}\right)^2 \tag{B.10}$$

and the electrical current is given as, where the dimensions refer to the EOF channel:

$$I = \frac{V\lambda_b w_{eof} h_{eof}}{L_{eof}} \tag{B.11}$$

Substituting and minimizing the terms the approximate efficiency of a planar EO pump is:

$$\eta = 3\left(\frac{\mu}{\lambda_b}\right)\left(\frac{\mu_{eof}}{h_{eof}}\right)^2 \tag{B.12}$$

The equations stated above can thus be used to design a planar EO pump assuming a thin EDL compared to channel height.

Appendix C: Chip Fabrication Procedure

Chip fabrication was done at the University of Waterloo Microfluidics and Biochips Laboratory. The general fabrication procedures for making the PDMS molds are discussed in Chapter 5. The fabrication of the EO pumps is discussed in Chapter 7. The steps associated with the complete chip fabrication are summarized below:

Master Fabrication

The following summarize the procedure for fabricating the master for the PDMS molds. Four levels of SU-8 features are fabrication on a silicon wafer.. The first layer is coated and exposed over the entire substrate. This layer improves adhesion between the microchannel structures and the wafer. The second layer is 2.5µm deep and contains the EOF channels of the EO pump. The third layer is 2.5µm deep but the structures are 5µm (summing the thickness of all the previous layers) and contains the intersecting microchannel. The final layer is 75µm deep and contains the rest of the microchannel network including the cell chambers.

1. **Mask Printing**
    - Masks were design in AutoCad and printed on Mylar transparency film from CAD/Art Services.
    - Once masks were received they were cut and trimmed for each specific design.
    - Masks were then kept in static free bags to prevent scratching.
    - 3 Masks were prepared with overlapping features. Mask #1 has the EOF pumping channels, #2, the intersecting channel and #3 the cell chambers and rest of the microfluidic network.

2. **Substrate Preparation**
    - The 4" Silicon wafers that were used were of virgin quality
    - Blown dry with N_2 to remove any dust particles on the substrate

3. **Dehydration Bake**
    - Removes H_20 molecules on the surface of the substrate
    - 20 minutes at 200°C, followed by 10 minute cool down
    - Afterwards hotplates are set to 95°C, 65°C, 50°C for soft bake and post bake.

4. **SU-8 Dispensing**
    - Use EFD pressurized dispenser, choose the appropriate syringe tube with the desired SU-8. Tips are connected to the syringe, the type of tip depends on the viscosity of the SU-8. For SU-8 2005 22g Taper Tip, Su-8 2025 18g Taper Tip. Pressures for these two conditions are 15psi and 25psi.

5. **Spin Coating #1: Adhesion Layer**
    - 5µm depth SU-8 2005
    - Coat entire substrate with SU-8 using the EFD dispenser.
    - 0-500 rpm @ 300rpm/s –hold for 5s
    - 500-3000 rpm @ 300rpm/s- hold for 30s

6. **Soft Bake #1: Adhesion Layer**
    - 2min @ 65°C, 2min 95°C, 30s 65°C, 30s 50°C

7. **UV Exposure #1: Adhesion Layer**
    - Place substrate in mask aligner, no mask is required as this is a flood exposure
    - 350mJ/cm^2 exposure dose entered (actually corresponds to 150mJ/cm^2)

8. **Post Exposure Bake #1: Adhesion Layer**
    - 2min @ 65°C, 2min 95°C, 30s 65°C, 30s 50°C
    - Followed by 10 minute cool down

9. **Spin Coat #2: EOF channels in EO Pump**
    - 2.5µm depth SU-8 2002
    - Coat entire substrate with SU-8 using the EFD dispenser.
    - 0-500 rpm @ 300rpm/s –hold for 5s
    - 500-3000 rpm @ 300rpm/s- hold for 30s

10. **Soft Bake #2: EOF channels in EO Pump**
    - 2min @ 65°C, 2min 95°C, 30s 65°C, 30s 50°C

11. **UV Exposure #2: EOF channels in EO Pump**
    - Place substrate in mask aligner, mask for EOF channels is place over top of the substrate. Vacuum of 5psi is used to improve mask to substrate contact.
    - 350mJ/cm^2 exposure dose entered (actually corresponds to 150mJ/cm^2)

12. **Post Exposure Bake #2: EOF channels in EO Pump**
    - 2min @ 65°C, 2min 95°C, 30s 65°C, 30s 50°C
    - Followed by 10 minute cool down

13. **Spin Coat #3: Intersecting Channel Layer**
    - 2.5µm depth SU-8 2002
    - Coat entire substrate with SU-8 using the EFD dispenser.
    - 0-500 rpm @ 300rpm/s –hold for 5s
    - 500-3000 rpm @ 300rpm/s- hold for 30s

14. **Soft Bake #3: Intersecting Channel Layer**
    - 2min @ 65°C, 2min 95°C, 30s 65°C, 30s 50°**C**

15. **UV Exposure #3: Intersecting Channel Layer**
    - Place substrate in mask aligner, mask for Intersecting Channel Layer is place over top of the substrate. Vacuum of 5psi is used to improve mask to substrate contact.
    - 350mJ/cm^2 exposure dose entered (actually corresponds to 150mJ/cm^2)

16. **Post Exposure Bake #3: Intersecting Channel Layer**
    - 2min @ 65°C, 2min 95°C, 30s 65°C, 30s 50°C
    - Followed by 10 minute cool down

17. **Spin Coat #4: Cell Chambers and Network**
    - 75µm depth SU-8 2025
    - Dynamic coating of substrate.
    - 0-100 rpm @ 300rpm/s –hold for 10s
    - 100-500 rpm @ 100rpm/s-hold for 5s
    - 500-1000 rpm @ 300rpm/s- hold for 30s

18. **Soft Bake #4: Cell Chambers and Network**
    - 3min @ 65°C, 10min 95°C, 2min 65°C, 2min 50°

19. **UV Exposure #4: Cell Chambers and Network**
    - Place substrate in mask aligner, mask for Cell Chambers and Network is place over top of the substrate. Vacuum of 5psi is used to improve mask to substrate contact.
    - 800mJ/cm^2 exposure dose entered (corresponds to 200mJ/cm^2

20. **Post Exposure Bake #4: Cell Chambers and Network**
    - 2min @ 65°C, 9min 95°C, 2min 65°C, 2min 50°C
    - Followed by 39 minute cool down on glass plate to slow thermal contraction.

21. **SU-8 Development**
    - 10 minutes in Su-8 Developer with agitation from N_2 gas.
    - Substrate is removed from developer, rinsed with isopropanol and then water.
    - Rinsed with fresh developer to remove residue, then isopropanol and DI water.
    - Blow dry with N_2 gas.

22. **Silanization of Master**
    - Place master in vacuum desiccator with 1mL of TCMS for 20-30 min.

23. **Storage of Master**
    - Master is stored when not used in specialized wafer holders.

Chip Fabrication with Gel Salt Bridges

The following summarizes the fabrication of the PDMS chip with EO pumps. This includes bonding the chip and fabricating the gel salt bridges.

1. **PDMS Replication**
    - Mix PDMS base and curing agent 10:1 (w/w) in disposable container. For silicon wafer total weight is between 35-40g for 2.5mm thick mold.
    - Mix for at least 5minutes, many bubbles should be trapped in the PDMS once fully mixed. Degass mixture in vacuum chamber at 27inHg vacuum pressure for 20min.
    - Substrate is placed in aluminium holding dish and mixture is poured over. The substrate is then placed in the vacuum chamber and degassed for another 10min.
    - PDMS is cured at 80°C for a minimum of 1.5hrs. However, extended baking times were extended to 12hrs to improve the quality of the PDMS.
    - Cured PDMS is trimmed and cut with a medical scalpel. Three designs are replicated at once and are cut out.
    - Reservoirs are punched with a leather tool punch (2mm).

2. **Air Plasma Bonding**
    - A glass slide cleaned with Pirahna etch or RCA 1 is obtained.
    - The mold and slide are cleaned with UP water and blown dry with N_2.
    - The pieces are placed in the plasma cleaner. The valve is closed and the vacuum pump turned on. Pump runs fro 10s before the plasma coil is turned on for 50s. Afterwards the vacuum is released.
    - The PDMS piece is laid over top of the glass slide and the sides of the PDMS are pinched lightly to increase the contact and remove trapped air.
    - Channels are filled with Bind Silane solution and left for 30 minutes. This treatment helps the gel adhere to the channel walls.

3. **Gel Salt Bridge Fabrication: Exposure**
    - While waiting for the Bind Silane treatment the gel exposure areas in the two EO pumps are taped off with electrical tape on the glass slide. The mercury lamp on the microscope is also turned on to warm up.

- The gel solution is then infused in the EO pumps by placing some of the solution in one reservoir and then using a vacuum created by a syringe to draw the solution through. Only one side of the EO pumps are filled with the solution at a time so that there is no inadvertent exposure.
- The chip is placed on the microscope stage and the gel post regions are visualized using the CCD camera and low power halogen lamp.
- Once the areas are in focus, the mercury lamp is switched on and the exposure is monitored in real time using the CCD camera. Using the microscope stage the objective is moved along the EO pump until all of the gel regions are exposed
- The process is then repeated for the rest of the gel regions (4x).

4. **Gel Salt Bridge: Flushing**
    - After exposure of the gels, the chip is flushed with several solutions in order to remove the excess gel solution.
    - Using the syringe pump and connecting to the chip via the Luer connectors with the EFD dispensing tips successive flushes of 10% IPA, UP water, and 0.5% NaOH are performed.
    - The flow rate in each case is 20μL/min for 5 minutes. This is also done for each branch of the channel (3x).

5. **Attaching Luer Connectors**
    - Luer connectors are attached to the PDMS chips over top of the reservoirs to extend the volume and to allow for direct connection with tubing and other medical devices.
    - To attach the connectors silicone sealant is gently spread over the bottom surface of the connector which is then pressed on the PDMS.
    - Curing takes approximately 30min. The bond is permanent with the PDMS but only semi-permanent with the polypropylene connectors so later the connectors can be removed.
    - The Luer connectors are then filled with water and either sealed with caps or tape until the chip is needed.

Appendix D: Diverting flow to the cell chamber with the EO pump

This appendix is a video file demonstrating the use of the EO pump to divert flow from the cell chamber. The file name is "Diverting flow from the cell chamber with the EO pump.avi"

If you accessed this thesis from a source other than the University of Waterloo, you may not have access to this file. You may access it by searching for this thesis at http://uwspace.uwaterloo.ca .

Note that this video was taken with the 3rd generation pump so the network dimensions are slightly altered but the overall geometry is similar. This video demonstrates the EO pump diverting flow away from the cell chamber. The location is at the junction between the intersecting channel and the EO pump/cell culture chamber as shown in Figure D.1. The channel that extends to the left of the image wraps around and becomes the bottom channel which leads to the inlet of the EO pump.

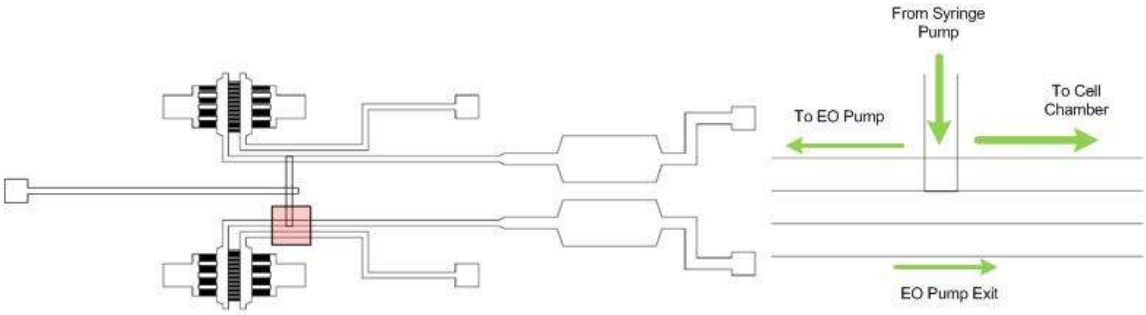

Figure D.1 Field of view of video #1. On the right a close up of the network geometry in the video indicating the flow direction and locations of the EO pump and cell chamber channels.

A syringe pump is used to provide a constant flow rate to the cell culture chamber at 1μL/min. The EO pump is already turned on at 100μA (0.25μL/min) and is drawing a small flow rate from the main flow. At the 8s mark the pump is set to 200μA (0.5μL/min) and the flow splits equally between the two channels. Again at the 12s mark the pump is set back to 100μA and the flow rate to the EO pump decreases accordingly. This video shows that with the integrated EO pumps dynamic control of the flow rate to the cell culture chambers is possible.

Appendix E: EO Pump operation has no affect on other pump

This appendix is a video file which demonstrates that the two EO pumps in the cell culture network operate independently from each other. The file name is “EO Pump operation has no affect on other pump.avi”

If you accessed this thesis from a source other than the University of Waterloo, you may not have access to this file. You may access it by searching for this thesis at http://uwspace.uwaterloo.ca .

The purpose of this video is to show that the two pumps are effectively isolated from each other. The system is in the second operation mode and the field of view in the video is shown in Figure E.1. At first only the syringe pump is operating and the focus is on the left junction. The camera pans across the intersecting channel to the opposite junction to demonstrate that the flow is symmetric. Then the camera pans back to the other junction and the left EO pump is turned on so that the flow rate changes in the left cell chamber. Again the camera pans to the right side to show that there is no noticeable difference in the flow rate while the left EO pump is operating which confirms the results from the 1D network analysis.

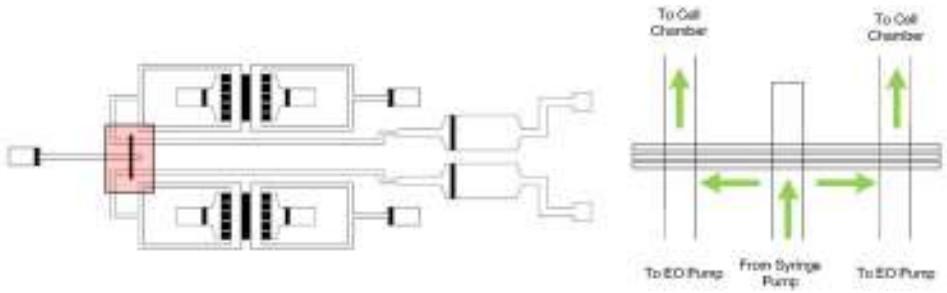

Figure E.1 Field of view of video #2. On the right a close up of the network geometry in the video indicating the flow direction and locations of the EO pump and cell chamber channels.

Appendix F: EO Pump injection into main stream

This appendix is a video file which demonstrates that the use of the EO pump to inject a small amount of fluid into the main stream. The file name is "EO pump injection into main stream.avi"

If you accessed this thesis from a source other than the University of Waterloo, you may not have access to this file. You may access it by searching for this thesis at http://uwspace.uwaterloo.ca .

This video demonstrates the third network configuration where the EO pump is used to inject fluid into the main stream. The incoming flow from the syringe pump contains 100μM fluorescein dye while the fluid from the EO pump does not. Initially the EO pump is turned off and the flow travels toward the cell chamber. At the 2s mark, the EO pump is turned on briefly to inject a small sample of non-dyed fluid into the mainstream which then travels towards the cell chamber. This video demonstrates the quick response of the EO pump in both continuous and intermittent flow control.

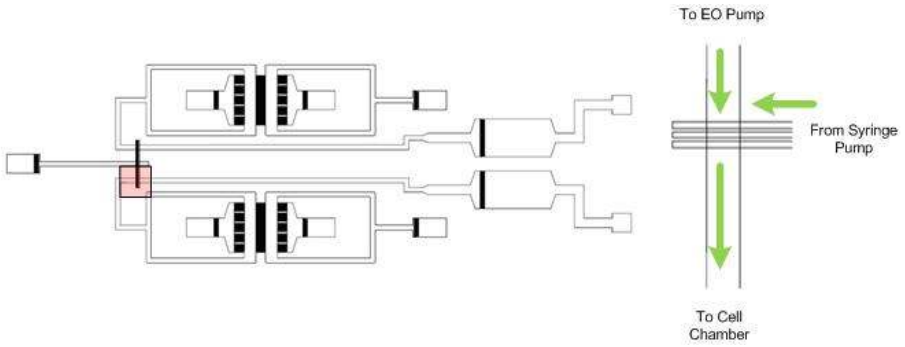

Figure F.1 Field of view of video #3. On the right a close up of the network geometry in the video indicating the flow direction and locations of the EO pump and cell chamber channels.

Appendix G: Cell inflow during seeding

This appendix is a video file which shows cells being transported into the cell chamber during the seeding step. The file name is “Cell inflow during seeding.mov”

For cell culture purposes, seeding cells and attaching them to the substrate is the first step in the experiment. The video shows the cells in suspension being transported with the fluid into the cell chamber. One notices that the cells do not pass individually but a grouped together in larger clusters. Although a single cell may be small (5-10μm) a cluster of cells is quite large (10-200μm in diameter) and may clog the microchannel.